SYSTEM INVESTIGATION OF LY303511-INDUCED SENSITIZATION OF HELA CELLS TO TRAIL-INDUCED APOPTOSIS: ROLE OF HYDROGEN PEROXIDE, PEROXYNITRITE, NITRIC OXIDE AND CALCIUM

SHI YUAN

(*Master of Computer Science, Wuhan University*)

A THESIS SUBMITTED

FOR THE DEGREE OF DOCTOR OF PHILOSOPHY

IN COMPUTATION AND SYSTEMS BIOLOGY (CSB)

SINGAPORE-MIT ALLIANCE

NATIONAL UNIVERSITY OF SINGAPORE

2012

DECLARATION

I hereby declare that this thesis is my original work and it has been written by me in its entirety.

I have duly acknowledged all the sources of information which have been used in the thesis.

This thesis has also not been submitted for any degree in any university previously.

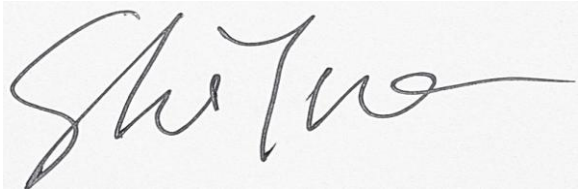

SHI YUAN
22 September 2012

Acknowledgements

It has been a long journey since 2007 when I started my PhD study in SMA program. Looking back, I do love the challenge and opportunity it brought to me. The experience taught me that life is a journey filled with excitements as well as disappointments. It also taught me to wait patiently and never worry too much.

To Professor Shazib Pervaiz and Professor Jacob K. White, Thank you for being my supervisors and mentoring during my PhD study and I always feel honored to be your student. I am really grateful to the valuable opportunity you provided in the field of cancer therapy using computational biology strategy. Thank you for the excellent guidance, persistent support and invaluable advice. During the period, you had been very patient and always encouraged me not to worry too much. In addition, I am thankful to the offering of financial support during the period of my thesis writing. Professor White, I also appreciate your input in reviewing my thesis during your recovery process from surgery. It really means a lot to me.

To Lisa Tucker-Kellogg, besides being a good mentor, you are also a good friend of mine. I will always remember the wide sincere heartwarming smile on your face. Thank you for offering help and care whenever you sensed my depression. Thank you also for supporting me through the whole project and providing a lot of valuable suggestion. I am very grateful to you for refining my thesis and providing many good texts.

To my ROS lab, Agnes Charline Cecile Maillet, Chong Jun Fei Stephen, Gregory David Mellier, Gregory Lucien Bello, Hirpara J Laljibhai, Ivan Low Cherh Chiet, Kang Jia, Karishma Sachaphibulkij, Kartini binte Iskandar, Kirthan Shenoy, Kothandharaman Subramaniam, Lee Soo Fern, Liu Dan, Loo Yu Ling, Majidah Binte Rezlan, Michelle Boo Wee Siew, Ng Chun Chi, Tay Pei Wen Patricia, Png Ziyun, Quek Shuwen Alan, Sanjiv Yadav, Seah Bee Kee Serena, Velaithan Rathiga, Wang Binbin, Zhou Ting, Zhu Yan, Wang Binbin, Huang Sinong, Inthrani Raja Indran and Wong ChewHooi, I felt very lucky to know you and make friend with you. Thanks for the sincere friendship, thanks for the encouragement, thanks for the happiness during lunch time. Together with you, I no longer feared with experimental failure; together with you, feel the wet lab is not that boring; together with you, I understand Philosophy of life. I will not be that blur any more.

To my SMA friends, Jagadish Sankaran, Zhu Shiwen, Chua Huey Eng, Wang Junjie, Yin Lu, Li Yan, Xu Shuoyu, Porkodi Panneerselvam, Liu Yachao, it was an invaluable memory of the old days in MIT. We studied together, cooked together, celebrated our birthdays together and shared our joy and sorrow together. Thank you for always remember my birthday. It is good that our friendship will last for even. Special thank goes to Junjie who has always been willing to discuss various modeling approaches.

To my friends from school of computing, Liu Bing, Han Zhen, Dong Difeng, Yang Peipei, Feng Mengling, Chiang Tsong-Han, Liu Shuning, Liu Feng, Liu Ning and Yu

Xinyu, life becomes so happy and interesting with you. Wish each of you a bright future. Special thanks go to Liu Bing, who taught me a lot of useful experience with Bayesian network and I learned much computational knowledge. Thank Difeng also for sharing with me a lot of your experience of career path building and providing me much good information on job hunting.

Also thank all the friends from MBI, Neftali Flores Rodrigue, Huang Lu, Liu cheng cheng, Zhang Bo, Zhao Chen, Yuan Xin, Le Xiaomin, Wenwei, Nim Tri Hieu, Umashankar Shivshankar and Lakshmi Venkatraman. Thank you for spending time with me and providing a lot of fun during the period of thesis writing. Thank you for the encouragement. Thank you also for inviting me to join lunch with you. Hieu, you can always find the suitable sentence to express my idea when I was running out of words.

To my dearest dad and mother, thank you for trusting me and encouraging me. I am very lucky to be the only apple in your eyes. You always feel proud of me; even I am not that good. Thank you.

To my husband Boxuan, thank you for the never ending love, thank you for the support to me, thank you for the encouragement, thank you for staying up in the night to check mistakes of the thesis.

Thank you, my Lord, the source of my joy and strength. My hope of mercy and grace through the ups and downs in my life, Thank you for bringing me close to you. You

were the one who provided me with all these beloved people in my life. Thank all the friends I meet in the church, thank you for the sincere care and pray for me.

Table of Contents

Summary

TRAIL has been widely studied for the ability to kill cancer cells selectively, but resistance has hindered its clinical usefulness. Among the multiple compounds which have been identified that sensitize cancer cells to TRAIL-induced apoptosis, LY303511 (LY30) combined with TRAIL, has shown synergistic (greater than additive) killing of multiple cancer cell lines.

In this thesis, we used computational modeling to study the synergistic killing of LY30 and TRAIL. The project involves two parts: using previous experimental data to model the dynamics of synergy and ROS; and performing new experiments and modeling to investigate the casual role of ROS in LY30-induced cell sensitization. In the first part, we used ordinary differential equations to model individual effect of LY30 and TRAIL on HeLa cells, and then predict the synergy upon combined treatment. Model-based predictions were compared with in vitro experiments, and the combination treatment model was successful at mimicking the synergistic cell death caused by LY30 and TRAIL. However, there were significant failures of the model to mimic upstream activation at early time points, particularly the initial increase of caspase-8 activation. This flaw led us to perform additional measurements of early caspase-8 activation. Surprisingly, caspase-8 exhibited a transient decrease in activity after LY30 treatment, prior to strong activation. cFLIP, an inhibitor of caspase-8 activation, was up-regulated briefly after 30 minutes of LY30 treatment, followed by a significant down-regulation

over prolonged exposure. A further model suggests that LY30-induced fluctuation of cFLIP might result from tilting the ratios of two key ROS species, superoxide and hydrogen peroxide.

In the second part of this thesis, to explore the hypothesis that ROS species mediate the ability of LY30 to increase death, we measured superoxide and hydrogen peroxide over time. Superoxide and hydrogen peroxide had been expected to increase, one after another, with similar degree, but we found that hydrogen peroxide, as measured by DCFDA, showed a rapid and significant elevation and superoxide did not. To unveil the truth beneath the perplexing phenomenon, we studied LY30-induced ROS through a close integration of in-vitro experiments and probabilistic modeling using Bayesian networks (BN). Bayesian network modeling interpreted the levels of measured species to infer that LY30-induced DCFDA fluorescence in HeLa is largely from a nitric oxide pathway. Confirming this prediction, our subsequent experiments found that LY30-induced death was dependent on peroxynitrite, and surprisingly independent of hydrogen peroxide. We also detected that LY30 causes calcium leaking (perhaps passive), which together with peroxynitrite, were responsible for 90% of LY30-induced cell sensitization to TRAIL. Bases on the phenomenon, we constructed a revised BN model to model LY30-regulated complex interaction among ROS, RNS and calcium in HeLa. Our results in LY30-induced sensitization of HeLa may be useful for understanding cancer sensitization in other cell types or with other similar drugs. Furthermore, our work demonstrates that computational modeling can exploit kinetic

data to identify novel effects, and to suggest which time intervals or which pathways may have transient effects that regulate a phenomenon of interest.

List of Figures

List of Tables

List of Abbreviations

Apaf-1	Apoptotic protease-activating factor-1
Bak	Bcl-2 antagonist/killer
Bax	Bcl-2 associated X protein
Bcl-2	B-cell lymphoma protein 2
BH	Bcl-2 homology
Bid	BH3 interacting domain death agonist
BIR	Baculovirus IAP repeat
BN	Bayesian network
Ca^{2+}	Free intracellular calcium
CARD	Caspase recruitment domain
Caspase	Cysteine-dependent aspartate-specific protease
cFLIP	Cellular FLICE like Inhibitory Protein
CHX	Cyclohexamide
Complex *I*	NADH-Coenzyme Q Reductase
Complex *II*	succinate dehydrogenase complex
Cu/Zn SOD	Copper/zinc superoxide dismutase
Cyt. *c*	Cytochrome c
DCFDA	5-(and-6)-chloromethyl-2',7'-dichlorofluorescin diacetate-dichlorofluorescein diacetate
DD	Death domain
DED	Death effector domain

DEVD-AFC	N-Acetyl-Asp-Glu-Val-Asp-7-amino-4-trifluoromethyl coumarin
DIABLO	Direct IAP-binding protein with low pI
DISC	Death-inducing signaling complex
DMEM	Dulbecco's Modified Eagle's Medium
DMSO	Dimethyl sulfoxide
DNA	Deoxyribonucleic Acid
DR	Death receptor
DTT	Dithiothreitol
EDTA	Ethylenediaminetetraacetic acid
EGTA	Ethyleneglycotetraacetic acid
ER	Endoplasmic reticulum
ETC	Electron transport chain
FADD	Fas-associated death domain-containing protein
FBS	Fetal bovine serum
H_2O_2	Hydrogen peroxide
IAP	Inhibitor of apoptosis protein
IETD-AFC	N-Acetyl-Ile-Glu-Thr-Asp-7-amino-4- trifluoromethyl coumarin
LEHD-AFC	N-Acetyl-Leu-Glu-His-Asp-7-amino-4-trifluoromethyl coumarin
MAPK	Mitogen activated protein kinase
MnSOD	Manganese superoxide dismutase
MOMP	Mitochondrial outer membrane permeabilization
MPT	Mitochondrial Permeability Transition
mTOR	Mammalian target of rapamycin

MTT	3-(4,5-dimethylthiazol- 2-yl)-2,5 diphenyltetrazolium bromide
NAC	N-Acetyl cysteine
NAD	Nicotine adenine dinucleotide
NFκB	Nuclear factor of kappa light
NHE	Na^+/H^+ exchanger
NO	Nitric oxide
NOS	Nitric oxide synthase
$O_2^{\bullet-}$	Superoxide radical
ODE	Ordinary Differential Equations
$ONOO^-$	Peroxynitrite
$OH^\bullet$	Hydroxyl radical
PARP	Poly(ADP-ribose) polymerase
PAK	p-21 activated kinase
PBS	Phosphate buffered saline
RI NG	Really interesting new gene
RIP	Receptor interacting protein
RNA	Ribonucleic acid
RNase	Ribonuclease
RNS	Reactive nitrogen species
ROS	Reactive oxygen species
SDCM	Spinning Disk Confocal Microscope
SDS	Sodium dodecyl sulphate
SDS-PAGE	SDS-polyacrylamide gel electrophoresis
siRNA	small interfering RNA

Smac/Diablo	Second Mitochondrail Activator of Caspases/ Direct IAP-binding protein with low pI
SOD	Superoxide dismutase
tBid	Truncated Bid
TNF	Tumor necrosis factor
TRAIL	TNF-related apoptosis inducing factor
XIAP	X-linked inhibitor of apoptosis protein
FAD	flavin adenine dinucleotide

1 Introduction to Biological background

1.1 Cancer and apoptosis

Cancer is a major cause of worldwide death. It accounts for one in four deaths in the United States [1] and one in eight deaths worldwide [2]. According to Cancer Registry in Singapore, the proportion of death caused by cancer in Singapore rose steadily from 14.8% (1972) to 27.1% (2002). The burden of cancer have doubled globally during the past decades [3]. In 2008, there is an estimates of over 12 million new cases and 25 million persons alive with the diagnosis of cancer [4].

Conventional cancer therapies include surgery, radiology and chemotherapy. As the oldest and most common method in cancer treatment, cancer surgeries have become less invasive in recent years with the development of techniques. However, the process still brings sufferings to the patients physically and emotionally. Chemotherapy refers to cancer treatment with an antineoplastic drug or drugs. Because chemotherapy targets multiple areas of the body at the same time, it can induce many adverse side-effects including depression of the immune system, tendency to bleed and gastrointestinal distress and such. Radiation refers to elimination of an entire tumor within a confined area and limits the damage to nearby cells. Radiation can cause the reduced white blood cells and platelets, which can lead to lower immunity to viruses. However, according to statistics in patients, it always followed with high rate of cancer recurrences and relapses and may develop resistant phenotype in patients.

The term “apoptosis” was coined in 1972 by an Australian pathologist John Kerr, who observed a number of common morphologic features in certain dying cells [5]. Apoptosis is the process of programmed cell death (PCD), which could occur in multicellular organisms [6]. The realization of the key role of apoptosis in cancer/malignant phenotype development dates back to the early 1970s that kinetic studies of tumor growth predicted that the growth is <5% of that observed cancer growth rates [7, 8]. For example, it is now clear that disrupted apoptosis by certain oncogenic mutations, such as Bcl-2 [9], p53[10, 11], leading to cancer initiation, progression and metastasis. Besides, it is well documented that most cytotoxic anticancer agents which are widely applied in chemotherapy-induced apoptosis, thus raising the possibility of treatment failure due to defects in apoptotic programs.

Apoptotic events are characterized by morphological cell changes and finally cell death. These changes include cell blebbing, cell shrinkage, chromatin condensation, chromosomal DNA fragmentation, chromatin margination, cytoplasmic vacuolization, increase in cellular density, nuclear fragmentation, and apoptotic body formation[7].

Apoptosis is controlled by various cell signals by either *extrinsic inducers* or *intrinsic inducers*. *Extrinsic apoptosi*s (Figure 1.1.1a), as suggested by its name, begins outside of the cells through the activation of pro-apoptotic receptors by its apoptosis ligand on cell surface, including Apo2L/TRAIL and CD95L/FasL. The *intrinsic pathway* (Figure 1.1.1b) is initiated from within the cell under cellular stress, such as DNA damage and hypoxia.

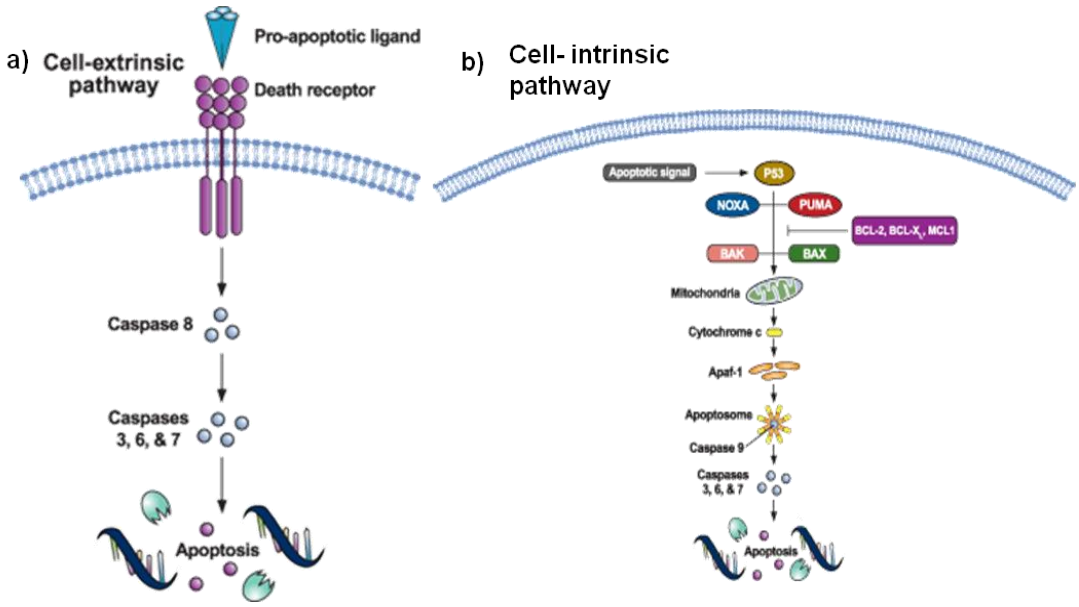

Figure1.1.1 Diagram of apoptosis pathway [12]**.** a) Extrinsic apoptosis pathway b) Intrinsic apoptosis pathway

In *extrinsic apoptosis*, ligands bind to cell membrane and induce receptor clustering and recruitment of the adaptor protein Fas-associated death domain (FADD) and initiator caspases 8 and caspase 10, thus forming a death-inducing signaling complex (DISC) [13-15]. Formation of the DISC facilitates autocatalytic processing of initiator caspases through bringing procaspase molecules into close proximity. Processed caspase 8/ caspase 10 are released into the cytoplasm to activate effectors caspases 3, caspases 6, and/or caspases 7[12, 16]. As a key step affecting extrinsic apoptosis, formation of DISC is modulated by several inhibitory mechanisms, the most famous one is c-FLICE inhibitory protein (c-FLIP), which interacts with FADD and block initiator caspase activation [17].

In *intrinsic apoptosis*(mitochondrial pathway) pathway, cell fate is tightly controlled by the balance between pro-apoptotic group and anti-apoptotic group of the Bcl-2 family featured with Bcl-2 homology (BH) domains (BH1, BH2, BH3, and BH4)[17].

Pro-apoptotic Bcl-2 promotes permeabilization of mitochondria membrane while anti-apoptotic Bcl-2 acts to prevent it. Anti-apoptotic Bcl-2 members include Bcl-2 and Bcl-xL which contain BH1, BH2 and BH3 domain. Based on BH domains, pro-apoptotic Bcl-2 proteins are divided into the subgroups which either contains several BH domains, *e.g.* Bax and Bak, or contains only the BH3 domain, like Bid, Bad, Bim, and NOXA [17]. Upon mitochondria membrane permeabilization, cytochrome c and the pro-apoptotic protein SMAC/DIABLO are then able to translocate from the inter-membrane space of the mitochondria into the cytosol [17]. SMAC/DIABLO protein released from the mitochondria promotes apoptosis by directly interacting with inhibitors of apoptosis proteins (IAPs) and disrupting their ability to inactivate the caspase [18, 19]. Released cytochrome c binds the adaptor apoptotic protease activating factor-1 (Apaf-1), forming a large multiprotein structure known as the apoptosome, which leads to catalytic activation of caspase 9 [12], and then activation of the downstream effector caspases 3, 6, and 7 [18].

1.2 TRAIL as an apoptosis trigger

TRAIL/Apo2L is short for Tumor necrosis factor-related apoptosis-inducing ligand. It belongs to the tumor necrosis factor (TNF) family of ligands which are capable of initiating extrinsic apoptosis through binding receptors. TRAIL is principally expressed by cells of the immune system in healthy organism [20]. TRAIL is a Type II transmembrane protein with an extracellular (C-terminus) domain, which can be cleaved, resulting in a soluble form. Among the 17 members in TNF family, TRAIL has been regarded as the most promising candidate in clinical application. In the following

section, we will give a detailed introduction of TRAIL about its pathway, clinical application and resistance.

1.2.1 TRAIL induced apoptosis

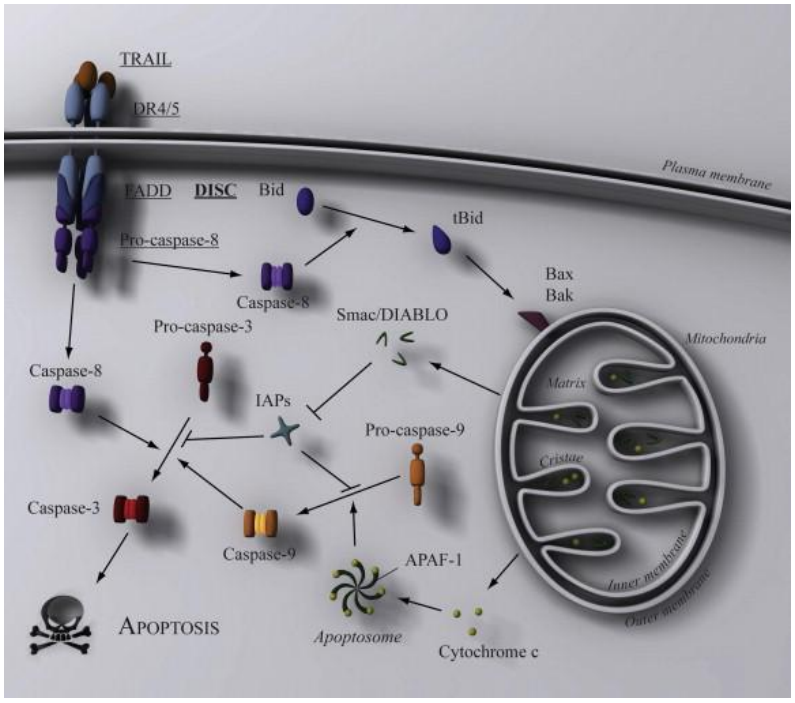

Figure 1.2.1 TRAIL induced apoptotic pathway [21]. TRAIL induces direct oligomerization of death receptors TRAIL1 (DR4) or TRAIL2 (DR5), which then leads to activation of the extrinsic and may also intrinsic pathways. ⟶ activation; ⊣ inhibition.

TRAI- induced apoptosis pathway is illustrated in figure 1.2.1. Upon TRAIL treatment, TRAIL receptor 1 (TRAILR1/DR4) or TRAIL receptor 1 (TRAILR2/DR5) bind to TRAIL and then form oligomerized receptors. The oligomerized receptors then recruit FADD and caspase 8/10 to form DISC. Upon DISC formation, caspase 8/10 is cleaved and activated, which in turn can cleave and activate caspase 3. The cells in which caspase-3 becomes directly activated by caspase-8 is defined as type I cells. In other tumor types, which are considered to be type II cells, the activated initiator caspases can

also activate the intrinsic pathway (mitochondrial pathway) [22, 23]. In the intrinsic pathway, the mitochondrial membranes permeabilization leads to the release of apoptotic factors such as cytochrome c. Upon entry into the cytosol, cytochrome c binds the caspase-activating protein Apaf-1 and procaspase-9, forming apoptosome and subsequently inducing processing and activation of caspase-9. Therefore, activated caspase-9 can cooperate with caspase-8 in the processing and activation of caspase-3, leading to the demise of the cell [24].

1.2.2 TRAIL and its clinical application

TRAIL has been long regarded as a promising ligand in cancer therapy. Firstly, it has been found of wide expression in various cell types. Compared with other members in the TNF family, mRNA of TRAIL is detected in wider variety of tissues including PBMC, prostate, ovary and such [25]. Besides, TRAIL is shown to induce apoptosis in a variety of cancer cell lines through TRAIL receptors DR4 and DR5, which are highly expressed on the surface of cancer cells but not in normal cells. Such feature of TRAIL favours its clinical application as a therapeutic strategy by selectively targeting of cancer cells while sparing normal tissues. TRAIL is currently undergoing phase I/II clinical evaluation for a variety of cancers and it holds real promise as a therapeutic strategy due to its selective targeting of cancer cells while sparing normal tissues [26, 27].

1.2.3 TRAIL Resistance

TRAIL resistance happens due to defects in apoptotic signaling or redundant survival mechanisms [28, 29].

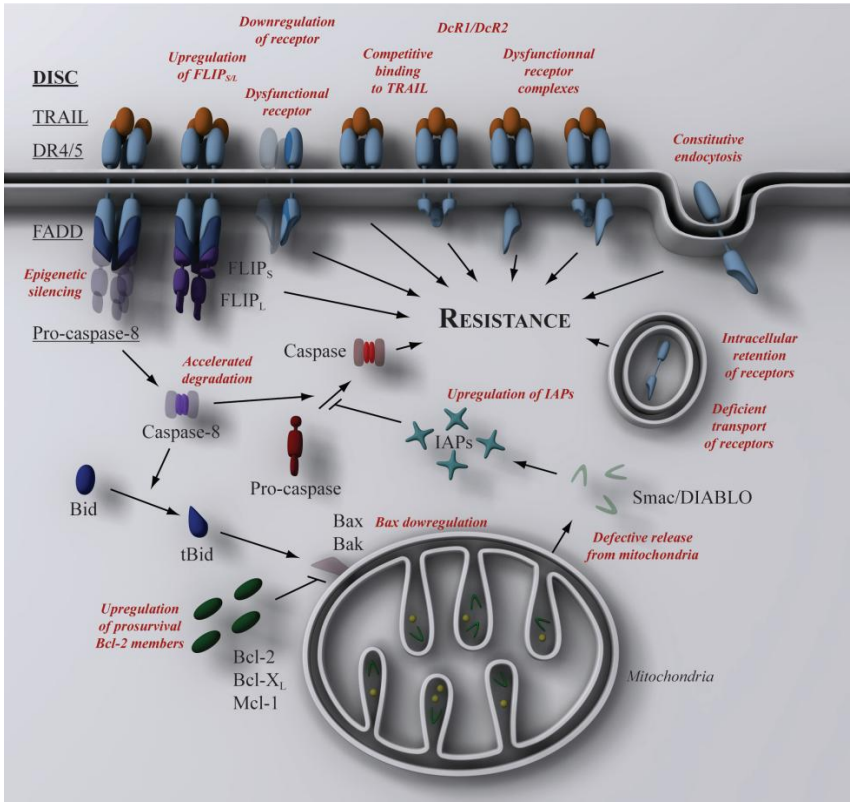

Figure 1.2.2 Mechanisms involved in TRAIL resistance [21]. TRAIL resistance can happens at 3 levels of the apoptosis signaling pathway: 1) at the DISC level where there are receptors down-regulation/ dysfunction, cFLIP upregulation, or caspase 8 down-regulation; 2) at mitochondrial level where there is regulation of Bcl-2 family members, and Smac; and 3) at IAP level with up-regulation of IAPs.

According to clinicaltrials.gov, which is a result database for clinical trials, several types of human tumor have been reported to be resistant to TRAIL [30], for example, majority of breast, prostate, ovarian, and lung carcinoma, and multiple myeloma cells are resistant to apoptosis induced by TRAIL [31]. Such resistance can also occur in resistant clones of TRAIL-sensitive cells upon continuous TRAIL exposure [32]. Moreover, TRAIL have been reported to induce proliferative effects in glioma and

small cell lung cancer cell lines [20]. Further research revealed that TRAIL resistance can happen at 3 levels: 1) at DISC level, with down-regulation of death receptors or increase with cFLIP expression[33, 34]; 2) at mitochondria level with overexpression of antiapoptotic proteins of the Bcl-2 family or down-regulation of proapoptotic Bcl-2 members [35]; and 3) at Inhibitor of Apoptosis Protein (IAP) level with up-regulation of IAPs to block caspase cascade [32]. Development of resistance in tumor is a serious obstacle to the effective clinical application of TRAIL. Therefore, the effort of exploring combination therapies to overcome resistance to TRAIL, or to induce re-sensitization to TRAIL, could be extremely important for enabling TRAIL-based therapies to succeed [27, 36-38].

Table1.1 Mechanisms of resistance in cancer cells to TRAIL-induced apoptosis[21]

Level of TRAIL resistance	Proteins involved	Causes
Receptor and DISC signaling	DR4 and DR5	Reduced levels of cell surface receptor available for transmitting apoptotic signal due to: (1) Downregulation of total receptor protein levels through silencing of receptor gene (2) Deficient transport of receptors to cell surface (3) Intracellular retention of receptors (4) Constitutive receptor endocytosis Dysfunctional receptor due to: (1) Mutation on receptor gene (2) Post-translational modifications: Lack of O-glycosylation/palmitoylation on receptors
	Decoy receptors 1/2	(1) Competitive binding with DR4/5 for TRAIL (2) Forms dysfunctional receptor complexes with DR4/5
	FLIP	Increase in protein levels has inhibitory effect on activation of initiator Caspase-8 at DISC
	Initiator capases-8	Reduced protein levels via: (1) Epigenetic silencing (2) Accelerated degradation
Mitochondria-dependent signaling	Pro-survival Bcl-2 members	Increase in levels of Bcl2/BclxL/Mcl-1: Blocks release of pro-apoptotic factors from mitochondria
	Pro-apoptotic BH3-only members	Deficiency in Bax protein levels: Negative effect on release of pro-apoptotic factors from mitochodria
	SMAC/DIABLO	Defective release from mitochondria – unable to play inhibitory role on IAPs
	Inhibitor of apoptosis protein	Increase in XIAP/survivin protein levels – inhibits activation/activity of caspases-3/9/7
Other major signaling pathways	NFKB	Predominant signal in TRAIL-resistant cells due to its ability to upregulate anti-apoptotic proteins e.g. XIAP, cFLIP, Bcl-X_L, DcR1
	MAPKs	Controversies with regards to their role in TRAIL-induced apoptosis
	PI3K-PKB/Akt	Pro-survival signaling pathway, able to increase anti-apoptotic proteins thus inhibiting TRAIL-induced apoptosis

1.2.3.1 cFLIP and TRAIL resistance

Cellular FLICE-inhibitory proteins (cFLIP) have been widely regarded as apoptosis inhibitors [39, 40]. There are 13 distinct splice variants of cFLIP and three of them are expressed as proteins which are $cFLIP_S$ (short form at 26 kDa), $cFLIP_R$ (found in Raji at 24 kDa) and $cFLIP_L$ (long form at 55 kDa) [39, 40] (Figure 1.2.3). In these three isoforms of proteins, $cFLIP_L$ and $cFLIP_S$ are widely distributed forms that have been well studied in biological research [41]. $cFLIP_S$ has a short c-terminal of 20 amino acids followed with two death effector domains (DED) and the c-terminal has been regarded as crucial for ubiquitination and degradation [46]. $cFLIP_L$ has a much longer c-terminal than $cFLIP_S$. It shares extensive homology with procaspase-8 but without a functional caspase domain [42].

While the precise mechanism still remains elusive, $cFLIP_L$ and $cFLIP_S$ has been shown with varied regulatory in apoptosis due to the structural differences [43]. $cFLIP_S$ has been demonstrated to play an crucial role in inhibiting TRAIL-induced apoptosis [40, 44, 45] through 1) disruption of DISC formation [40, 44, 45], 2) activation of Akt and sustained XIAP protein level [46, 47], and 3) inhibition of caspase-8 [46-48] at different levels of procaspase-8 processing [49]. $cFLIP_L$, compared to $cFLIP_s$, has been reported with dual role in apoptosis. $cFLIP_L$ has been shown to inhibit caspase-8 activation at high levels, but enhance caspase-8 activation at low levels [40, 44]. The opposing effect with $cFLIP_L$ might reflect the fact that $cFLIP_L$ is capable of forming heterodimeric enzyme molecules with procaspases-8 and procaspases-10, which can cleave and activate the procaspases [44].

1.2.3.2 Death Receptors (DR4/5) and TRAIL resistance

Death receptors belong to the super-family of tumor necrosis factor receptor. They are characterized by a cytoplasmic region which enables them to initiate cytotoxic signals in the presence of ligands [50]. Interaction of TRAIL with death receptor 4 (DR4) and death receptor (DR5) triggers the transduction of TRAIL-induced apoptotic signaling via the formation of DISC, allowing for activation of the downstream death executor caspases. Therefore, any changes with regard to the total protein level and/or surface expression level of DR4 or DR5 have a profound effect on the ability of TRAIL to function efficiently as a death-inducing ligand.

A mutation of DR5 is a frequent event in many cancers and is often associated with aggressive cases, such as head and neck squamous, breast cancer cells and non-Hodgkin's lymphoma [51-55]. A lack of expression of DR4 in ovarian cancer cells was reported to be correlated with resistance to TRAIL-induced apoptosis [56]. Similarly, deficient surface expression of DR4 increase the resistance of colon cancer cells to TRAIL [57].

1.2.3.3 Inhibitor of apoptosis (IAP) and TRAIL resistance

The inhibitor of apoptosis (IAP) family of proteins consists of X-linked inhibitor of apoptosis (XIAP), cellular IAP1 (cIAP1), cellular IAP2 (cIAP2) and survivin [58]. All IAP proteins are structurally characterized with baculoviral IAP repeat (BIR) domain, a 70−80 amino acid long motif which is important with its apoptosis inhibitory effect. They may contain one or several additional functional domains, such as really interesting new gene (RING) domain and the caspase activating and recruitment domain (CARD) domain [58].

High IAP expression has been reported to be the cause of resistance to TRAIL in pancreatic cancer cells and colon carcinoma [59-62]. Down-regulation of IAP members restores cells' sensitivities to TRAIL-induced apoptosis [63-67]. The inhibitory effect by IAPs can be relieved by mitochondrial protein Smac/DIABLO. Smac/DIABLO binds to and inhibits IAPs upon its release from the mitochondria during apoptosis, eliminating the interaction between caspases and IAPs.

As TRAIL-induced apoptosis pathway requires proper collaboration of all the species involved in the pathway, disturbed balance between anti-apoptotic species and pro-apoptotic species, specifically strength tittering towards anti-apoptotic species due to either one species or multiple species may result in TRAIL resistance. However, it is usually difficult to identify the exact the cause to TRAIL resistance for each tumor type through pure biology approach, because it involves a systematic calibration and quantification of all the species in the TRAIL pathway.

1.2.4 TRAIL Sensitization

A direct solution to overcome TRAIL resistance is to identify the cause of resistance and then target at the cause to restore the cells' sensitivity. However, it is usually costly and time consuming to identify the cause for each resistance cancer type. Currently, research has been carried out to find an ideal way to tackle cells' resistance using chemical compounds or treatments. Reported effective chemical compounds include co-treatment of TRAIL with cycloheximide [68], Quercetin [69, 70], resveratrol [71], cucumin [72, 73], LY30 [74, 75] and so on. Effective treatments include radiation of ultraviolet B light (UVB) at sub-lethal dose [76], chemotherapy such as ADR, VP-16

and vincristine [77]. In addition, several molecule agents, such as Nitric Oxide (NO) [78], H_2O_2 [79], have been tested and confirmed with TRAIL sensitization effect.

So far, 5 major mechanisms have been reported among all the sensitization methods and compounds, which including 1) up-regulation/oligomerization of Death Receptors (DR) [74, 75], 2) down-regulation of cFLIP[74, 80, 81], 3) ROS production[75, 82], 4) NF_KB inhibition [78], and 5) restoration of caspase-8 expression [83].

1.3 LY303511 (LY30), a small molecule that re-sensitizes cancer cells to TRAIL

1.3.1 LY30 is an inactive analog of LY29

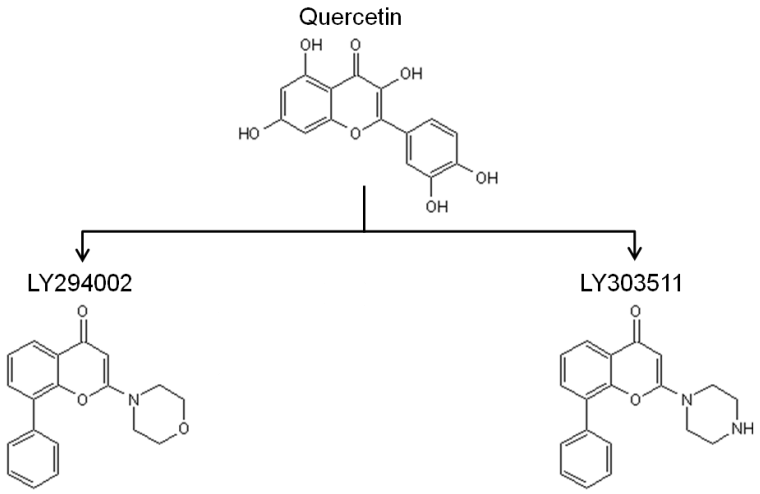

Figure 1.3.1 Structures comparison among LY303511, LY294002 and Quercetin.

LY303511 (LY30) and LY294002 (LY29) are both derivative of quercetin which is a plant-derived flavonoid widely found in nature [84]. LY29 was developed based on the structure of Quercetin with a substitution of a morpholine ring. The morpholine ring of greatly enhances LY29's specificity for PI3K inhibition, and LY29 has been widely

used as a specific PI3K inhibitor [85]. As a structural analogue of LY29, LY30 is usually employed as a negative control for PI3K inhibitory activity of LY29 [86, 87] (Figure 1.2.3).

Despite a supposedly inactive compound of LY29, recent research has shown that LY30, instead of simply being a negative control of LY29, also triggers cellular events which may lead to its potential as anti-tumor candidates. This discovery opened a new door for TRAIL-sensitization.

1.3.2 LY30 induces cell sensitization to TRAIL

The small molecule compound LY30 (LY303511) has been reported to sensitize several cancer cell lines to TRAIL-induced apoptosis and vincristine-induced apoptosis [88-90]. Poh *et al.* [74] observed that LY30 can sensitize cervical cancer cell line (HeLa) to TRAIL-induced apoptosis in a great extent. LY29 was also reported to sensitize HeLa to TRAIL but with less potency. As observed in HeLa under combination treatment of LY30 and TRAIL, there is a strong activation of apoptosis cascade evidenced with rapid caspase-8 activation, significant mitochondria permeabilization and XIAP cleavage. Towards the goal of finding out the mechanism of LY30-induced sensitization, Poh *et al.* conducted extensive experiments to measure possible targets for TRAIL sensitization. Among the targets, they detected down-regulation of cFLIP and oligomerization of DR5 under LY30 treatment in HeLa. They hypothesized LY30 induced sensitization in HeLa through cFLIP down-regulation and DR5 oligomerization. Similar effect of sensitization to TRAIL was also observed in an acute T cell leukemia (Jurkat).

In an independent study, Shenoy *et al*. reported that LY30 can greatly sensitize a neuroblastoma cell line (SHEP-1) to TRAIL-induced apoptosis [75]. To address the question of how LY30 sensitize SHEP-1 to TRAIL, they measured the concentrations of death receptors and found that LY30 elevated both of their concentrations by 1 folds increase [75], which suggested that LY30 increases sensitivity of SHEP-1 through increasing concentrations of death receptors.

1.3.3 LY30 induces ROS production

Poh *et al*. reported that in several cancer cell lines, LY30 also greatly enhanced cell death by vincristine (a chemotherapeutic agent) at non-apoptotic concentrations [85]. In their work, they also found a significant increase of intracellular ROS as detected by DCFDA in LY30-treated cells. As it has been well documented that abnormal ROS production affects cell death [91-94], including apoptosis [95, 96], they hypothesized that LY30 induced cell sensitization to vincristine through significant H_2O_2 production.

Shenoy *et al*. [75] also observed that LY30 significantly increased ROS level in SHEP-1 as evidence with great increase of DCFDA fluorescence insensitivity in LY30-treated SHEP-1. Through additional administration of catalase, they were able to prevent cell death and block LY30-induced increase of death receptors. They proposed that LY30 induces SHEP-1's sensitization to TRAIL through Hydrogen Peroxide-dependent elevation of death receptor.

1.3.4 Other findings about LY30

Researches revealed that LY30 is a compound with many interesting effects including anti-tumor properties. In a 2003 study, Wasim *et al.* observed that both LY30 and LY29, but not wortmannin, are capable of blocking Kv currents in MIN6 ß cells in a potent manner [97]. They reported that LY30 can block Kv channel accurately and directly (with current inhibition occurrence within 1 min after introduction) through a pathway which is neither PI3-K dependent nor CKII-dependent [97].

After that, Kristof *et al.* in 2005 reported that LY30, compared to LY29, has more specificity inhibiting mammalian target of rapamycin (mTOR)-dependent cell proliferation through inhibiting its downstream effector p70 S6 kinase (S6K). Their study revealed that administration of LY30 in both A549 and primary pulmonary artery smooth muscle cells leads to significant reduction of proliferation without causing apoptosis. Furthermore, they found that LY30 is able to inhibit cell proliferation through inhibiting casein kinase 2 (CK2) which regulates reduced G(2)/M progression as well as G(2)/M-specific cyclins which is independent of mTOR pathway. The anti-proliferation effect of LY30 was confirmed on athymic mice implanted with human prostate adenocarcinoma tumor [98].

1.4 Reactive oxygen species (ROS) and cell viability

ROS represents a family of chemical species with high reactivities, and they are usually formed due to incomplete reduction of oxygen [99]. We will introduce intracellular ROS sources, ROS family and ROS scavenge mechanisms in following sections.

1.4.1 Introduction to reactive oxygen species

Reactive oxygen species (ROS) is a collective term that describes the high reactive chemical species which are formed through incomplete reduction of oxygen. ROS can be converted from triplet oxygen by either energy transfer or electron transfer reaction. The former reaction produces singlet oxygen and the later one results in sequential production of superoxide, hydrogen peroxide and hydroxyl radical and so on. Under physiological conditions, ROS is continuously produced in cellular organism as a by-product of various metabolic pathways localized in different cellular compartments [100]. ROS family contains oxygen radicals such as superoxide ($O2^{\bullet-}$), hydroxyl (OH.) and nonradicals that are can easily converted into radicals, such as peroxynitrite ($ONOO^-$), HOCl, and H_2O_2 (Table 1.2).

Table 1.2 ROS species

	Name	Radical	Reactivity	Half-life	Statistics from Pubmed
$O_2^{\bullet-}$	Superoxide	yes	Low	microsecond	72418
$OH^{\cdot}$	Hydroxyl radical	yes	extremely High	nanosecond	13328
H_2O_2	hydrogen peroxide	no	Medium	minutes	50731
$ONOO^-$	Peroxynitrite	no	extremely high	milliseconds	6295
$RO_2^{\cdot}$	Peroxyl Radical	yes	high	ten milliseconds	1179
$RO^{\cdot}$	Alkoxyl	yes	extremely high	one microsecond	204

$^1O_2$	Singlet oxygen	no	high	one microsecond	5305
HOCl-	Hypochlorous acid	no		minutes	4965
O_3	Ozone	no	high	minutes	
HO2·	Hydroperoxyl	yes	high	seconds	276

1.4.2 Sources of ROS

Mitochondria, especially mitochondria membrane, are the major physiological sources of ROS. ROS is formed as "by-product" from Electron-transferring chain(ETC) or enzymatic system in mitochondria, which account for 1-2% of total O_2 consumption [101]. The predominant ROS production sites in mitochondria are Complex I (NADH Hydrogenase) [102, 103] and Complex III (Ubiquinol/cytochrome c oxidio-reductase) [104] where electrons may leak out of the ETC to partially reduce molecule oxygen, via a single electron transfer, to form $O_2^{\bullet-}$. Formed $O_2^{\bullet-}$ is then converted to H_2O_2 in the presence of high SOD inside mitochondria.

The *Endoplasmic Reticulum (ER)* is another membrane-bound ROS production site. In smooth ER, cytochrome P-450 and b5 are the enzymes that can oxidize unsaturated fatty acids and xenobiotics and at the same time, reduce O_2 to $O_2^{\bullet-}$ and/or H_2O_2 [85]. Evidence showed that the high oxidative environment in ER create a milieu that favors protein folding and secretion [86, 87]. Besides inside ER, Gillette *et al.* observed ROS production on the membrane of ER when supplemented with NADH or NADPH [88]. It has been proved that ROS production on ER membrane is related with the residence of two newly identified members in NADPH oxidase (NOX) family, NADPH oxidase

4 (NOX4) and NADPH oxidase 5 (NOX5) [89-95], which have been reported to produce H_2O_2 directly.

Peroxisomes are another important source of total cellular H_2O_2 production [105]. A number of H_2O_2-generating enzymes have been found in peroxisomes, such as glycolate oxidase, L-a-hydroxyacid oxidase, and fatty acyl-CoA oxidase [106, 107]. Generated H_2O_2 in Peroxisomal can oxidize a variety of substrates in "peroxidative" reactions, which are important in proper function of liver and kidney cells to detoxify a variety of toxic molecules [107].

ROS is also widely reported to be produced by NOX family which is composed of five NOX isoforms (NOX 1–5) and two homologous oxidases (Duox1 and Duox2). These NOX members all share the ability to generate $O_2^{\bullet-}$ and/or H_2O_2 through reduction of molecule oxygen using NADPH as the electron source .[108]

In addition to the intracellular organelles that produced ROS, cells also contain a number of soluble enzymes in cytosol such as *xanthine oxidase* and *tryptophan ioxygenase*, which can generate ROS during catalytic cycling. Among the enzymes, xanthine oxidase is the most extensively studied one to generate $O_2^{\bullet-}$ in vitro with the effect of ROS on diverse cellular processes [109].

1.4.3 ROS stress and ROS scavenger system

Although ROS has been traditionally regarded as a detrimental bi-product of cellular respiration, accumulating evidence suggests that ROS are not only injurious by-products of cellular metabolism but also essential participants in cell signaling and

regulation [110]. Generation of H_2O_2 in response to various pathogens elicits localized cell death to limit spread of the pathogen in plant cells [111] and a more systemic response with the induction of defence genes [112].

On the other side, disturbed ROS level may induce cellular stress which is called ROS stress. Cellular systems generate oxidative stress in response to a number of adverse environmental factors (e.g., photo-oxidations and emissions) [100]. Increased ROS levels are known to regulate various biological pathways, including promoting cell proliferation through constant activation of transcription factors like NF-kB and AP-1 [113], activation of associated receptor tyrosine kinases [114], and promoting apoptosis by stimulating pro-apoptotic signaling molecules, such as JNK and p38 and so on [115].

Severe oxidative stress may induce DNA damage that leads to genomic instability, which may contribute to cancer. To avoid cellular damage from oxidative stress, cells evolved with sophisticated antioxidative defence strategy to tightly control the equilibrium of ROS. Roughly, ROS scavenging mechanism can be divided into nonenzymatic and enzymatic mechanisms.

Nonenzymatic antioxidants include major cellular redox buffers ascorbic acid (ASH) [116, 117], glutathione (GSH) [219,220], phenolic compounds, alkaloids, non-protein amino acids and a-tocopherols [100].

Enzymatic ROS scavenging mechanism include superoxide dismutase (SOD), glutathinone peroxidast (APX) and catalase (CAT), Glutathione peroxidase (GPX) and so on.

SOD is widely expressed in all cellular organisms and in all subcellular compartments to defend with oxidative stress [118]. According to metal cofactors, SODs are classified into three types: the manganese SOD (MnSOD, SOD-2) [119], the copper/zinc SOD (Cu/ZnSOD, SOD-1) [120] and the iron SOD (FeSOD) [121], which are mainly localized in cytosol, mitochondria and peroxisome, and chloroplast in plants, respectively. SOD has been proposed as one of the most effective intracellular enzymatic antioxidant that provides the first line of defence against the toxic effects of elevated ROS levels. SOD removes $O_2^{\bullet-}$ through catalyzing the conversion from $O_2^{\bullet-}$ to H_2O_2, which is 10,000 fold faster than spontaneous dismutation [59].

Catalase was first identified in 1818 as a potential breakdown substance of H_2O_2 and later was named as catalase by Oscar Loew in 1900 [68]. Catalase has been reported as one of the enzymes with highest turnover number. Specifically, one catalase molecule is able to scavenge 6 million molecules of H_2O_2 to H_2O and O_2 per second [68, 69]. Catalase is found to be widely expressed in peroxisome and responsible for removing of H_2O_2 generated in peroxisomes by oxidases [70].

1.4.4 ROS signaling and cell death

It is well accepted that ROS, according to the type and concentration, plays key roles in diverse signaling pathways to regulate cell proliferation and cell death [122]. For example, ROS has been reported in regulating cell-cycle checkpoints, cysteine proteases and transcriptional activation or repression, and mitogen-activated protein kinases (MAPK) [73]. Excess production of intracellular ROS causes necrotic cell death, which is an inflammatory cell death as compared to apoptosis, in fibrosarcoma

cells [123]. Oxidative stress with milder elevation of ROS may lead cell to apoptosis [124], featured with the activation of the caspases cascade. ROS induced apoptosis pathway may involve inhibition of MnSOD, activation of MAP kinase kinase kinase (MAPKKK) or both [123]. Reduced concentration of intracellular ROS tends to promote cell proliferation with mitogenic responses through tyrosine phosphorylation of phosphatises, activation of growth factor receptors or activation of transcription factors that control proliferation such as NF-κB [125]

More recent finding revealed that it is specifically the ratio of $O_2^{\bullet-}$ to H_2O_2, in a high extent, determines the cell fate of necrosis, apoptosis or proliferation [74-77]. A high ratio of $O_2^{\bullet-}$ to H_2O_2 antagonizes apoptosis by triggering pro-survival pathways such as PI3K/Akt and ERK [78, 79]. In contrast, a low ratio of O_2^{-} to H_2O_2 promotes apoptosis through intracellular acidification [74], activation of caspase-3 and caspase-9 [80], down-regulation of cFLIP [81], and down-regulation of NHE-1 [75, 82]. In this thesis, we will mainly focus on H_2O_2 and $O_2^{\bullet-}$ as the two species have been received most attention.

2 Introduction to computational modeling in biology

2.1 The significance of computational modeling in biology

With the development of biological techniques, biologists have made amazing advances on understanding cellular behaviour such as apoptosis and cell cycle [126, 127], response to cytokines, growth factors and hormones [128-130], gene regulation and expression [131, 132] , ion channels[133, 134] and so on. Although the advances in biological approaches towards more accurate and more quantitative experimental results will continue, it is well accepted that to obtain an in-depth insight into the functioning of biological systems through pure biological techniques is almost impossible [135]. Biological system are regarded as "complex systems" which involves a large number of functionally diverse sets of elements interact selectively and nonlinearly to cooperate in a highly regulated network, thus producing coherent rather than complex behaviours [135], and it is difficult to understand the cooperative relationship of the cellular components, e.g. synergistic, additive, or exclusive, using conventional biological techniques.

To develop a systematic view of how cells work, how cellular processes are regulated, and how cells response to their changing environments, it has motivated the emergence of systems biology which seeks to integrate various method to achieve a full picture of how the individual bio-molecules interact and evolve in time and space to realize the various cellular functions [136]. Systems biology integrates many different disciplines including biology, mathematics, computer science, and so on towards the goal of a

systematic understanding of a specific biological phenomenon [136]. A basic task is to incorporate all the relevant biological processes into a computational model that is able to represent a whole cell or even an entire organism [136]. Simulation through various computational models provide a way to predict dynamics of the system and thus to test the underlying assumption through comparison with experimental observation. In detail, computer models are able to predict detailed behaviours of the system based on known and assumed interactions. Such predictions are then compared with experimental observations. Inconsistency between prediction and observation suggests that the assumption under the model is either incomplete or incorrect while models that can pass the initial validation can be used for further predictions and experimental validation [135].

2.2 Methods of computational modeling in biology

To facilitate studying the complex behaviour of biological pathways, a variety of computational models have been proposed ranging from qualitative models that focus on the generic properties of biological networks [137] to quantitative models that can simulate the time course of biological pathways under various conditions [138]. The choice of modelling method, whether qualitative or quantitative, is highly dependent on the target of the modelling task and also constraint with data quality and quantity. Widely-used biological models include Boolean network models, models that defined as a set of Ordinary Differential Equations (ODE), and Bayesian network models [139].

Computational biology has been applied in two major fields of knowledge discovery and hypothesis test. In knowledge discovery, hidden patterns or features can be extracted from huge quantities of experimental data using sophisticated data mining approaches, and thus forming hypotheses. In hypotheses test, various biological hypotheses can be verified with in silico experiments, therefore providing reference information for in vitro and in vivo studies.

Knowledge discovery has been applied extensively in bioinformatics to predict protein structure from sequence and regulatory networks from gene expression profile. The predictions are formed with heuristics methods that often involve sophisticated statistical approaches (hidden Markov models) [135].

Model simulation attempts to simulate the dynamics of biological systems in order to test the validity of the underlying assumptions through comparison between behaviours of computer-executable models and experimental observation. Under the situation of inconsistency between simulation and experimental results, we can be informed that our knowledge on the system is incomplete and the key points that causes the inconsistency may be tested; under the situation of consistency between simulation and experimental results, we can utilize the models that survive initial validation for further predictions with experiments [135].

2.3 Applications of computational modeling in biology

As an efficient aid in theoretical and experimental study of complex biological pathways, a variety of computational models have been constructed ranging from

qualitative models [137] and quantitative models [138]. With the development of specific techniques of various algorithms and software [140, 141], we are capable of answering specific biological questions of varying details that may be not intuitive to human brains [142, 143].

As a promising candidate in cancer therapy, TRAIL has also received a lot of attention in the field of pathway modelling. There have been several research groups working on TRAIL-induced apoptosis pathway with varied resolutions. This work has uncovered a more systematic understanding of the network dynamics.

The most comprehensive work on modeling TRAIL-induced apoptosis was carried out by Albeck *et al*. [142]. By integrating various experimental assays with sophisticated mathematic modeling on apoptosis pathway, they identified that XIAP and degradation of effector caspases are the cause that delay the gap between initiator caspase activation and mitochondrial outer membrane permeabilization (MOMP) [142]. Their later study further demonstrated that Bcl-2 family members, Smac, and the pore assembly on mitochondria are all critical for "snap-action switch" of MOMP [143]. More details of Albeck's modelling techniques will be introduced in section 4.1.4.

Another relevant modeling work focused on the upstream of the TRAIL pathway [144]. Zhang *et al*. [144] looked at the inhibitory effect of decoy receptor (inactive form of death receptors) on the apoptosis pathway and confirmed the "pre-ligand binding hypothesis" that decoy receptors inhibits TRAIL pathway through pre-occupying with death receptors. They also concluded that TRAIL-receptor interactions, the caspase-8 and caspase-3 activation, the Smac/IAP inhibition, and Bid activation are all the key events towards cells' decision of death [144].

To investigate the resistance mechanisms to TRAIL human fibrosarcoma cells, Selvarajooa's group constructed a big network that incorporates apoptosis pathway and cell survival pathway [91]. Their finding suggested targeting at p62 may overcome TRAIL resistance, which offers a valuable prospective to TRAIL-based cancer therapy [91].

This thesis is organized as follows: we will describe the details of materials and methods of biological assays and mathematic models in chapter 3; in chapter 4, we will start with analysis of the dynamics of synergy of LY30 and TRAIL and end with the prediction of LY30 induced changes of $O_2^{\bullet-}$ and H_2O_2 ; in chapter 5, we begin with testing the predictions that emerged at the end of chapter 4, and identified a variety of puzzling results, including species beyond of $O_2^{\bullet-}$ and H_2O_2 that are implicated in death, such as nitric oxide (NO) and calcium(Ca^{2+}); chapter 6 will apply a probabilistic modeling method, Bayesian networks, to the task of interpreting the complex data from chapter 5. Finally we will conclude in chapter 7 with a summary of LY30-induced effects.

3 Materials and methods

3.1 Biological Experiments

3.1.1 Cells and Treatments

HeLa was purchased from *American Type Culture Collection (*ATCC, Rockville, MD, USA) and maintained in Dulbecco's Modified Eagle's Medium (DMEM) supplemented with 10% FBS, 1% L-glutamine, and 1% S-penicillin. HeLa cells were plated at 0.125 million cells/well in 24-well plates (and proportionally for other size plates) and grown overnight until 80% confluent.

3.1.2 Chemicals and Reagents

LY30 was obtained from Alexis Biochemicals (Lausane, Switzerland).

EGTA-am, BAPTA-am and *Thapsigargin* were purchased from Invitrogen life science (Eugene, Oregon, USA).

Tiron (4,5-Dihydroxy-1,3-benzenedisulfonic acid disodium salt), *catalase*, *crystal violet, DMSO, Tween-20, EDTA, DTT, DDC, L-NAME, ATP releasing agent*, *Lucigenin* (bis-N-methylacridinium nitrate) were purchased from Sigma Aldrich (St. Louis, MO).

TMB-8, 2APB were purchased from Calbiochem (Darmstadt, Germany)

TRAIL and fluorogenic substrates of caspase-8 (Ac-IETD-AFC), caspase-3 (Ac-DEVD-AFC) were purchased from Biomol (Plymouth Meeting , PA, USA).

The Coomassie Blue reagent were purchased from Pierce Biotechnology (Rockford, IL,USA).

Trypsin was purchased from Hyclone, Logan, UT.

10x PBS, 10 x SDS, Tris HCl buffer (pH 7.4) were purchased from NUMI Media Preperation Facility (NUS, Singapore).

3.1.3 Antibodies

Rabbit polyclonal Anti-cFLIP, Mouse Monoclonal Anti-β-Actin, Mouse Monoclonal Anti-GAPDH were from Santa Cruz Biotechnology (Santa Cruz, CA, USA).

Rabbit polyclonal Anti-Caspase-8 was purchased from Cell Signaling Technology, Inc. Danvers, MA.

3.1.4 Flow cytometry or confocal microscopy

CM-H2DCFDA-am(DCFDA), *DAF-FM, DHE (Dihydroethidium), MitoSOX, ER tracker, Mito-Tracker were from invitrogen, Fluo-4 AM Calcium Indicators, Fura2-am, Fluo-4 NW (no wash) calcium assay kit* were purchased from molecule probe, Eugene, Oregon, USA.

bis-N-methylacridinium nitrat (Lucigenin) were purchased from Sigma Aldrich (St. Louis, MO).

3.1.5 Treatments

All treatments with LY30 (Alexis, Switzerland) and TRAIL (Biomol, Plymouth Meeting, PA, USA) used the methods and doses following Poh's protocal [88]; all combination treatments of LY30 and TRAIL involved pre-incubation of cells with 25 μM LY30 for one hour before adding 20 ng/ml TRAIL.

Experiments with superoxide scavenger Tiron was applied 10mM to cells 1 hour before adding LY30. Experiments with the H_2O_2 scavenger catalase (C3511 catalase from bovine liver, Sigma-Aldrich) were administrated into wells at doses of 2000 units/ml one day before the treatment of LY30. On the second day, cells were changed with fresh media and catalase was added again at the same concentration (2000units/ml; 4000 units/ml) together with LY30 (25uM). Peroxynitrite scavenger FeTPPS was administrated into cell samples at concentrations of 25uM, 50uM and 100uM one hour before LY30 treatment. Cu/ZnSOD (SOD-1) inhibitor DDC was applied to cells at concentrations of 200mM or 400mM with 2 hour pre-incubation before LY30. Thapsigagin was applied at the concentrations of 1mM.

3.1.6 Cell viability assays

In cell viability assay, HeLa cells were plated in 24 well plates (1×10^5 cells/well) overnight to reach 80% confluent next day prior to treatment. For single treatment, HeLa cells were treated with either LY30 (25uM) or TRAIL (20ng/ml) for 25 hours and 24 hours (LY30 was added 1 hour earlier to be consistent with combination treatment). For combination treatment of LY30 and TRAIL, HeLa were pre-incubated with 25 μM LY30 for 1 hour and then treated with 20ng/ml of TRAIL for a period of 24 hour. For

inhibitory effect, various inhibitors were added into sample wells with optimized concentrations specified in Treatment section (section 3.1.5). For example, Tiron was added at concentration of 10mM before incubation with LY30. Cytotoxicity was determined by the crystal violet assay.

After drug treatment, cells were first washed with 1xPBS, and then stained with crystal violet for 20 minutes. The excess crystal violet solution was washed away using distilled water. For quantification, crystal violet was dissolved in 1% SDS and shaked for 1 hour before conducting measurement using absorbance at 595nm with a Tecan microplate reader.

3.1.7 Caspase activity assays

HeLa cells, after the indicated treatments and incubations, were harvested, washed with 1xPBS, re-suspended in chilled cell lysis buffer (BD Pharmingen, San Diego, CA, USA), and incubated on ice for 10 min. Caspase-3 and Caspase-8 enzyme activities were measured using fluorogenic substrates Ac-DEVD-AFC and Ac-IETD-AFC respectively as reported previously [88].

3.1.8 SDS-PAGE and Western blotting

HeLa cells were grown in 60mm Petri dishes (6 well-plate) until 80% confluent, and treated with LY30 (25uM) for the indicated durations. Cells were harvested and washed once with 1xPBS before lysis using cell lysis buffer (150mM NaCl, Tris-HCl 7.4 and 1% Nonidet P40) with a cocktail of protease inhibiors (1mM PMSF, 10 μg/ml aprotinin, 20 μg/ml pepstatin A and 10 μg/ml leupeptin). 100 μg of cell lysate was then subjected to

SDS-PAGE on a 12% polyacrylamide gel before being electro-transferred onto Immobilon-P membranes (Millipore Corporation, Bedford, MA). Membranes were blocked using 5% non-fat dry milk in TBST (TBS with 0.5% Tween20) and probed overnight at 4^{o}C with cFLIP antibody (Santa Cruz Biotechnology Inc. Santa Cruz, CA. U.S.A). β-actin or GAPDH (both from Santa Cruz Biotechnology Inc. Santa Cruz, CA.) was used as a loading control. Primary antibodies were detected using HRP conjugated anti-mouse or anti-rabbit antibodies and visualized using enhanced chemiluminescence detection (ECL reagents from Roche, Indianapolis, IN, USA). Densities were quantified using Image J (http://rsb.info.nih.gov/ij/).

3.1.9 Flow cytometry measurements

Data collection

After specific treatments, cells were firstly washed with 1XPBS, and then loaded with fluorescent dyes at 37℃ for 15 minutes. After that, cells were washed again with 1XPBS and then placed under flow cytometry with optimal wave lengths. DCFDA for H_2O_2 and $ONOO^-$, DAF for NO, and Fluo-4 am for Ca^{2+} are analyzed with excitation wavelength 488 nm and emission 517 nm. For DHE, detection was conducted with excitation at 400 nm and emission at 590 nm. For each treatment, at least 10,000 events were obtained.

Data Analysis

First of all, cell gating is applied to all the cells under Flow cytometry to get rid of unhealthy cells according to side scatter (SS) and Forward scatter (FS), which measure cell size and optical homogeneity correspondingly. Once a gate is set, it will be applied

to all the samples through the experiment. Fluorescence yield in each gated sample is visualized through either scatter plot or histogram, and absolute fluorescence is the average fluorescence of the gated population. For clear comparison, each sample is normalized according to the formula $R_i = \frac{F_{i\_measured} - F_{unstained}}{F_{CTL\_measured} - F_{unstained}}$ where R_i is the normalized concentration of sample *i*. $F_{i\_measured}$ is the absolute fluorescence from *i*th sample, $F_{unstained}$ is the absolute fluorescence from unstained control. $F_{CTL\_measured}$ is the absolute fluorescence from untreated control sample.

H_2O_2 measurements

Intracellular concentration of H_2O_2 was determined with DCFDA, which is oxidized to a fluorescent form by H_2O_2 and its free radical products. After specific treatments, cells were washed with PBS, trypsinized and after that loaded with 5 μmol/L of DCFDA at 37 ℃ for 15 min, and then placed under flow cytometry using excitation wavelength of 488 nm and emission of 517 nm. For each treatment, at least 10,000 events were obtained and then analyzed using software Submit.

NO measurement using DAF-FM

For Nitric Oxide (NO) measurement, NO indicator is chosen as cell membrane permeable indicators DAF-FM diacetate[145]. DAF-FM diacetate is an sensitive reagent for quantifying NO concentrations. Its fluorescence yield is reported to increase 160-folds after reacting with NO.

After specific treatments, cells were washed with PBS, loaded with 5 μmol/L of DAF-FM diacetate at 37 ℃ for 15 min, and then placed under flow cytometry using excitation wavelength of 488 nm and emission of 517. For each treatment, at least

10,000 events were obtained. Obtained data are then analyzed using software SUMMIT.

$O_2^{\bullet-}$ measurement using DHE and MitoSOX

For superoxide ($O_2^{\bullet-}$) measurement, cell membrane permeable indicators DHE is incubated at a concentration of 20uM for 15-20 minutes. It is reported that DHE forms a red fluorescent product upon reaction with superoxide anions [146]. Fluorescence of DHE is obtained at excitation of 400 nm and emission at 590 nm.

For specific detection of mitochondrial superoxide, treated cells are stained with MitoSOX at concentration of 10uM for 15-20 minutes. Fluorescence is obtained at the same wavelength as DHE.

Ca^{2+} measurement using Fluo-4 am

For Ca^{2+} measurement, cells were firstly washed with 1 x PBS and then stained with cell membrane permeable indicators Fluo-4 am at a concentration of 5uM for 30 minutes. Then, cells were changed to indicator-free medium for another 30 minutes to remove any dye that is non-specifically attached on the cell surface. After that, cells were placed under flow cytometry for further analysis.

3.1.10 $O_2^{\bullet-}$ measurement using lucigenin

Lucigenin is a di-acridinium compound to detect intracellular superoxide. [147, 148]. In our experiments, chemoluminescence is obtained after adding lucigenin to fresh cell lysate.

HeLa cells were seeded in 100-mm tissue culture plates 24 hours before performing the experiment. After washed once with lX PBS, the cells are then detached with 1X trypsin and transferred to a sample cuvette, and centrifuged at 1200 rpm at 25 °for 5 min. The supernatant is removed, and the cell pellet is re-suspended in 400 ml of lx ATP releasing buffer at room temperature, after that 100 ul of 850 uM lucigenin stock solution was added into cell lysate immediately before the reading.

3.1.11 Ca^{2+} measurement using Fura-2

Data collection

Cells were incubated with Fura-2 AM in calcium measurement buffer at a concentration of 5uM for 30 minutes at room temperature, and then they were changed into indicator-free buffer (HBSS containing 1mM Ca^{2+}) for 30 minutes for de-esterification of intracellular AM esters. After that, cells were brought to spectrofluorimeter for calcium measurement. Once the baseline ($\frac{F_{\lambda=380}}{F_{\lambda=380}}$: fluorescence intensity ratio between bound calcium and free calcium) is stable, drugs (LY30 or Thapsigargin) were added according to specified concentrations, sequence and incubation time. After that, cells were finally treated with 0.05% Triton X-100 for calculation of R_{max} and 100 mM EGTA (5 mM final) for R_{min}.

Data analysis

Intracellular free calcium concentration is calibrated through formula:

$$[Ca^{2+}] = K_d Q \frac{(R - R_{\min})}{(R_{\max} - R)}$$

In this formula, R refers to measured fluorescence ratio between 340 and 380 ($\frac{F_{\lambda=380}}{F_{\lambda=380}}$), where R_{max} and R_{min} are calculated maximum fluorescence ration (calculated through Triton X-100 treatment) and minimum fluorescence ration (calculated through EGTA treatment). K_d is the Ca^{2+} dissociation constant of the Fura-2, which can be calculated with known concentration Ca^{2+}. Q is the calculated ratio of F_{min} to F_{max} at λ2 (~380 nm).

3.1.12 Ca^{2+} measurement using Spinning Disk Confocal Microscope (SDCM)

Cells are seeded win 8-well chamber with 25000 cells per well and then let them grow for 24 hours. On the next day, cells were first washed with warm tyrosin buffer and then stained with Fluo-4 am at 25uM and probenecid at 250uM in tyrosin buffer for 1 hour at room temperature. After that, they were washed twice before measurement under Spinning Disk Confocal Microscope (SDCM). For Calcium measurement with Thapsigagin treatment, images were taken for 6 minutes with interval of 2 seconds. For calcium measurement with LY30 treatment, images were taken for 45 minutes with interval of 15 seconds.

Data analysis was conducted through fully-automated image processing software developed by Fivaz group. Refer to [149] for details and procedure. The algorithm description and example demonstration is taken from their published paper and shown in Figure 3.1.1.

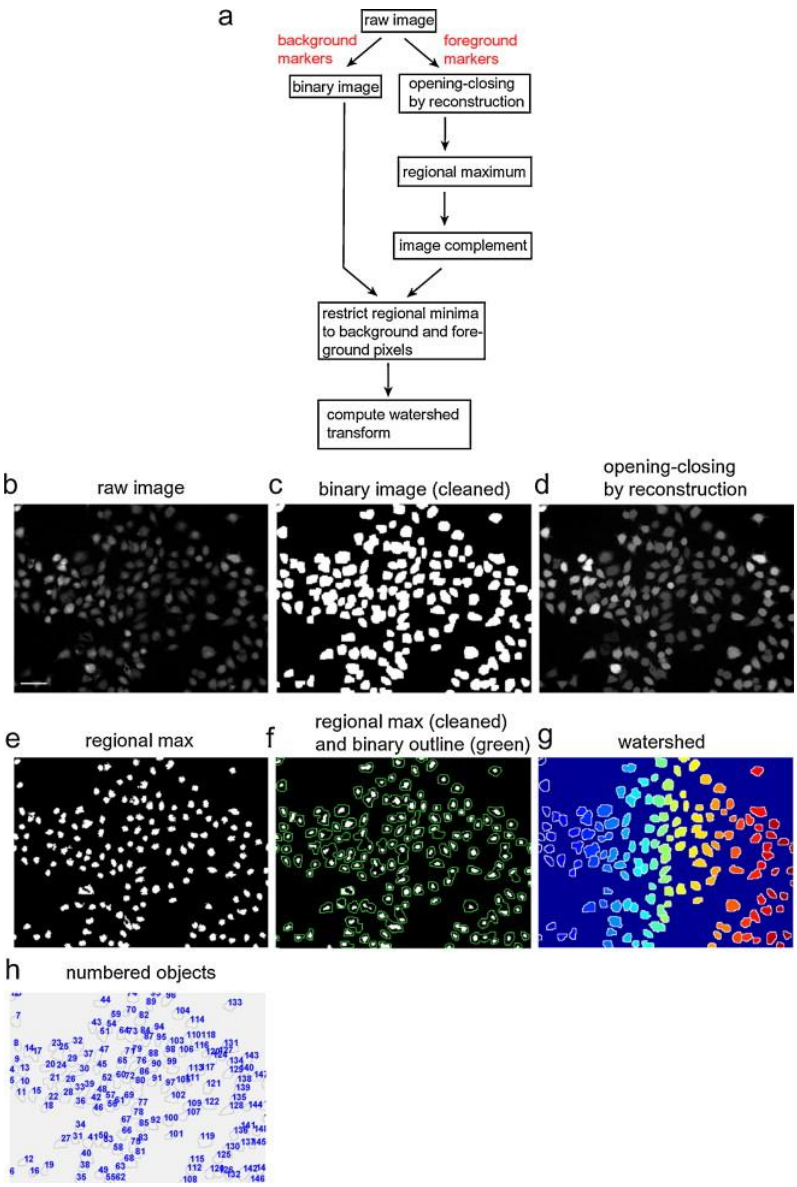

Figure 3.1.1 Algorithm description of Marker-based watershed segmentation by Wong *et al.* [149]. (a) Workflow for cell segmentation algorithm. (b) Raw image of cells from confocal microscopy. (c) Binary processed image (d) Image processed after "opening-by-reconstruction" and "closing-by-reconstruction". (e) Identification of cell regions. (f) Cell outline (green) after cleaned-up. (g) Processed result using segmentation algorithm. (h) Numbered objects from panel g.

HeLa cells were placed under SDCM for image acquisition after stained with Fluo-4 45 minutes. Refer to materials and method for detail procedure. Each Treatment was carried out at the 5th round of image acquisition.

3.1.13 Ca^{2+} measurement using Microplate reader

HeLa cells were seeded in 96 black well-plate (FluoroNunc™, Themo Scientic, Black plates for fluorescence reading with minimum back-scattered light and background fluorescence) 25000 cells per well and grew for 24 hours. On the next day, cells were washed with 1 x PBS, and were incubated with Fluo-4 NW buffer with probenecid (5 mM) at 37 ℃ for 30 minutes and then at room temperature for an additional 30 minutes.

After designed treatments were conducted on the cells, fluorescence intensities were obtained through reading of fluorescence emission at 517 nm and excitation at 488nm.

3.2 Computational Simulations

3.2.1 ODE model construction and simulation of LY30+TRAIL model

KroneckerBio toolbox [150] in MATLAB (Natick, MA, USA) and Copasi [151] were used for simulating the ODE models. In the TRAIL pathway model, synthesis and degradation effects were only modeled for caspases. Protein degradations were modelled as first-order reactions, and protein synthesis were modelled as zeroth-order reactions. Noted that the synthesis rates and degradation rates were estimated so that the steady state concentrations of capases will be consistent with that of initial concentrations in Albeck model [152]. Monte Carlo simulations were carried out with sample size of 10,000 cells with normal distributions of initial concentrations (mean equal to the initial concentration in the Albeck model, and variance equal to 40% of the mean initial concentration). PLOT [153, 154] was used for visualizing simulations.

We converted the simulated absolute caspase numbers into relative caspase activity through a weighted function according to the reports in by McStay *et al*. [155].

$$IETD\_abs = 0.026 * C8 + 0.8 * C8^{*} + 0.015 * C9^{*}$$

$$IETD\_rel = IETD\_abs \Big/ IETD\_abs_{untreated}$$

$$DEVD\_abs = 30.04 * C3^{*} + 0.068 * C3 + 0.07 * C9^{*}$$

$$DEVD\_rel = DEVD\_abs \Big/ DEVD\_abs_{untreated}$$

Here, *IETD_abs* refers to absolute IETD fluorescence as measured by IETD which is dye used to detect caspase-8 activity. *IETD_rel* refers to relative fold change of IETD fluorescence as compared to that in untreated control. *DEVD_abs* refers to absolute DEVD fluorescence as measured by DEVD which is dye used to detect caspase-3 activity. *DEVD_rel* refers to the relative fold change of DEVD fluorescence as compared to that in untreated control.

3.2.2 Bayesian Modeling

Bayesian network model consists of network structure and conditional probability tables. Network structure, which composed of directed arrows from parent species to children species, captures cause and effect relationships among the species. Conditional probability tables quantitatively describe the impact of parent species on their children species. Each Bayesian network model is evaluated with a Bayesian score which indicate its consistency with observation.

Bayesian network involves data processing including normalization, discretization, structure learning, parameter estimation and model inference. Model selection, parameter estimation and inference were carried out in Bayesian Network Toolbox (BNT) [156, 157] implemented on MATLAB developed by Kevin Murphy.

3.2.2.1 Data processing

Normalization: Data are firstly normalized by comparing the concentration of each sample to that of untreated control, as described in the formula of where f_m^i represents measured fluorescence intensity of sample *i*, $f_m^{un\_ctl}$ represents measured fluorescence intensity in unstained and untreated control, f_m^{ctl} represents measured fluorescence intensity in untreated control, $C_{normalized}^i$ represents calculated normalized concentration.

Discretization: Normalized data (DCFDA, DAF, DHE and Fluo-4) were discretized into 3 levels (represented by 1, 2 and 3) with equal width interval binning. We chose 3 intervals as it is likely more true to underlying biological phenomenon of low, medium and high concentration. Specifically, the minimum and maximum values of the species were first determined and then whole range of values was divided into the 3 intervals of equal width. LY30, as the model input, is discretized into 3 levels, which corresponds to no incubation (0 minute), brief incubation (0~30 minutes) and long incubation (30 minutes or longer).

3.2.2.2 Structure learning

Structure learning was carried out to select the optimal model which has the highest Bayesian score (refer to section 6.2). We used a Markov Chain Monte Carlo (MCMC)

algorithm called Metropolis-Hastings (MH) to search the space of possible model structures [156]. We set number of steps to take before drawing samples to be 25 and number of samples to draw from the chain after burn-in to be 500 in accordance to the recommended setting with BNT [156, 157]. To get rid of residual effect with starting point, the process was repeated for 10,000 times with random staring points. After 10,000 repeats, we selected the top 12 models with the highest Bayesian scores.

3.2.2.4 Parameter estimation in Bayesian networks

Parameter estimation is to estimate CPT (Conditional Probability Table) for all the nodes in a specified network structure given a set of observations, so that there is minimum difference between inferred data of the model and observation. For all the tasks involved in parameter estimation, we applied function of *learn_params_em* which learns parameters through Expectation-Maximisation principle [158].

3.2.2.5 Model inference

Given a Bayesian network model with a specific structure and a set of estimated parameters, we are able to infer the values of unmeasured species (also called hidden nodes, H) according to the measured species (evidence, E). Model inference is to compute the conditional probability of $P(H_i \mid E)$ for all hidden nodes H (H_i is one member of H). We conducted model inference using pearl's algorithm [159] which can fuse and propagate the impact of new evidence.

3.2.2.6 Model Averaging

Following the idea of Sachs [160] on model averaging, we averaged among the top 12 models for the inferred values of hidden nodes (which is DCFDA) given the evidence

of LY30 and inhibitors (inhibitor for NO, Ca^{2+} and $O_2^{\bullet-}$ specifically). In particular, we adopted equal voting in averaging the models so that averaged DCFDA is calculated as $DCFD^{k}_{averaged} = \frac{\sum_{i}^{12} DCFDA^{k}_{i}}{12}$. Here, k can take values from 1, 2 and 3 corresponding to low, medium and high. $DCFDA^{k}_{i}$ refers to inferred probability of DCFDA at state k in model *i*. Noted that in every model, the sum of inferred DCFDA at states 1, 2, and 3 is 1.

In order to compare DCFDA between inferred probability distribution at low, medium and high states, and measured fluorescence, we converted the inferred probability distributions into a single value according to the formula:

$$DCFDA_{averaged} = 0.1 * DCFDA^{1}_{averaged} + 0.4 * DCFDA^{2}_{averaged} + 0.9 * DCFDA^{3}_{averaged}.$$

Here $DCFDA^{1}_{averaged}$ $DCFDA^{2}_{averaged}$ and $DCFDA^{3}_{averaged}$ represented averaged probability values of DCFDA in state low, medium and high, respectively.

3.2.2.7 Extension of model with inhibitors

Extension of dummy inhibitors: Dummy inhibitors were the inhibitors assumed with 100% capability in inhibiting the target specifically. Dummy inhibitors includ NO inhibitor, Ca^{2+} inhibitor and $O_2^{\bullet-}$ inhibitor, which were incorporated into the Bayesian network models in section 6.4. Each inhibitor has two states of 1 or 2, corresponding to the situation of without or with the inhibitor. When the state of the inhibitor is 1, there is no influence on its inhibiting target; when the state of the inhibitor is 2, the parameter is adjusted so that its target will be at low concentration only.

Extension of real inhibitors: Real inhibitors include DDC, Tiron, FeTPPS, EGTA-am, each of which has two states 1 and 2, as similar to dummy inhibitor. For a specific inhibitor X, it has n targets Y_1, ..., Y_n with inhibitory effect at I_1, …, I_n. When X state is 1, there is no influence on its targets; when its state is 2, it will adjust the probability distribution of its targets accordingly. Take Y_i for example, its probability will be adjusted to I_i (1- I_i)/2, (1- I_i)/2 for low concentration, medium concentration and high concentration, respectively.

3.2.3 Statistical Analysis

All experiments were performed at least three times for statistical significance. Numerical data were expressed as mean +/- SD. Statistical analysis was performed using the one-tailed paired Student's t-test considering the variances unequal. P-values < 0.05 were considered significant.

4 Computational Modeling of Pathway Dynamics by LY30 and TRAIL Revealed non-monotonic effect of LY30 on cFLIP

In this chapter, we analyzed the synergistic effects of LY30 and TRAIL on cell killing and caspase dynamics through modelling the signalling pathways with ordinary differential equations.

4.1 Introduction to Ordinary differentiation equation (ODE) modeling of biological pathways

A biological pathway usually involves many species and can be viewed as a network of biochemical reactions. In ODE models, the concentration of each species in the network will be determined by the rates of reactions that produce or consume this species. Reaction rates of each reaction can be derived through physical and chemical laws. Once we obtained all the rate equations for in a network, the rate of change of each species can then be derived by summing all reaction rates that produce this species and subtracting all reaction rates that consume this species [161].

Example Take a simple reaction for example, species *A* and *B* react together to produce *AB* with forward reaction rate at *k1* and reverse reaction rate at *k2*. The reaction is expressed as

$$A + B \underset{k2}{\overset{k1}{\rightleftarrows}} AB$$.

According to mass action law, rate equations of A, B and AB in the reaction are expressed as

$$\frac{d[A]}{dt} = k2*[AB] - k1*[A]*[B]$$,

$$\frac{d[B]}{dt} = k2*[AB] - k1*[A]*[B]$$,

$$\frac{d[AB]}{dt} = -k2*[AB] + k1*[A]*[B]$$.

ODE models are composed with model structure, kinetic rate constants and initial concentrations three elements. Model structures incorporate all the chemical reactions in a network, kinetic rate constants quantify the reaction speeds and initial concentrations describe starting concentrations of all the species in the network. Given the three elements, an ODE model will calculate a unique solution specifying how the system will evolve over time [162]. Choice of parameter values of ODE models, in a great extent, controls dynamic behaviour. Therefore, accurate setting of parameters values becomes essential in ODE capability. We will introduce parameter estimation and sensitivity analysis in the following sections.

4.1.1 Parameter Estimation in ODEs

Parameters of ODE models consist of rate constants for reactions and initial concentrations for species. Parameters are not easily obtained but usually involve

laborious calibration from various biological assays. It was also realized that parameters taken from literature are of limited use because they are often inconsistent because measured under varied conditions [163] . In addition, parameter values (both rate constants and initial concentrations) may vary from cell type to cell type, and such variance has also been found to be common in cells within the same cell type [164]. Since the accuracy of ODE model is highly dependent on parameter values, we apply parameter estimation for an accurate calibration of the parameters[165].

In the context of biological pathway modelling, parameter estimation is defined as calibrating model to reproduce the experimental results [166]. Parameter estimation is formulized as minimizing the difference between model-simulated output and corresponding experiment data sets, subject to a series of constrains such as dynamics of the system [166, 167]. Mathematically, it is to find *p* to minimize *J*, in the formula:

$$J = \int_0^{t_f} (y_{msd}(t) - y(p,t)^T W(t)(y_{msd}(t) - y(p,t))dt$$

With constraint

$$\begin{aligned} & f(\frac{dx}{dt}, x, y, p, v, t) = 0 \\ & x(t_0) = x_0 \\ & h(x, y, p, v) = 0 \\ & g(x, y, p, v) \le 0 \\ & p^L \le p \ \le p^U \end{aligned}$$

where *J* represent the cost to be minimized; *p* are the parameters to be estimated; y_{msd} is the experimental measurement of output state variables; *y(p, t)* is the model prediction f; *W(t)* is a weighting (or scaling) matrix; *x* is the differential state variables; *v* represent

other parameters which will not be estimated; f is the set of equality constraints describing the system dynamics; h and g are the possible equality and inequality constraints as additional requirements for the system performance; and p is subject to (upper and lower) bounds [166].

Several approaches have been proposed for estimating parameters in biological signalling pathways, *e.g.* genetic algorithm [168], unscented Kalman filter [169], and particle filtering [166].

4.1.2 Sensitivity analysis in ODEs

The dependence of a system on its parameter (initial conditions or rate constants) values can be addressed through sensitivity analysis, which involves monitoring the change of model output with systematically varying parameters [164]. Sensitivity analysis is a systematic approach to analyze the change of a system according to the change of parameter values [170]. An important feature of sensitivity is that it is able to quantitatively describe the influence of a certain parameter on system output.

The characteristics of sensitivity analysis make it an important tool in ODE modelling and understanding of biological phenomenon. Parameter sensitivity analysis can be applied to Drug target selection [171], Biomarker selection [172], Model reduction [173], Robustness analysis [174] and experiments design [170].

Sensitivity analysis includes local sensitivity analysis and global sensitivity analysis. Local sensitivity analysis is a particular form of sensitivity analysis similar to metabolic control analysis [175]. The sensitivity coefficients S_{ij} is defined as first order

derivatives of the model output O_i according to model parameter P_j in a normalized form of:

$$S_{ij} = \frac{\partial O_i}{\partial P_j} \bullet \frac{P_j}{O_i}$$

The accuracy of local sensitivities is based on the assumption the actual values of model parameters represent the real situation, which, however, is not the case in most of the pathway models. An alternative to overcome the limitation of local sensitivity analysis is global sensitivity analysis in model analysis [176]. Global sampling composed of drawing representative samples from the sampling space, simulating the model with each sample, and then calculating the parameters sensitivities through a statistical or mathematical analysis of the simulation results. As an example, Monte Carlo scheme is one popular methods in global sensitivity analysis [177].

4.1.3 ODE model of TRAIL-induced apoptosis in HeLa (Albeck et al.)[143]

4.1.3.1 Model description and structure

In Abeck *et al.* model, there are 58 species of which 18 are direct gene product and the remaining 40 represents complex, cleaved forms. There are 28 reactions and 70 non-zero rate constants. The four main parts in the model comprises (1) DISC formation and the subsequent Caspase-8 activation (C8*); (2) an enzyme cascade from C8* to C3* [178] and then lead to the cleavage of PARP to cPARP [179]; (3) positive feedback loop from C3* to C8* through caspase-6 (C6) [180]; and (4) an apoptosis signal amplification through mitochondria from C8* to tBid [92, 93, 94].

4.1.3.2 Parameter estimation

In the model, Albeck *et al*. obtained a large quantity of single cell and cell population data through a large range of TRAIL doses. Single data were obtained through Förster resonance energy transfer-based reporter proteins for C3*, C8* and MOMP [143]. Cell population data were obtained through Western blot and flow cytometry. All the obtained data are integrated for parameter calibration in the equation $c(t) = f - \frac{f}{1+e^{(t-T_d)/4T_s}}$ where *c(t)* represent the amount of substrate cleaved at time *t*, *f* is the cleaved of the reaction, T_d is the half-life of substrate, and T_s represents the process time to complete effector substrate cleavage. In order to obtain accurate parameters, Alebck *et al*. also studied TRAIL-treated cells perturbed by small interfering RNA (siRNA) or protein over-expression.

4.1.3.2 Contribution

Besides can accurately reproduce experimental results, the model showed the mechanism of "snap-action" switching of apoptosis signal from gradual C8* activation in response to death stimuli and the key role of caspase-8 in MOMP delay [142, 143].

4.2 Results

4.2.1 Construction of TRAIL model

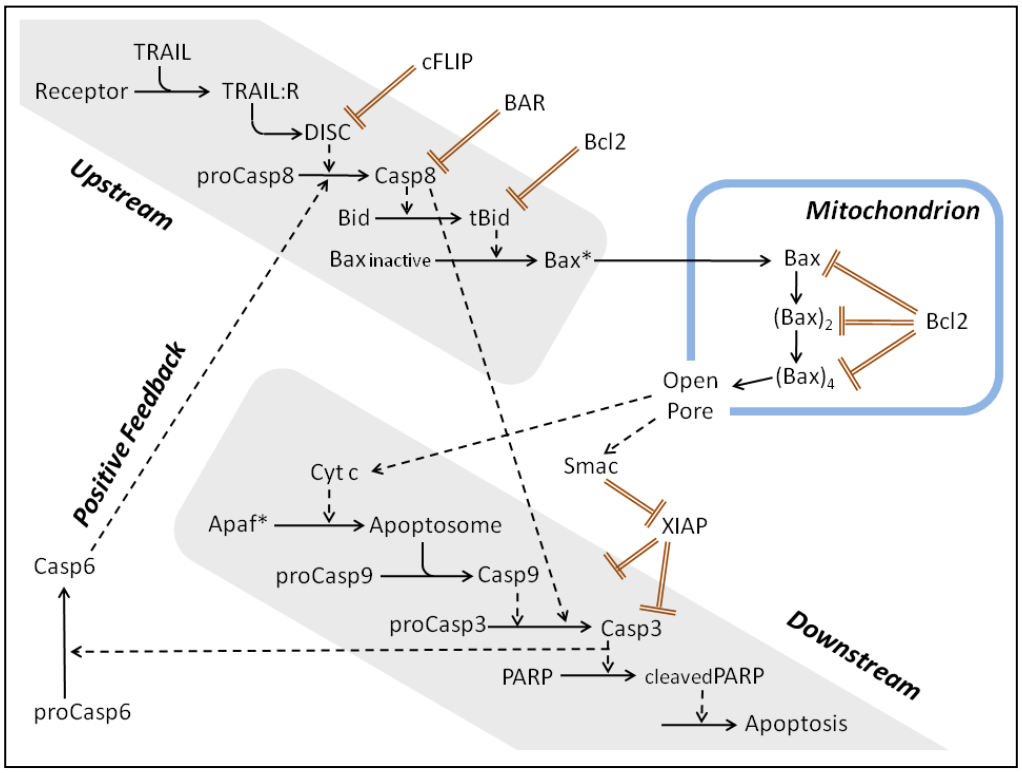

Figure 4.2.1 Schematic diagram of TRAIL-induced apoptosis. The dashed arrows indicate catalytic effects. Solid arrows indicate that the species at the base is consumed or translocated. For example, the oligomerization of mitochondrial Bax leads to formation of a pore in the mitochondrial outer membrane, which allows release of Cytochrome c and Smac into the cytosol. Double-lines in a T indicate inhibitory effects.

To study the synergy between LY30 and TRAIL, we adapted a previous model of TRAIL-induced apoptosis by Albeck as described in 4.1.3 [152], and added reaction equations for the impact of LY30 on the network. Although the Albeck model is supported by extensive experimental measurements in HeLa cervical carcinoma cells, the experiments involved cycloheximide, an inhibitor of protein synthesis. A lack of turnover effects in the Albeck model means that even an insignificant pro-apoptotic input is able to accumulate without degradation, until the cell eventually dies [181, 182]. To permit the system to have a stable steady state other than apoptosis, we included complex biological influences, such as synthesis and degradation, by approximating

them with mass-action rate equations (Figure 4.2.1). This modification renders the model less quantitative (not appropriate for predicting absolute concentrations) but this level of simplification is still highly informative for inferring system-level effects. We made two further additions to Albeck's TRAIL model: incorporated the feedback from activated caspase-3 to activated caspase-9, and increased initial concentration of protein cFLIP, which is particularly sensitive to cycloheximide [183].

4.2.2 Construction of LY30 model

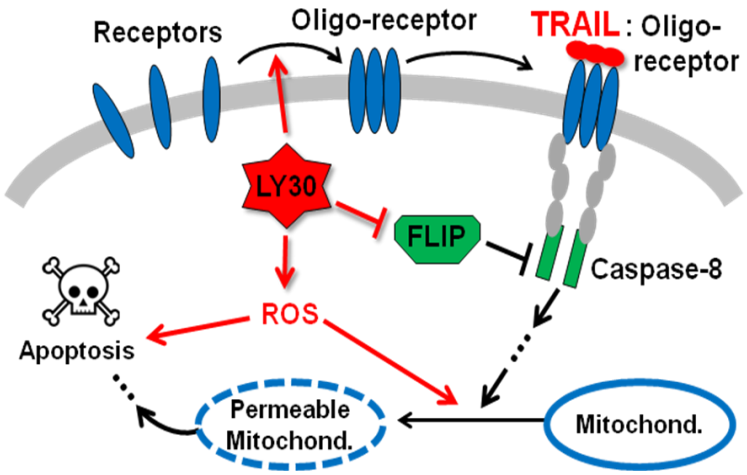

Figure 4.2.2 Schematic of how LY30 affects TRAIL-induced apoptosis. The receptors alone would have slower reaction rates than the Oligo-Receptors..

Poh *et al.* identified two effects of LY30 that could contribute to its ability to sensitize cells to TRAIL [88]: a) clustering of TRAIL receptors, and b) down-regulating the pro-survival protein cellular FADD-like interleukin-1β-converting enzyme inhibitory protein (cFLIP) [184]. Figure 4.2.2 illustrates how these effects have been modeled. Clustering is modeled by an LY30-catalyzed transition in the TRAIL receptor, converting the slow-reacting "monomer" form into a faster-reacting form that we call "R_oligo". The cFLIP down-regulation is modeled as an LY30-catalyzed degradation

reaction, which is intended to represent a variety of possible mechanisms including transcriptional repression, ubiquitylation, etc. In addition, LY30 had previously been shown to elevate intracellular hydrogen peroxide (H_2O_2) [88, 89] which can regulate cell death through intracellular acidification , activation of caspase-3 and -9 [186], down-regulation of cFLIP [184], and down-regulation of NHE1 [187, 188]. Here we model H_2O_2 as causing low levels of mitochondrial permeability [186, 189], and also causing a small amount of death independent of mitochondria [190]. This model is specific to TRAIL-induced apoptosis in HeLa cells, and we did not model additional phenomena found in other cell types or in other death pathways.

LY30-induced Receptor oligomerization

Quantification was conducted on pull down experiments of DR5 in HeLa cells (Figure). Results showed that: 1) the total number of DR5 is the same in LY30-treated cells and untreated cells (Figure 4.2.3), and 2) the ratio of concentration of pull-downed DR5 in untreated cells and LY30-treated cells is 1:5.8, meaning that on average, each oligomer is composed of 5.8 DR5 monomer after LY30 treatment.

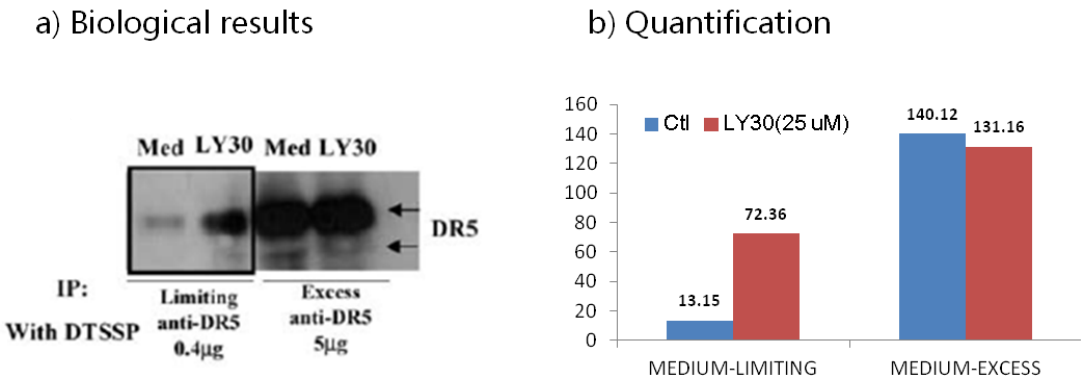

Figure 4.2.3. LY30-induced receptor oligomerization. a) experimental results from Poh.et al [74].2) quantified results of DR5 using ImageJ

Based on the results, we estimated the parameter *K_f* in reaction below to have conversion of monomer receptor to oligomer within 1hour. For the other three parameters, *K_rr* is assumed to be fast so that there is low concentration of intermediate product R:LY30, and *k_r* and *k_ff* are set to be small compared with *K_f* so that there is few reverse conversation from oligomer to monomer.

$$R + LY30 \underset{k\_r}{\overset{K\_f}{\rightleftarrows}} R:LY30 \underset{k\_ff}{\overset{K\_rr}{\rightleftarrows}} R\_oligo + LY30$$

LY30-facilitated DISC formation upon TRAIL

It has been reported that TRAIL can induced DISC formation more efficiently through pre-oligomerized DRs than DR monomers [74]. The knowledge is incorporated in the reactions below, where *k1* and *k_1* are estimated through the experimental results (Figure 4.2.4).

$$R\_oligo + TRAIL \underset{k\_1}{\overset{k1}{\rightleftarrows}} R\_oligo:TRAIL \xrightarrow{KK1} R^* \qquad (5)$$

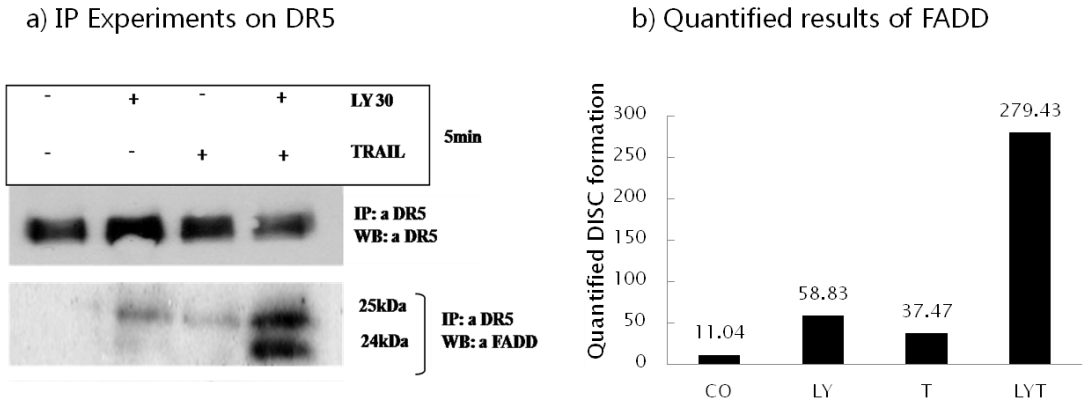

Figure 4.2.4: Time kinetics of DISC assembly upon LY30+TRAIL treatment. a) Western blot experiment of FADD through immuno-precipitated with anti-DR5 in

HeLa cells. HeLa cells were exposed to TRAIL(20ng/ml) for 5 min with or without prior addition of LY30(25μM) for one hr [74]. b) Quantified results of FADD in a).

- **LY30-induced cFLIP reduction**

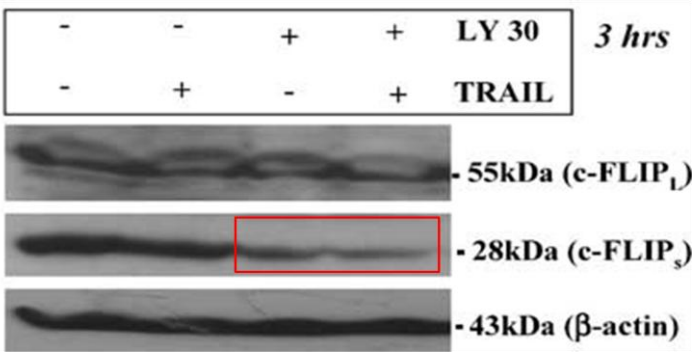

Figure 4.2.5. western blot experimental results of cFLIP upon LY30, TRAIL and LY30+TRAIL treatment [74]

The phenomenon of cFLIP down-regulation upon LY30 treatment is represented with the LY30-induced FLIP degradation $FLIP + LY30 \xrightarrow{k37} LY30$, where the parameter *k_37* is estimated on previous experimental results (Figure 4.2.5).

- LY30-induced ROS production

As we did not know the exact mechanism behind the phenomenon of distinctive ROS production upon LY30 treatment, a simple reaction expressing LY30 induces ROS production was designed as $LY30 \xrightarrow{k35} LY30 + ROS$, where LY30 can directly induces ROS production. To implement a delay of ROS effect in the pathway, we added another reaction $ROS \underset{k\_36}{\overset{k36}{\rightleftharpoons}} ROS*$ where the ROS* represents effective form ROS that contributes to apoptosis.

4.2.3 Construction of LY30+TRAIL model

The TRAIL model of section 4.2.1 and the LY30 model of section 4.2.2 were combined into a single system of ordinary differential equations (ODEs). To simulate combined treatment, we followed the experimental protocol of Poh *et al*., pre-incubating cells with LY30 for one hour before treating with TRAIL. In other words, the initial concentration of TRAIL is zero during the first hour, and then the TRAIL level is shifted to the delivered dose of 20 ng/mL.

4.2.4 Modeling Synergy

Our previous measurements of apoptotic signaling in HeLa cells after treatment with LY30 [88] showed that the combination of LY30 and TRAIL induced synergistic (greater than additive) activation of the apoptotic pathway at many stages, including initiator and executioner caspases. To increase the confidence of the cell death quantization, we performed additional measurements of cell death. The pooled dataset (Figure 4.2.3) shows cell death occurs synergistically, with the rate of killing 30% higher than the rate expected from a purely additive effect.

Apoptosis proceeds in an all-or-nothing fashion, as a "snap action" switch, preceded by a variable time delay [152, 191]. This creates significant discrepancy between the concentrations in individual cells, and the average concentrations in a population of cells that undergo apoptosis with variable delay. Individual cells exhibit much sharper slopes in their activation levels than the population average. Because our model will be compared with data from populations of cells (immunoblots and enzyme activity assays), we need to model population effects. We used Monte Carlo sampling to compute an average trajectory, using simulations of 10,000 instances for each treatment

condition, and normally distributed initial concentrations with 40% variance. For each cell instance, 50% PARP cleavage is considered as apoptotic. Under this condition, we were able to obtain viability percentage under different treatments according to PARP cleavage.

The simulated apoptosis was compared with experimental measurement of cell viability (Figure 4.2.6) for each of the treatment combinations. Our simulations were successful at recapitulating the observed synergy. This finding provides a "proof of plausibility" that death receptor clustering, cFLIP down-regulation and H_2O_2 production, are sufficient to facilitate significant sensitization, in cells treated with otherwise sublethal doses of TRAIL.

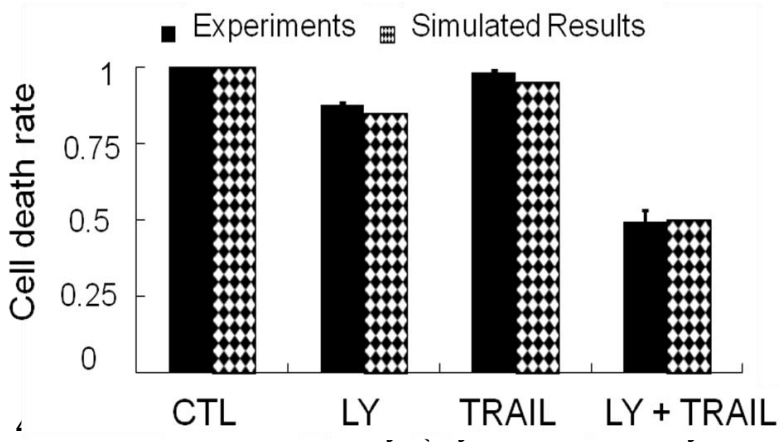

Figure 4 hrs) after treatment with LY30 and/or TRAIL.

4.2.5 Mismatch of the Model

After comparing cell viability between simulations and experiments, we further inspected the temporal profiles of caspases, which are the key species internal of apoptosis pathway. Note that the experimental measurements of caspases are fold change relative to control rather than absolute units while our model simulate generates

absolute molecule number of activated caspases. In order to resolve the unit difference for better comparison, we translate simulated absolute molecule number into relative number according to previously published paper. When we inspected the temporal profiles of the caspases, we found the simulations did not resemble the experimental data. A variety of estimated parameter sets and model optimization efforts were unable to alleviate the qualitative divergence between the model and the data.

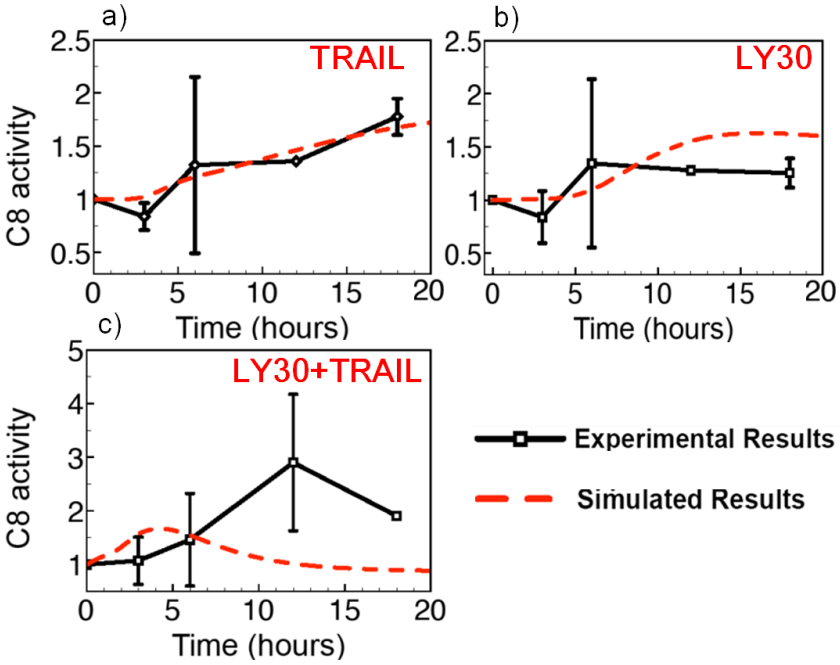

Figure 4.2.7 Time kinetics of capase-8 activity after treatment with LY30 and/or TRAIL. a) Time kinetics of caspase-8 activity after TRAIL treatment. b) Time kinetics of caspase-8 activity after LY30 treatment. c) Time kinetics of caspase-8 activity after LY30 and TRAIL treatment. Red line represents averaged results of 10,000 Monte Carlo simulations and black lines are the measured results from caspase activity assay.

Fig 4.2.7 (a-c) shows Monte Carlo simulations of caspase-8 compared with experimental measurements. Our single drug treatment model of either LY30 or TRAIL alone is able to match experiment dynamics. However, simulations predict that the synergistic effect of LY30 and TRAIL on caspases begins quickly and increases

steeply, relative to the rate at which the caspases get activated by LY30 alone or TRAIL alone. In contrast, experiments show the combination treatment resembles the individual treatments at early time points, then a sharp rise occurs after a delay, and the synergistic effect does not occur at early time points. A milder version of the same effect was seen in caspase-3. At later time points, caspase activity measured data diverged from simulated results, but the slopes were more comparable between theory and experiments at these later times. We hypothesized that the early time points were more likely to be the source of the disagreement.

4.2.6 Experimental Measurements

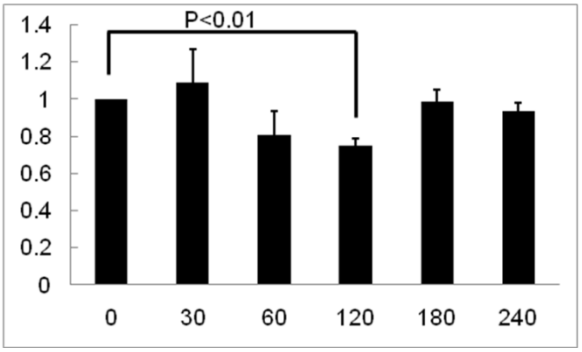

Figure 4.2.8 Caspase-8 activity measurement in HeLa cells after different duration of LY30 treatments. Each set of measurement consists of cells treated with LY30 at 0, 1/2, 1, 2, 3and 4 hours. The result is obtained through 3 independent set of measurements. Student's t-test for whether the observations are significantly lower than the untreated case (i.e., time 0) yielded 0.058 for the observations at 1 hr, and 0.0034 for the observations at 2 hrs**.**

The mismatch between model and experiments for the onset of LY30+TRAIL synergy provided us with a narrow specification for the molecules and time points in greatest need of clarification. Therefore, we applied new experiments to measure caspase-8 activity after treatment with LY30.

Figure 4.2.8 shows the effect of LY30 on caspase-8 enzymatic activity over time, with frequently spaced time-points after treatment. We had expected LY30 to increase caspase-8 activity. But this experiment showed unexpected transient behaviors, with LY30 causing decreased caspase-8 activity at early time-points. Our model of LY30 effects (Figure 4.2.2) does not include any possible way for LY30 to delay or inhibit apoptosis. This puzzle motivated us to perform more detailed measurements upstream of caspase-8 dynamics.

Some unknown effect of LY30 must occur, and we can infer it to be upstream of caspase-8 prior to 3 hours. Knowing that LY30 affects cFLIP and cFLIP has complex regulation [192, 193], we repeated the measurements of cFLIP concentration from 1 to 4 hours with denser intervals during the first 1 hour. Surprisingly, cFLIP-s was initially up-regulated by LY30 treatment, and the most significant increase happened around 30 minutes with p-value <0.05 (Figure 4.2.9).

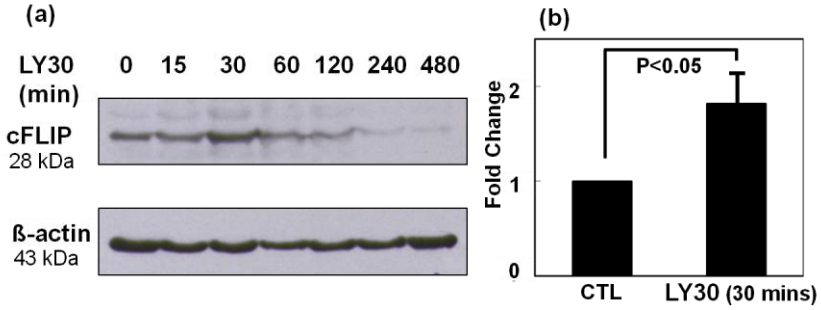

Figure 4.2.9 Western blot analysis of cFLIP-s in HeLa after different durations of LY30 treatment. (a) Western blot of time dynamics of cFLIP after LY30 treatment (b) densitometry of three repeats of cFLIP with untreated and 30 minutes of LY30 treatment. For each sample in each repeat, cFLIP is firstly normalized to its b-actin as its relative concentration, and then within each repeat, both the untreated and treated relative concentration are normalized to untreated concentration. Student's t-test for whether the observations are significantly higher than the untreated case yielded p-value less than 0.05.

These up-regulation and down-regulation results demonstrated that the effect of LY30 on cFLIP is more complex than a simple down-regulation. To find a pathway to explain the non-monotonic regulation of cFLIP by LY30, we need to consider upstream regulators of cFLIP and downstream effectors of LY30. We next studied ROS effects in greater detail because ROS are known to be produced by LY30 [88-90] and known to regulate cFLIP [194].

LY30 induced significant ROS production as demonstrated by Fluorescent measurements of DCFDA, which are the most common way to measure ROS but this method does not address subtypes of ROS. ROS is a family of several species, with H_2O_2 (hydrogen peroxide) and $O_2\bullet^-$ (superoxide) being the most abundant. In many cases, the ratio of $O_2\bullet^-$ to H_2O_2 determines whether ROS will promote or hinder apoptosis [185, 187, 195, 196]. A high ratio of $O_2\bullet^-$ to H_2O_2 antagonizes apoptosis by triggering pro-survival pathways such as PI3K/Akt and ERK [197, 198]. In contrast, a low ratio of $O_2\bullet^-$ to H_2O_2 promotes apoptosis through intracellular acidification [185], activation of caspase-3 and caspase-9 [186], down-regulation of cFLIP [184], and down-regulation of NHE1 [187, 188].

We constructed a simple hypothetical model of $O_2\bullet^-$ and H_2O_2 production and degradation, emphasizing the specific effects of $O_2\bullet^-$ and H_2O_2 on cFLIP (Figure 4.2.7a). H_2O_2 is known to decrease the expression of cFLIP [184]. And we represent this effect as H_2O_2 inhibiting cFLIP production. The impact of $O_2\bullet^-$ on cFLIP is less clear, but $O_2\bullet^-$ is known to activate NF-κB [199] which would increase cFLIP levels [199, 200]. $O_2\bullet^-$ can also inhibits NO which is known to induce S-nitrosylation of cFLIP [201]. This hypothetical possibility is modeled as superoxide blocking cFLIP

degradation. Our model (Figure 4.2.7a) includes cFLIP production, cFLIP degradation, inhibition of cFLIP degradation by $O_2^{\bullet -}$, inhibition of cFLIP production by H_2O_2, as well as $O_2^{\bullet -}$ production, $O_2^{\bullet -}$ conversion into H_2O_2, and H_2O_2 degradation.

Our model of ROS and cFLIP was then simulated to explore whether the dynamics of $O_2^{\bullet -}$ and H_2O_2 would plausibly explain both the cFLIP increase at 30 minutes and the cFLIP decrease at 6 hours. Many compounds can cause production of $O_2^{\bullet -}$ and H_2O_2, and we designed the model to be generally applicable to ROS-producing anti-cancer drugs. Simulations (Figure 4.2.7b) show that LY30-induced ROS could cause cFLIP levels to rise at 30 minutes and then fall in subsequent hours, due to faster pro-cFLIP influences from $O_2^{\bullet -}$, and slower anti-cFLIP influences from H_2O_2.

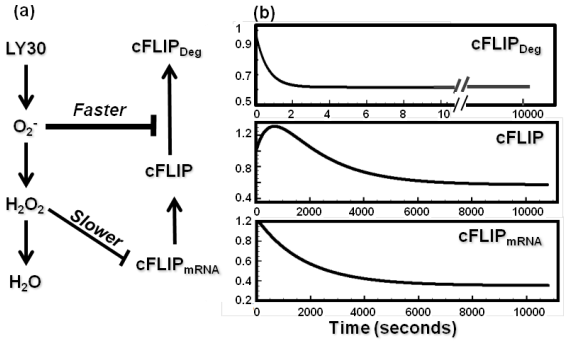

Figure 4.2.10 Hypothetical model for LY30 to cause non-monotonic regulation of cFLIP via O_2^- and H_2O_2. (a) Simplified diagram of LY30's influence on cFLIP. This model is roughly divided into two phases. In the earlier phase, O_2^- is produced after LY30 treatment, and the increased O_2^- will block the degradation of cFLIP, thus inducing its up-reguation. In the later phase, H_2O_2 is produced by conversion of O_2^-, and inhibits the production of cFLIP, lowering its concentration. (b) Simulations of cFLIP, cFLIP_mRNA and degraded cFLIP(cFLIP_Deg) over time, as predicted by the model in (4.2.7a).

Finally we performed preliminary experiments to test the hypothesis of Figure 4.2.10, by using anti-oxidant treatments (ROS scavengers) that are specific to certain sub-types of ROS. If LY30 is causing cFLIP to go up at 30 minutes via $O_2^{\bullet -}$, removing $O_2^{\bullet -}$ via

Tiron treatment would be expected to halt the ability of LY30 to raise cFLIP at 30 minutes. Fig 4.2.11(a) shows that LY30 failed to increase cFLIP at 30 minutes when Tiron was present. If LY30 is causing later levels of cFLIP to go down via H_2O_2, removing H_2O_2 by adding catalase would restore cFLIP levels to the same as untreated. Fig 4.2.8(b) shows that cFLIP at 6 hour after treatment with both LY30 and catalase had the same relative intensity as in untreated cells.

Figure 4.2.11 Western blot analysis of cFLIP-s in HeLa by LY30 in the presence of ROS scavengers. (a) Western blot of cFLIP-s after 6 hour LY30 treatment in the absence/presence of catalase. HeLa is pre-incubated overnight with catalase 4000 units/ml. (b) Western blot of cFLIP-s after 30 minutes LY30 treatment in the absence/presence of Tiron. HeLa is pre-incubated with Tiron with 15mM 1 hour before adding LY30.

4.3 Discussion and summary

We constructed an ODE model for combining the effects of two anti-cancer compounds, LY30 and TRAIL. The TRAIL effects were adapted from a previously published model [191], and the LY30 effects were approximated from our previously published experiments on LY30 [88-90]. Through a systematic integration of modeling and experiments, we found non-monotonic regulation of cFLIP-s which contributes to

delayed synergistic activation of caspase-8. Furthermore, we depicted the non-monotonic regulation of cFLIP-s as a result of functional variance among different ROS species though a revised ODE model. Specifically, $O_2^{\bullet -}$ reduces cFLIP-s level while its downstream H_2O_2 increases its level. Some effects of LY30 are common to multiple drugs, and our model was designed to be maximally generic for similar cases. For example, the standard chemotherapeutic drugs doxorubicin and cisplatin both cause ROS production and cFLIP down-regulation. Also, resveratrol, the widely-studied compound in red wine, causes ROS production and cFLIP down-regulation [33, 202, 203]. The ability of ROS to affect cFLIP is enormously important for determining whether cells are vulnerable to apoptosis[204], because multiple TRAIL-resistant cancers have shown re-sensitization to TRAIL after cFLIP-s levels were lowered [184, 194, 205, 206].

Every protein signaling network has abundant uncertainty, because every drug can have undiscovered effects, and every time-series experiment can have undiscovered peaks or dips occurring between the observed time points. Most such effects are minor, but some are significant enough to disrupt our ability to reason about system behavior. Any modeling research, in addition to its primary goal, can be considered to have an implicit surveillance function of checking the consistency of the "known" facts. In building the initial model of LY30 effects, we interpolated from a few measured time-points of cFLIP, to obtain a simple approximation of LY30-induced decay of cFLIP-s. When the LY30 and TRAIL effects were combined, our inability to simulate the observed dynamics of caspase-8 suggested an error in the model. This error proved to be our simplistic interpolation of how LY30 affects cFLIP-s. We performed subsequent

experiments that showed a non-monotonic, “up-and-down” concentration of cFLIP-s after LY30. These effects do not contradict the previous findings, but rather refine the kinetics. The new observations of cFLIP-s explain the delayed activation of caspase-8 and the delayed onset of synergy in the execution of apoptosis, because significant concentrations of cFLIP-s inhibit the activation of caspase-8 [207]. Previous studies have used kinetic models of signaling pathways to detect mismatches between models and observations [208, 209]. This work is among very few that have used pathway modeling to guide experiments towards actually confirming a previously unknown phenomenon [210].

The remaining question was how LY30 causes non-monotonic effects on cFLIP-s. A simple explanation would be: LY30 triggers two opposing pathways that regulate cFLIP-s in opposite ways. We built a model of “typical” ROS production and degradation (Figure 4.2.10a), including the known ability of H_2O_2 to cause gradual down-regulation of cFLIP-s [184], and a hypothetical opposite effect of $O_2^{\bullet -}$ on cFLIP-s. In this model, the fundamental upstream-downstream relationship between $O_2^{\bullet -}$ and H_2O_2, combined with the fast effects of $O_2^{\bullet -}$ versus the slow-acting effects of H_2O_2, would together cause a time difference between the $O_2^{\bullet -}$ -dominant phase (early cFLIP-s increase) and the $H_2O_2^{\bullet -}$dominant phase (late cFLIP-s decline) of ROS-mediated effects. We performed immunoblots for the plausibility of this model, by blocking ROS species and testing if LY30-induced changes in cFLIP-s were disrupted. Our model of ROS_FLIP regulation was not falsified by these tests, and future work can perform more comprehensive experiments to characterize and validate the effects of LY30-induced $O_2^{\bullet -}$ and H_2O_2 on cFLIP-s.

If LY30 is unique in causing complex cFLIP-s dynamics, it may be of narrow significance, but our model describes a general dynamic of ROS homeostasis. LY30 is one of many possible triggers for ROS, which might then cause two opposing effects on cFLIP-s. If this model is correct, the predicted trend could occur with other ROS-producing drugs. Future work can determine whether the same dynamics occur with doxorubicin, cisplatin, and resveratrol. The timing of cell vulnerability to apoptosis ("sensitization") is very important for designing optimal schedules of multi-drug treatments.

5 LY30-induced ROS production in silico and in vitro

Followed with the prediction of ROS production by LY30 in chapter 4, we tested the prediction through an integration of modelling of mitochondria ROS pathway and experiments measurement of ROS production by LY30.

5.1 LY30 induced DCFDA increase is not through canonical ROS pathway with earlier $O_2^{\bullet -}$ production—Naïve Model

In this chapter, we will discuss the Ordinary Differential Equation (ODE) model of canonical ROS production pathway considering mitochondria as the major intracellular source of ROS. In the model, LY30 inhibits mitochondrion complex *I* which leads to sequential production of $O_2^{\bullet -}$ and H_2O_2. Predicted dynamics from modelling were compared with measured dynamics of ROS after LY30 treatment.

5.1.1 Modeling ROS production of LY30 through mitochondrial superoxide

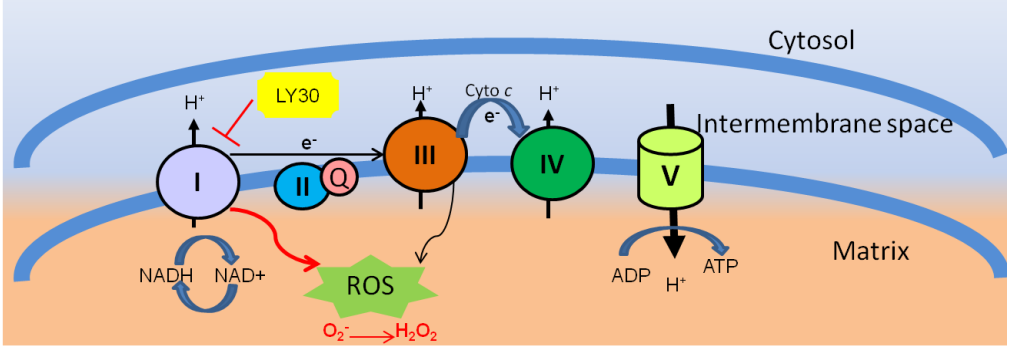

Figure 5.1.1 Hypothesized pathway for LY30 to cause production of ROS (reactive oxygen species) in mitochondria. Mitochondrial complexes I–V of the electron transport chain are in the inner membrane of the mitochondria. Complexes I and II transfer electrons into this chain. Complex II transfers an electron to coenzyme Q (Q). Cytochrome c (Cyto c) transfers those electrons from complex III to complex IV. On acceptance of the electron, complex IV then converts H^+ and O_2 to water. Complexes I to IV pump protons from the matrix to the intermembrane space, which causes a charge difference between the matrix and the intermembrane space. This charge difference creates a potential which is then used by complex V to convert ADP into ATP. Complex I and III have been reported to produce ROS. We assume that LY30 produces ROS through blocking complex I as Rotenone.

As Mitochondria are a major source of ROS production [211-214], we hypothesized that intracellular ROS is mainly produced by LY30 through the mitochondrial Electron Respiration Chain (ETC) which is embedded in the inner membrane of Mitochondria [215]. In this project, we assumed that LY30 triggers ROS production through mitochondria complex *I* and built an ODE model, named as LY30-ETC model, based on reported mitochondrial ROS pathway [211-214]. In the model, LY30 catalyzes the conversion from NAQ to reduced NAQ, which leads to superoxide production. The produced superoxide would be consequently converted to H_2O_2 in the presence of MnSOD. Finally, H_2O_2 would be converted into H_2O in the presence of GPX. We listed the reactions in table 5.1.1. Parameters including initial concentrations and rate constants are presented in tables 5.1.2 and 5.1.3 respectively.

Table 5.1.1 List of reactions of LY30-ETC model

Number	Reaction	Reaction type	parameters
1	CoQ- + O2 = CoQ + $O_2^{\bullet-}$	Mass action (reversible)	k1,k_1
2	Mn3SOD + $O_2^{\bullet-}$ = Mn3SOD:$O_2^{\bullet-}$	Mass action (reversible)	k2, k_2
3	Mn3SOD:$O_2^{\bullet-}$ = Mn2SOD + O2	Mass action (reversible)	k3, k_3
4	Mn2SOD + $O_2^{\bullet-}$ = Mn2SOD:$O_2^{\bullet-}$	Mass action (reversible)	k4, k_4
5	Mn2SOD:$O_2^{\bullet-}$ + 2 H+ = Mn3SOD + H_2O_2	Mass action (reversible)	k5, k_5
6	Mn2SOD:$O_2^{\bullet-}$ = DEP	Mass action (reversible)	k6,k_6
7	2 H+ + 2 $O_2^{\bullet-}$ = O2 + H_2O_2	Mass action (reversible)	k7, k_7
8	GPXr + H_2O_2 + H+ = GPX0 + H2O	Mass action (reversible)	k8, k_8
9	GPX0 + GSH = GSGPx + H2O	Mass action (reversible)	k9,k_9
10	GSGPx + GSH = GPXr + GSSG + H+	Mass action (reversible)	k10, k_10

11	CoQ- + $O_2^{\bullet-}$ + 2 H+ -> CoQ + H_2O_2	Mass action (reversible)	k11,
12	CoQ = CoQ-	Mass action (reversible)	k12,k_12
13	O2 ->	Mass action (irreversible)	k13
14	-> O2	Constant flux (irreversible)	k14
15	2 GSH = GSSG	Mass action (reversible)	k15,k_15
16	LY30 + CoQ = CoQ -	Mass action (irreversible)	k16, variant

Table 5.1.2 List of parameters in the model

	Rate m ³/(mmol*s)	**Reference**
k1	8000	[214]
k_1	800000	[214]
k2	1.50E+09	[216, 217]
k_2	35000(1/s)	[216]
k3	25000(1/s)	[216]
k_3	0	[216]
k4	1.50E+09	[216, 218]
k_4	35000(1/s)	[216]
k5	25000	[216]

k_5	300	[216]
k6	650	[216]
k_6	10	[216]
k7	240000	[219]
k_7	0	[219]
k8	2.10E+07	[217, 220, 221]
k_8	0	[217, 220]
k9	40000	[217, 220]
k_9	0	[217, 220]
k10	1.00E+07	[217, 220]
k_10	0	[217, 220]
k11	3.00E+06	[222]
k12	100(1/s)	
k_12	450000(1/s)	
k13	2.50E-06	
k14	0.1	
k15	10000	
K_15	1000	

Table 5.1.3. List of initial concentrations of the species

Species	Initial concentration
O_2	2.49E-05
$O_2^{\bullet-}$	1.23E-11
Mn_3SOD	1.00E-06

Mn_2SOD	1.00E-06
$Mn_3SOD{:}O_2^{\bullet-}$	3.08E-13
$Mn_2SOD{:}O_2^{\bullet-}$	3.08E-13
DEP	2.00E-11
GPX_0	1.96E-10
GPXr	1.00E-06
H^+	1
H_2O	55.01695
GSGPx	7.85E-13
GSH	0.000981
GSSG	9.62E-06
CoQ	0.00045
CoQ^-	1.00E-07
H_2O_2	3.66E-10
LY30	1

5.1.2 Model predictions from LY30-ETC model

We simulated the LY30-ETC model with constant input of LY30 and varied its catalytic influence on conversation from CoQ to CoQ^- by adjusting the value of k16. Simulated time-course of molecule concentrations of H_2O_2 and $O_2^{\bullet-}$ are shown in Figure 5.1.2. The simulated results suggested that k16 linearly affects the fold change of $O_2\bullet^-$ and H_2O_2. Higher value of k16 resulted in higher steady state of $O_2^{\bullet-}$ and H_2O_2. We observed another phenomenon that the steady states of $O_2\bullet^-$ and H_2O_2 increased to

similar level in the unit of fold change (the trajectory of $O_2^{\bullet -}$ and H_2O_2 is overlapped in Figure 5.1.2 a) with hardly detectable delay (0.4 seconds).

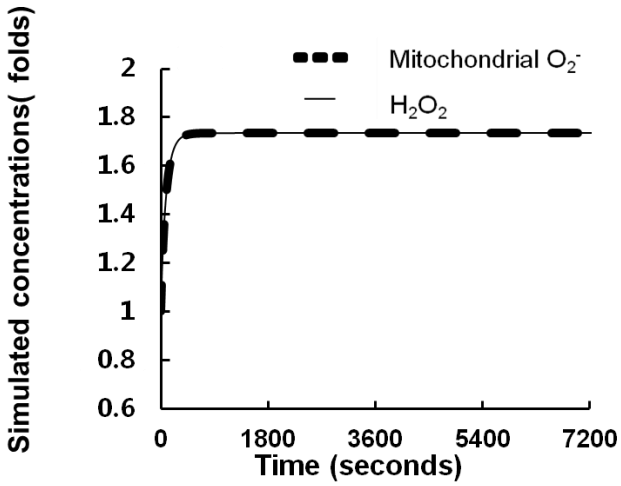

Figure 5.1.2 Simulated ROS dynamics in LY30-ETC model. a) ROS ($O2^{\bullet -}$ and H2O2) dynamics in the unit of fold change according to varied inhibition of LY30 on mitochondria complexes. H2O2 and $O2^{\bullet -}$ were overlapped in each condition. b) Small delay between $O2^{\bullet -}$ and H2O2 was observed with increased resolution.

5.1.3 Experiments testing the LY30-ETC model

In order to test the hypothesis of the ETC model, we carried out a set of Flow Cytometry measurements using fluorescent dyes CM-H_2DCFDA (DCFDA) [223] and MitoSOX™ Red (MitoSOX) [223, 224], which are used to detect H_2O_2 and Mitochondrial $O_2^{\bullet -}$, respectively. To reach statistic significance, we measured in total 10,000 cells from each sample and obtain averaged fluorescence from the population for further analysis. In each set of independent experiments, single untreated sample is compared with the LY30-treated samples at all time points. Figure 5.1.3 shows the normalized averaged ROS dynamics according to incubation time of LY30 with 4 independent repeats. The experimental results in Figure 5.1.3 showed that in HeLa

cells, DCFDA levels (solid line) rapidly increases to 1.25 folds after 5 minutes of treatment and stays at 1.25 folds till 15 minutes. After that, DCFDA level increases again from 1.25 folds to 1.6 folds. MitoSOX dynamics (represented by the dashed line) showed a minor increase trend peaked at 1.1 folds after 15 minutes of LY30 as compared with DCFDA intensities.

The experiment observation conflicts with our model prediction in two aspects: 1. the model predicted that H_2O_2 and Mitochondrial superoxide would increase to the similar fold change after LY30 treatment. But the experimental data showed that the fold-change increase of the DCFDA intensity (H_2O_2) is much bigger than the MitoSOX intensity (mitochondria $O_2\bullet^-$); 2. The model predicted that the rise of $O_2\bullet^-$ comes earlier than that of H_2O_2 with very little delay. However, experimental results showed that the H_2O_2 increase occurs earlier than the $O_2\bullet^-$ increase.

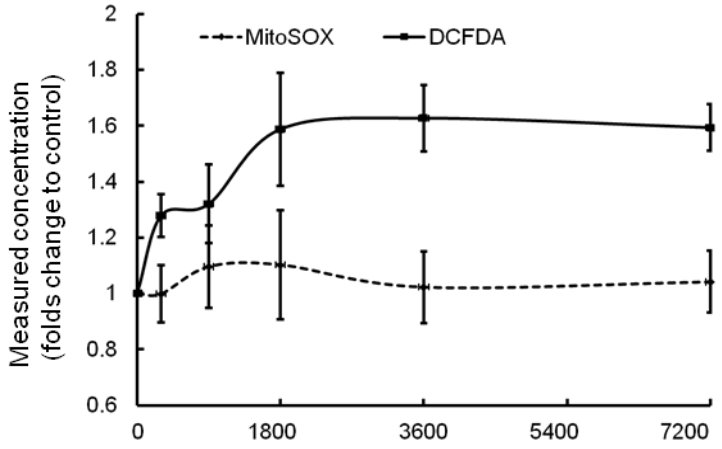

Figure 5.1.3 Experiment results of ROS ($O2^{\bullet-}$ and H2O2) dynamics with LY30 incubation. The solid and dotted lines represent the averaged fluorescence intensity of DCFDA and MitoSOX, respectively. Each treatment was repeated for4 times.

To further confirm that the rise of H_2O_2 is earlier and more significant than that of $O_2^{\bullet -}$, we double stained each sample with DCFDA and MitoSOX. The purpose of this experiment is to track the fluorescence change of DCFDA and MitoSOX in the same set of cells. Double stained results are shown in panels of Figure 5.1.4 with x-axis representing DCFDA (H_2O_2) fluorescence level and y-axis representing MitoSOX (mitochondrial $O_2^{\bullet -}$) fluorescence level with one dot representing one cell. From left to right are the sample without drug treatment, sample with LY30 treatment for 5 minutes, and sample with LY30 treatment for 15 minutes. A right shift of the cell population (an increase in DCFDA signal) occurs in the sample with 5 minutes of LY30 treatment compared to the untreated sample. And the amount of rightward shift becomes larger in the sample with longer LY30 treatment (15minute). The phenomenon of right shift indicated that DCFDA intensity increases in cells with LY30 treatment, suggesting intracellular H_2O_2 production. However, MitoSOX intensity, as indicated by y-axis, didn't show significant increase after LY30 treatment as there is little upward shift.

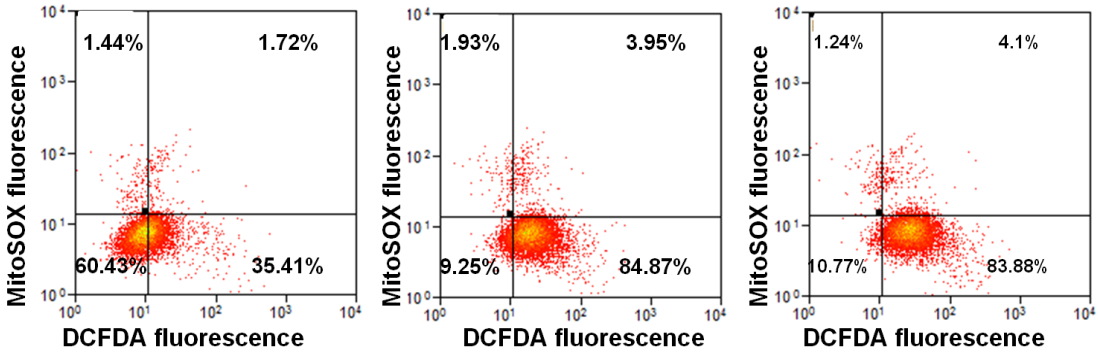

Figure 5.1.4 Intracellular ROS levels demonstrated by double staining of DCFDA (x-axis) and MitoSOX (y-axis). From left to right are panels are the ROS levels in untreated sample, LY30-treated sample for 5 minutes, and LY30-treated sample for 15 minutes, respectively.

5.1.4 Sensitivity analysis in LY30-ETC model

If Electron Transport Chain (ETC) in mitochondria is the major source of ROS by LY30, we would expect LY30 might modify the kinetics in some way which might allow the canonical ROS dynamics to be different from predicted ROS kinetics in LY30-ETC model. To resolve the conflict, we performed sensitivity analysis on LY30-ECT model to understand how the change of each parameter (initial concentration and rate constants) affects system outcome (such as $O_2\bullet^-$ and H_2O_2). Generally, the parameters with negative influence on $O_2\bullet^-$ and positive influence on H_2O_2 were the potential candidates for further analysis.

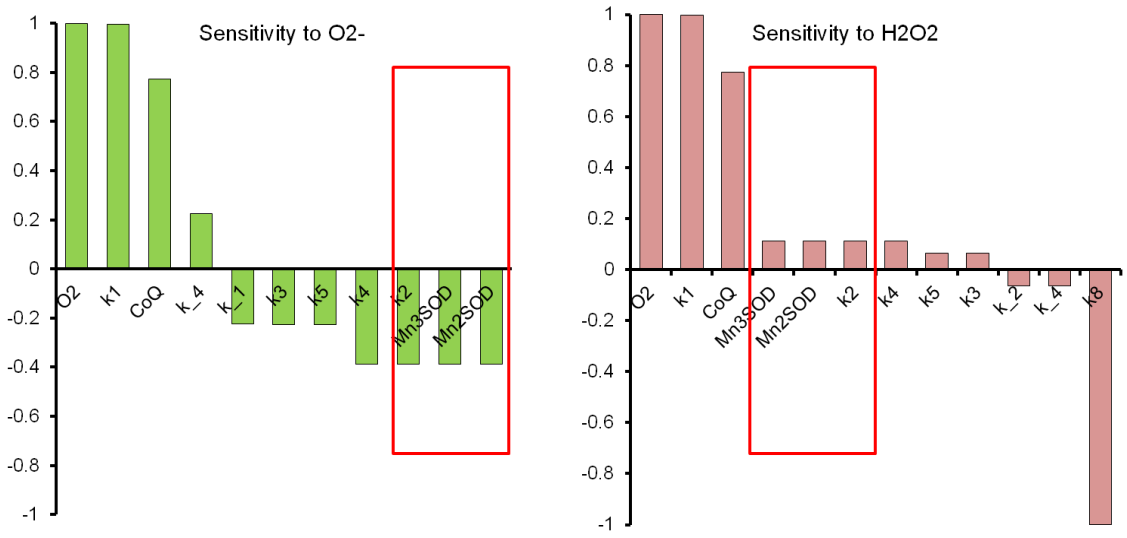

Figure 5.1.5 Sensitivity analysis of different parameters on $O_2^{\bullet-}$ and H_2O_2. Left panel shows the normalized sensitivity values of parameters on $O_2^{\bullet-}$. Right panel shows sensitivity values of parameters on H_2O_2. Red rectangular contains all the parameters with both negative values on $O_2^{\bullet-}$ and positive values on H_2O_2.

According to the sensitivity analysis for H_2O_2 and $O_2\bullet^-$ (shown in Figure 5.1.5), we identified 6 possible candidates including two species (Mn_3SOD and Mn_2SOD), and four rate constants (k2, k4, k5 and k3). All the 6 targets are involved in the following 4 reactions.

$Mn_3SOD + O_2^{\bullet-} = Mn_3SOD{:}O_2^{\bullet-}$ (1)

$Mn_3SOD{:}O_2^{\bullet-} = Mn_2SOD + O_2$ (2)

$Mn_2SOD + O_2^{\bullet-} = Mn_2SOD{:}O_2^{\bullet-}$ (3)

$Mn_2SOD{:}O_2^{\bullet-} + 2 * H+ = Mn_3SOD + H_2O_2$ (4)

Sensitivity results suggested that we should look at the reactions that convert $O_2^{\bullet-}$ to H_2O_2. As the change of reactants concentration and change of reaction rates can produce similar effect on products of one reaction, we performed parameter scan of SOD (including Mn_2SOD or Mn_3SOD) on $O_2\bullet^-$ and H_2O_2 dynamics.

5.1.5 Parameter scans of SOD

According to sensitivity analysis of various parameters on ROS, SOD has been selected as a key species to affect the ratio between $O_2\bullet^-$ and H_2O_2. Therefore, we took the assumption in improved model that besides inhibiting ETC, LY30 also affects level or activity of MnSOD. Simulated concentrations of ROS ($O_2\bullet^-$ and H_2O_2) and corresponding SOD (Mn_2SOD) concentrations are presented in Figure 5.1.7.

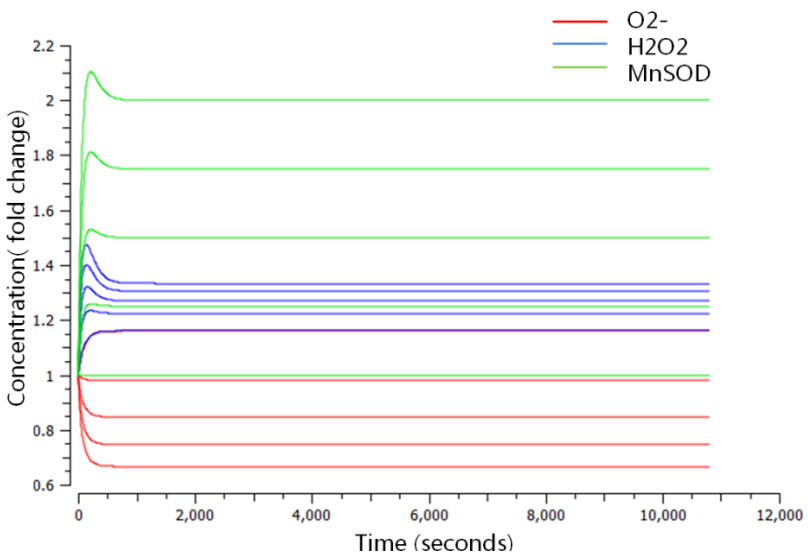

Figure 5.1.6 Simulated ROS dynamics (H2O2 and $O2^{\bullet-}$) according to MnSOD variation in LY30-ETC model. Different ROS trajectories correspond to varying degrees of influence from LY30 on MnSOD. the level of MnSOD was changed from 1 fold to 2.2 fold.

As we can see from the simulated result, increased concentrations of MnSOD correspond to increased ratios of H_2O_2 to $O_2\bullet^-$. And $O_2\bullet^-$ may even display decreased trend when MnSOD reaches a value to counteract the increasing effect on $O_2\bullet^-$ from LY30. In addition, the model predicted that the change of MnSOD is greater than that of H_2O_2 according to the increasing magnitudes of concentration and increase rate. To be more specific, if we observe H_2O_2 increases to 1.2 fold at 5 minutes, we are supposed to observe the increase of MnSOD (activity or concentration) for about 1.5 fold within 5 minutes. Although we have not done the experiments, a relevant work showed that increasing dose of LY30 treatment for up to 1 hour has little effect on SOD enzyme activity [225].

5.2 Literature review of DCFDA sources: involvement of reactive nitrogen species (RNS) and free Calcium

Since extensive effort was not able to resolve the conflict between model prediction and experiment results, we decided to look at other potential cellular sources of ROS, reactive nitrogen species (RNS) and free calcium (Ca^{2+}).

5.2.1 Reactive Nitrogen Species (RNS), ROS and cell viability

It is well established that an intimate relationship exists between RNS family and the ROS family [226]. Production of NO has been shown to inhibits complex *IV* [227] thus enhancing ROS generation at Q_O [228]. ROS and RNS are increasingly recognized to interact with each other closely, and contribute to various physiological signaling [229].

5.2.1.1 Reactive Nitrogen Species (RNS)

Reactive nitrogen species (RNS) are a family of chemical intermediates with contrasting and distinct properties derived from nitric oxide (NO) [230] including NO, NO^2, $ONOO^-$, ROONO and such. Generally, RNS may be formed either through direct reactions of NO with ROS or as results of enzymatic activities [231]. Important insight of RNS, regarding its biology, biochemistry and potential contribution to disease, has been revealed by recent advances [230].

In biological systems, the primary source of all RNS is NO. NO is the most interesting and typical species among other members of RNS. NO is able to freely cross cell membranes and diffuse inside cells and interact with a variety metal centres in proteins or with other free radicals and oxygen [230]. Physiological steady state concentration of NO is within range of 20 nM-2uM [232]. When the intracellular concentration of NO

is higher than 300nM, it will significantly drive the reaction with $O_2\bullet^-$ towards the formation of $ONOO^-$ [233].

As the major source of NO, Nitric oxide synthases (NOS) was first identified and described in 1989 [234]. There are three isoforms of NOS, including inducible NOS(iNOS), vascular endothelial NOS (eNOS) and neuronal NOS isoform(nNOS). iNOS is the inducible isoform that is involved in immune response and is expressed in a wide range of cells and tissues; eNOS is the predominant isoform in endothelial cells; and nNOS is the predominant isoform in neuronal tissue [234].

5.2.1.2 RNS and ROS

Nitric oxide (NO) and its derivatives were known to inhibit mitochondrial respiration through a variety of pathways. At low concentrations (nano molar), NO can inhibit cytochrome oxidase in a immediate, specific and reversible manner [235]. According to in-vitro experiments carried out with isolated mitochondria, high concentrations of NO or its derivatives ($ONOO^-$) can cause irreversible inhibition of the mitochondria respiratory chain [207], uncoupling and even permeability transition [235] .

Among the complicated interaction between RNS and ROS, reaction between NO and $O_2^{\bullet-}$ is the most well-studied one. The rapid reactions of NO with superoxide ($O_2\bullet^-$) to form peroxynitrite ($ONOO^-$) happen at a rate of 6.7×10^9 $M^{-1}Sec^{-1}$ [230, 232, 236], which is more than 2-4 times faster than the reaction between $O_2\bullet^-$ and $O_2\bullet^-$ dismutase, at the rate of $2.37 \pm 0.18 \times 10^9 M^{-1}Sec^{-1}$ [237]. NO has been regarded as the only biological molecule which is capable of out-competing with $O_2^{\bullet-}$ dismutase for $O_2^{\bullet-}$. At high concentrations, NO often triggers rapid reactions with ROS, e.g. $O_2^{\bullet-}$, to produce

excessive RNS including peroxynitrite ($ONOO^-$) and nitrogen dioxide (NO_2), which may trigger cell death processes potentially [238].

5.2.1.3 Peroxynitrite ($ONOO^-$)

$ONOO^-$ is a short lived and high oxidative species, and it is the only species that belongs to both RNS family and ROS family. Among all the derivatives of NO, $ONOO^-$ is one of the best characterized species which seems to have the highest biological activity [239]. $ONOO^-$ is formed by the reaction of NO and $O_2^{\bullet-}$ at a near diffusion-limited rate of $6.7 \times 10^9\ M^{-1}Sec^{-1}$ [240]. Although NO is often described to be exert highly toxic and reactive effects on cells, many of the toxic effects are more likely to be mediated by $ONOO^-$ other than itself.

Production site of $ONOO^-$ is spatially associated with the source of $O_2^{\bullet-}$. $ONOO^-$ has short half life around 10 milliseconds at physiological pH of 7, resulting in low steady state concentration. In spite of short half life and low concentration, $ONOO^-$ is able to cross cell membrane, targeting with 1 to 2 cell diameters from its generation site.

5.2.1.4 Peroxynitrite and cell death

Peroxynitrite has been reported to induce DNA damage and apoptosis in a variety of cell types including thymocytes and HL-60 leukaemia cells. Mechanisms of $ONOO^-$ induced cell injury include DNA base modifications, DNA single and double-strand breakage [241]. In addition, $ONOO^-$ can also trigger mitochondrial dysfunction through impairment of mitochondria respiration, suppression of oxygen and induction of mitochondria permeability transition [242].

Depending on concentration and exposure period, $ONOO^-$ can induce necrosis as a premature form of cell death as well as apoptosis [242]. High levels of $ONOO^-$ lead to necrosis partly through activation of the PARP pathway [242]. In contrast, lower concentrations of $ONOO^-$ can lead to delayed, programmed, apoptotic-type cell death through the activation of caspase cascade [242].

5.2.2 Calcium and DCFDA and cell viability

5.2.2.1 Calcium and ROS

During the last decades, it is well-accepted that significant interactions exist between Ca^{2+} and ROS, which lead to modification of a variety of proteins as well as affecting cell fate [243]. Extensive study showed that changes in intracellular Ca^{2+} can regulate the activity of ROS through RNS-dependent (e.g. mitochondria respiration) [235, 244] and RNS-independent (e.g. NOX) pathways [245]. At the same time, alteration in intracellular ROS and RNS production can also alter Ca^{2+} signaling networks through several post-translational modifications.

From Calcium to ROS

Ca^{2+} is known to affect ROS homeostasis by regulating ROS in both the mitochondria and the cytosol [235, 244].

Biologists have not reached a conclusive understanding of the underlying mechanism for calcium-induced ROS generation in mitochondria yet. Cadenas *et al*. proposed that calcium-triggered mitochondria depolarization is responsible for the ROS effect [246], whereas Sorsa *et al.* attributed the ROS regulation to the alteration of mitochondrial membrane structure by Ca^{2+} [247]. Conducted experiments on isolated mitochondria

[248, 249] have demonstrated that in the situation of high concentration Ca^{2+}, occurrence of MOMP will lead to ROS production.

In addition to mitochondrial ROS generation, Ca^{2+} can also regulate multiple ROS-generating enzymes in the cytosol. In response to intracellular Ca^{2+} concentration increase, NADPH oxidase 5 (NOX5) is activated through conformation change [250] and generates large amounts of ROS [245]. In addition to its direct interaction with catalytic subunits, Ca^{2+} can also control NOX activity by regulating cytosolic components of NOX1 and NOX 2 [251, 252].

5.2.2.2 Intracellular Ca^{2+} store

Endoplasmic Reticulum (ER) is the largest intracellular calcium store. Extracellular Ca^{2+} is 1 to 1.4mM [243], ER Ca^{2+} ($[Ca^{2+}]_{ER}$) is around 100–500 uM while cytosolic Ca^{2+} ($[Ca^{2+}]_c$) is only 50 and 300 nM [253]. ER is a key regulator of cytosolic calcium levels through SERCA. SERCA pumps $[Ca^{2+}]_c$ into ER lumen and calcium channels of IP_3R. RyR regulate $[Ca^{2+}]_c$ through pumping ER calcium out of cytosol. Most Ca^{2+} in ER is present with bounding proteins such as calsequestrin.

Mitochondria are another intracellular calcium store. Experiments showed that once a physiological stimulus elicits a $[Ca^{2+}]_c$ rise, a large Ca^{2+} fluxes occur across the mitochondrial membranes [254]. Such flux occurrence is, in a large extent, due to the spatially proximity of mitochondria to ER and/or the plasma membrane, allowing them to be exposed to Ca^{2+} and thus produces rapid and large accumulation of the Ca^{2+} in the matrix [254]. It is now realized that mitochondrial Ca^{2+} also determine mitochondrial function and integrity [228].

5.2.2.3 Calcium and apoptosis

Recognition of Ca^{2+} in cell death dates back to early history of apoptosis, when scientists found that molecules capable of transporting Ca^{2+} across membranes are highly toxic to cells [5]. Ca^{2+}, as a key player in triggering mitotic division in numerous cell types, is highly involved in the regulation of cell death [255]. Reports suggested that less increase of $[Ca^{2+}]_c$ promote cell death through apoptosis and $[Ca^{2+}]_c$ increase at very high intracellular levels can induce necrosis [256]. Furthermore, $[Ca^{2+}]_c$ elevation is reported to occur during both early and late stages of apoptosis [257-259] either through release from ER or influx through plasma membrane [260].

5.3 Measured concentrations of $O_2^{\bullet-}$, RNS (NO), $[Ca^{2+}]_c$ under LY30 treatment

5.3.1 Total intracellular $O_2^{\bullet-}$

To check whether LY30 induced increase of $O_2^{\bullet-}$ other than mitochondria $O_2^{\bullet-}$, we measured intracellular total $O_2^{\bullet-}$ after LY30 treatments (5 minutes,10 minutes,15 minutes, 30 minutes, 120 minutes and 240minutes) with Dihydroethidium (DHE) and Lucigenin. Detailed information about procedure on materials and methods are available in Materials and Method 3.1.9 and 3.1.10.

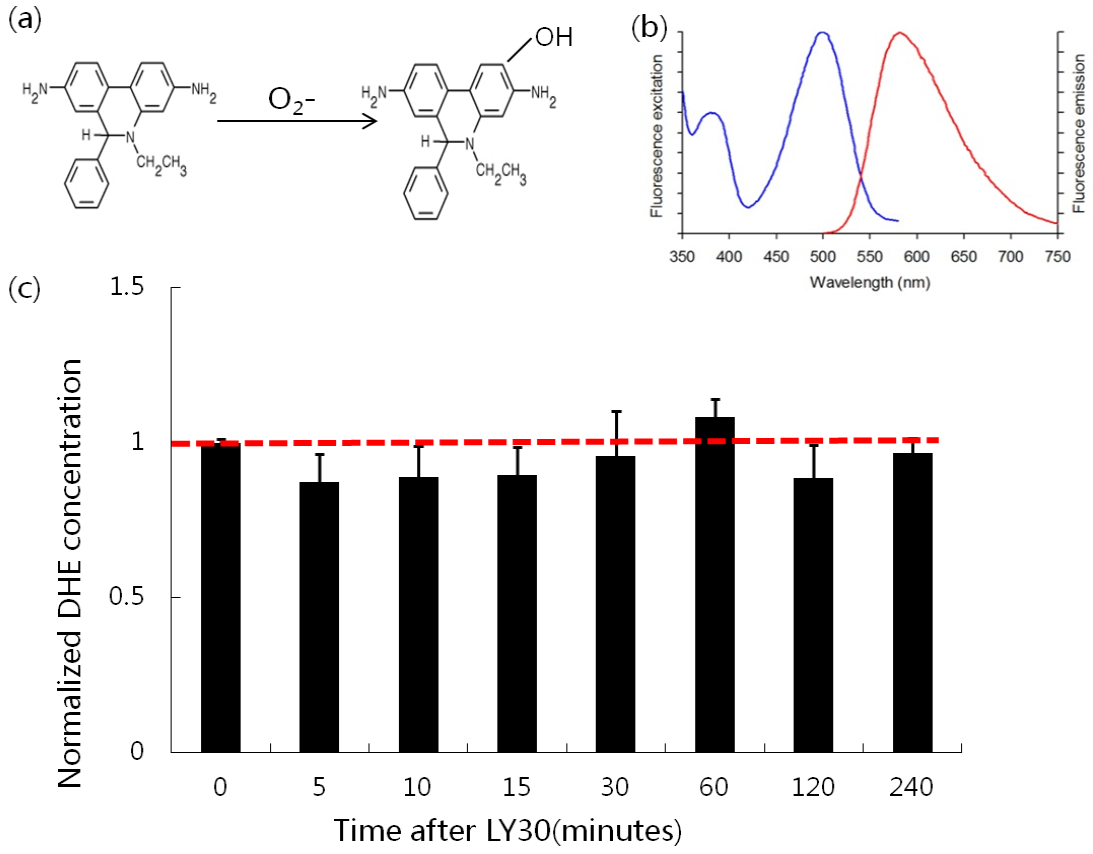

Figure 5.3.1 Experimental measurement of DHE in HeLa after LY30 treatment. a) Structure of DHE. b) Fluorescence shift of DHE under oxidization; c) averaged fluorescence intensity of DHE in HeLa of several repeats (n=3).

Dihydroethidium (DHE, Figure 5.3.1a) is a cell permeant dye and has been used extensively to monitor superoxide production [261, 262]. We carried out flow cytometry experiment to measure DHE fluorescence level in each sample and then normalized it to untreated control. Normalized fluorescence levels are presented in Figure 5.3.1c. We observed no significant increase of $O_2^{\bullet-}$ in LY30-treated cell samples (5-minutes incubation to 240-minutes incubation) compared to that in untreated samples.

In addition to DHE, we used Lucigenin to measure intracellular $O_2^{\bullet-}$ by LY30. HeLa cell samples were incubated with LY30 for 0, 15, 30, 60, 120 and 240 minutes.

Averaged results of 3 replicates were shown in Figure 5.3.2b. Consistent with the results from MitoSOX and DHE assays, Lucigenin experiment didn't detect any significant increase in $O_2^{\bullet-}$ after LY30 before 60 minutes.

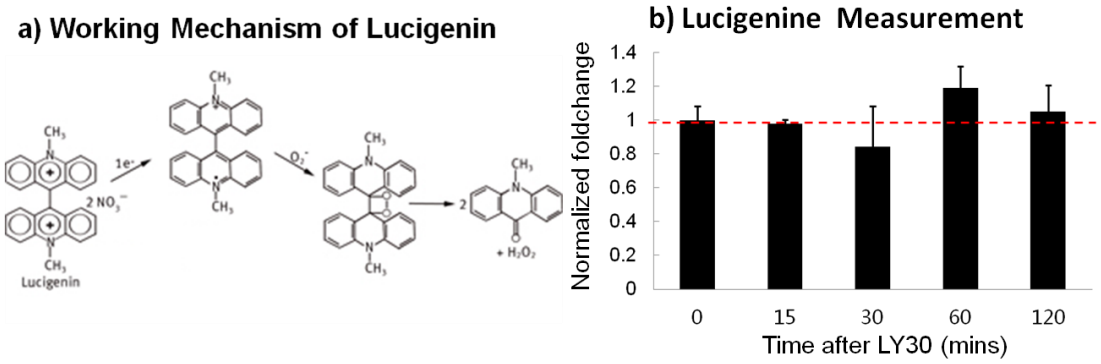

Figure 5.3.2 Mechanism of Lucigenin and measured $O2^{\bullet-}$ concentrations in HeLa with LY30 treatment. a) Structure of Lucigenin before oxidization; b) averaged result of Lucigenin of several repeats (n=3).

5.3.2 Experimental Measurement of RNS and Ca^{2+}

Other pathways that can lead to ROS production include non-mitochondrial O_2^- production through Peroxisomes [105], NADPH oxidases 1-4 [108], or Ca^{2+}-dependent activation of NADPH oxidase 5 [108]; H_2O_2 production from the Endoplasmic Reticulum [263]; and peroxynitrite (ONOO-) production from the combination of Nitric Oxide (NO) and O_2^- [232]. To explain the rapid increase of DCFDA signal without distinctive $O_2^{\bullet-}$ production (as tested by MitoSOX, DHE and Lucigenin) under LY30 treatment, we checked the intracellular change of RNS and Ca^{2+} with LY30 treatment as they have been frequently linked with ROS [230, 232, 236] and cell death [242].

5.3.3 Intracellular RNS increases in HeLa after LY30 treatment

We selected diaminofluorescein DAF-FM (DAF) [264] for quantitative measurements of RNS (mainly NO) [265]. From left to right panels in Figure 5.3.3a, we measured DAF-FM fluorescence in unstained sample (unstained CTL), sample with DAF staining and no treatment (untreated CTL), sample with DAF staining and LY30-treatment for 30 minutes (LY30-30minutes), sample with DAF staining and LY30-treatment for 60 minutes (LY30-60 minutes). Each panel in the figure is represented by a scatter plot of the DAF signal (FITC represented by x-axis) verse cell size (Forward Scatter represented by y-axis). A rectangular is drawn for each panel to quantify DAF-positive cells in each sample. Compared with Untreated CTL, samples of LY30-30 minutes (3rd panel) and LY30-60 minutes (4th panel) showed DAF-positive cells at 66% and 67% respectively. NO increase with 22% of the whole cell population. In histogram representation of the same samples (Figure 5.3.3b), LY30-treated sample (blue and yellow histogram) demonstrated distinctive right shift compared to untreated CTL (green histogram). Quantification of the fluorescence intensity of each sample is conducted according to the function of $f_n^i = \frac{F_m^i - F_m^u}{F_m^c - F_m^u}$. Where F_m^i represents measured fluorescence for sample *i*, F_m^u represents measured fluorescence in unstained CTL, F_m^c represents mean fluorescence for untreated CTL and f_n^i is the normalized fluorescence for sample *i*. The result of quantified fluorescence (Figure 5.3.3c) showed that sample of LY30-30minutes and sample of LY30-60minutes demonstrated 0.3-0.4 folds increases of NO as compared with untreated CTL.

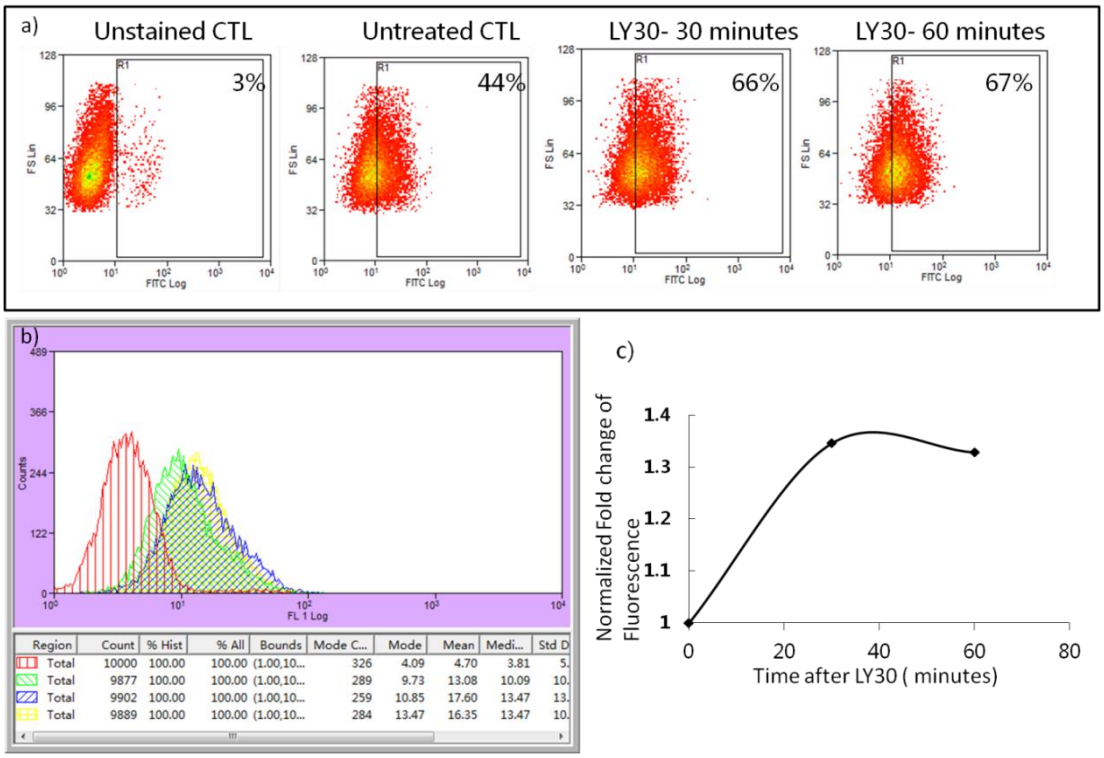

Figure 5.3.3 Intracellular NO measurement through flow cytometry. a) Dot plots of DAF fluorescence in cells upon different treatments. From left to right, the four panels represent cells without DAF stain, cells with DAF stain without LY30 treatment, cells with DAF stain and LY30 treatment for 30 minutes and LY30 treatment for 60 minutes. b) Histgram of DAF fluorescence in 10,000 cells. X-axis represents DAF fluorescence and y-axis represents cell number. c) Quantified intracellular NO in HeLa according different time of LY30 treatment

To further confirm the effect, we conducted 3 independent DAF measurements in HeLa with more intense time points. Figure 5.3.4 plotted pooled average dynamics of NO in HeLa upon LY30 treatment, with x-axis demonstrating cell incubation time with LY30 and y-axis representing folds change of DAF in each cell sample versus that in untreated cell sample. There is approximately 0.5-fold increase of DAF fluorescence from 0 minutes to 5 minutes. Such increase of 0.5-fold lasts until 10 minutes, and then a drop to 0.25 folds happens at 15 minutes. After that, we observed another rapid increase from 1.2 folds at 15 minutes to 1.7 fold at 30 minutes. Such increase is maintained

steadily with a less extend to 2 folds at 240 minutes. Statistic analysis of DAF results showed significant increase of DAF happen as early as 5 minutes (p= 0.011).

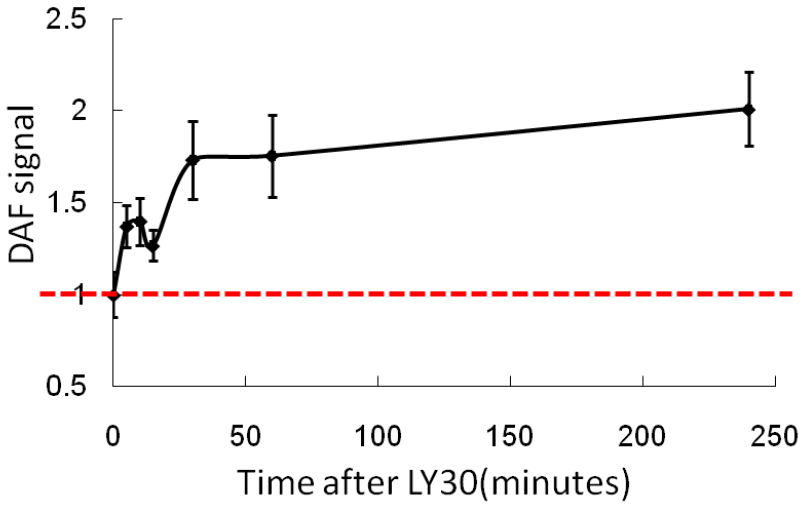

Figure 5.3.4 Averaged NO levels in HeLa upon LY30 treatment. The NO level for each specific period is obtained through averaging over measured DAF signals of at least 3 replicates (except for NO measurement at 240 minutes is obtained through 2 replicates).

5.3.4 Ratiometric measurement of Intracellular Ca^{2+} increases in HeLa after LY30 treatment by Using Fura-2

To gain a comprehensive understanding of intracellular Ca^{2+} regulation by LY30, we carried out Ca^{2+} measurement assays using ratiometric dye Fura-2 [266] and non-ratiometric dyes Fluo-4 AM and Fluo4 NW AM [267].

As a ratiometric dye, Fura2-AM can measure both free Ca^{2+} (cytosolic Ca^{2+}) and bound Ca^{2+} through collecting emission at 510nm with excitation at wavelengths of 340 nm and 380 nm. We selected Thapsigargin (TG) as the positive control in the experiments, which is a non-competitive inhibitor of a class of SERCA enzymes. Thapsigargin raises cytosolic calcium concentration by blocking the ability of the cell to pump calcium into

the sarcoplasmic and endoplasmic reticula which causes these stores to become depleted [268]. In the first experiment, HeLa cells were firstly treated with LY30 (25uM) for 100 seconds and then added with TG at 1mM (Fig 5.3.5).

Black line and blue line in Figure 5.3.5a represents concentrations of intracellular free Ca^{2+} and bound Ca^{2+} corresponding to different treatments specified in x-axis respectively. Increase of free Ca^{2+} occurs right after LY30 (black line) without distinctive decrease of bound Ca^{2+} (blue line). More significant increase of free Ca^{2+} and decrease of bound Ca^{2+} were observed with TG. Figure 5.3.5b demonstrate calculated ratio between free Ca^{2+} and bound Ca^{2+}. Calibrated Ca^{2+} concentration (based on measured raw data) is plotted in Figure 5.3.5c according to the function $[Ca^{2+}] = K_d Q \frac{(R - R_{\min})}{(R_{\max} - R)}$. Here, K_d is the dissociation constant of the fura2-Calcium binding. R is the measured ratio between free calcium and bound calcium as plotted in Figure 5.3.5b. The values of R_{max} and R_{min} are the ratio values measured under conditions of saturating calcium levels and in the absence of calcium respectively. In this experiment, slight rise of Ca^{2+} occurs right after LY30 treatment (demonstrated with red arrows); TG treatment, as positive control followed LY30, is able to induce sharp and tremendous increase of Ca^{2+}.

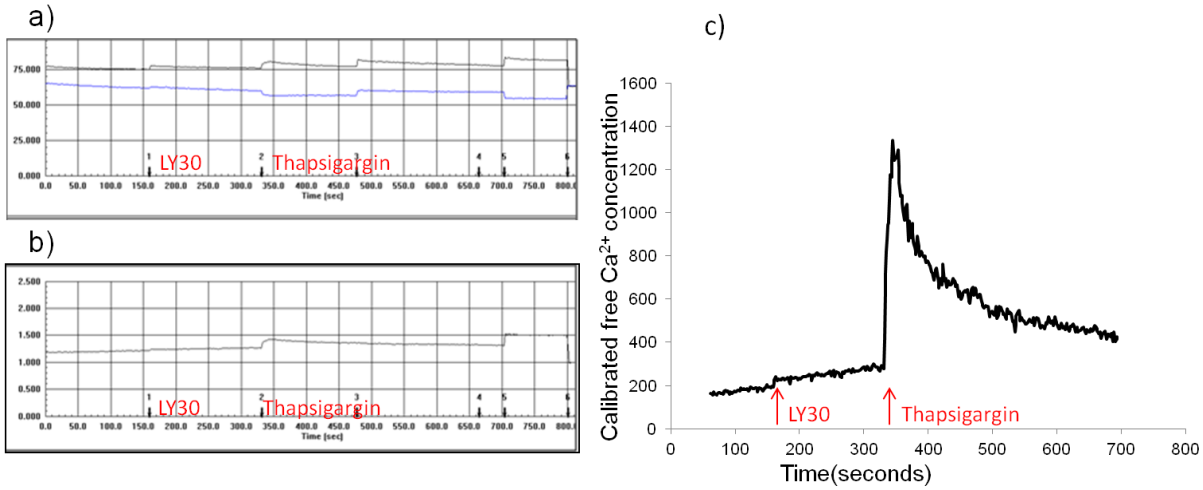

Figure 5.3.5 Ratiometric Ca^{2+}measurement using Fura-2 demonstrate increased ratio of free Ca^{2+} to bound Ca2+ in HeLa upon LY30 treatment. a) Change of fluorescence intensities of Fura-2 given specified treatments. From left to right are treatments of LY30, Thapsigargin, LY30, EGTA and Triton, respectively. Black line and blue line indicate fluorescence obtained at excitation wavelength of 380 and 340, representing free calcium and bound calcium respectively. b) Ratio between free $Ca^{2+}$and bound calcium. c) Calibrated free Ca^{2+}concentration.

To check the source of Ca^{2+} increase in HeLa by LY30, we treated HeLa with TG (1mM) firstly to deplete ER Ca^{2+} before adding LY30. As TG is known to deplete ER Ca^{2+}, we would expect to observe no further increase of Ca^{2+} with LY30 treatment if LY30 increases intracellular Ca^{2+} through ER. As demonstrated in Figure 5.3.6, TG treatment induces a sharp elevation of Ca^{2+} while the following LY30 treatment doesn't show distinctive increase of Ca^{2+}. Interestingly, LY30 treatment caused a brief, sharp decrease of Ca^{2+}, followed by a sharp increase (similar or slightly higher) to the original level. We hypothesized the phenomenon may be related with physiological pH change from the LY30.

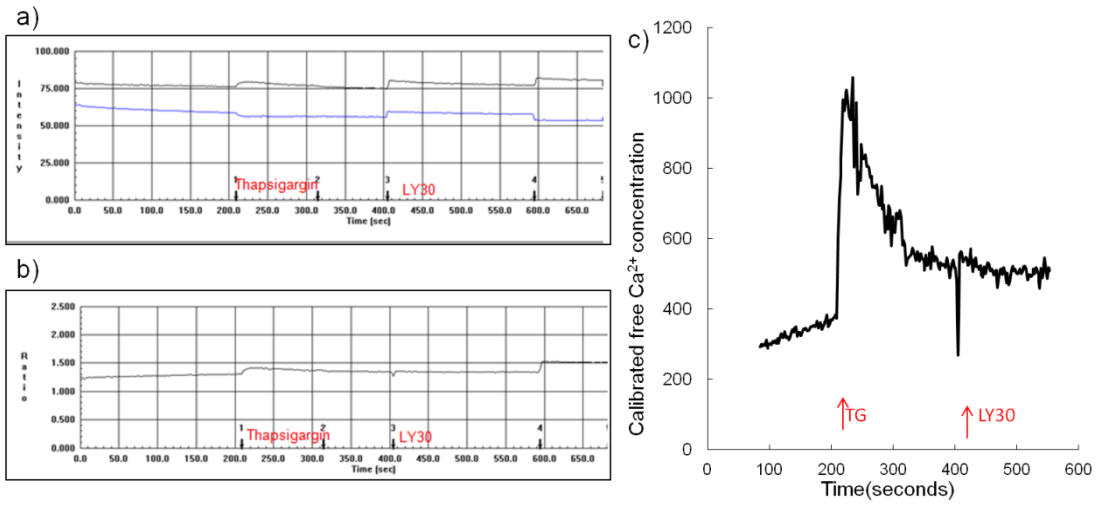

Figure 5.3.6 Ratiometric Ca^{2+} measurement using Fura-2 demonstrated pretreatment of thapsigargin is able to abolish LY30 induced Ca2+ increase. a) Change of fluorescence intensities of Fura-2 given different treatments. Black line and blue line indicate fluorescence obtained at excitation wavelength of 380 and 340, representing free calcium and bound calcium respectively. LY30 is added into cells after TG. b) Ratio between free calcium and bound calcium. c) Calibrated free calcium concentration.

5.3.5 Non-Ratiometric measurement of Ca^{2+}

Besides checking Ca^{2+} concentration using Ratiometric dye Fura-2, we also tracked intracellular Ca^{2+} change using a non-ratiometric dye Fluo-4 AM (Fluo-4), which was reported to specifically picks cytosolic free Ca^{2+} ($[Ca^{2+}]_c$) [267]. Towards a comprehensive understanding of LY30-induced $[Ca^{2+}]_c$ dynamics, we used Flow Cytometry, spinning disk confocal microscopy (SDCM) and microplate reader to assess $[Ca^{2+}]_c$ levels from different aspects. Specifically, flow cytometry measures $[Ca^{2+}]_c$ levels for a large cell population at a single time point; SDCM [149] enables us to visualize and quantify $[Ca^{2+}]_c$ dynamics in every single cell; microplate reader, as a low-cost alternative to SDCM, can calibrate total $[Ca^{2+}]_c$ fluorescence from cell samples with varied treatments in parallel.

5.3.5.1 Flow cytometry experiments showed significant Ca^{2+} increase in HeLa upon LY30 treatment

We measured fluorescence in cell samples of unstained untreated control, stained untreated control, and LY30 treated sample for 5 minutes, 10 minutes, 15 minutes and 30 minutes. Scatter plot of each sample is presented in Figure 5.3.7, where x-axis represents Fluo-4 intensity and y-axis represents cell size. We saw a distinctive right shift of Fluo-4 signal in LY30-treated sample (90.5%) compared with untreated sample (3^{rd} upper panel in Figure 5.3.7a). Furthermore, 95%, 98.5%, 98.7% positive cells were observed in LY30-treatment at 10 minutes, 15 minutes and 30 minutes, respectively. We quantified fluorescence intensity for the whole population as shown by the histogram in figure 5.3.7b and time-kinetics in figure 5.3.7c. Note that in the plot, the fluorescence intensities on the y-axis are normalized using the function described in figure 5.3.7c. From the plot, we can see that Fluo-4 intensity increases steadily from 1-fold to 3-fold from untreated to 30 minutes of treatment with LY30 (25uM).

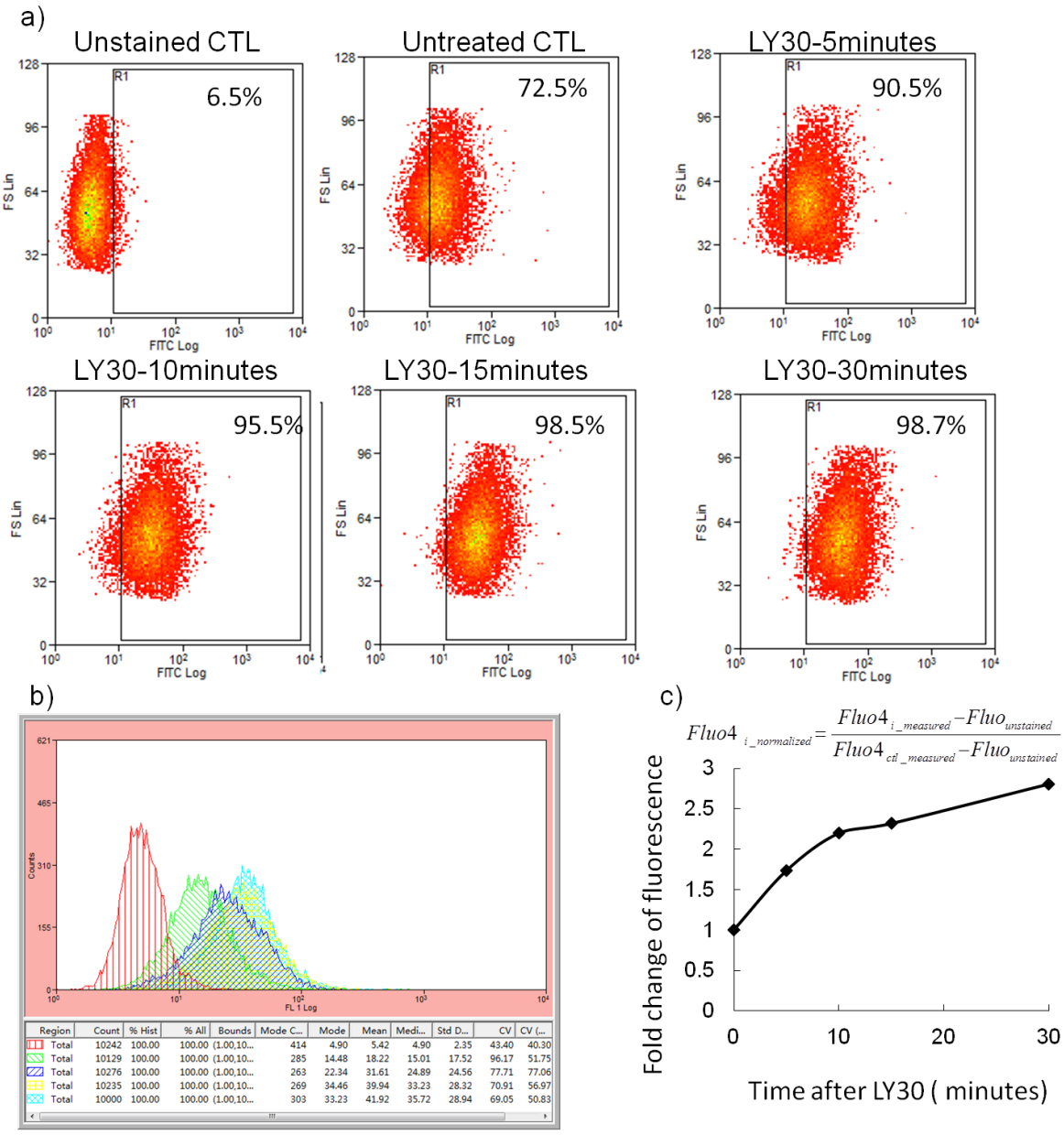

Figure 5.3.7 Fluo-4 experiment in HeLa measured by flow cytometry showed significant increase of Ca^{2+} by LY30. a) Dot plots for Fluo-4 in each treatment; b) overlapped histogram of Fluo-4 in all treatments. c) Dynamics of normalized intensity of Fluo-4 according to LY30 treatment.

To confirm the dynamics of Ca^{2+} increase with LY30 showed in Figure 5.3.7, we carried out 3 more repeats for Fluo-4 flow and the averaged dynamics are shown in Figure 5.3.8a.

As we know, increase of $[Ca^{2+}]_c$ may come from either extracellular calcium through plasma membrane (plasma membrane Ca^{2+} ATPase (PMCA)) [269] or intracellular calcium store (e.g. ER, mitochondria) through various calcium channels (e.g. IP3R, Ryanodine receptor [270]). To test whether extracellular calcium is involved, we conducted another sets of $[Ca^{2+}]_c$ measurement in calcium-free media. To be more specific, the experiment is carried out in the same conditions (e.g. Fluo-4 staining and drug treatment) as the experiment shown in Figure 5.3.8a except that the media is always kept as calcium free. The averaged results of 3 replicates are shown in 5.3.8b. By comparing fluorescence intensity in normal media and calcium free media (5.3.8a verse 5.3.8b), we found that LY30 induces 1 fold increase of $[Ca^{2+}]_c$ in both normal media and calcium-free media in 5 minutes, and then the increase sustained until LY30 treatment for 20 minutes. Difference of fluorescence between normal media and calcium-free media arise from 20 minutes. We observed a further increase of fluorescence occurring from 2.5 to 3 folds in normal medium, which however, is not seen in calcium-free medium.

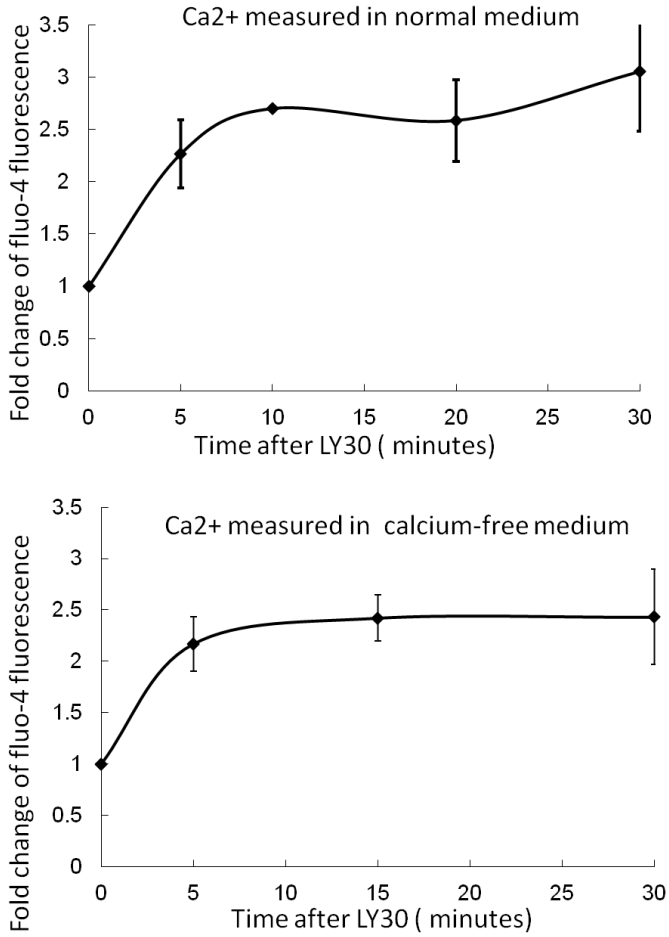

Figure 5.3.8 Averaged dynamics of [Ca2+]c in HeLa with LY30 treatments using flow cytometry. a) LY30 triggered $[Ca^{2+}]_c$ dynamics in normal medium. b) LY30 triggered $[Ca^{2+}]_c$ dynamics in calcium-free medium.

Under the same experiment condition, we also did $[Ca^{2+}]_c$ measurement with TG treatment (incubation of HeLa cells with TG at 1mM and 2mM for 5 minutes). Measured result is presented in the form of scatter plot and histogram (Figure 5.3.9). Scatter plot shows that sample with TG treatment at 1mM had 80.2% Fluo-4- positive concentration (2^{nd} panel) and 86% positive concentration at 2mM (3^{rd} panel). Compared with untreated control which showed 77.99% cells with fluo4-positive, there is about 2.2% and 8% increase, much lower than the increase of LY30. In the histogram,

we observed little increase of average fluoresce of the whole cell population with TG treatment compared with untreated control.

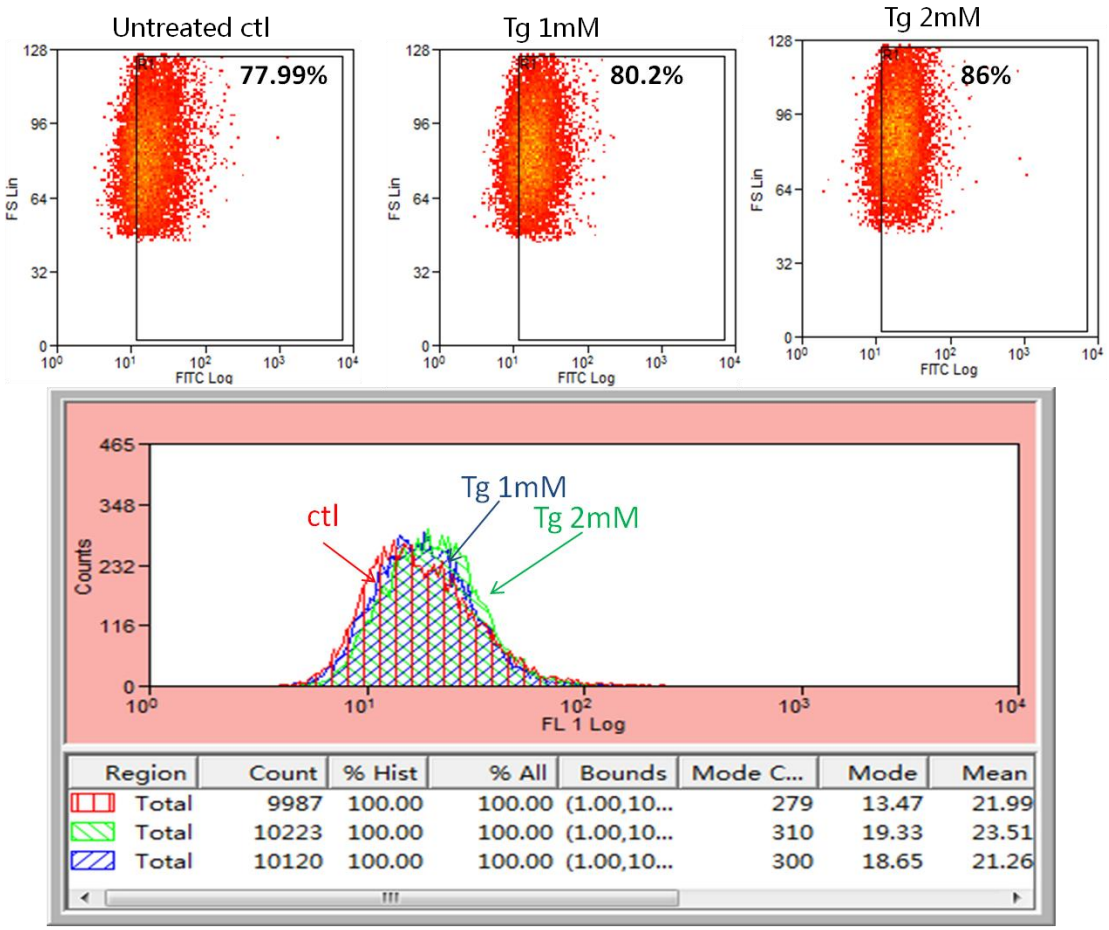

Figure 5.3.9 Flow cytometry failed to demonstrate obvious increase of Ca2+ increase in HeLa by thapsigargin. a) From left to right panels are dot plots of Fluo-4 fluorescence in HeLa upon no treatement, TG 1mM and TG 2mM. b) histgram of Fluo-4 intensity corresponding to treatments shown in a).

5.3.5.2 Spinning Disk Confocal Microscopy showed a slow and steady increase of Ca^{2+} induced by LY30 in HeLa

In addition to flow cytometry, we obtained $[Ca^{2+}]_c$ data through direct imaging from spinning disk confocal microscope (SDCM) and a fully-automated image processing software developed by Dr. Marc [149].

$[Ca^{2+}]_c$ is measured independently with DMSO (0.25ul/ml calculated according to the LY30 concentration), Thapsigargin (1mM) and LY30 (25uM). TG was used as a positive control because it has been well-studied to induce $[Ca^{2+}]_c$ increase within seconds. DMSO is the negative control since it is the dissolvent of both LY30 and TG. Figure 5.3.10c shows the raw images of Fluo-4 fluorescence in the same set of cells before/after LY30 treatment. The cell samples underwent same preparation before treated with DMSO for 45 minutes (designed to be consistent with LY30 treatment), TG for 6 minutes (designed according to previous calcium measurement with TG) and LY30 for 45 minutes, respectively. After obtaining raw image of each sample with the specific treatment, we quantified fluorescence intensity for each treatment according to a automated image processing software [149] and plotted time-intensity of every single cell in Figure 5.3.10b with thin blue line. The averaged result is represented by thick red line with calculated error bar of the whole cell population at the specific time point. For clearer visualization, Figure 5.3.10b demonstrated only the averaged fluorescence for the cell population of a specific treatment. DMOS treatment (1^{st} panel of figure 5.3.10b) did not induce any observable increase of calcium. TG (2^{nd} panel of figure 5.3.10b) induces rapid and significant increase of $[Ca^{2+}]_c$ and then restore it back to basal level in about 6 minutes. LY30 treatment (3^{rd} panel of figure 5.3.10b), compared with DMSO, produced more $[Ca^{2+}]_c$. Compared with TG, it induces $[Ca^{2+}]_c$ in a steady and slowing manner. We also plotted raw image of the cell population with LY30 treatment in Figure 5.3.10c. It shows that Fluo-4 fluorescence level in the same cell population is significant increased after LY30 treatment compared with before treatment.

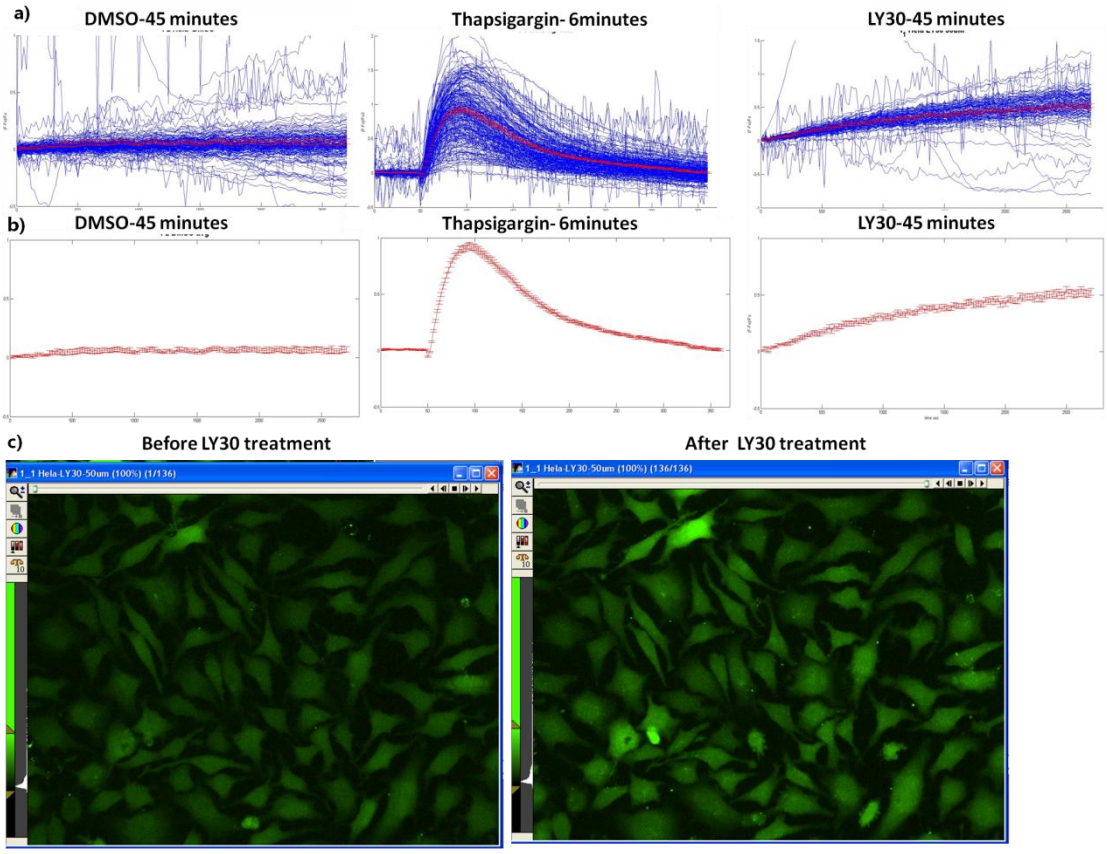

Figure 5.3.10 LY30 induces significant increase of Fluo-4 intensity in HeLa. a) dynamics of quantified fluorescence intensity in every single cell. From left to right are cells treated with DMSO for 45 minutes, thapsigargin for 6 minutes and LY30 for 45 minutes. b) averaged dynamics of Fluo-4 fluorescence intensity of the entire individual cells upon same treatments, corresponding to similar treatment in a). c)image of Fluo-4 fluorescence in a large number of cells, left panel is taken from cells before LY30 treatment and the right panel is taken from the same set of cells after LY30 treatment for 45 minutes;

To test the involvement of ER in the increase of $[Ca^{2+}]_c$, we carried out experiments with sequential and reverse administration of TG (1mM for 6 minutes) and LY30 (25uM for 10 minutes). If LY30 induces $[Ca^{2+}]_c$ from ER, we would expect there is no further increase of $[Ca^{2+}]_c$ with LY30 following TG, as TG will deplete $[Ca^{2+}]_E$ store from ER in 6 minutes. The reverse administration of LY30 and TG is to confirm the phenomenon of $[Ca^{2+}]_c$ increase with LY30 treatment shown before. In the experiment with early TG and later LY30 treatment (Figure 5.3.11b), we can no longer observe

increase of $[Ca^{2+}]_c$. The experiments with early LY30 and later TG showed that LY30 induces steady $[Ca^{2+}]_c$ increase in HeLa, which is in consistent with results presented in Figure 5.3.10.

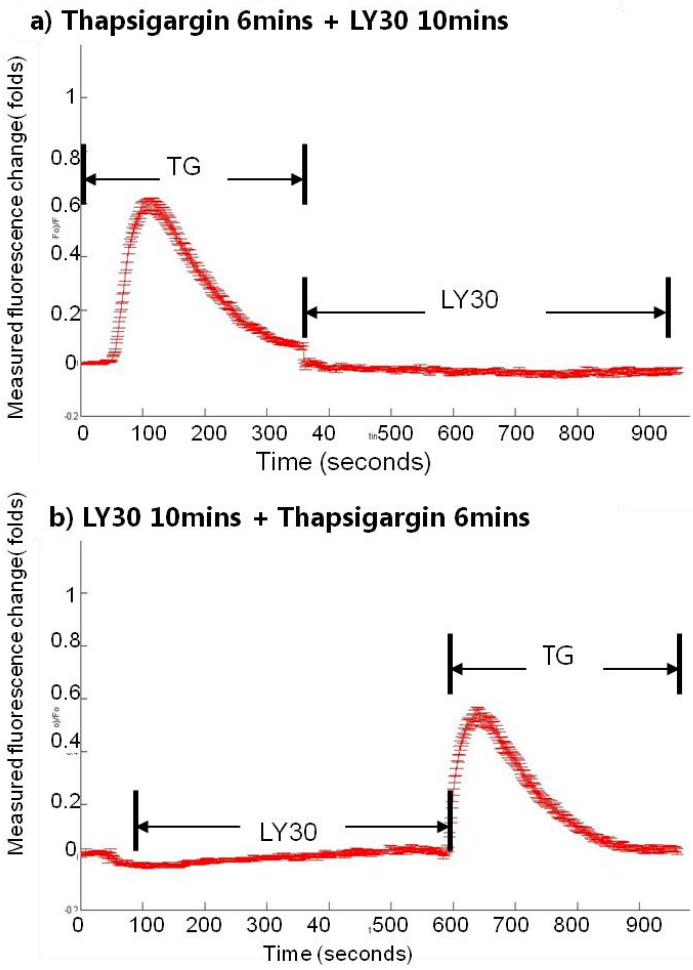

Figure 5.3.11 Quantified Ca^{2+} concentration with sequential administration of thapsigargin and LY30 or reverse. a) Fluo-4 dynamics in cells treated with TG treatment for 6 minutes followed by Ly30 10 minutes; b) Fluo-4 dynamics in cells with LY30 for 10 minutes followed by TG for 6 minutes

5.3.5.3 Microplate reading of Ca^{2+}

Fluo-4 NW (No-Wash) Calcium Assay is introduced as no-wash dye for calcium measurement under microplate reader. It offers a proper assay formulation that requires neither a wash step nor a quencher dye, which makes the measurement convenient. The

Fluo-4 NW assay is claimed to reach larger fluorescence intensity increases compared to Fluo-3 and Fluo-4 [271]. We chose to measure $[Ca^{2+}]_c$ with microplate reader as it is a cheaper alternative of SDCM. Another advantage of microplate reader for $[Ca^{2+}]_c$ measurement is its high-throughput screening capability. It is able to simultaneously measure fluorescence intensities from multiple wells which correspond to various treatments.

To test the feasibility of microplate reader with Fluo-4 NW assay in $[Ca^{2+}]_c$ measurement, we firstly generated time-series plots for cell samples treated with either TG (1mM: positive control) or DMSO (0.25 ul/ml: negative control) measured at 488nm for 6 minutes with time interval of 5 seconds. Measured fluorescence intensity of each time point is normalized to the fluorescence intensity of the same sample before treatment. From the normalized dynamics shown in Figure 5.3.13b, we can see that TG induced significant increase and decrease of $[Ca^{2+}]_c$, which qualitatively, is in agreement with the results from SDCM in figure 5.3.10 and 5.3.11. After confirmed the feasibility of the assay, we measured $[Ca^{2+}]_c$ dynamics in HeLa cells with LY30 treatment at 25uM for 30 minutes. As we can see, cell sample treated with LY30 showed a steady increase of $[Ca^{2+}]_c$, the trend of which is consistent with the kinetics shown in Figure 5.3.12. Compared with SDCM, microplate is not as sensitive as microplate. But it is still able to capture the dynamics of the calcium signals.

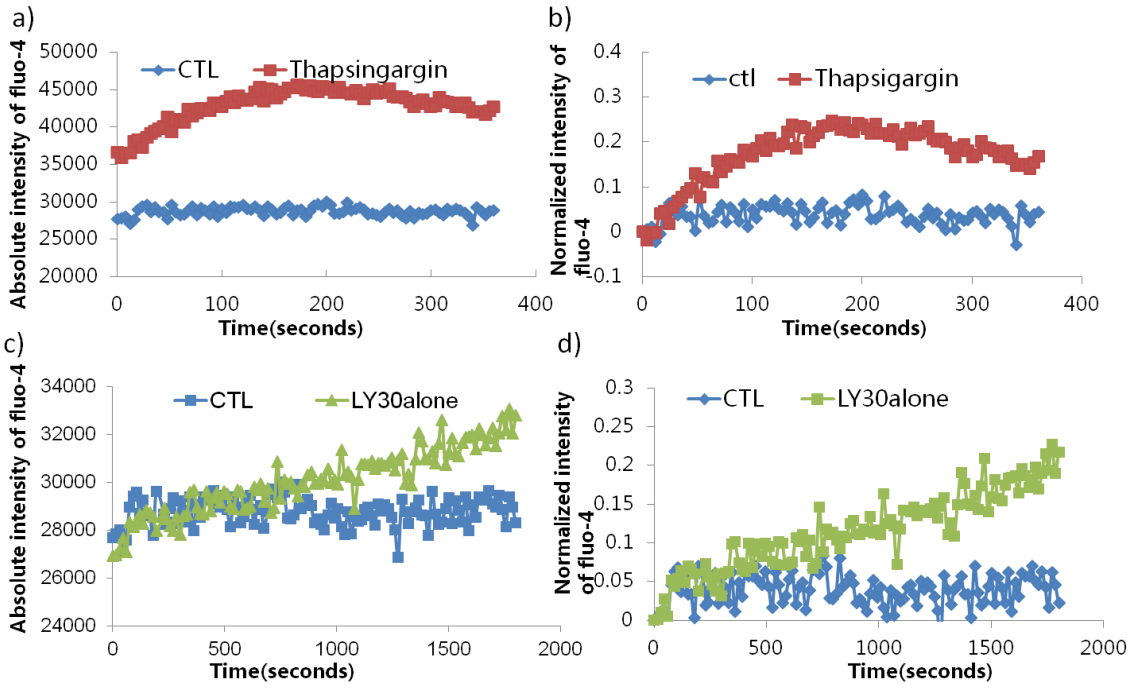

Figure 5.3.12 Microplated reader showed significant increase of Fluo-4 fluorescence under TG treatment and LY30 treatment. a) Absolute intensities of Fluo-4 in cells with/without tg treatment. b) Normalized intensities of Fluo-4 correspond to results obtained from a). c) Absolute intensities of Fluo-4 in cells with/without LY30 treatment. d) Normalized intensities of Fluo-4 correspond to data in c).

5.4 Discussion and Summary

5.4.1 ODE model of canonical $O_2^{\bullet-}$ to H_2O_2 pathway is inconsistent with experimental observations

According to computational system study of LY30-induced sensitization to TRAIL, we found the non-monotonic regulation of cFLIP by LY30 in HeLa. Further investigation suggested that the non-monotonic regulation might root in the opposing pathways of H_2O_2 and $O_2^{\bullet-}$ induced by LY30. In order to characterize and verify the effect, we constructed an Ordinary Differential Equation (ODE) model which incorporated the

hypothesized effect of LY30 into a well-studied ROS pathway (Figure 5.1.1). The model predicted an earlier production of $O_2^{\bullet-}$ to that of H_2O_2 (Figure 5.1.2 b) while the experiments showed that H_2O_2 (as detected by DCFDA) increased earlier than $O_2^{\bullet-}$ (as detected by MitoSOX). In addition, the model predicted that the steady states concentrations of H_2O_2 and $O_2^{\bullet-}$ in LY30-treated samples will increase to the same level relative to that of untreated sample (Figure 5.1.2 a) while the experiment data showed a more significant increase of the steady state of H_2O_2 (around 1.6 folds) than that of $O_2^{\bullet-}$ (Figure 5.1.3).

In order to verify the experiment observations with $O_2^{\bullet-}$ and H_2O_2, we further employed double staining to measure intracellular $O_2^{\bullet-}$ and H_2O_2 in parallel. Compared with single staining which can only measure single fluorescence in one set of cell sample, double staining has the advantage of tracking the change of $O_2^{\bullet-}$ and H_2O_2 simultaneously within the same set of cell sample. With the method of double staining of $O_2^{\bullet-}$ and H_2O_2, we observed that LY30 induced increase of H_2O_2 happened earlier than that of $O_2^{\bullet-}$ (Figure 5.1.4), which is consistent with the dynamics of H_2O_2 and $O_2^{\bullet-}$ with single staining (Figure 5.1.3)

As model predictions can be greatly affected by its parameters, we performed sensitivity analysis on the model in order to find the sensitive parameters which have high influence on H_2O_2 and $O_2^{\bullet-}$. By adjusting the "sensitive parameters" in the model, we tried to harmonize the model prediction with our experimental results. However, we were unable to unify our model and experiments though extensive adjustments of parameters (Figure 5.1.7). Our extensive effort to recapitulate observations using the

canonical ROS pathway suggested that ROS induced by LY30 doesn't follow the canonical ROS pathway with superoxide and then hydrogen peroxide.

5.4.2 LY30 does not induce significant $O_2^{\bullet-}$ increase in HeLa

Considering that MitoSOX detects only mitochondrial $O_2^{\bullet-}$, we used DHE (Figure 5.3.1) and lucigenin (Figure 5.3.2) to measure the change of total $O_2^{\bullet-}$ caused by LY30. In both experiments, we were unable to observe increase of $O_2^{\bullet-}$ prior to the increase of H_2O_2. Instead, both experiments demonstrated an unexpected effect on $O_2^{\bullet-}$: starting with an initial drop (0.8-fold from 5 to30 minutes) and later an increase (1.2-fold at 60 minutes) and finally another decrease (0.8 fold at 120 minutes). This non-canonical effect on $O_2^{\bullet-}$ further supports the alternative hypothesis that in LY30-induced ROS production, $O_2^{\bullet-}$ is not the upstream source of the observed ROS signal (DCFDA fluorescence).

5.4.3 LY30 induces NO increase in HeLa

It has been reported that NO and Ca^{2+} are closely linked to ROS production. NO could be an upstream cause of the observed ROS signal (DCFDA fluorescence) because NO interacts with $O_2^{\bullet-}$ to form the reactive species peroxynitrite ($ONOO^-$) at a rate of $6.7*10^9 M^{-1}sec^{-1}$, which is about 2-4 folds faster than the rate of catalysis of $O_2^{\bullet-}$ by superoxide dismutase (CuZn-SOD) [232, 272]. LY30-treated cells showed increased DAF fluorescence compared with untreated cells, which indicates increased NO concentration in LY30-treated cells (Figure 5.3.3). In order to confirm the observation of LY30-induced NO increase, we repeated DAF measurement with more time points

after LY30 treatment. The averaged results showed that there is a rapid increase of NO concentration, followed by a slight decrease, and then another increase till a steady state around 2 folds (Figure 5.3.4). The observations confirmed that LY30 treatment increases intracellular NO concentration.

The phenomenon of NO increase has been reported in Quercetin-treated hypobaric hypoxic rats [273] and conducted clinical trials of Quercetin treatment in 12 healthy men [274]. In contrast, research in IL-1ß–stimulated hepatocytes showed that Quercetin inhibits NO production through the inhibition of inducible nitric oxide synthase (iNOS) expression [275]. Most research consider LY29 as a NOS inhibitor through inhibition of NF-kappaB (NF-KB) activation [276], while Boscá L. showed that LY29 can also trigger iNOS and the synthesis of nitric oxide [277].

As NO is synthesized by a family of NO-synthases (NOS), eNOS, iNOS and nNOS in mammals, increased NO suggests that LY30 activates one or multiple isoforms of NOS in a short time. The mechanism of NO effects by LY30 in HeLa remains to be clarified. Our inability to decrease NO production through L-NAME may be the result of technical problems or it might imply the involvement of iNOS activation by LY30. Future work could knock-down individual NOS isoforms to determine which are activated by LY30. In addition to a significant increase of NO, we also observed that the dynamic trajectory of NO is similar to that of ROS measured by DCFDA, suggesting there may be a causal link between LY30-induced NO and LY30-induced DCFDA fluorescence.

5.4.4 LY30 induced an increase in cytosolic Ca^{2+}

Calcium could also be an upstream cause of ROS because increased intracellular free Ca^{2+} is known to induce $O_2^{\bullet-}$-dependent ROS production through mitochondrial respiration [261, 278, 279], and $O_2^{\bullet-}$-independent ROS production through NOX activation [108, 280]. Based on these findings, we carried out experiments to measure the intracellular change of NO and $[Ca^{2+}]_c$ by LY30.

Measurement of $[Ca^{2+}]_c$ is a difficult experiment because it requires fast speed and high accuracy to capture the transient dynamics of $[Ca^{2+}]_c$. In this research, we used four assays to measure the change of $[Ca^{2+}]_c$ in HeLa upon LY30 treatment: ion measurement, flow cytometry, microplate reading, and imaging with a spining disk confocal microscope.

Our $[Ca^{2+}]_c$ measurement using the ratiometric dye Fura-2 (Figure 5.3.5) showed an immediate and small (compared with the high increase with Thapsigargin treatment) elevation of $[Ca^{2+}]_c$ upon LY30 treatment. Such immediate elevation of cytosolic Ca^{2+} was followed by a slow and steady increase.

Our Ca^{2+} measurement using flow cytometry with Fluo-4 showed that the cytosolic Ca^{2+} concentration in LY30-treated cells (5 minutes) was about 1.2 fold higher than that in untreated cells (Figure 5.3.7). Longer incubation of LY30 (30minutes) increased the concentration to 3 folds of the basal level before any treatment. In the experiment, we failed to observe significant increase of Fluo-4 fluorescence with Thapsigargin treatment (Figure 5.3.9).

Under spinning disk confocal microscopy (SDCM), we observed a steady and slow increase of cytosolic Ca^{2+} in LY30-treated cells (Figure 5.3.10). An independent image

of Fluo-4 with Thapsigargin (TG) showed a sharp and dramatic increase of Ca^{2+}, demonstrating that the assay can accurately capture the dynamics of Ca^{2+}.

Compared with SDCM, $[Ca^{2+}]_c$ measuring Fluo-4-NW fluorescence with a microplate reader produced data with less resolution. But it produced similar dynamics of $[Ca^{2+}]_c$ under various treatments. Consistently, there was no distinctive change of Ca^{2+} under DMSO treatment; there was a slow and steady increase of $[Ca^{2+}]_c$ under LY30 treatment; and there was a sharp and high-magnitude increase of $[Ca^{2+}]_c$ under TG treatment (Figure 5.3.12).

The results of ion measurement using Fura-2, confocal microscopy with Fluo-4, together with microplate reading with Fluo-4 showed a sharp and high elevation of $[Ca^{2+}]_c$ after TG treatment, which reproduced the reported phenomenon that TG can deplete the $[Ca^{2+}]_E$ stores within seconds. The results confirmed that the three assays are capable of capturing the dynamics of $[Ca^{2+}]_c$ correctly. All the three assays consistently demonstrated a slow and steady increase of $[Ca^{2+}]_c$. We observed that the increase of $[Ca^{2+}]_c$ accumulated to 0.6 fold higher than the basal level within 45 minutes of LY30 treatment, which is more than half of the total $[Ca^{2+}]_E$ storage (as observed in Figure 5.3.10b with the peak value of 1-fold- increase under TG treatment).

Interestingly, our fluorescence measurement with flow cytometry (Figure 5.3.8a) showed a much more significant increase of cytosolic Ca^{2+} with short LY30 incubation (1.2 folds increase was observed with 5 minutes incubation Figure 5.3.8s) than the increase of longer LY30 incubation in the other three assays (0.5 folds increase was observed with 45 minutes Figure 5.3.10). Under the same protocol with flow cytometry, we were not able to observe distinctive $[Ca^{2+}]_c$ increase in HeLa with TG treatment

(Figure 5.3.9). Our speculation about the difference between the results from flow cytometry versus other experimental assays resides in the preparation procedure. For $[Ca^{2+}]_c$ measurement using flow cytometry, we treated HeLa cells with LY30 for a specific period, say 5 minutes before staining the cells with Fluo-4 for 1 hour (followed the Ca^{2+} measurement protocol using flow cytometry of Invitrogen website); the staining introduces a delay in the experiment, and it is highly possible that there could be a further accumulation of cytosolic Ca^{2+} during the staining procedure. For $[Ca^{2+}]_c$ measurements using the ion-measurement machine, SDCM and microplate reader, we stained the HeLa cells with Ca^{2+} dyes prior to LY30 treatment. Although we washed away extra LY30 from the LY30-treated cells with PBS and changed fresh media for Fluo-4 staining, the portion of LY30 that had already entered the cells continued to increase $[Ca^{2+}]_c$. In that case, the measured $[Ca^{2+}]_c$ concentration corresponds to LY30 treatment with the specified drug incubation (5 minutes) time plus the dye incubation (longer than 1 hour). Therefore, a higher elevation of $[Ca^{2+}]_c$ was observed with flow cytometry. The explanation also applied to TG treatment where the significant $[Ca^{2+}]_c$ increases that were recorded with the three assays was not observed under flow cytometry.

5.4.5 LY30 may induce passive calcium leakage in HeLa

TG, a known SERCA pump inhibitor, induced a very fast and sharp increase of Fluo-4 fluorescence, which goes back to basal level in about 6 minutes. LY30, in contrast, induced a slow and steady rise of Fluo-4 fluorescence which lasted for more than 45 minutes. One possible explanation for this difference is that LY30 causes a passive increase of $[Ca^{2+}]_c$ and TG causes an active increase of $[Ca^{2+}]_c$. To determine the source

of $[Ca^{2+}]_c$, we firstly emptied the $[Ca^{2+}]_E$ store with TG and then measured the dynamics of $[Ca^{2+}]_c$ by LY30. After the pre-treatment of TG, we no longer observed LY30-induced fluorescence increase (Figure 5.3.11a). The results demonstrated that LY30-induced increase of $[Ca^{2+}]_c$ is from the Endoplasmic Reticulum. These results were consistent with the possibility that LY30 causes passive calcium leakage from the ER.

Passive calcium leakage is a graded and continuous process which does not completely empty calcium stores [281]. Leak rates vary in different cell lines and with different treatments from 10uM/mins to 400uM/mins [282]. Although the exact mechanism and nature of calcium leakage is still an enigma, researchers have found that it is not affected by ryanodine receptors or IP3 receptors, but is responsive to ATP levels [283] and to the Bcl-2 family [284]. In our experiments, we found that application of neither IP3 inhibitor 2-APB nor RYR inhibitor TMB8 was capable of reducing LY30-induced $[Ca^{2+}]_c$, which is consistent with LY30 causing passive Ca^{2+} leakage.

6 Bayesian networks for LY30-induced ROS production and sensitization to death

In this chapter, we applied Bayesian Network to learn LY30-induced signaling pathway in order to explain the significant fluorescence increase of DCFDA, DAF and Fluo-4 am upon treatment of LY30.

6.1 Introduction to Bayesian network

A Bayesian network is a type of probabilistic graphical model which depicts the dependencies among variables (such as proteins or genes in a cellular network) through a series of probability distributions. While Ordinary Differential Equations (ODE) has been widely applied in well-studied cellular networks [142, 143, 173], Bayesian network is more suitable for learning and inferring cellular networks where the network is less-understood and the models have too many parameters relative to the data. Many applications in biological studies have taken advantage of Bayesian networks, such as gene expression analysis [285, 286], cellular network [287] and pathway modelling [288, 289].

6.1.1 Bayesian Network and relevant terms

Firstly, several key terms are explained as below before introducing Bayesian network and its applications.

Variable

Variables here refer to biological entities, including LY30 and species in the pathway such as proteins or genes, to be studied in the network. In Bayesian network, each variable is represented as one node.

Dependency

Dependency specifies the causality between variables through an acyclic directed graph. Each acyclic arrow in dependency graph links two variable starting from parent (*P*) to its child (*C*): $P \rightarrow C$, meaning that *C* is dependent on *P*. In other words, *P* can induce *C*. One variable depends on all the variables that point to it.

Conditional Probability Distribution (CPD)

Dependency depicts the causality among all variables. Conditional probability distribution (*CPD*) describes the influence from parent(s) to its direct child in a quantitative way. This relationship is represented in the form of $P(C=x_i|Pa=y_j)$, where *Pa* and *C* refer to parent and child, x_i and y_i are the elements of the assigned values sets for *C* and *Pa*, respectively. It means the probability of *C* being x_i given that *Pa* is y_j (the vertical bar '|' means given that). Note that the conditional probabilities are constrained to be a probability distribution, meaning they are non-negative and the sum of probability of *C* under all conditions given a known condition of Pa is 1: $(\sum_i p(C = x_i \mid Pa = y) = 1)$.

Generally, variables in a Bayesian network can be either continuous or discrete. In this thesis, we consider only the discrete situation and use only multinomial distributions. Thus, CPD can be represented by conditional probability tables (CPTs). For a node

which has parent(s) in the network, CPT is the table that records the strength of its dependencies on all its parents. From the CPT, we can look up the probability of the node given the value(s) of its parent(s). High values of $P(C=x_i|Pa=y_j)$ means there is high probability that the child will be x_i whenever the parent is y_i, and vice versa. If there are several parents of C, say $\{P_{a1},\ldots,P_{ak}\}$, the conditional probability of C is specified as $P(C=x_i|P_{a1}=y_{j1},\ldots,P_{ak}=y_{jk})$ in multi-nominal conditions for all the nodes. The conditional probability distribution (CPD or CPT) is described by a vector of parameters θ (we will use θ later to represent parameters).

Joint probability

Given X_i as one node in the network, its parents are denoted as $P_a(X_i)$. Assuming X_i has n parents, each of which are independent, the joint probability of X_i in the network can be expressed as the product of its conditional probability on each parent. Expressed as

$$P(X_i|Pa_1(X_i),\ldots,Pa_n(X_i))=\prod_{j=1}^{n} P(X_i \mid Pa_j(X_i)) \ .$$

Bayes' rule

As a central theorem in probability theory, Bayes' rule expresses how a subjective degree of belief should rationally change to account for evidence.

Bayes rule [290] specifies the relationship between the probability of parameter θ ($P(\theta)$) and the observations O ($P(O)$) in the form of $P(\theta \mid O) = \frac{P(O \mid \theta)P(\theta)}{P(O)}$. In the equation, $P(\theta)$ is the prior of parameter θ, which specifies the initial belief in θ; $P(O)$ is the probability of observation; $P(\theta \mid O)$ is the calculated posterior which represents belief of parameters θ given observation O.

Bayesian network

A Bayesian network is a graphical structure together with a family of Conditional Probability Distributions (*CPD*) that describes a set of random variables and their probabilistic dependence (causalities) [291]. A Bayesian network is composed of a set of nodes (variables), a directed acyclic graph (*DAG*) specifying direct dependence among the nodes and a conditional probability distribution (*CPD*) for each node given its parents specified in the graph. In the case of multi-nomial conditions, the *CPD* can be simplified into a conditional probability table (*CPT*).

As demonstration of Bayesian network, we illustrated a small Bayesian network in figure 6.1.1. In this network, there are 4 nodes (variables) *A*, *B*, *C* and *D*. The dependence relationship among the 4 nodes are specified through the arrows *A→B; A→C; {B, C}→D*, meaning that variable *B* and *C* are dependent on variable *A*, and variable *D* is dependent on *B* and *C*. The CPDs that define the causalities among the species are shown in the right panel of the figure, noted that we assumed *A*, *B*, *C* and *D* are Boolean variables which can only take on values 0 and 1,.

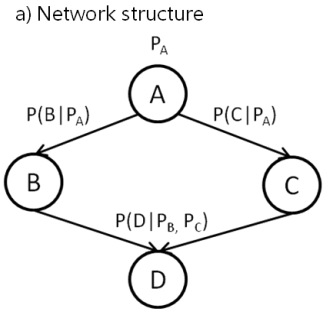

b) Parameter for node *A*

A	Probability
	1 P(A)
	0 P(^A)=1-P(A)

d) Parameter for node *B*

A	B	Proability
1		1 P(B|A))
1		0 P(^B|A))
0		1 P(B|^A))
0		0 P(^B|^A))

c) Parameter for node *C*

A	C	Proability
	1	1 P(C|A))
	1	0 P(^C|A))
	0	1 P(C|^A))
	0	0 P(^C|^A))

e) Parameter for node *D*

B	C	D	Probalility
	1	1	1 P(D|B,C))
	1	1	0 P(^D|B,C))
	1	0	1 P(D|B,^C))
	1	0	0 P(^D|B,^C))
	0	1	1 P(D|^B,C))
	0	1	0 P(^D|^B,C))
	0	0	1 P(D|^B,^C))
	0	0	0 P(^D|^B,^C))

Figure 6.1.1 demonstration of Bayesian network with a simple example. A) Network structure. A is the root of the network and it is the parent of B and C. B

and C are both the parents of D. b), c), d) and e) are parameters of conditional probability for A, B, C and D, respectively.

Bayesian networks has three advantages in modelling biological pathways(refer to [292] for more details about advantages of Bayesian network): 1) Bayesian networks are capable of modeling incomplete data sets; 2) Bayesian networks enable us to learn about causal relationships, which are a direct representations of our beliefs; and 3) Bayesian network together with Bayesian statistic techniques facilitate the integration of knowledge and data [293].

In the task of explaining the significant fluorescence increase of intracellular DCFDA (H_2O_2) without distinctive increase of $O_2^{\bullet-}$ after LY30 treatment, we chose Bayesian network among the modelling techniques due to the following two limitations. Firstly, there is lack of information on LY30 induced ROS pathway, including the source of ROS, the species get involved and reactions and the parameters describe the reactions. In addition, our measured data (RNS, $O_2^{\bullet-}$, Ca^{2+} and DCFDA) are so called low-resolution data regarding quantity and quality: 1) they were measured at different time and from different cell samples; 2) they were obtained with different methods . For example, we used flow cytometry for RNS, $O_2^{\bullet-}$ and H_2O_2, but SDCM for Ca^{2+}; and 3) data quantity is low as we have at most 8 timepoints measurement for each species. These limitations make Bayesian network a good choice.

6.1.2 Parameter Estimation in Bayesian networks

We are given a network structure *G* and a set of observations $O = \{o_1, o_2, ..., o_i\}$, the task of parameter estimation is to find an estimate of parameters θ (consists of a set of

conditional probability distributions) of G, denoted as finding a $\hat{\theta}$, which maximize the possibility of observation denoted as $arg\max_{\theta} P(D = O \mid \theta)$. Here, D is the data, O is the observation, $arg\max_{\theta}$ is a mathematical expression that indicates the value of θ which causes the subsequent function to be maximized. There are several methods available for parameter estimation, including Maximum likelihood Estimation (MLE), Bayesian estimation for complete datasets and the Expectation-Maximization algorithm for incomplete datasets.

Maximum likelihood estimation (MLE)

Maximum likelihood estimation (MLE), as suggested by its name, is to maximize the probability of $\hat{\theta}$ given O. MLE is a standard method of parameter estimation given complete observation of all the variables and its algorithms is described as the following.

Step1: define likelihood functions for the observations given the model

$$f(o_1, o_2, ..., o_i) = f(o_1 \mid \theta) \times f(o_2 \mid \theta) ... \times f(o_i \mid \theta)$$

Step 2: Exchange in identity of θ and O as "variable" and "parameters". Consider the observed values $o_1, o_2, ..., o_i$ to be fixed "parameters" of this function, and θ to be the function's variable. From this point of view, this distribution function will be called the likelihood.

$$L(\theta \mid o_1, o_2, ..., o_i) = f(o_1, o_2, ..., o_i \mid \theta) = \prod_n f(o_n \mid \theta)$$

Step 3: Estimation of $\hat{\theta}$. Maximum likelihood is applied to find $\hat{\theta}$ for observations $o_1, o_2, ..., o_i$, such that the likelihood of $\hat{\theta}$ is maximized:

$$\hat{\theta} = \arg\max_{\theta} L(\theta \mid o_1, o_2, ..., o_i)$$

.

MLE has the advantages of 1) providing an adaptable methods of parameter estimation over a large variety of estimation situations; and 2) being able to generate parameters with minimum bias and narrow confidence intervals given a large sample size [294].

At the same time, the application of MLE is also restricted by the following features [294]: 1) it is often difficult to solve the estimation numerically and 2) it may produce poor estimation of models if there is not enough training data [294].

Bayesian estimation

Before introducing Bayesian estimation, we will first review several key terms including prior, posterior and Bayes' rule.

Prior

Prior probability distribution P(θ) [294, 295] is the probability distribution expressing one's initial beliefs about the values of parameter θ, before any data has been observed (observation O). Prior distributions are often uniform (equal probability for each possibility) to represent a parameter that is totally unknown at the start of the experiment.

Posterior

Posterior [296] or posterior probability distribution $P(\theta|O)$, is the conditional probability assigned to parameter θ when evidence (O) is taken into account.

Bayesian estimation

Bayesian estimation was proposed to overcome the limitation of MLE in the condition of small sample size through introducing prior distributions. Bayesian estimation assumes that the parameter θ has a distribution $P(\theta)$. If we observe data O, the posterior probability for θ is computed according to Bayes' rule:

$$P(\theta|O) = \frac{P(O|\theta)\bullet P(\theta)}{P(O)} = \frac{P(O|\theta)\bullet P(\theta)}{\int P(O|\theta)\bullet P(\theta)d\theta}.$$

Here, $P(\theta|O)$ is the posterior distribution of parameter θ in the presence of observations O; P(θ) is the prior distribution of θ; P(O) is the probability distribution of the observation; and P($O|\ \theta$) is the dependent distribution of observation O given a particular value for parameter θ.

Bayesian estimation enables people to incorporate knowledge about a particular hypothesis. In addition, quantitative computation of prior and posterior (conditional) probabilities allows people to infer conclusions in the presence of multiple alternative hypotheses, models, observations, or assumptions. One of the disadvantages of a Bayesian approach is that we may get very different posterior distributions by changing the priors of parameters [297]..

In this thesis, we use multinomial distribution [298] for data and Dirichlet prior [299] for our parameter estimation using Bayesian method.

Expectation-Maximization algorithm (EM)

The Expectation-Maximization (EM) algorithm is a statistical method to estimate parameters θ, where the model depends on unobserved variables.

In the condition of parameter estimation with missing data, we have a statistical model consisting of observed data (O), a set of unobserved data or missing data(M) , and a vector of unknown parameters (θ) , along with a likelihood function L(θ;O,M)=P(O,M|θ). The EM algorithm seeks to find the optimum estimation of θ by iteratively calculating expectation and maximization [300].

In the step of expectation, we will first calculate the expected value of log likelihood function with respect to the conditional distribution of M given O and parameter $\theta^{(t)}$ (parameter estimated in tth round) as $Q(\theta \mid \theta^{(t)}) = E_{M|O,\theta^{(t)}}(\log L(\theta; O, M))$. Noted that log likelihood function is *log(L(θ;O,M))*.

In the step of maximization, we will then find parameter θ that can maximize the expected value as $\theta^{(t+1)} = \arg\max_{\theta} Q(\theta \mid \theta^{(t)})$.

6.1.3 Structure Learning

Bayesian network structure learning, in the context of a biological pathway, is to learn the causal influence (or the interaction) relationships among various species given a set of measured quantities of the species. In another word, the task of structure learning is

to search the space of possible graphs (or structures) to find the one that can best capture the probabilistic relationships among the variables that comprise the cellular network.

The learned relationship is demonstrated as an acyclic directed graph, where the nodes represent the species and the edges represents the causal influence among the species. As introduced in dependence, each arrow in the graph points from a parent node to its child node, meaning that the parent can influence child (directly or indirectly). One child can have multiple parents.

Bayesian network has been regarded as an optimal tool in structure learning according to the following aspects: 1) Bayesian network is capable of reconstructing the network with incomplete data [301]; and 2) Bayesian networks and its related statistical methods can avoid over-fitting to the training data during learning process [302]. Over-fitting refers to the condition that the model describes measurement noise instead of the underlying relationship.

The structures are typically learned through combing a search method, an exhaustive or heuristic search procedure over possible network structures, with a scoring method (e.g. Bayesian score) to find the optimal modelling network [303].

Bayesian Score (BS)

Bayesian Score (BS) is a scoring method used in Structure learning to evaluate each structure. BS is calculated for each structure as an indication of the fitness between the structure *M* and observation *O* as:

$BS(M,O) = P(O \mid M)P(M)$ or

$$BS(M,O) = \log(P(O \mid M)) + \log(P(M))$$

P(M) represents the *prior* probability distribution over the model *M*; *P(O)* represents data distribution; *P*(*O*|*M*) is the marginal likelihood of observation *O* given model *M*.

Exhaustive search

A naive idea to search for the best structure is to explore the whole sample space which includes all the possible parent-child networks. Given the number of variables *n*, the size of sample space (number of directed acyclic graphs) is *s(n)*, which is determined according to the formula $s(n) = \sum_{i=1}^{n} (-1)^{i+1} \binom{n}{i} 2^{i(i-1)} s(n-1) = n^{2^{O(n)}}$ [304]:

Table 6.1 illustrates how the number of possible networks *s(n)* increases with respect to the number of variables *n*. The large sample size makes it impossible to take exhaustive search for a big variable number *n*.

Table 6.1 Sample size of network according to the number of variables

Variable(*n*)	1	2	3	4	5	6	7	8
sample size(*s(n)*)	1	3	25	543	29,281	3,781,503	1.10E+09	7.80E+11

Heuristic search

In structure learning, an alternative to exhaustive search is heuristic search, which searches the sample space through experience. For example, one would expect to find high-scoring graphs in the vicinity of where you already found some high-scoring graphs. This is one of most popular heuristics called “locality”. Heuristic search usually gets better scoring answers more quickly than exhaustive search. A lot of heuristic

algorithms have been discussed, including *Markov Chain Monte-Carlo (MCMC)*, *K2*, *Hill-climbing*. In this thesis, we learn the causality between intracellular signals (e.g. Ca, NO, H_2O_2) based on observed levels of these signals, for different durations of LY30 treatment using a *MCMC* algorithm called *Metropolis–Hastings* algorithm [305, 306].

6.1.4 Inference

Inference, also called model evaluation, is the process of evaluating the probabilities of missing values of the hidden species *H* (the variables that we didn't measured) based upon the causality dependence in the model *G* and the observed variables, *O* (which have been measured). Inference is to answer the question like what the probabilities of missing values *H* is, given the observation (*O*) and Model (*M*). The task can be formulized as $P(H \mid O, M)$. For a predefined structure and a set of data, parameter estimation will generate a unique set of CPT, which can be easily computed using the chain rule [307].

We take a simple pathway (Figure 6.1.2) as the example to demonstrate inference. This pathway consists of a stimulant (ST) and a signal (SI) which are connected through an arrow from ST to SI. ST has "present" and "not present" two states and SI has "high", "low" and "medium" three states. The concentration of SI is determined by SI according to the parameters (CPT on the right panel of figure). In this network, inference can be applied to answer question regarding the probability of any species at any state given the state of the other species. For example, what is the probability of ST is *present* given SI is *high*? To infer the probability of *ST=present*, we can calculate the

posterior probability of ST given SI according to:

$$P(ST = present \mid SI = high) = \frac{P(SI = high \mid ST = present)P(ST = present)}{p(SI = high)}.$$

Noted that $P(SI = high) = \sum_{st} P(SI = high \mid st)P(st)$.

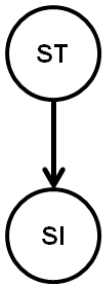

SI: p(signal/stimulant)			
	high	medium	low
present	0.6	0.2	0.1
not present	0.3	0.3	0.6

Figure 6.1.2. A simple example to demonstrate inference in Bayesian network. In the example, ST represents the stimulant which has present and not present two states and SI represents the signal with low, medium and high three states. Inferred probabilities of ST given SI are demonstrated in the table.

6.1.5 Our application of Bayesian Network

We applied Bayesian network(BN) strategies including structure leaning(6.1.3), parameter estimation(6.1.2) and inference (6.1.4) to reconstruct and describe the underlying pathway of LY30-induced ROS production (measured by DCFDA) and cell sensitization (measured by cell viability).

Our Bayesian network learning of LY30 pathway is conducted in Bayes Net Toolbox(BNT) developed by Kevin P.Murphy [308] using measured kinetic data of RNS, $O_2^{\bullet -}$, Ca^{2+} and DCFDA (H_2O_2, $ONOO^-$). Before modelling the pathway, we firstly pre-processed the data through normalization and discretization. Then, we conducted the model structure of the causality dependence among the nodes through a

MCMC algorithm called *Metropolis–Hastings* [305, 306]. After structure learning, we estimated parameters for the models to specify the quantitative dependence among the species through Expectation-Maximization (EM) algorithm.

6. 2 Model learning for a Bayesian network with measured data

6.2.1 Data Preprocessing

Measured $[Ca^{2+}]_c$ (Fluo-4am), RNS(DAF), $O_2^{\bullet-}$**(**DHE**)**, ROS(DCFDA), were processed with normalization and discretization before structure learning.

Normalization

We normalized the concentration of each species by normlize the measured concentration of treated sample to that of untreated sample after subtracting background noise according to the formula: $C^i_{normalized} = \frac{f_m^i - f_m^{un\_ctl}}{f_m^{ctl} - f_m^{un\_ctl}}$. Noted that f_m^i is the *measured* fluorescence intensity of sample *i* after certain treatment; f_m^{un-ctl} is the *measured* fluorescence intensity of *unstained* and *untreated* control, which represents background noise; f_m^{ctl} is the *measured* fluorescence intensity in *untreated* control, which represents base level; and $C^i_{normalized}$ is the normalized concentration. Normalized results for $[Ca^{2+}]_c$, [RNS], $[O_2^{\bullet-}]$ and [DCFDA] were shown in Figure 6.2.1.

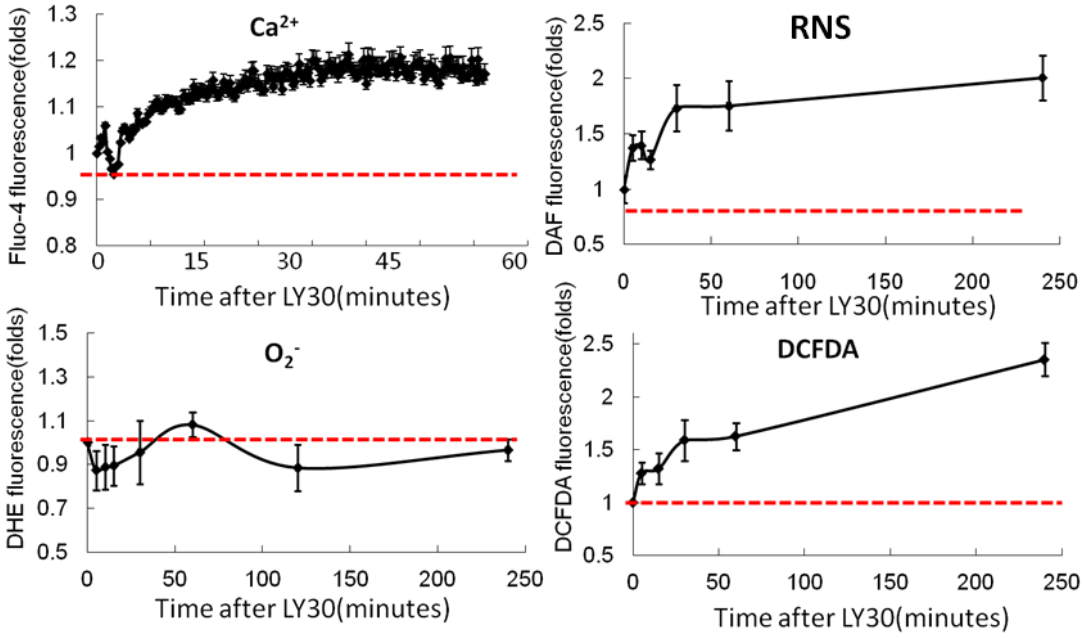

Figure 6.2.1. Normalized experimental data of Fluo-4, DAF, DHE and DCFDA obtained from HeLa after LY30 treatment. For each panel, x-axis represents incubation time after LY30, y-axis represents fold change of fluorescence intensity of each measured fluorescence according to untreated control.

Discretization

All the data were discretized into three levels with equal interval, low, medium, and high concentrations. The method of equal interval into three levels has been reported in many previous researches on cellular signaling [288]. As the input of the network, LY30 is discretized into three levels according to its incubation time, corresponding to the condition of "no LY30 treatment" (treatment period=0), "brief LY39 treatment" (5 minutes~30 minutes) and "long LY30 treatment" (30 minutes~ 240 minutes) (Figure 6.2.2).

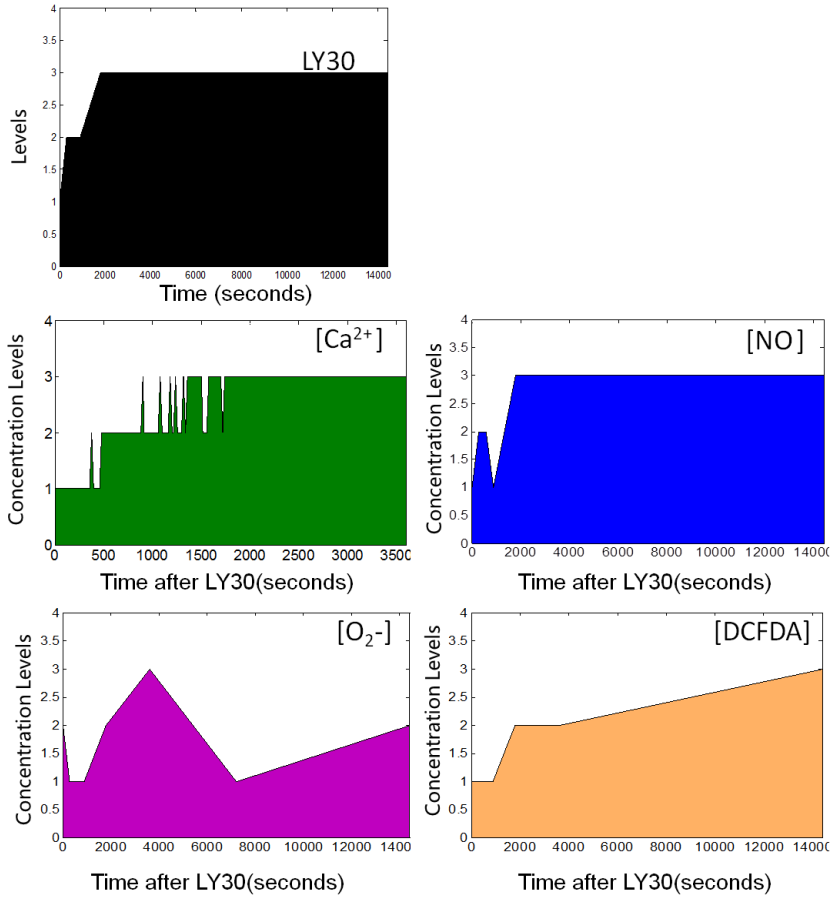

Figure 6.2.2. Processed data using discretization on Fluo-4, DAF, DHE, DCFDA and incubation time of LY30

6.2.2 Model learning

We utilized Bayesian networks to represent possible networks of causality downstream of LY30 and upstream of DCFDA. The node for LY30 was constrained to be the causal "root" of the tree, upstream of all other variable nodes. The node for DCFDA was constrained to be the downstream output of the system, upstream of nothing. We selected three additional variables— $O_2^{\bullet -}$, RNS and Ca^{2+} — to be additional variable nodes in network, and we required the values of these variable nodes to be discretized into 3 states representing low, medium, and high levels of the species. The LY30

variable was divided into three possible values representing the duration of treatment: untreated, brief, and long incubation times (see 6.2.1). Not knowing the cause/effect relationships of $O_2^{\bullet -}$, RNS and Ca^{2+} towards each other or toward DCFDA, we did not impose any constraints on the placement or relative connectivity of the $O_2^{\bullet -}$, RNS and Ca^{2+} nodes in the network (including dead-ends with no impact on DCFDA). Instead, we used a computational strategy to search among the 12,800 possible combinations of directed edges for the whole network, using the Bayesian Network Toolbox (BNT) [156, 157]. The resulting process will identify network configurations that agree with experimental observations.

The Metropolis-Hastings (MH) algorithm was chosen for generating and testing possible network structures, and the Bayesian score (refer to section 6.1.3) [309] was used for evaluating the agreement of each network structure with the training dataset. We took the 12 network structures with highest Bayesian scores to be our candidate models (Figure 6.2.5). For each candidate model, contingency table parameters were estimated using the Expectation-Maximization algorithm (EM, refer to section 6.1.2).

6.2.2.1 Use of Metropolis-Hastings (MH) to explore the sample space

A key process in MH is the tuning phase which consists of a number of loops in order to achieve a "satisfying" distribution. An evaluation of the efficiency of MH sampling is through acceptance ratio [310]. A high acceptance ratio suggests that most new samples occur right around the current data point while a low acceptance rate means that most of searched samples are often rejected. Therefore, an efficient MH sampler should have an acceptance neither too high nor too low. It has been proved that the optimal acceptance probability for the Markov chain should be around 0.45 [311].

To demonstrate the convergence of MH sampling, the acceptance ratio according to rounds of sampling is plotted in Figure 6.2.3a (denoted as "number of rounds"). Acceptance ratio converges to 0.45 after 100 rounds of sampling, suggesting that the algorithm can efficiently explore the sample space.

Posteriors of the selected models with *BS>threshold* were plotted in Figure 6.2.3b. Among the selected models, certain models demonstrated higher posteriors than the rest, meaning that the models may better represent the LY30-induced signalling pathway.

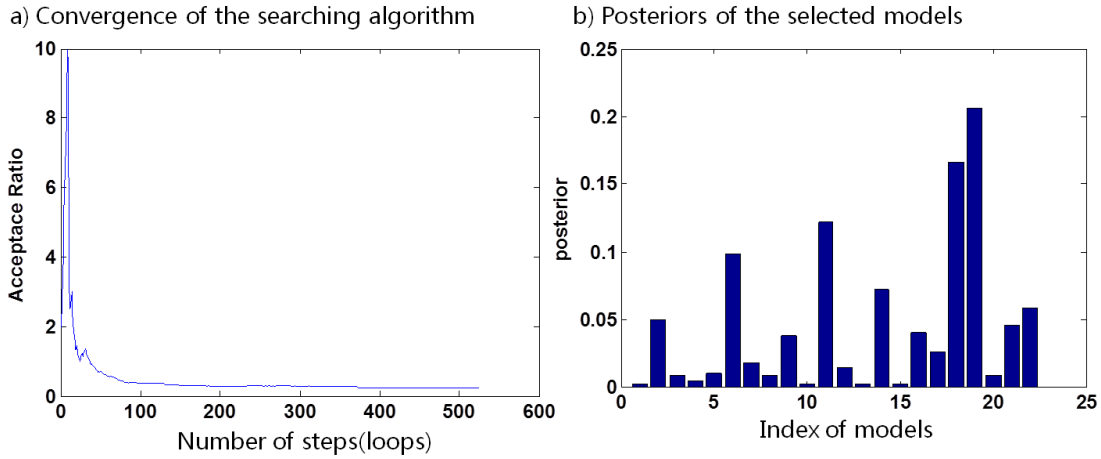

Figure 6.2.3 Demonstration of the efficiency of Metropolis-Hastings algorithm in structure learning. a) Convergence of the algorithm in finding new models. X-axis is number of loops in sample searching; y-axis is the acceptance ratio. b) Posterior of selected models during one round. X-axis is the model index and y-axis is the posterior of each selected model. The posterior of a model structure is calculated through counting the frequency of the model among all the selected models.

6.2.2.2 Model selection after repeated MCMC

Residual effect is a common limitation of MCMC approach [312]. In order to avoid residual effect, we repeated the searching process for large number rounds each of

which started with random starting points. After 10,000 rounds of MCMC, 375 model structures were selected as "high scoring models" according to evaluated BSs.

Topology analysis

Topology analysis was conducted through counting the total number of all the directed edges from any other nodes to DCFDA, e.g. RNS to DCFDA, $[Ca^{2+}]_c$ to DCFDA (later, we will use Ca^{2+} for short) and $O_2^{\bullet-}$ to DCFDA among the 375 "high scoring models". The total in-degree of DCFDA over all the selected models are presented in Figure 6.2.4. From the figure, we observed most links from NO to DCFDA, lowest links from $O_2^{\bullet-}$ to DCFDA.

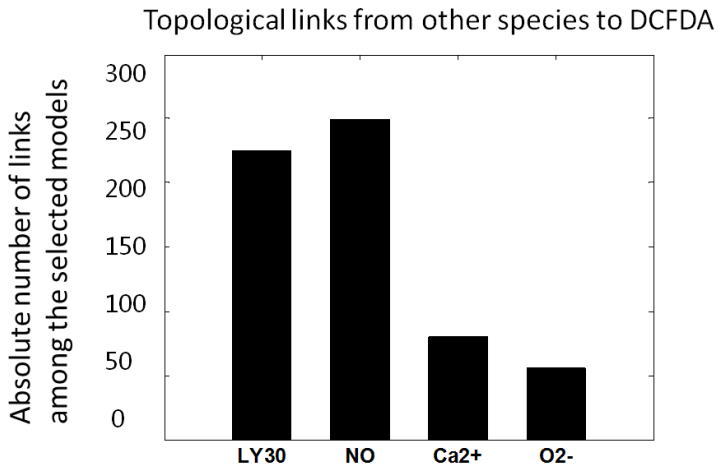

Figure 6.2.4. Topological information about sources of DCFDA. Each bar in the figure represents counted number of arrows from the node (specified by x-axis) to DCFDA node according to all the "high scoring" models.

6.2.3 Inferences from the models

To represent the consensus of the selected models, we calculated the marginal of DCFDA from the top 12 models (Figure 6.2.5). All the parameters of the top models are evaluated through Expectation Maximum algorithm.

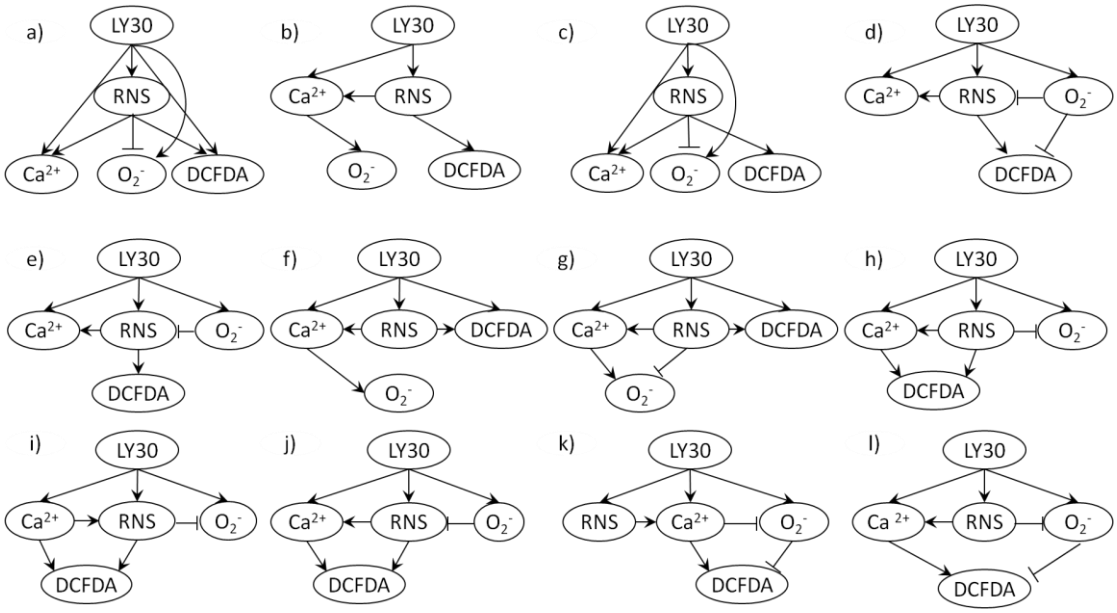

Figure 6.2.5 Structures of the top 12 models selected through model learning

6.2.3.1 Model inference with LY30 treatment

For the 12 top-scoring candidate networks, we simulated the probabilities for the RNS, Ca^{2+}, $O_2^{\bullet -}$ and DCFDA variables, under 3 conditions: no LY30 treatment, brief LY30 incubation, and long LY30 incubation. The averages of these probabilities were taken as our consensus, and plotted in Figure 6.2.6. For example, the Figure 6.2.6 simulations show 100% probability that RNS levels would be low after no LY30 treatment, 28% probability RNS would be low and 72% probability that RNS would be medium with brief LY30 incubation, and over 90% probability that RNS would be high with long LY30 incubation. The simulated consensus probabilities for the levels of RNS, Ca^{2+}, $O_2^{\bullet -}$ and DCFDA in Figure 6.2.6 are consistent, at low resolution, with the experimental observations in Figure 6.2.2. For example, simulation showed RNS will be at high probability in low, medium and high concentrations upon no LY30, brief LY30 and long LY30 treatment while RNS showed low, medium and high

concentration under corresponding treatments. This consistency indicates that our modelling has "learned" [313] the information in the training dataset, but it does not indicate whether the Bayesian modelling has predictive ability beyond the training set it was given, nor whether the causal linkages are correct.

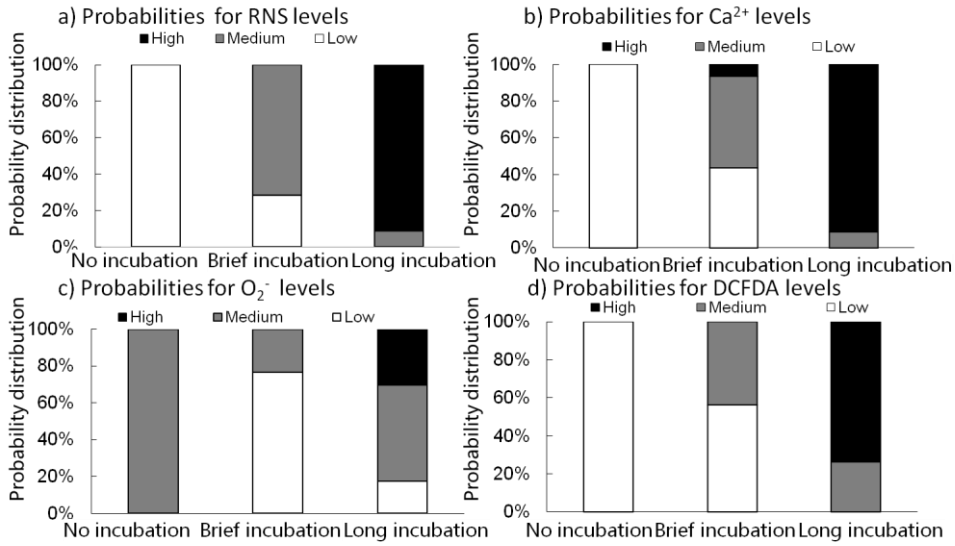

Figure 6.2.6 Inferences generated from the Top-scored models according to no LY30 incubation, brief LY30 incubation and long LY30 incubation three situations. a) probability of NO at low, medium and high concentrations with different treatments of LY30; b) probability of Ca^{2+} at low, medium and high concentrations in three concentrations of LY30;c) probability of $O_2^{\bullet-}$ at low, medium and high concentrations in three concentrations of LY30; d) probability of H_2O_2 at low, medium and high concentrations in three concentrations of LY30.

6.2.4.2 Model inference of DCFDA with combination treatment of LY30 and dummy inhibitors

Next we predicted the causal contribution (not the correlation) of each intermediate variable ($O_2^{\bullet-}$, RNS and Ca2+) toward DCFDA fluorescence, by simulating the levels of DCFDA in the 12 top-scoring models after virtual experiments inhibiting each variable individually (blocking RNS, chelating Ca^{2+}, scavenging $O_2^{\bullet-}$, or media). For the three possible LY30 treatment durations (no treatment, brief incubation, and long

incubation), we simulated the probability of low, medium or high DCFDA levels, yielding a total of (4 scavengers)*(3 incubation times) * (3 levels of DCFDA) = 36 probabilities. Figure 6.2.7a illustrates how the Bayesian network probability distributions can be interpreted as pie charts. Figures 6.2.7b-d shows the averaged inferences for all 12 (*4 scavengers*3 incubation times*) probabilities.

The most significant inference from these probability distributions is that RNS blockage would cause the "high DCFDA" state to decrease from 75% to 12% probable (dark blue versus light blue bars in the "long incubation" row of Figure 6.2.7 d). In other words, the modelling predicted that scavenging RNS would show a strong inhibitory effect on the DCFDA signal, particularly for LY30 treatments >30 minutes. Note that in 10 of the 12 top-scoring models, RNS was a direct, positive mediator from LY30 to DCFDA, explaining the importance of RNS in the averaged inferences.

Another inference from the simulations was that Ca^{2+} chelation would cause the "medium DCFDA" state to decrease from 45% to 37% under brief LY30 treatments. Finally, $O_2^{\bullet -}$ was predicted to have no significant effect on DCFDA, but interestingly, this inference was not based on DCFDA being independent of $O_2^{\bullet -}$. Observe that 9 of the top 12 modes predicted antagonism between RNS and $O_2^{\bullet -}$ (with uncertainty about whether the antagonism was from RNS to $O_2^{\bullet -}$ or vice versa), and 4 of those 9 models predicted that the RNS-$O_2^{\bullet -}$ antagonism would be upstream of DCFDA. In sum, the modelling predicts $O_2^{\bullet -}$ to have an antagonistic relationship with NO, but little impact on DCFDA.

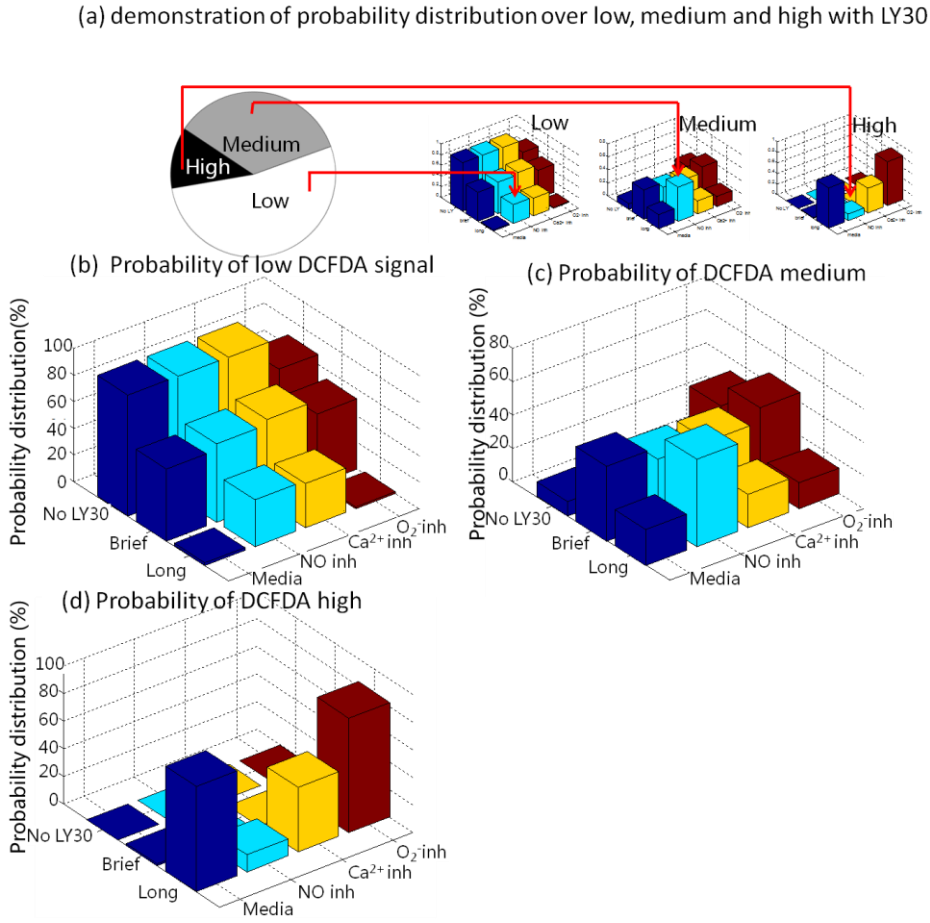

Figure 6.2.7. The predicted intensities of DCFDA, expressed as conditional probabilities from the Bayesian networks. a) An example of how to read tabulated probabilities is demonstrated by comparing with a familiar pie chart. The conditional probabilities for each context will always sum to 100%. The probability that DCFDA signal intensity will be (b) low, (c) medium and (d) high, was predicted by simulating the 12 top models (Figure 2) and averaging the results. Each predicted probability (vertical axis) corresponded to a combination of LY30 treatment duration (untreated, brief, and long) and inhibitor treatment (Control media, RNS inhibitor, Ca^{2+} inhibitor, or $O_2^{\bullet-}$ inhibitor) along the horizontal axes.

For each dummy inhibitor, we selected the model which shows most differences of the combination treatment (LY30 plus the inhibitor) compared to LY30 treatment alone. The model selected for the inhibitor is called "typical model" and the inferred probability distribution of DCFDA from the typical model is called "typical result". We plotted the typical results in Figure 6.2.7.

Compared the combination treatment of NO inhibitor and LY30 with LY30 alone, the probabilities of DCFDA at low concentration are elevated with short LY30 incubation (about 20%) and long incubation (60%). The probabilities of DCFDA at medium concentration dropped with short LY30 incubation (about 20%) and increased with long LY30 incubation (about 15%). The probabilities of DCFDA at high concentration dropped to zero with long LY30 incubation. Such a typical phenomenon is observed in 10 models out of 12.

Compared the combination treatment of Ca^{2+} inhibitor and LY30 with LY30 alone, the probability of DCFDA at low concentration is elevated with short LY30 treatment (about 40%), but the probability is not change with long LY30 treatment. The probability of DCFDA at medium concentration is dropped with short LY30 incubation (about 40%, which is the same amount of probability increased at low concentration). With long LY30 treatment, the probability of DCFDA to be high is dropped about 60% with same amount of probability increase in DCFDA to be medium concentration. Such a typical phenomenon for $[Ca^{2+}]_c$ inhibitor is observed in 10 models out of 12.

Compared between the combination treatment of $O_2^{\bullet-}$ inhibitor and LY30 and LY30 treatment alone, there is little change of probability distribution of DCFDA among all the 12 models.

Given the observations, we speculated that LY30-induced DCFDA signal in HeLa may arise as the following (Figure 6.2.8b):

1) RNS (NO) inhibition can greatly inhibit DCFDA fluorescence. DCFDA is known to detect various ROS species, among which two main species are H_2O_2 and $ONOO^-$. NO

is reported to produce $ONOO^-$ through reacting with H_2O_2 or $O_2^{\bullet-}$ [232, 272, 314], meaning increased NO induces increased $ONOO^-$ while decreasing H_2O_2 and $O_2^{\bullet-}$. In this case, testing experiments of NO effect can be carried out through either NO inhibition or direct inhibition of $ONOO^-$.

2) Inhibition of Ca^{2+} slightly decreases DCFDA. Ca^{2+} has been reported to increase H_2O_2 through NOX activation [250]. To test the influence of Ca^{2+} on DCFDA, experiments were carried out through inhibiting Ca2+ or inhibiting NOX.

3) Inhibition of $O_2^{\bullet-}$ may exert little influence on DCFDA signal.

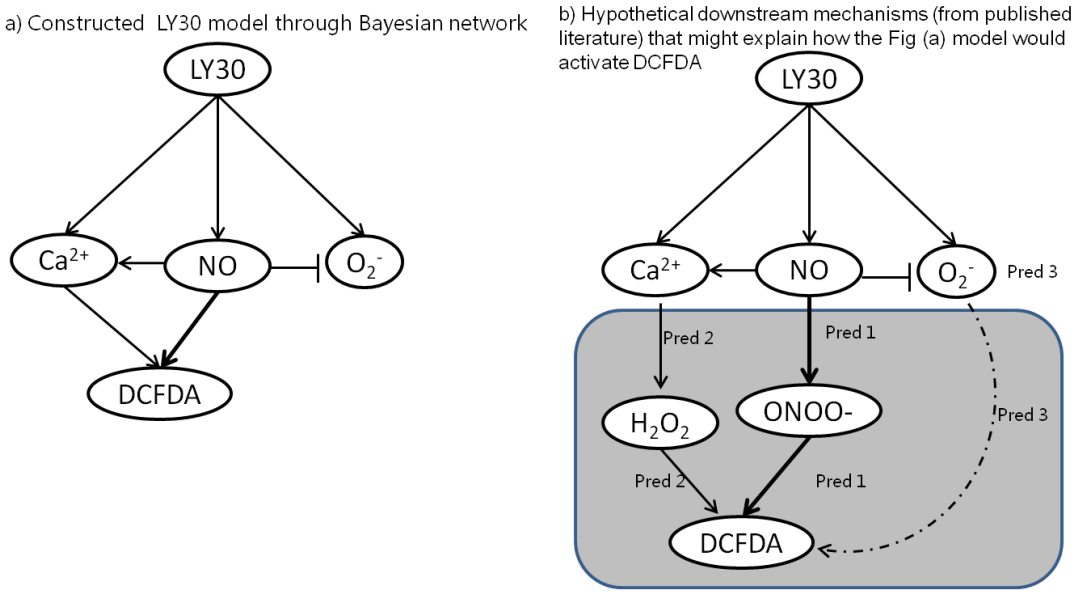

Figure 6.2.8 Predicted pathway of DCFDA signal under LY30 treatment. a) Constructed LY30 model through structure learning. In the network, LY30 can directly induce Ca^{2+}, NO and $O_2^{\bullet-}$. NO negatively affect $O_2^{\bullet-}$ and positively affect Ca^{2+}. Both $O_2^{\bullet-}$ and Ca^{2+} up-regulate DCFDA level. b) Hypothesized downstream mechanism of LY30 on DCFDA activation in a) with pulished biological knowledge. Solid arrow represents the connection that is supported by the models. Thickness of the line indicates the strength of support from the models. Dashed arrows means the connection is not well supported by the models.

6.3 Testing model predictions experimentally

Experimental tests to determine the causal contributions of RNS, Ca^{2+} and $O_2^{\bullet-}$ to LY30-induced DCFDA were conducted using FeTPPS to scavenge $ONOO^-$, EGTA-am to chelate Ca^{2+}, and Tiron to scavenge $O_2^{\bullet-}$.

6.3.1 Pre-incubating FeTPPS confirmed the hypothesis of late $ONOO^-$

To test the hypothesis of NO induces DCFDA through $ONOO^-$ by LY30, we pre-treated HeLa cells with FeTPPS (50uM) for one hour before administration of LY30 (25uM). As we can see from Figure 6.3.1, LY30 consistently raised DCFDA fluorescence intensity in HeLa cells, and pre-treatment of FeTPPS can greatly decreased DCFDA fluorescence and the significant decrease happen at 60 minutes and 180 minutes (from 2 folds to 1.3 folds with 60 minutes treatment of LY30; from 2.5 folds to 1.1 folds with 180 minutes treatment of LY30). The experiment results suggested that long incubation of LY30 produces a lot of $ONOO^-$ in HeLa and $ONOO^-$ being produced is the major species that oxidize DCFDA.

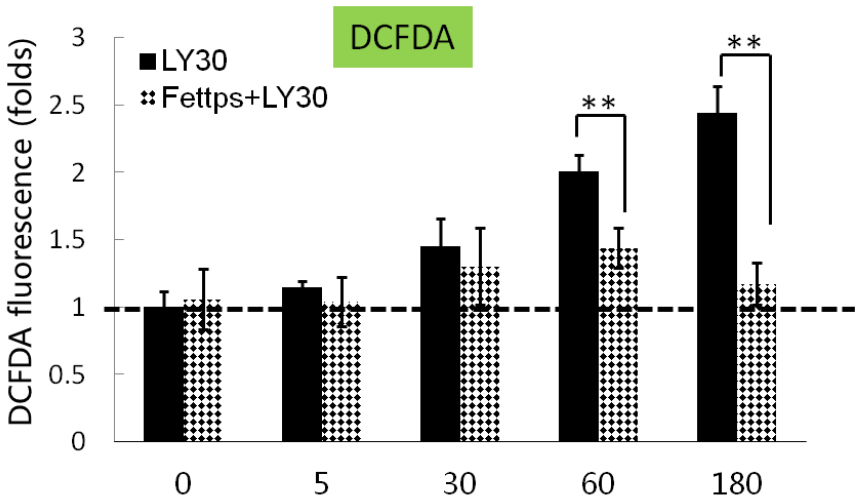

Figure 6.3.1. Inhibitory effect of FETPPS on LY30-induced DCFDA signal. HeLa cells are treated with for 5 mins, 30 minis, 60 mins and 180 mins. To see the inhibitory effect, cells are pre-incubated with FEPTTS(100uM) for 1 hour.** means p-value<0.01

6.3.2 L-NAME experiments were inconclusive

In order to further confirm the involvement of NO, we carried out experiment with L-NAME which is a known Nitric Oxide Synthase Inhibitor. Our measured result shown in figure 6.3.2, however, failed to reflect inhibitory effect of L-NAME in either DAF fluorescence or DCFDA fluorescence. Further effect is incapable of demonstrating the inhibitory effect of L-NAME with optimizing dose and incubation time. Previous work reported several cases that L-NAME is unable to inhibit NO increases [315, 316] related with different NOS isoforms.

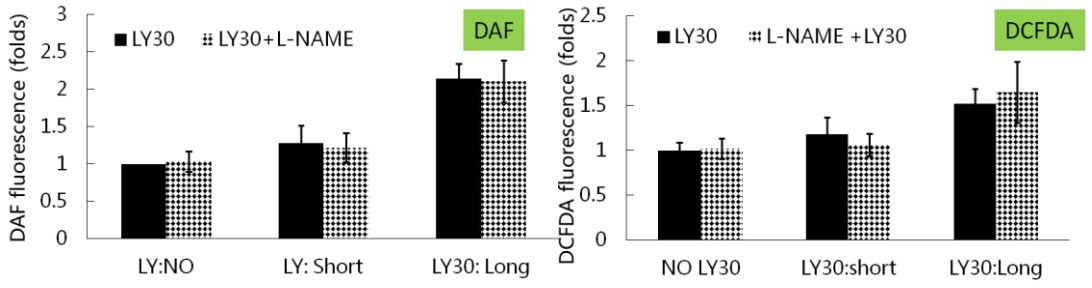

Figure 6.3.2. No inhibitory effect of L-NAME on either DAF or DCFDA. a) Averaged DAF signal with LY30 treatment, L-NAME treatment or both. b) Averaged DCFDA signal with LY30, L-NAME or both.

6.3.3 EGTA-am, as a Ca^{2+} chelator, is able to block the early LY30-induced increase in DCFDA fluorescence

We firstly tested the efficiencies of EGTA-am on chelating Ca^{2+}. Experiments were carried out to compare the Fluo-4 fluorescence between cells with combination treatment of LY30 (25uM) plus EGTA-am (50uM). EGTA-am was administrated into

cells 15 minutes prior to LY30 treatment and cells with LY30 alone. Cells with EGTA-am pre-treatment showed a reduction from 2 folds to 1.25 folds with short LY30 treatment; and a reduction from 2.5 folds to 1.3 folds with long incubation of LY30 (Figure 6.3.3a). Similar effect was confirmed with microplate reader (Figure 6.3.3a). The experimental results demonstrated that EGTA-am is able to diminish LY30 induced Fluo-4 increase in HeLa, suggesting EGTA-am in our system has high efficiency on chelating Ca^{2+}.

To test the effect of Ca^{2+} on ROS, we then measured DCFDA fluorescence in HeLa cells by pre-treating the cells with EGTA-am. As shown in the figure 6.3.3c, EGTA-am is able to significantly reduce the increased DCFDA fluorescence with short LY30 treatment (reduced from 1.5 folds to 1.2 folds), and such decrease is not observed in long period.

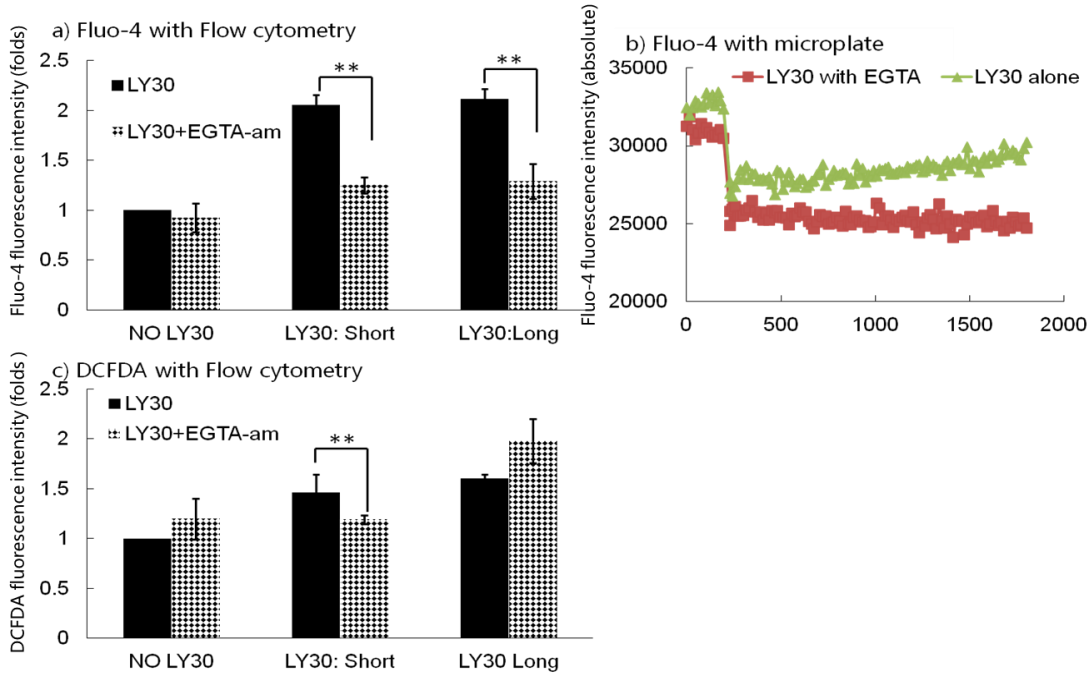

Figure 6.3.3 Inhibitory effect of EGTA-am on Fluo-4 and DCFDA. a) Fluorescence intensity of FLUO-4 with LY30 and EGTA-am treatments using flow cytometry. b) Fluorescence intensity of FLUO-4 with LY30 and EGTA-am treatments using microplate reader. c) DCFDA signal with LY30 and EGTA-am or both.

6.3.3.1 NOX experiments suggests that Ca^{2+} can increase DCFDA fluorescence through NOX-5 mediated H_2O_2 production

Ca^{2+} has been reported to induce H_2O_2 production through (NADPH) oxidase (NOX). Among the 5 NOX members, NOX5 has been identified as a unique homolog of directly Ca^{2+} sensitive and direct H_2O_2 production [280].

In order to test the involvement of NOX, we measured general NOX activity. In the first step, NOX activity is measured and compared in untreated cells, LY30-treated 5 minutes cells and LY30 treated 0 minutes cells. As shown in figure 6.3.4a, slope of each line reflects intracellular NOX activity. Higher slope meaning higher NOX activity and vice versa. We observed significant increase of NOX activity in the LY30 treated sample to untreated sample. Furthermore, the increase of NOX activity gets bigger with longer treatment of LY30.

In the second experiment, we tested whether NOX activation is Ca^{2+} dependent through pre-treating cells with Ca^{2+} inhibitor EGTA-am. Measurement is carried in untreated cells, cells treated with LY30 for 30 minutes and cells treated with LY30 for 30 minutes in the presence of EGTA-am. The experiment showed a reduction of the slop of the line corresponding to LY30 plus EGTA-am treatment compared with the line corresponding to LY30 treatment alone (Figure 6.3.4 b).

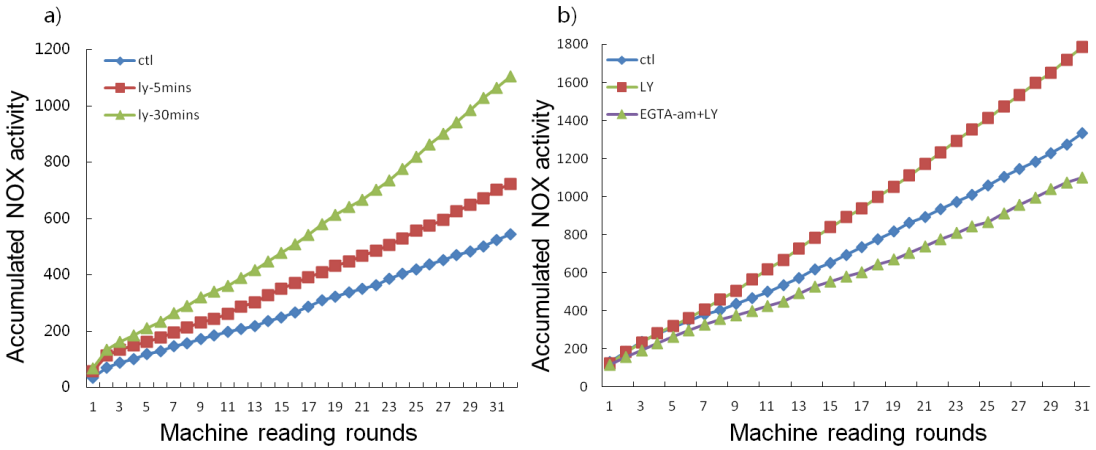

Figure 6.3.4 Measurements of NOX activity and inhibitory effect of EGTA-am on NOX activity. a) NOX activity measured in cell samples with no treatment, LY30 treatment for 15 minutes and LY30 treatment for 30 minutes. B) NOX activity measured in cell samples with no treatment, LY30 treatment for 30 minutes and LY30 treatment for 30 minutes with EGTA-am pre-incubation. Cells are preincubated with EGTA-am(25uM) for 15 minutes before adding LY30(25uM).

To exploit the involvement of NOX in the increase of DCFDA intensity, we measured the change of DCFDA fluorescence with LY30 treatment in NOX5 knock-out HeLa cells. Through comparing the DCFDA fluorescence in HeLa with NOX5 knock out (si-NOX5) and HeLa without NOX5 knock out (negative silence control, si-neg), we observed a distinctive reduction of DCFDA fluorescence in si-NOX5 knock down cells compared to the DCFDA fluorescence in s-neg sample with short LY30 incubation (0.9 folds verse 1.5 folds). We did not observe any change of DCFDFA fluorescence with long LY30 treatment in si-NOX5 cell sample to si-neg cell sample (Figure 6.3.5a).

To test whether NOX5 is involved in LY30 induced Ca^{2+} release, we measured the Fluo-4 fluorescence in HeLa cells with/without si-NOX5. Results (Figure 6.3.5b) showed little difference of Fluo-4 fluorescence by LY30 between si-NOX5cell sample and si-neg cell sample.

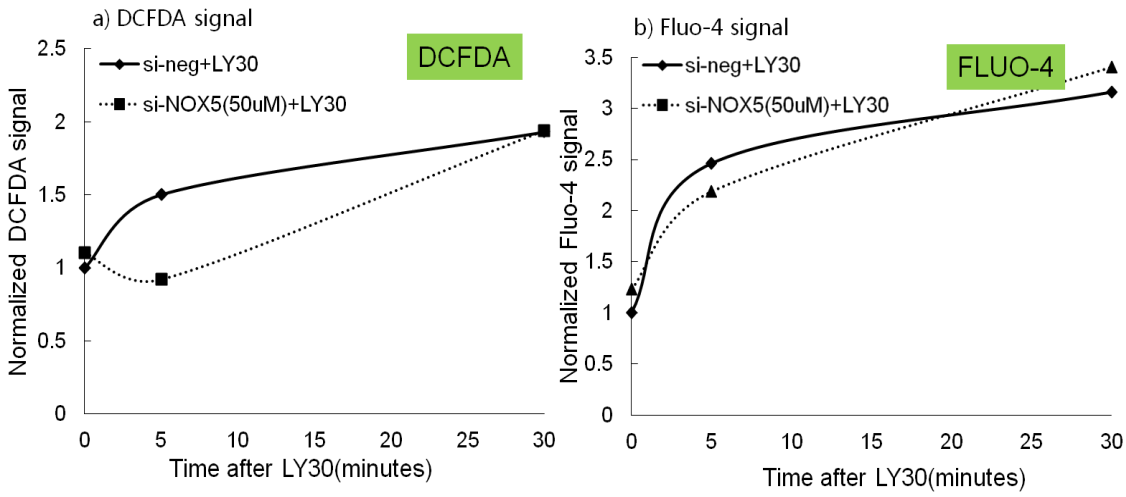

Figure 6.3.5 Involvement of NOX in LY30 induced DCFDA signal and not in FLUO-4 signal. a) DCFDA fluorescence measurement with LY30 with/without NOX-5 knock-out; b) Fluo-4 measurement with LY30 with/without NOX-5 knock out.

6.3.4 Inhibition of O2•– by Tiron is also able to reduce DCFDA fluorescence level

BN models predict that $O_2^{\bullet-}$ has little influence on DCFDA (as shown in Figure 6.2.9). In order to test the hypothesis, we conducted DCFDA measurement with administration of $O_2^{\bullet-}$ inhibitor Tiron together with LY30. Results showed that Tiron significantly reduced DHE signal with 2 hour incubation of LY30 (Figure 6.3.6 a), confirming that Tiron is able to scavenge superoxide. We omitted DHE measurement with shorter LY30 treatment since we are not able to observe significant increase. Figure 6.3.6 b) showed Tiron also abolish DCFDA increase significantly with both short LY30 treatment and long LY30 treatment. No additional DCFDA increase is observed with LY30 from short incubation to long incubation in the presence of Tiron. The experiment results were inconsistent with model prediction that inhibition of $O_2^{\bullet-}$ with Tiron would have little effect on DCFDA fluorescence.

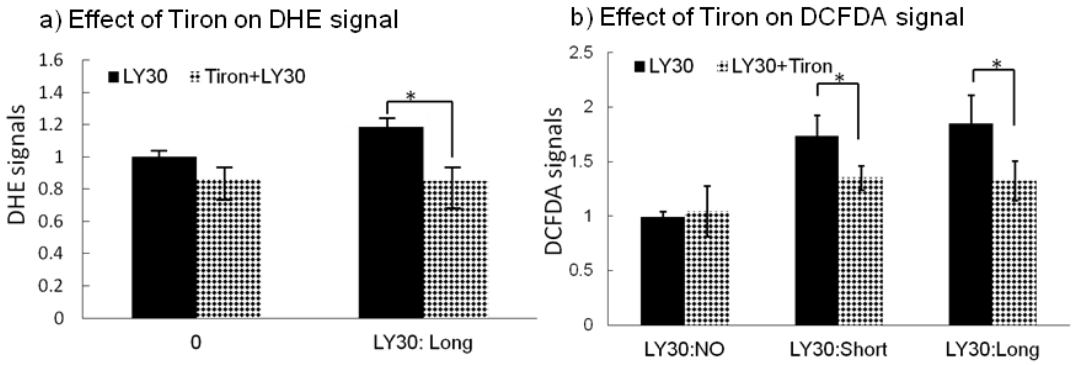

Figure 6.3.6 Measurements of LY30-induced DHE and LY30-induced DCFDA in the presence of Tiron. a) Normalized DHE signal with LY30 (25uM) treatment with/without Tiron (10mM). Tiron is applied to cell 1 hour before adding LY30. DCFDA fluorescence after 2 hours treatment of LY30 is measured as long. b) Normalized DCFDA signal with similar dose of LY30 (25uM) with/without Tiron. Short refers to averaged results from 5 minutes to 30 minutes and long referes to averaged result after 30 minutes.

6.3.5 DDC is able to reduce LY30-induced DCFDA fluorescence

Besides the selected inhibitors/scavengers above, we also conducted measurements of DCFDA with DDC, which is a common inhibitor of MnSOD. Therefore, DDC can decrease intracellular H_2O_2 and increase intracellular $O_2^{\bullet-}$ through inhibiting conversion from $O_2^{\bullet-}$ and H_2O_2. Since NO is known to interact with $O_2^{\bullet-}$ rapidly ($6.7\times10^9\ M^{-1}Sec^{-1}$) [317] and there is significant production of NO, we would expect to see that after adding DDC, there is more significant $ONOO^-$ production during late period. H_2O_2 being produced though Calcium-dependent NOX5 would not be affected in the early period.

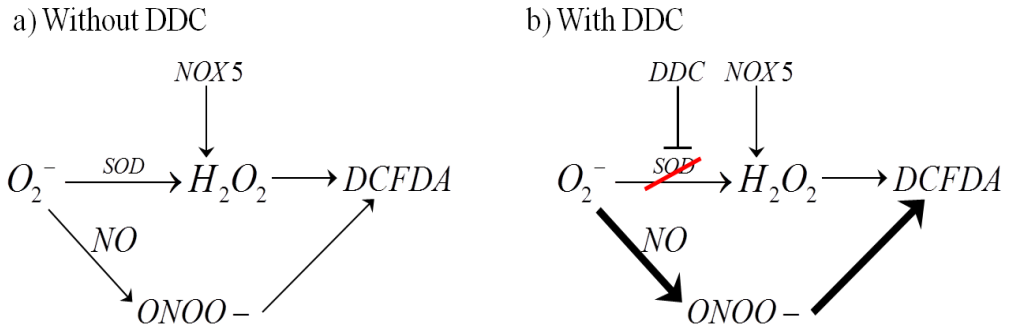

Figure 6.3.8. Hypothesized pathway diagrams from O2•– to DCFDA with/without DDC. a) Increased O2•– leads to increased DCFDA signal through either H2O2 or ONOO-. NOX 5 can directly contribute to H2O2 and DCFDA fluorescence. b) In the prescence of DDC, conversion from O2•– to H2O2 is blocked and there is more production of ONOO-, which leads to more DCFDA increase. Thicker arrow represents stronger conversion.

In order to test the hypothesis, DCFDA fluorescence measurement is carried out in HeLa with LY30 in the presence/absence of DDC. As we can see from Figure 6.3.9a, the increasing slope from 0 minutes to 5 minutes is similar in HeLa cells with LY30 alone or combination treatment of LY30 and DDC. This phenomenon supports previous results that NOX5 contributes to initial increase of DCFDA through H_2O_2 production. However, DDC fails to induce further increase of $ONOO^-$ measured by DCFDA with long incubation of LY30 late DCFDA fluorescence. On the contrary, DDC seems to decreases its level at late period. For demonstration, we conducted more repeats of DCFDA measurement in HeLa with DDC treatment. Pooled results s(Figure 6.3.9b) demonstrated significant decrease of DCFDA signal with DDC at later period, less inhibitory effect is also observed during early period.

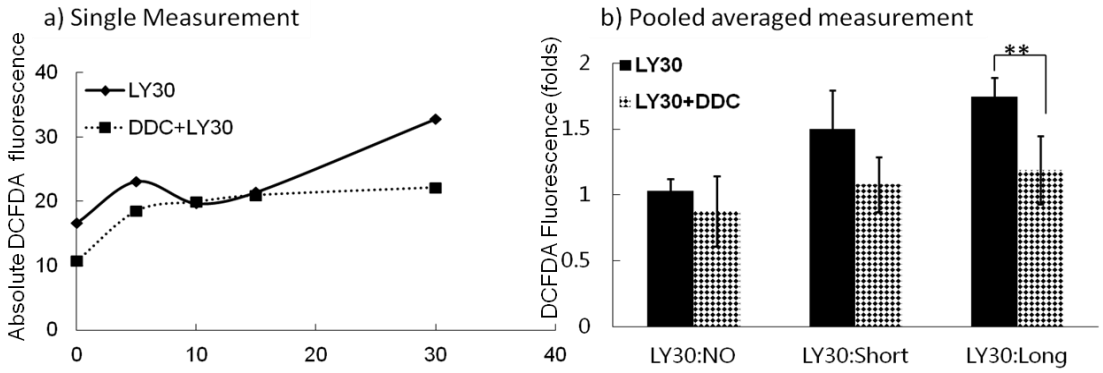

Figure 6.3.8 Measurement of influence of DDC on DCFDA fluorescence induced by LY30. a) One set of comparison experiment between HeLa with LY30 treated alone and combination treatment of DDC together with LY30. Cell are pre-treated with DDC (200uM) for 2 hours before adding LY30.b) pooled average results of DCFDA between LY30 alone and combination treatment.

To investigate the cause of the mismatch between hypothesis and results, we conducted experiment to measure the two upstream of $ONOO^-$, intracellular NO and $O_2^{\bullet-}$ in the presence of DDC. Result showed that DDC increase $O_2^{\bullet-}$ distinctively in the presence of LY30 (figure 6.3.9a), which is in consistent with previous report of DDC. Figure 6.3.9b showed that DAF fluorescence decreases obviously in the presence of DDC, suggesting that DDC possesses high potency in reducing NO.

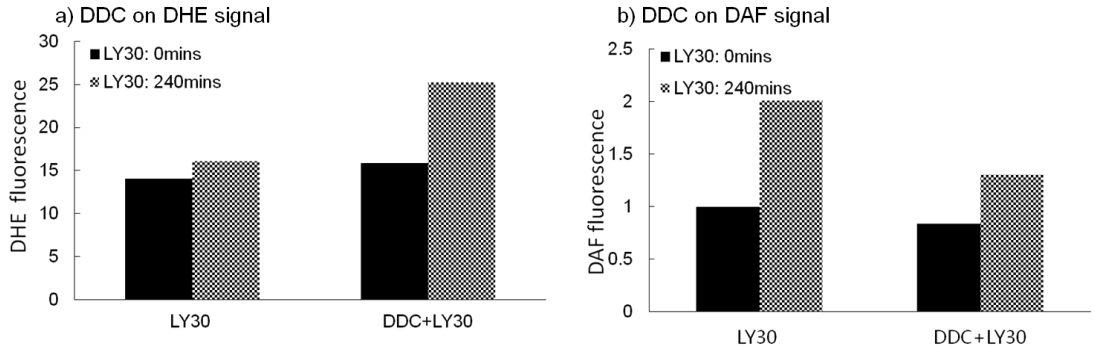

Figure 6.3.9 Measured effect of DDC on $O_2^{\bullet-}$ and NO. a) Normalized level of DHE fluorescence with either LY30 treatment or combination treatment of DDC

with LY30. b) Normalized level of DAF fluorescence with either LY30 treatment or combination treatment of DDC with LY30. For combination treatment, cells are pre-treated with DDC (400uM) for 2 hours before adding LY30.

6.3.6. Consistency between model inference and experimental measurement

To facilitate the comparison between time-series measurements of fluorescent dyes, and simulated probabilities of discrete high/medium/low states, we constructed the following plot: the experimental observations were converted into 3 categories of LY30 treatment based on time of incubation (Figure 6.3.7a); and the Bayesian probability distributions of DCFDA concentrations (Figure 6.2.7) were heuristically converted into predicted concentrations (Figure 6.3.7b), as explained in the figure caption. In addition, error bars were constructed for the modeled concentrations in Figure 6.3.7b, based levels of disagreement among the top-12 models. Small error bars suggest agreements among all the models and big error bars indicate disagreements in the results.

The peroxynitrite scavenger FeTPPS (100 μM) decreased DCFDA fluorescence slightly for short LY30 incubations ($p=0.048$), and very strongly for long LY30 incubations ($p=0.03$), suggesting that ONOO- is responsible for much of the DCFDA fluorescence caused by LY30, particularly at later time-points. The FeTPPS experiments agreed with the computational prediction, except for the magnitude of the effect after brief LY30 incubations.

Experiments showed that the Ca^{2+} chelator EGTA-am was able to block the early increase in DCFDA fluorescence induced by brief LY30 incubations (from 1.5-fold to 1.2-fold with $p=0.03$), but this effect was not observed with long incubations in consensus of the models according to a big error bar. This is in agreement with the

model inference that a Ca^{2+}-dependent pathway of ROS production contributed to the initial rise in DCFDA after LY30 treatment.

The $O_2^{\bullet -}$ scavenger Tiron (10mM) caused a slight decrease in DCFDA fluorescence (from 1.45-fold to 1.38-fold p=0.047) for short incubations, and a significant decrease (from 1.89-fold to 1.53-fold with p=0.02) for long incubations, suggesting that $O_2^{\bullet -}$ plays a causal role in LY30-induced ROS production, especially at late time points. The significant decrease of DCFDA after Tiron treatment would seem to refute the inference that $O_2^{\bullet -}$ would not significantly affect DCFDA.

Overall, the comparison between modelling and experiments (Figure 6.3.7) showed that Bayesian modelling was capable of reproducing the experimental effects of $ONOO^-$-dependent late ROS production, and Ca^{2+}-dependent early ROS production, but it underestimated the impact of Tiron.

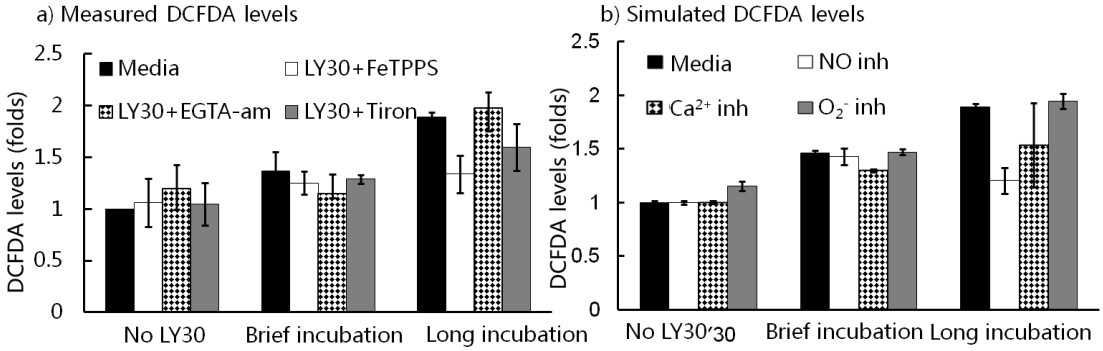

Figure 6.3.7. Comparison between simulated DCFDA and measured DCFDA, for scavenger/chelator experiments. a) The probability distribution of DCFDA from figure 4 has been plotted as fold-change relative to untreated control. The predicted probability distributions of DCFDA at low, medium and high levels have been converted into absolute concentration using the formula $DCFDA_{averaged} = 0.1 * DCFDA^1_{averaged} + 0.4 * DCFDA^2_{averaged} + 0.9 * DCFDA^3_{averaged}$, where $DCFDA^1_{averaged}$, $DCFDA^2_{averaged}$ and $DCFDA^3_{averaged}$ represented averaged probability distributions of DCFDA at low, medium and high levels, respectively. $DCFDA_{averaged}$ is the absolute DCFDA level after

conversion, and it is then normalized to the calculated DCFDA levels for untreated control. The error bars represent standard deviations for each average of the top 12 models. b) DCFDA intensity was measured after HeLa treatment with various scavenger/chelator compounds plus LY30, and Tiron was used as $O_2^{\bullet -}$ scavenger.

6.3.6 Effects of inhibitors in LY30-induced cell sensitization to TRAIL

We have thus far studied LY30 effects on ROS but not on cell viability. To understand how LY30 induces HeLa cell sensitization to TRAIL-induced apoptosis, we measured cell viability after LY30+TRAIL treatment, in cells that had been pre-treated with one of the following scavengers/inhibitors: FeTPPS, EGTA-am, Tiron, DDC, or Catalase (Figure 6.3.10). DDC is an inhibitor of SOD (superoxide dismutase), and it causes increased $O_2^{\bullet -}$ accumulation. Catalase is an antioxidant enzyme that specifically scavenges H_2O_2.

HeLa cells treated with LY30+TRAIL exhibited 40% viability, compared with untreated HeLa (100% viability). Pre-treatment with FeTPPS (100 μM) improved cell viability from 40% to 65% (25% rescue with p=0.0063), and the inactive analogue $FeCl_3$ had no effect (Figure 6.3.11), suggesting an essential role for $ONOO^-$ in LY30-induced sensitization to apoptosis. Quantified cell viability showed that EGTA-am, Tiron and DDC were also able to rescue cell death significantly (18% and 20% and 28%, respectively). Interestingly, catalase did not cause significant rescue of cell death, so we measured whether catalase decreased LY30-induced ROS. Catalase suppressed a significant fraction of DCFDA fluorescence induced by 5 minutes of LY30 treatment, but it had no significant impact on the DCFDA levels induced by longer incubations of LY30. This suggests that H_2O_2 is not a significant fraction of LY30-induced ROS in HeLa, except at very early time points.

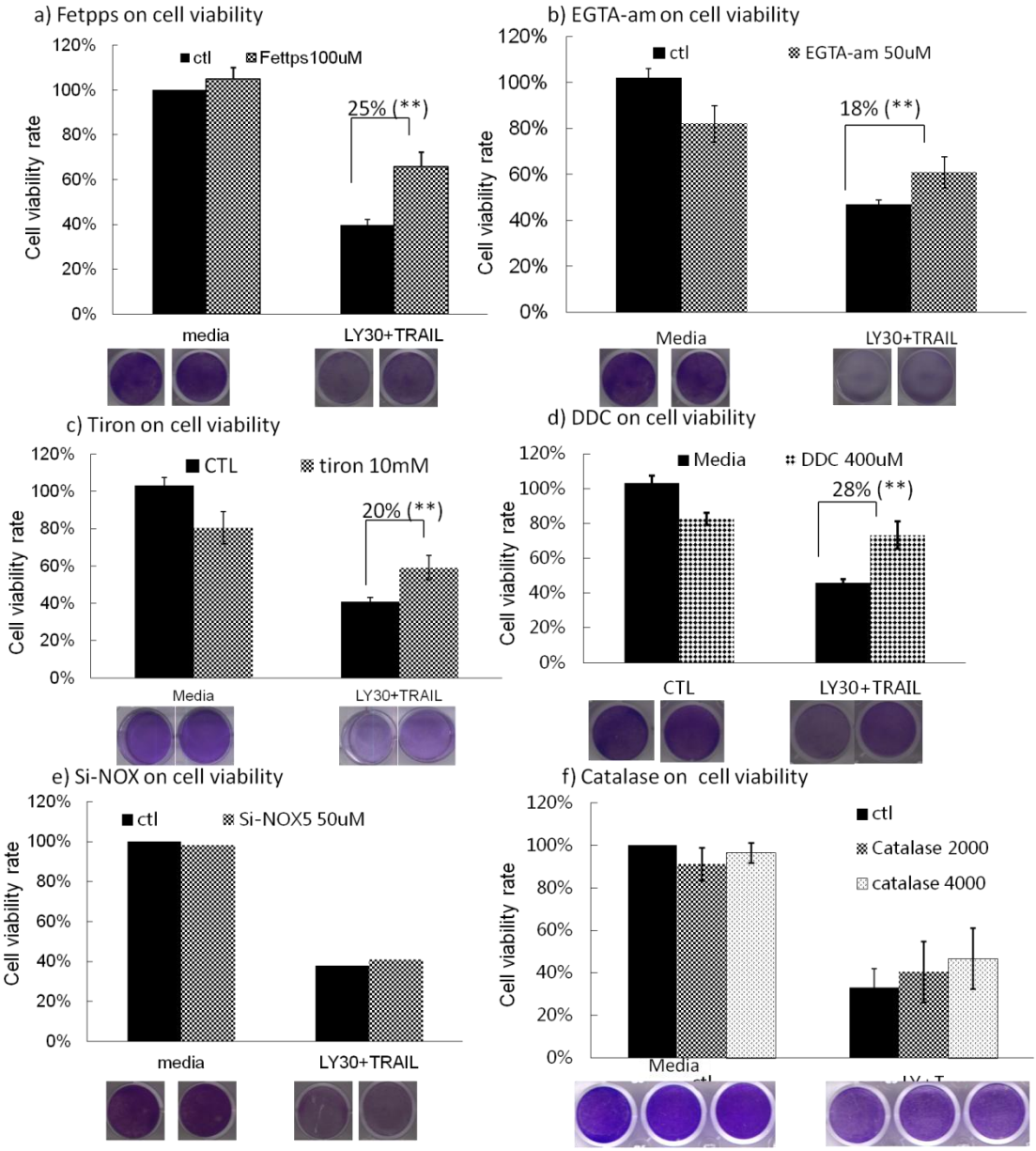

Figure 6.3.10 Cell viability of HeLa cells under LY30+TRAIL treatment with/without inhibitors. a) Cell viability with/without FETPPS (100uM), b) Cell viability with/without EGTA-am(50uM), c) Cell viability with/without Tiron (10mM), d) Cell viability with/without DDC(200uM), e) Cell viability with si-NOX at 50uM, f) Cell viability with/without catalase 2000 units/ml and 4000 units/ml.

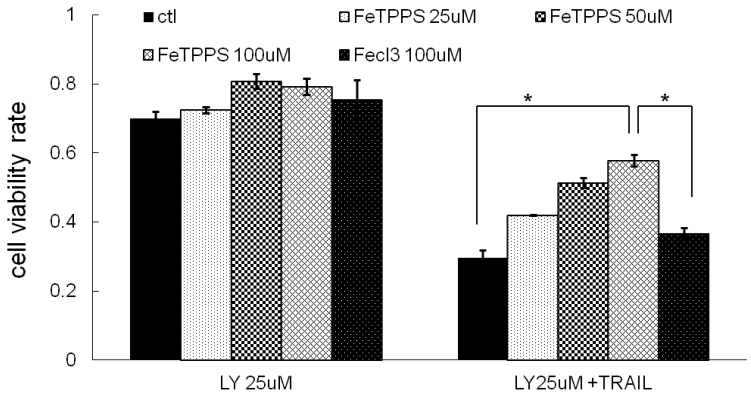

Figure 6.3.11 Measured cell viability with treatment of LY30, LY30+TRAIL in the presence of FeTPPS and its inactive form $FeCl_3$. FeTPPS was added with varied levels of 25uM, 50uM and 100uM. Fecl3 was added at 100uM, which is equal to the highest level of FeTPPS. * represents $P<0.05$.

6.4 Extension of the LY30 model with inhibitors/chelators/scavengers and cell sensitization

In section 6.2, we modelled DCFDA in Bayesian network as one node because the dye DCFDA has been reported to be unspecific to H_2O_2. Since Bayesian network model helped us find out that LY30 triggered $ONOO^-$ and H_2O_2 production, we expanded the model (Figure 6.2.9) with $ONOO^-$ and H_2O_2 accordingly. After that, we added cell sensitization to TRAIL ("Sensit") as an output of the model to represent cell sensitivity to TRAIL.

6.4.1 Construction of comprehensive Bayesian network model of LY30-induced pathway LY30-induced DCFDA & sensitization model (LDSM)

6.4.1.1 Extension with H_2O_2 and $ONOO^-$

To include H_2O_2 and $ONOO^-$ into the model, we dissected the time-course of DCFDA levels into H_2O_2 and $ONOO^-$ through inhibitory results with si-NOX/catalase and FeTPPS. For example, LY30-induced H_2O_2 is calculated through subtracting the DCFDA levels of LY30+catalase treatment from that of LY30 treatment, and LY30-induced $ONOO^-$ is calculated through subtracting the DCFDA levels of LY30+FeTPPS treatment from that of LY30 treatment. The processed dynamics of the two species were presented in figure 6.4.2. By conducting parameter estimation, we extended the previous table with H_2O_2 and $ONOO^-$, each having three states of low, medium and high.

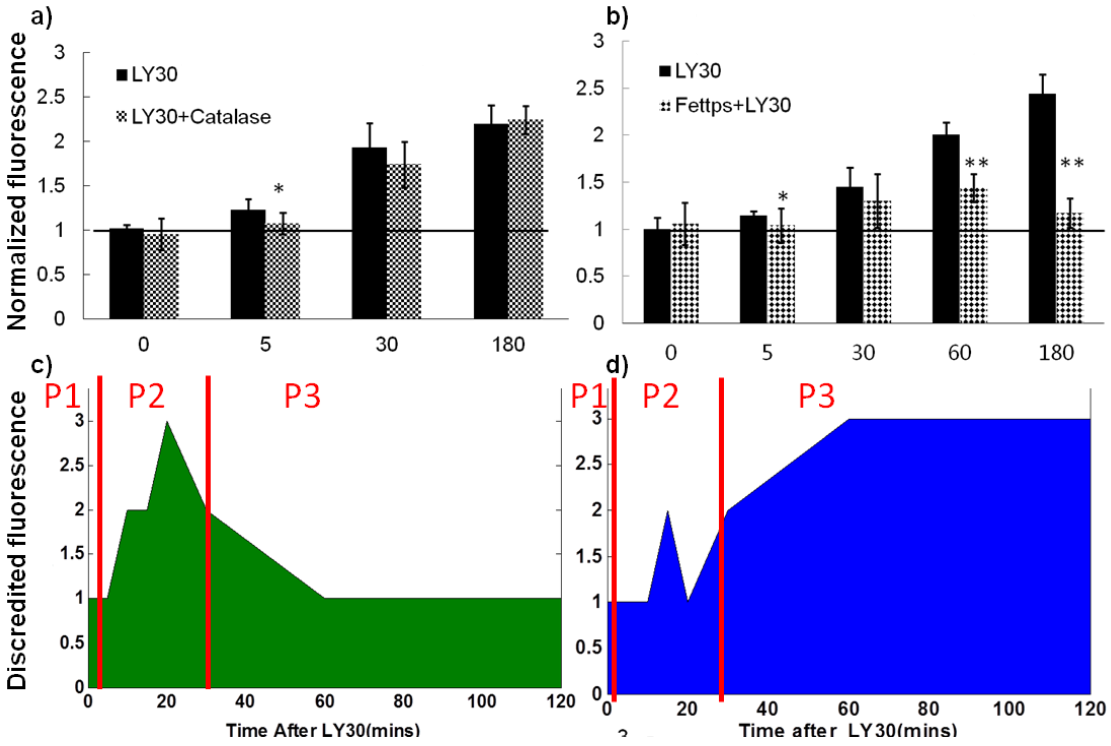

Figure 6.4.1 Dataset of H_2O_2 and ONOO- based on DCFDA fluorescence with ROS scavengers of catalase and FeTPPS. a) Normalized DCFDA fluorescence intensisty in HeLa with administration of LY30/catalase/LY30+catalase for time specified in x-axis, b) Normalized DCFDA fluorescence intensisty in HeLa with

administration of LY30/FeTPPS/LY30+FeTPPS for time specified in x-axis; c) discretized H_2O_2 data based on catalase+LY30 data shown in a); d) discretized ONOO- data based on FeTPPS+LY30 data shown in b).

In the extended model, DCFDA was modelled as a child node of both H_2O_2 and $ONOO^-$. The original link from NO to DCFDA was replaced by the link from NO to $ONOO^-$ and the original link from Ca^{2+} to DCFDA is replaced by the link from Ca^{2+} to H_2O_2. In order to incorporate the knowledge of the involvement of $O_2^{\bullet-}$ in the production of $ONOO^-$ [239], we included a direct link from $O_2^{\bullet-}$ to $ONOO^-$; to represent the conversion from $O_2^{\bullet-}$ to H_2O_2 [318], we added a directed link from $O_2^{\bullet-}$ to H_2O_2. The new parameters were estimated using Expectation-Maximum algorithm with extended data table. After extension with H_2O_2 and $ONOO^-$ in the model, we got the structure of the extended model as shown in Figure 6.4.2.

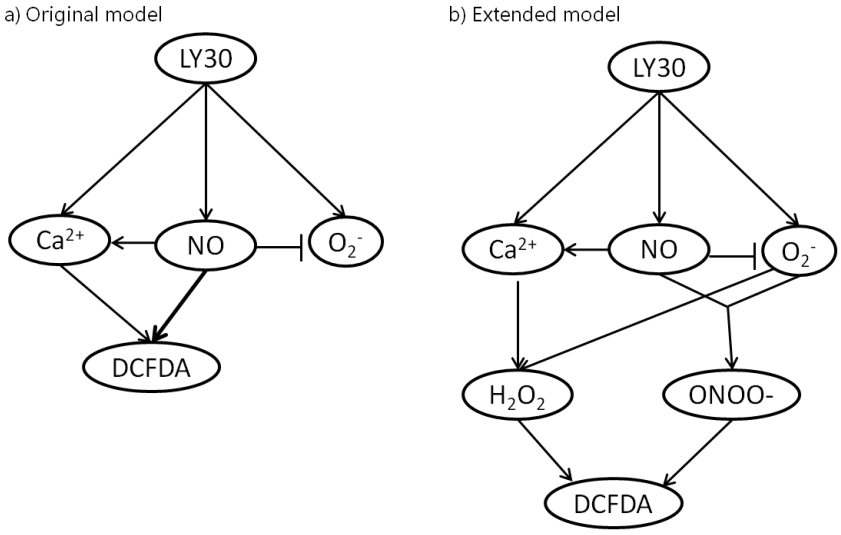

Figure 6.4.2 Comparison between the original model and the extended model from experimental evidence. a) In the original model, LY30 induces NO increase, Ca^{2+} increase and $O_2^{\bullet-}$ increase, NO inhibits $O_2^{\bullet-}$, both Ca^{2+} and NO contributes to DCFDA signal. b) In the extended model, H_2O_2 and ONOO- are the two parents of DCFDA, Ca^{2+} induces H_2O_2 through NOX, NO affects $ONOO^-$ through interaction with $O_2^{\bullet-}$.

6.4.1.2 Extension with biological inhibitors and TRAIL sensitivity —final stage of LY30-induced DCFDA & sensitization model (LDSM)

To represent our best current understanding of LY30 effects in HeLa, the Bayesian modelling consensus from Figures 6.4.2 was extended as follows. The consensus links between RNS, $O_2^{\bullet -}$, Ca^{2+} and DCFDA were retained (depicted as straight, solid lines in Figure 6.4.2a), and RNS was renamed nitric oxide (NO) because its training data came from the NO-specific dye DAF. New variable nodes were created for ONOO-, H_2O_2, and cell sensitization to TRAIL ("Sensit"). Then, to connect the new variables with the network, possible pathways (dotted arcs in Figure 6.4.3) were added manually based on published literature. Directed edges were inserted from $O_2^{\bullet -}$ and NO to the ONOO- variable node because $O_2^{\bullet -}$ and NO react strongly to produce ONOO-. Additional "dotted" arrows were added from Ca^{2+} to H_2O_2, and from $O_2^{\bullet -}$ to H_2O_2, and from most of the species to apoptosis sensitization. Finally, exogenous binary variables (present/absent) were created for the inhibitors FeTPPS, EGTA-am, Tiron, DDC, and catalase. Negative influences were added for FeTPPS towards ONOO-, for EGTA-am towards Ca^{2+}, and for catalase towards H_2O_2. The obvious effect of DDC on superoxide was added, as well as the published side-effect that DDC can suppress NO levels. A negative effect of Tiron on superoxide was added, along with the published side-effect that Tiron can decrease $ONOO^-$. The "exogenous" variables (the inhibitors and scavengers) and their causal links are shaded grey in Figure 6.4.3.

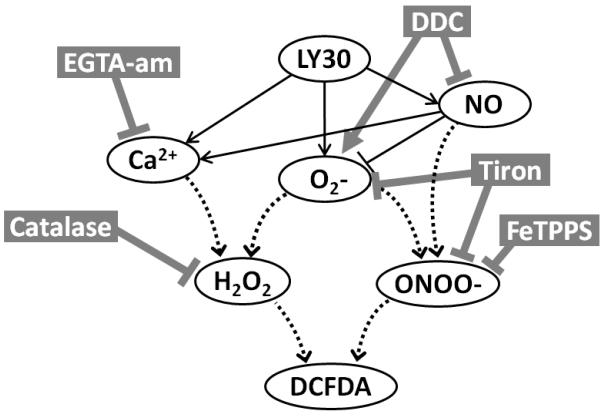

Figure 6.4.3. Extended model structure with H_2O_2, $ONOO^-$ and various inhibitors.

Cell sensitization has two states in the model, 0 represents the cell is resistant to TRAIL and it is viable, while 1 represents the cell is sensitive to TRAIL and it is dead. Since H_2O_2, $ONOO^-$, Ca^{2+} and $O_2^{\bullet-}$ have all been widely reported to affect cell, we modelled sensitization as the child node of H_2O_2, Ca^{2+}, $ONOO^-$ and $O_2^{\bullet-}$. Specifically, rise of intracellular level of H_2O_2, Ca^{2+} or $ONOO^-$ promotes cell death [5, 94, 242] and increase of intracellular $O_2^{\bullet-}$ inhibits cell death by activating cell survival pathway [319].

To estimate the conditional probability table of sensitization on its parents, we used the measured cell viability under 8 different conditions: no treatment, LY30 treatment, LY30+catalase treatment, LY30+Tiron treatment, LY30+EGTA-am treatment, LY30 + FeTPPS treatment, LY30 + DDC treatment, and LY30 + si-NOX treatment.

As we known, the size of CPT is determined by the states of its parents in the form of $Child = \prod_i^m Parent_i$. Since the "Sensit" node in the network has four parents (m=4) and each parent has 3 states (Parent=3), the size of the estimated CPT will be 3^4=81.

Fitting the big CPT of 81 conditions with available dataset of 8 conditions will result in serious problem of under-fitting. In order to solve the problem, , we reduced 3 states (low, medium and high) to 2 states (low and high) for each parent node of "Sensit" according to the conversion table(Table 6.1).

Table 6.1 conversion table of species from 3 states to 2 states

Parent	Child	Probability
1	1	1
1	2	0
2	1	0.5
2	2	0.5
3	1	0
3	2	1

To be consistent to measured viability and simulated viability, we randomly generated 50 samples using binomial sampling for each treatment. CPT table for sensitivity is then estimated using Expectation Maximum algorithm implemented in Bayes Net Toolbox.

After extension of the model with the procedures above, we built a comprehensive Bayesian network named LY30-induced DCFDA & sensitization model (LDSM, Figure 6.4.4) which incorporates a comprehensive pathway from LY30 to DCFDA, from LY30 to cell sensitization and variable biological inhibitors.

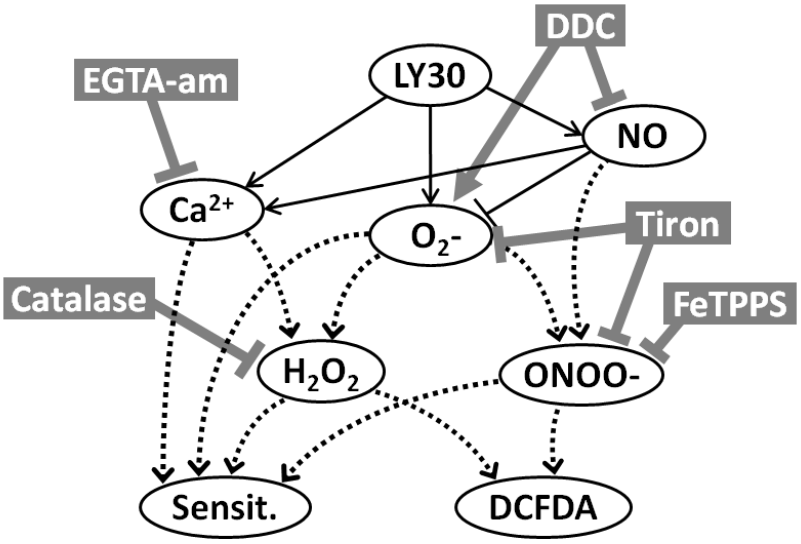

Figure 6.4.4. Comprehensive pathway model describing effect of LY30 on HeLa. LY30 is the input of the system, DCFDA fluorescence and cell sensitization are represented with green ovals are two outputs of the system. Besides LY30, DCFDA and sensitization, there are another five variables in the pathway, Ca^{2+}, NO, $O_2^{\bullet-}$, H_2O_2, and ONOO-. Solid arrows between the variables are the 'learned' effect from selected BN models and dashed lines are the 'reported' relationship by literature. Inhibitors like EGTA-am, si-NOX, catalase, DDC, Tiron and FeTPPS are also included into the model with their targets specified above.

6.4.2 LY30-induced DCFDA & sensitization model (LDSM) predicts the correct output under conditions of single treatment and combination treatments

6.4.2.1 Inference of internal nodes: NO, Ca^{2+}, $O_2^{\bullet-}$, H_2O_2, $ONOO^-$ with single inhibitor

To test the accuracy of the mode, we conducted inference on LDSM of internal nodes as well as outputs upon combinational treatment of LY30 and various inhibitors. Noted that the internal nodes refer to the nodes which are neither inputs nor output, for example, H_2O_2, $ONOO^-$, Ca^{2+}, NO and $O_2^{\bullet-}$. The outputs refer to DCFDA and

sensitization. Inhibitors include EGTA-am, FeTPPS, Tiron, DDC and catalase, each of which has “on” and “off” two states.

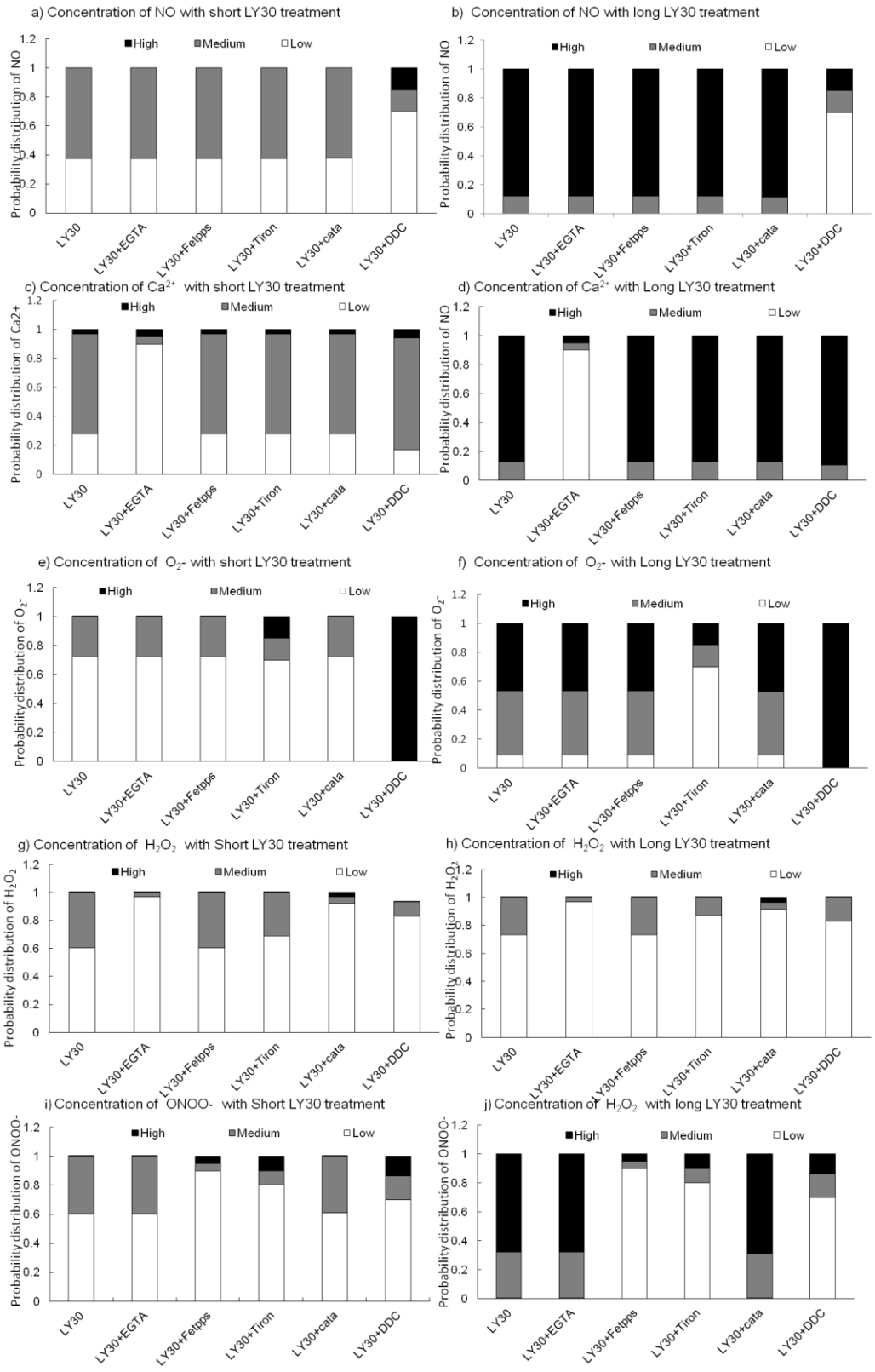

Figure 6.4.5 simulated probability distributions of internal nodes NO, Ca^{2+}, $O_2^{\bullet-}$, H_2O_2 and ONOO- under combined treatments of LY30 with single

inhibitors. a) simulated level of NO with short incubation of LY30 with/without inhibitors; b) simulated level of NO with long incubation of LY30 with/without inhibitors; c) simulated level of Ca^{2+} with short incubation of LY30 with/without inhibitors; d) simulated level of Ca^{2+} with long incubation of LY30 with/without inhibitors; c) simulated level of $O_2^{\bullet-}$ with short incubation of LY30 with/without inhibitors; d) simulated level of $O_2^{\bullet-}$ with long incubation of LY30 with/without inhibitors; e) simulated level of H_2O_2 with short incubation of LY30 with/without inhibitors; f) simulated level of H_2O_2 with long incubation of LY30 with/without inhibitors; g) simulated level of $ONOO^-$ with short incubation of LY30 with/without inhibitors; h) simulated level of $ONOO^-$ with long incubation of LY30 with/without inhibitors;

For inferences of concentration levels of internal nodes, we included *short LY30 incubation* and *long LY30 incubation* in order to be consistent with experimental conditions. Predicted levels of internal nodes with the treatment specified on x-axis were shown in Figure 6.4.5 showed.

EGTA-am is able to reduce LY30-induced Ca^{2+} increase. As shown in Figure 6.4.5c, combination treatment of EGTA-am and short LY30 incubation, compared with short LY30 incubation alone, can reduce the probability of Ca^{2+} at medium level about 60% and increase of the probability at low level about 60%. Greater reduction of Ca^{2+} level by EGTA-am was observed with long LY30 incubation. With long LY30 treatment, EGTA-am reduces the probability of Ca^{2+} at high level from 85% to about 5%. Furthermore, LDSM showed that EGTA-am changes H_2O_2 level from medium to low with short and long LY30 incubation. Little effect was observed under EGTA-am treatment on NO, $O_2^{\bullet-}$ and $ONOO^-$.

FeTPPS: According to the inferred result of $ONOO^-$ from LSDM (Figure 6.4.5j), FeTPPS can decrease LY30-induced $ONOO^-$ production. In Figure 6.4.5j, we observed a reduction of 40% of $ONOO^-$ at medium level with combination treatment of LY30+FeTPPS compared to single treatment of LY30. More distinctive reduction was

observed with long LY30 incubation, where there was a 60% reduction at high level and 30% reduction of $ONOO^-$ at medium level. Little effect of FeTPPS was observed in other species.

Tiron can reduce the levels of three species, H_2O_2, $ONOO^-$ and $O_2^{\bullet-}$ according to LSDM. Tiron decreased the level of $O_2^{\bullet-}$. Compared to long LY30 treatment alone, combination treatment of LY30 and Tiron led to about 30% reduction at medium level and high level (Figure 6.4.5i, j). Besides, Tiron decreased the level of H_2O_2 (Figure 6.4.5g and 6.4.5h). Combination treatment of Tiron and LY30, compared to LY30 treatment alone, slightly decreased the level of H_2O_2 at medium level (about 10% with short LY30 incubation and 20% with long incubation). Tiron also reduced the level of $ONOO^-$. It decreased the probability of $ONOO^-$ at medium about 30% with short LY30 incubation (Figure 6.4.5i, 6.4.5j), and decreased the probability at high level about 50%.

Catalase: As shown in figure 6.4.5g, catalase specifically reduced H_2O_2 about 30% at medium level with short and long LY30treatment.

DDC: is predicted to affect NO, $O_2^{\bullet-}$, H_2O_2 and $ONOO^-$. With long incubation of LY30, addition of DDC decreased level with 70% reduction at high level (Figure 6.4.5b). Besides, DDC increased $O_2^{\bullet-}$. With short and long incubation of LY30, addition of DDC increased $O_2^{\bullet-}$ to 100% high level (Figure 6.4.5e, 6.4.5f). DDC decreased H_2O_2. With short and long incubation of LY30, addition of DDC decreased H_2O_2 with 30% reduction at medium level (Figure 6.4.5h). DDC decreased $ONOO^-$. With short incubation of LY30, addition of DDC didn't change the level of $ONOO^-$ much (20% increase at high level and 20% reduction at medium level) (Figure 6.4.5i). With long

incubation of LY30, addition of DDC decreased the level of $ONOO^-$ 15% at medium level and 60% at high level (Figure 6.4.5j).

6.4.2.2 Inference of DCFDA and viability from LDSM with single inhibitor

To be consistent with our biological experiments, we predicted DCFDA upon short and long incubation of LY30 while sensitivity is predicted with only long incubation of LY30. Inputs include LY30, LY30+EGTA-AM, LY30+FeTPPS, LY30+Tiron, LY30+catalase, and LY30+DDC.

Combination treatments of LY30+EGTA-am or LY30+catalase or LY30+FeTPPS, compared to LY30 treatment alone, reduced the DCFDA levels 10% at high level and medium level (Figure 6.4.6). Addition of Tiron increased high level about 10% and decreased medium level about 10%. Addition of DDC showed 10% increase at high level and about 20% reduction at medium level.

To evaluate the accuracy of the model, we compared the inferred DCFDA levels with the measured DCFDA level (Figure 6.4.7). Noted we inferred DCFDA levels from LDSM as probability distributions in low, medium and high levels, respectively. For a direct comparison between experiments and models, the inferred probability distributions at three levels are converted to a unique concentration according to the formula $DCFDA = 0.1 * P_{low} + 0.4 * P_{medium} + 0.8 * P_{high}$. Here, $DCFDA$ is the estimated concentration of DCFDA. P_{low}, P_{medium}, and P_{high} indicates the inferred probabilities of DCFDA at low level, medium level, and high level, respectively.

In the condition of short LY30 incubation, LSDM predicted that compared with DCFDA in untreated sample, DCFDA levels were at 1.4 folds 1.2 folds, 1.25 folds, 1.4

folds, 1.23 folds and 1.27 folds, upon treatment of LY30, LY30+EGTA-am, LY30+FeTPPS, LY30+Tiron, LY30+catalase and LY30+DDC, respectively (black bars in Figure 6.4.7a). The predicted DCFDA levels in LDSM were able to reproduce the experiment measurements (grey bars in Figure 6.4.6a).

In the condition of long LY30 incubation, LSDM predicted that, compared to the level with LY30 treatment alone (2 folds), the inhibitors (EGTA-am, FeTPPS, Tiron, catalase and DDC) reduced the DCFDA level for about 0, 0.64, 0.53, 0 and 0.57 folds. The inferred DCFDA level (black bars in Figure 6.4.6b) is able to reproduce the experiment measurements (grey bars in Figure 6.4.6b).

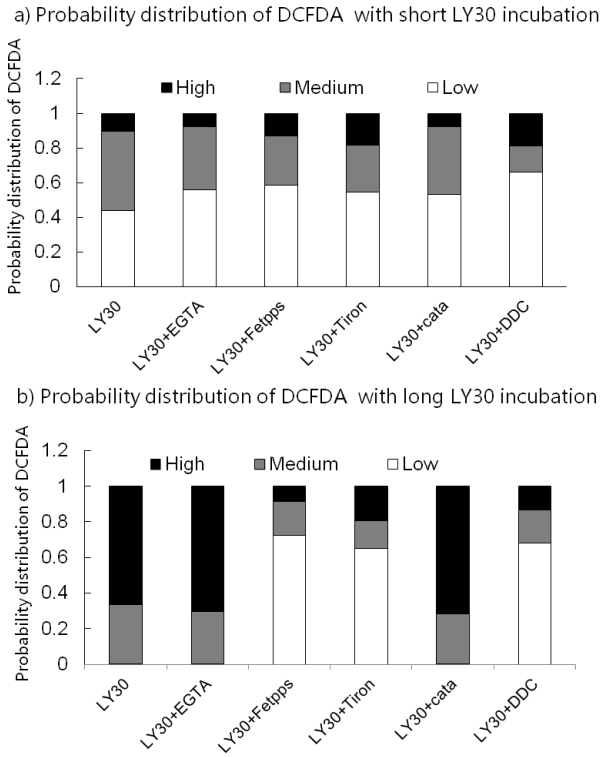

Figure 6.4.6 Simulated result of level of model output including DCFDA and Viability with combined treatment of LY30 and various inhibitors. a) Simulated early DCFDA with treatment of LY30 with/without inhibitors; b) Simulated late DCFDA with long incubation of LY30 with/without inhibitors.

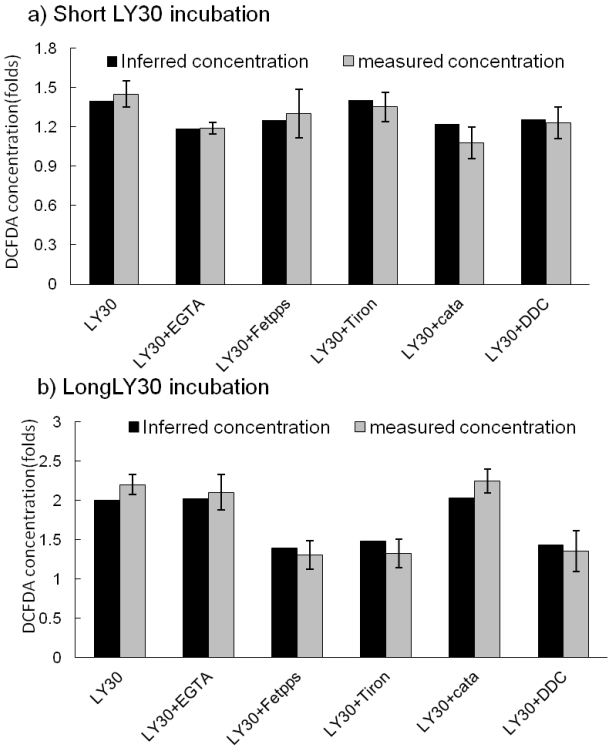

Figure 6.4.7 Comparison of DCFDA levels between model predictions and experimental measurements. a) Early DCFDA with treatment of LY30 with/without inhibitors; b) Late DCFDA with long incubation of LY30 with/without inhibitors. Black bars represent simulated levels of DCFDA after conversion function; grey bars represent measured DCFDA levels averaged from 3 independent experiments.

Cell sensitization rate, as represented by "Sensi" node in LSDM, showed that FeTPPS, EGTA, Tiron and DDC can greatly reduced the cell death whereas no obvious cell rescue is observed with pre-treatment of catalase (black bars in Figure 6.4.8). The model inference is consistent with experimental results (grey bars in Figure 6.4.8).

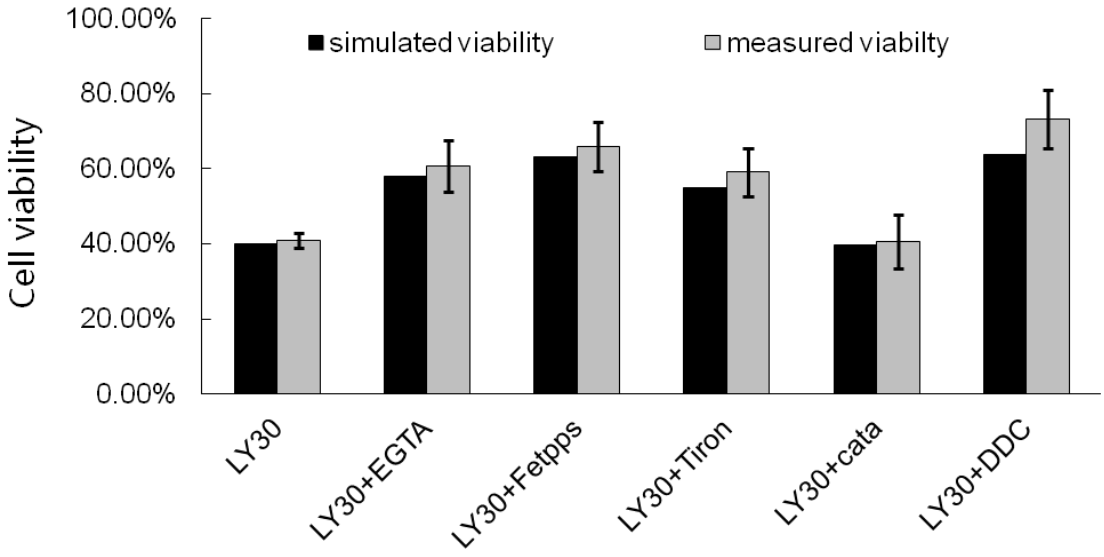

Figure 6.4.8 Measured and simulated cell viability from LSDM with combined treatment of LY30 and TRAIL together with various inhibitors. Black bars represent simulated cell viabilities under specified treatments in x-axis together with TRAIL and grey bars represent averaged cell viabilities measured from 3 repeats under the same treatment as simulations.

6.4.2.3 Inference of cell viability with double inhibitors

Our simulated cell sensitivity (viability) from LDSM demonstrated consistent results with experimental measurement with the 5 inhibitors (Figure 6.4.8). To test the interplay of the internal species on LY30-induced cell sensitization, we further inferred cell viability under the combination treatment of LY30 with double inhibitors, which include all the possible combination among EGTA, FeTPPS, EGTA, Tiron and DDC. Figure 3.5.6-a shows predicted intracellular DCFDA levels with all the defined treatments.

Inference of cell sensitivity: Interestingly, LDSM predicted that double inhibitors of EGTA together with other inhibitor (FeTPPS, Tiron and DDC) were able to rescue more than 40% of cell death, much higher than the rescue with any of the single

inhibitor. However, other 3 combinations like FeTPPS+Tiron, FeTPPS+DDC and DDC+Tiron showed only around 20% cell rescue, which is similarly to single inhibitor.

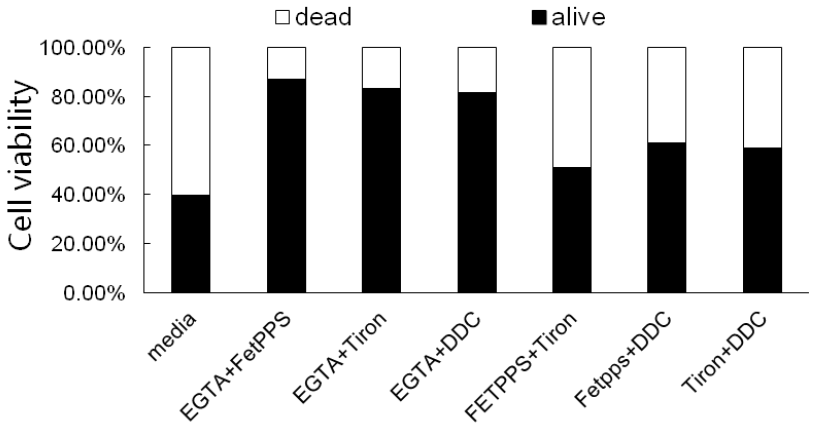

Figure 6.4.9 Inferred cell viability with combined treatment of LY30 and double inhibitors. Black bars represent probability distribution of sensitivity at 0 and white bars represent probability distribution of sensitivity at 1.

6.4.3 Experimental validation of cell viability with double inhibitors

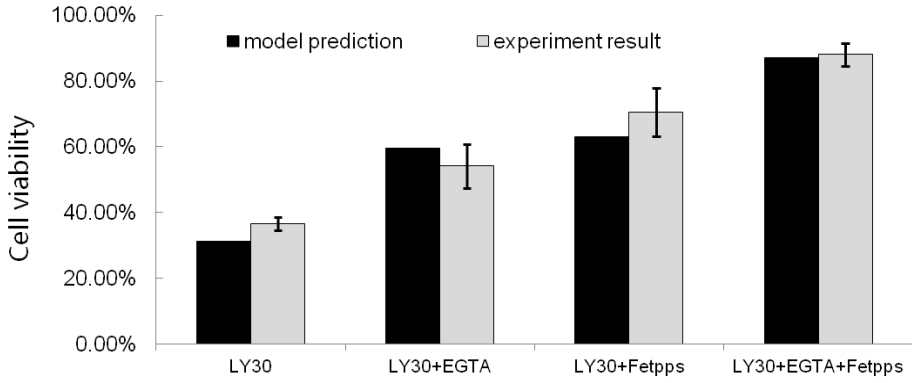

Figure 6.4.10 Comparison of model predicted cell viability and experiment generated cell viability treated with EGTA-am, FeTPPS or their combination together with LY30+TRAIL. Experiment result of cell viability is obtained after 24 hours treatment of LY30+TRAIL with/without FETPPS, EGTA-am and their combination. For FETTPS, HeLa cells were incubated with FETTPS (50uM) one hour before adding LY30. For EGTA-am, cells were added with EGTA at level of 50uM 15 minutes before adding LY30. For combined inhibitors treatment,

FETPPS was added in specific well with chosen level, after 45 minutes, EGTA-am was added and wait for 15 minutes before adding LY30.

To test the prediction of LDSM with double inhibitors, specifically with EGTA-am and FeTPPS which showed with the highest rescue of 45%, we conducted cell viability assay with FeTPPS and EGTA-am, together with LY30 and TRAIL. We expected to observe that the two inhibitors together are able to rescue cell percentage of the sum of percentage of the cells rescued by single inhibitors by LY30+TRAIL. As shown in figure 6.4.10, we observed that a quantitative agreement of cell viabilities between experiments measurement and model predictions under all the treatments specified in x-axis.

6.5 Discussion and summary

6.5.1 Probabilistic inference using Bayesian networks identified causal roles for NO and Ca^{2+} in LY30-induced ROS.

Computational modeling provides visualization of complex dynamics in biological pathways that may be unintuitive to biologists. Many studies adopt ordinary differential equation (ODE) for model construction [142, 143, 173], but this format requires extensive knowledge of network structure and parameters from published literature. This requirement does not apply in our system as little published evidence is available about either the model structure or the parameters. Therefore, we chose to use Bayesian networks to model LY30-induced ROS pathways, due to several reasons. Firstly, the flexible architecture of Bayesian networks enables us to test and generate many hypotheses very quickly. Secondly, adding additional reactions to a Bayesian networks

does not require elaborate re-estimation of model parameters, in contrast to an ODE model [320, 321]. Thirdly, the inferences derived with a Bayesian model are qualitative and thus are less sensitive to changes in parameter values [322].

We took the following strategies to study the unknown pathway from LY30 to ROS using Bayesian network. Firstly, we chose a Markov Chain Monte Carlo (MCMC) [323] algorithm called Metropolis-Hastings to learn the model structure. As we know, Bayesian network model consists of network structure and conditional probability tables (also called "contingency tables"). Network structure, which composed of directed arrows from parent species to children species, captures cause and effect relationships among the species. Conditional probability tables quantitatively describe the impact of parent species on their children species. Each Bayesian network model is evaluated with a score (Bayesian score) which indicate its consistency with observation. Compared with other structure learning methods, such as K2, MCMC is capable of selecting a collection of "high-scoring" models (Figure 6.2.5) instead of picking the "highest-scoring" model. Since measurement noise is unavoidable in biological experiments [324], there is a high chance of over-fitting if we only choose a single 'highest-scoring' model to match the noisy data. Through selecting the common features with topological analysis (Figure 6.2.4) and model inference (Figure 6.2.6) that existed among most of the "high-scoring" models, we can improve the accuracy of the inference by reducing the interference from data noise. The strategy, called 'model averaging', was adopted to study the pathway of key phosphorylated proteins in human T cell signaling [160]. Secondly, we imposed two constraints on structure learning based on biological relevance. One was that LY30 must be the input of the system, meaning it is a parent or ancestor for the other species in the network. The other

constraint was that DCFDA must be the model output, meaning it must have parents in the network but no children. Thirdly, we applied 10,000 random repeats in MCMC algorithm to avoid bias from the random initial guess.

6.5.1.1 Topological analysis through model averaging suggested a close link from NO to DCFDA

Topological analysis based on data structure [325] was performed to score different directed edges to DCFDA. In topological analysis, the node with higher score has higher probability of causing a direct influence on DCFDA. According to topological analysis through model averaging (Figure 6.2.4), we observed that NO, compared with LY30, $O_2^{\bullet-}$ and Ca^{2+}, has a higher score for the directed edge to DCFDA, suggesting the change of DCFDA level has high dependence on the NO level. To link the gap between NO and DCFDA, we hypothesized an intermediate formation of $ONOO^-$ between the increase of NO and the increase of DCFDA, which including 1) $ONOO^-$ is a downstream product of Nitric Oxide; and 2) $ONOO^-$ production could account for the DCFDA fluorescence increase.

In addition, topological analysis also showed a high score for the direct edge from NO to $O_2^{\bullet-}$ with inverse correlation, meaning that high level of NO will cause high probability of $O_2^{\bullet-}$ at low level. It is consistent with the idea that LY30 increases NO which then decreases pre-existing $O_2^{\bullet-}$ in the reaction of $ONOO^-$ formation, which causes DCFDA activation. This further supports the hypothesis of $ONOO^-$ production downstream of NO.

Since $O_2^{\bullet-}$ is an essential reactant in the production of $ONOO^-$, we would expect to observe high score of the direct edge from $O_2^{\bullet-}$ to DCFDA. On the contrary, averaged

results among the "high scoring" models demonstrated a low occurrence of the edge. We speculated the low score is due to the lack of correlation between intracellular NO levels and intracellular $O_2^{\bullet-}$ levels. Intracellular $O_2^{\bullet-}$ has been reported to be 2-10 uM, and intracellular NO level to be less than 0.2 uM [232]. Such a difference in level gap implies that $ONOO^-$ production would be less sensitive to $O_2^{\bullet-}$ than to NO. The equal stoichiometry of $O_2^{\bullet-}$ and NO in producing $ONOO^-$ would therefore not be expected to cause equally weighted edges between $O_2^{\bullet-}$ and NO in a Bayesian network. This is consistent with our findings, that the causal link from NO to $ONOO^-$ had high score and the causal link from $O_2^{\bullet-}$ to $ONOO^-$ had low score in topological analysis.

6.5.1.2 Predicted effects of inhibitors suggested the involvement of Ca^{2+} and NO in DCFDA signaling

Among the "high scoring" models, we firstly tested whether they were able to reproduce the known intracellular changes in LY30-treated cells. Approximate levels of NO, Ca^{2+}, $O_2^{\bullet-}$ and DCFDA were inferred from the high-scoring models, and comparison with observed levels showed the high-scoring models were consistent with observations (Figure 6.2.6). This success is not remarkable because these same observations were utilized for building the models. A side effect of the model-building process is the construction of causal models which predict the mediator(s) of Ca^{2+} LY30-induced DCFDA increase.

An important benefit of computational modeling is the potential to provide in silico predictions of novel experiments. We next predicted how various additional inhibitors would affect LY30-induced DCFDA fluorescence. The "high scoring" models from the initial Bayesian network MCMC search were extended to include three specific

inhibitors, targeting NO, Ca^{2+} or $O_2^{\bullet-}$. The extended models (Figure 6.4.3) predicted the following.

1) In cells with long-term (more than 30 min) LY30 treatment, inhibition of NO would show a higher inhibitory effect on the DCFDA signal, compared with the other two inhibitors.

2) Shortly after LY30 treatment (less than 30 min), inhibition of Ca^{2+} would show the highest inhibitory effect on the DCFDA increase, compared with the other two inhibitors.

3) Inhibition of $O_2^{\bullet-}$ showed little inhibitory effect on DCFDA increase, with either short or long incubation of LY30.

Seeking to interpret these predictions, we speculate that NO could affect DCFDA because NO can lead to production of $ONOO^-$ [242, 326], which is an effective trigger for DCFDA fluorescence [242, 326]. If NO and $ONOO^-$ are indeed a cause of DCFDA fluorescence (in contexts with more than 30 minutes of LY30 treatment), such an effect might be confirmed using an $ONOO^-$ scavenger and observing whether it causes a decrease in LY30-induced DCFDA levels. Regarding prediction for Ca^{2+}, we speculate that Ca^{2+} could affect DCFDA through mitochondria pathway which, however has been disputed with LY30-ETC model, or it could affect DCFDA by direction production of H_2O_2 through Ca^{2+} dependent NOX activation [108]. If Ca^{2+} does indeed mediate the short-term rise of DCFDA after LY30 treatment, such an effect might be confirmed using NOX activity assay in LY30-treated cells or using NOX knock-out to block NOX activity.

Given the inferred DCFDA levels with various inhibitors, we hypothesized that

1) There is a significant $ONOO^-$ increase with long LY30 incubation;

2) There is mild H_2O_2 production through Ca^{2+} with short LY30 incubation;

3) The LY30-induced increase in DCFDA is a combination effect of early H_2O_2 production, and late-peaking $ONOO^-$ production.

6.5.2 Biological experiments confirmed the role of NO and Ca^{2+} in LY30-induced DCFDA signaling

6.5.2.1 FeTPPS treatment confirmed the role of $ONOO^-$ in late DCFDA activation

To verify the intracellular $ONOO^-$ production by LY30, we treated cell samples with FeTPPS, which is a ferric porphyrin complex that catalytically scavenges peroxynitrite. As a potent $ONOO^-$ scavenger, FeTPPS was able to significantly reduce LY30-induced increase of DCFDA fluorescence, with > 80% of the total fluorescence increase in HeLa with long incubation of LY30 (120 minutes, 240 minutes Figure 6.3.1), confirming the model prediction about LY30-induced late $ONOO^-$ production. DCFDA measurement also showed that FeTTPS scavenged only < 30% of the total fluorescence increase with short LY30 incubation (5 minutes, 15 minutes Figure6.3.1), supporting the prediction of "significant $ONOO^-$ increase with long LY30 incubation".

6.5.2.2 EGTA-am treatment confirmed the role of Ca^{2+} in early DCFDA activation

To verify the hypothesized role of Ca^{2+} in contributing to early DCFDA increase by LY30, we incubated HeLa cells with a specific Ca^{2+} chelator EGTA-am. After

confirming EGTA-am can efficiently chelate free Ca^{2+} using flow cytometry (Figure 6.3.3a) and microplate reader (Figure 6.3.3b), we compared DCFDA fluorescence between LY30+EGTA-treated sample and LY30-treated sample (Figure 6.3.3c). HeLa samples with LY30+EGTA treatment, compared with LY30-treated samples, showed decreased DCFDA fluorescence with short LY30 treatment and slight increase with long LY30 treatment compared with time zero, confirming the contribution of Ca^{2+} on increased DCFDA fluorescence with short LY30 incubation.

To ascertain the involvement of H_2O_2, we tested the effect of catalase on LY30-induced DCFDA. Lower fluorescence in catalase+LY30-treated sample than in LY30-treated sample (Figure 6.4.1a) was observed, confirming that H_2O_2 accounts for much of the early DCFDA increase.

Elevated cytosolic Ca^{2+} has been reported to trigger NOX activation, and it is highly possible that NOX5 could produce H_2O_2 directly [108]. To test a causal link from Ca^{2+} release to DCFDA fluorescence increase, we first checked NOX activity under LY30 treatments. Compared to untreated sample, increased NOX activity was observed in LY30 treated sample (Figure 6.3.4a) and the increase could be blocked by EGTA-am pre-treatment (Figure 6.3.4b), indicating that LY30 triggered Ca^{2+}-dependent NOX activation.

To verify the causality from the NOX activation to ROS production, we then tested the effect of NOX5 knock down (si-NOX5) on LY30-induced DCFDA increase. In the sample with NOX5 knock down, we observed no increase of DCFDA fluorescence under short LY30 treatment (Figure 6.3.5a), indicating that NOX-5 knock down can block LY30-induced DCFDA increase. In other words, NOX activation leads to

DCFDA increase in LY30-treated cells. This would likely occur through H_2O_2, because NOX-produced superoxide is constitutively converted into H_2O_2, and H_2O_2 is a prime signal for DCFDA [108]. Our experimental results of measured NOX activity, together with measured DCFDA during NOX knock down and EGTA-am treatment, illustrated that LY30 induced Ca^{2+}-dependent early H_2O_2 production through NOX5.

Our in-vitro experiments with EGTA-am, si-NOX and catalase supported that "LY30 induced Ca^{2+}-dependent early H_2O_2 production through NOX5", reconfirming the conclusion that LY30 doesn't induced ROS production through the canonical Mitochondria ROS pathway.

6.5.2.3 $ONOO^-$ and H_2O_2 contributed to DCFDA fluorescence

DCFDA, reported in 1965 by A.S. Keston and R. Brandt, was initially regarded as a specific assay for the measurement of H_2O_2 in the presence of peroxidise [327]. The fluorogenic compound DCFDA has been utilized extensively as a marker for oxidative stress, and is suggested to reflect the overall oxidative status of the cell [146, 328]. Subsequent work has shown that DCFDA is not specific for H_2O_2, but it can detect many other ROS/RNS, especially $ONOO^-$ species with higher oxidation rate [329].

Through a system investigation method, we identified combined contribution of $ONOO^-$ and H_2O_2 in the increase intensity of DCFDA fluorescence. In addition, our work dissects the production of $ONOO^-$ and H_2O_2 into late and early period after LY30 treatment.

Lack of specificity is not a unique problem for DCFDA. In fact, a lot of chemicals has been reported to issues. Another example is that commonly used caspase inhibitors

designed based on substrate specificity profiles lack selectivity. Therefore, caution need to be taken with various chemicals in future in order to avoid wrong conclusion.

6.5.3 $ONOO^-$ and Ca^{2+} were the two key modeled players in LY30 induced sensitization

To study the sensitization mechanism with LY30, we used the "averaged model" (Figure 6.2.5) generated from "high scoring models" to create an extended model with several inhibitors and with two output nodes, sensitization and DCFDA. The extended model was trained with experimental viability data, with and without inhibitors. The inhibitors included FeTPPS, EGTA-am, catalase, Tiron and DDC, which were combined with LY30 and TRAIL. They were found to rescue cell death with 25%, 20%, 0%, 20% and 28%, respectively (Figure 6.3.10).

The trained model was used to predict the cell viability treated with different pairs of inhibitors (Figure 6.4.8). The pair of inhibitors with highest predicted effect was EGTA-am and FeTPPS together. Compared with other pairs of inhibitor, its rate of cell rescue was 45% (Figure 6.4.9), compared with 25% rescue from FeTPPS alone and 20% with EGTA-am alone (Figure 6.3.10). Note that our extended model predicted an additive effect of FeTPPS and EGTA-am on cell recue.

To test the prediction, we conducted in-vitro experiments to measure the effect of EGTA-am and FeTPPS on cell viability by LY30+TRAIL. The measured viability (Figure 6.4.10) showed around 40% rescue of cell death with the pair of inhibitor compared with that without inhibitor. As the measured result is consistent with model

prediction, we concluded that, in LY30-treated HeLa, increased cytosolic Ca^{2+} and increased $ONOO^-$ contribute to cell sensitization to TRAIL in an additive manner.

6.5.4 $ONOO^-$ rather than H_2O_2 contributed to cell sensitization in HeLa

Exposure to high levels of $ONOO^-$ usually leads to rapid cell death as necrosis due to acute and severe cellular damage [242]. In contrast, low levels of $ONOO^-$ can lead to delayed cell death in the form of apoptosis. We saw a strong effect from $ONOO^-$ but that doesn't necessarily mean we have a high level of $ONOO^-$ with LY30 since cell death with LY30+TRAIL treatment occurs as typical apoptosis according to the evidence of increased sub-G1 population using PI staining [74] and complete cell rescue with Z-VAD-FMK (a pan inhibitor of caspases) [74].

Our cell viability assay conducted in HeLa of combination treatment of LY30 and TRAIL together with si-NOX5 (Figure 6.3.10e), or catalase (Figure 6.3.10f) showed little cell rescue, suggesting that H_2O_2 may not be an important player in LY30-induced sensitization to TRAIL. In addition, treatment with NAC (N-acetylcysteine), which replenishes glutathione as a major intracellular antioxidant, also could not prevent LY30-induced sensitization to TRAIL. These observations are in consistent with previous result (supplementary of [74]) where overexpression of catalase in HeLa failed to prevent apoptosis from combined treatment of LY30 and TRAIL. Therefore, we confirmed that H_2O_2 is not a key player in long-term LY30-induced sensitization to TRAIL-induced apoptosis in HeLa.

Based on the current evidence and discussion, we come to the conclusion that $ONOO^-$ instead of H_2O_2 is the major driver of LY30-induced cell sensitization in HeLa. However, LY30 does cause significant H_2O_2 production, especially at early time points. That raises the question of why LY30-induced H_2O_2 does not contribute significantly to cell death. The apoptosis-inducing effect of LY30-induced H_2O_2 may be masked by the high levels of $ONOO^-$ which cause death more rapidly than H_2O_2. Thus it would not be surprising if there exist low-NO cell types in which LY30 sensitizes to death, more slowly, through H_2O_2. Our previous work in SHEP-1 neuroblastoma cells, which have lower iNOS levels [330], showed that catalase is able to reduce both DCFDA levels and cell viability, in LY30 treatment and LY30+TRAIL treatments, respectively. To explain the different phenomenon in the two cell lines, we may need to look at the NOS and NOX levels and activations respectively. We speculate that LY30 induces more NO production in HeLa than in SHEP-1, and/or that LY30 induces more NADPH oxidase function in SHEP-1 than in HeLa. Lower NO levels would cause less $ONOO^-$ and less peroxynitrite-dependent death. Future work should compare the expression of NOS isoforms and NOX isoforms in different cell lines, to understand the differential regulation of sensitization in these cell lines.

6.5.5 Superoxide was involved in LY30-induced DCFDA increase and cell sensitization

Tiron is a SOD mimetic which has been widely applied to scavenge superoxide anion [331]. Although the result through "model averaging" predicted a weak influence from $O_2^{\bullet-}$ to DCFDA, our measured fluorescence of DCFDA showed that Tiron is able to reduce LY30-induced DCFDA (Figure 6.3.6b). We speculated that the inconsistency

between the model prediction and experiment results may be due to the intracellular level different between NO and $O_2^{\bullet-}$. As reported, intracellular $O_2^{\bullet-}$ level is around 2-10 uM and the intracellular NO level is less than 0.2 uM [232]. Such difference between their levels makes NO the bottleneck in $ONOO^-$ production. In other words, $ONOO^-$ (and the increase of DCFDA fluorescence) should be less sensitive to $O_2^{\bullet-}$ than to NO. Therefore, increased level of NO triggered by LY30 can greatly drive the rapid reaction with $O_2^{\bullet-}$ towards $ONOO^-$ formation. In the presence of Tiron, the level of $O_2^{\bullet-}$ is greatly reduced and may no longer be available in excess of LY30-induced NO. In other words, Tiron may cause $O_2^{\bullet-}$ to become a new bottleneck in the system, and may decrease $ONOO^-$ production. Similar effect on DCFDA is also observed with incubation of Tempo, another SOD mimic [332].

To examine the role of superoxide in sensitization, we administrated Tiron or Tempol in HeLa cells, together with LY30 and TRAIL, and then measured cell viability. Cell viability results shows that Tiron can significantly rescue 20% cell death (Figure 6.3.10), suggesting an essential role of $O_2^{\bullet-}$ in LY30-induced cell sensitization to TRAIL. Similar cell rescue was also observed with Tempol at 4mM. We reasoned that both Tiron and Tempo rescued peroxynitrite-dependent cell death through scavenging $O_2^{\bullet-}$, which is in light with previous reports that Tempo can attenuate peroxynitrite-induced stress [333], and cells pre-treated with Tiron showed a decreased apoptotic response with iNOS inducer [334]. The interpretation of our experiments with Tiron and Tempol is more complex, however, because Tiron and Tempol also bind Ca^{2+} [335], causing calcium-dependent effects independent of $O_2^{\bullet-}$. Our cytometry measurements showed some impact of Tiron on Ca^{2+} levels, but the effect was not statistically significant. We conclude that Tiron and Tempol have a significant impact

on LY30-induced sensitization, but we cannot conclude whether some of this effect may be partially mediated by a calcium scavenging effect.

6.5.6 DDC decreased ROS production through NO inhibition.

N,N-Diethyldithiocarbamate (DDC), an inhibitor of superoxide dismutase[336], significantly blocked the LY30-induced DCFDA increase (Figure 6.3.8). This phenomenon is in contrary to our initial expectation. As DDC can greatly elevate the level of $O_2^{\bullet-}$ and the increase of $O_2^{\bullet-}$ can push forward the production of $ONOO^-$, we would expect to observe increased DCFDA with DDC.

To address this dilemma, we first measured the levels of both $O_2^{\bullet-}$ and NO with DDC treatment. We observed a significant increase in $O_2^{\bullet-}$ level, which was expected (Figure 6.3.9), but we also observed a surprising decrease in the levels of NO (Figure 6.3.9). Seeking to confirm the impact of DDC on NO, we found several studies showed DDC can reduce intracellular NO through inhibiting inducible NO synthase (iNOS) [337, 338]. If this mechanism occurs in our system, then DDC would block LY30-induced $ONOO^-$ increase in HeLa. Therefore, we concluded that DDC reduces DCFDA increase and reduces cell death through inhibition on NO.

6.5.7 Bayesian Network modeling suggests revised hypothesis for cFLIP-ROS model: NO may increase cFLIP expression and $ONOO^-$ may accelerate cFLIP degradation

We now revisit the topic of cFLIP regulation from chapter 4, in light of our Chapter 4 results about LY30-induced effects in HeLa. Based on the non-monotonic dynamics of

cFLIP by LY30, we hypothesized that 1) LY30 induces sequential increase of $O_2^{\bullet-}$ and H_2O_2 levels, and 2) increased $O_2^{\bullet-}$ concentration leads to early cFLIP up-regulation and increased H_2O_2 leads to late cFLIP down-regulation. Our measurement of intracellular $O_2^{\bullet-}$ and H_2O_2, however, does not support the proposed kinetics of sequential increase of $O_2^{\bullet-}$ and H_2O_2 by LY30 (Figure 4.2.7). Through Bayesian network modeling and experiments, we interpret LY30-induced effects to include early NO production and H_2O_2 production, and late $ONOO^-$ production.

Although our result about H_2O_2 and $O_2^{\bullet-}$ is inconsistent with the initial hypothesized explanation of cFLIP regulation, the following finding of sequential production of NO and $ONOO^-$ by LY30 can well explain the fluctuation of cFLIP. Previous work has established that NO blocks cFLIP degradation through s-nitrosylation of its caspase-like domain [339, 340]. Levrand et al. showed that $ONOO^-$ is a potent inhibitor of NF-kB [341], which has been well-established to induce cFLIP expression [342], meaning that $ONOO^-$ reduce cFLIP expression through inhibiting NF-KB. In light of these RNS-dependent effects, it is logical that LY30 regulation of cFLIP would occur first through NO-dependent up-regulation and subsequently through peroxynitrite-dependent down-regulation.

Our work provided a modified hypothesis that LY30 initially up-regulated cFLIP through nitrosylation by NO and late down-regulation through ubiquination by $ONOO^-$ (Figure 6.5.1). Further work can be pursued to test the role of NO and $ONOO^-$ in the regulation of cFLIP.

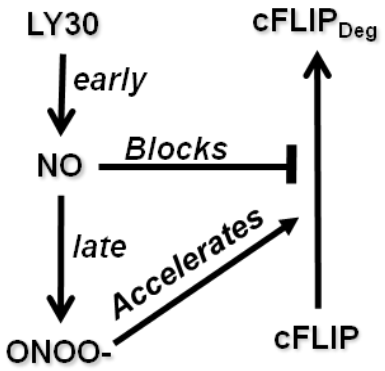

Figure 6.5.1 Hypothetical model for LY30 to cause non-monotonic regulation of cFLIP via NO and ONOO$^-$. Simplified diagram of LY30's influence on cFLIP. This model is roughly divided into two phases. In the earlier phase, NO is produced after LY30 treatment, and the increased NO will block the degradation of cFLIP, thus inducing its up-reguation. In the later phase, ONOO$^-$ is formed from NO, and inhibits the production of cFLIP, lowering its concentration.

6.5.8 Bayesian network modeling predicted causal effects in complex system with uncertain network structure

Bayesian Network is a mathematically unbiased method to integrate experimental evidence. Our study to uncover LY30-induced pathways of ROS production and TRAIL sensitization demonstrated the power of Bayesian network modeling for interpreting data in a complex system. The complexity arises because everything can potentially affect everything, individually or in higher-order combinations, with great uncertainty [160]. Another benefit of using Bayesian networks is that non-specific effects were spontaneously discovered by the model. For example, DCFDA is a marker for H_2O_2 but Bayesian models of DCFDA induction (Figure 6.2.5) showed a stronger causal link from NO to DCFDA than from H_2O_2 to DCFDA. Although we never provided any input information to the model about potential activation of DCFDA by RNS, the model inferred this causality based on the patterns of correlation in the data.

As defined, Bayesian network is capable of encoding all the possible relationship through probabilistic causality [343]. Bayesian networks can discover negative as well as positive results. For example, when building the model of Figure 6.4.4, we initially input that H_2O_2, Ca^{2+}, and $ONOO^-$ should have a causal link to cell death. The parameter estimation for the strength of the causal links interpreted the data to conclude that that H_2O_2 has negligible effect on cell death, and essentially removed the incorrect relationship that we had assumed would be present. These features enables Bayesian network to "correct" the prior knowledge with provided data [343].

The decision whether to use BN for cell signaling depends on the presence of sufficient data to make inferences. Our system is a good application for BNs because it has a relatively small number of key species (small number of nodes in the network), many datapoints (due to measuring the same species in different experiments and timepoints), and enormous uncertainty about the causal relationships between the measured species. A large pathway, or a small pathway with better-known causality, would not stand to gain as much from a BN approach. With the growing popularity of high-throughput measurement methods such as multi-parameter flow cytometry and protein assays [160, 289], we would expect that Bayesian network modelling will become applicable to more and more cell signaling questions.

Another of the limitations of application of Bayesian network is that they are restricted to be acyclic, meaning devoid of feedback loops (positive or negative). Feedback loops are common in biological pathways, and blindness to such relationships can causes mistaken inferences. Indeed, our inference missed the influence of $O_2^{\bullet-}$ on NO while capturing the negative influence from NO to $O_2^{\bullet-}$. The true relationship between NO

and $O_2^{\bullet -}$ is mutual, and therefore, by definition, could never be accurately captured in any BN model. Extended BN technologies such as Dynamic Bayesian networks can capture such effects, but the disadvantage of Dynamic BNs is that they require significantly more data to be collected.

7 Conclusion

Our study uses a computational systems biology approach by coupling biological assays (e.g., Western blot, flow cytometry, confocal microscopy) with various mathematical modelling techniques (e.g., ODEs, Bayesian networks and related toolboxes) to investigate LY30-induced effects in HeLa cells, including significant increases of DCFDA fluorescence and efficient TRAIL-induced apoptosis. Through comparing model predictions and biological data, we identified several non-intuitive facts, including:

- Non-monotonic regulation of cFLIP by LY30. Inspired by the inconsistency of caspase-8 dynamics between model simulations and experimental results, our Western blot of cFLIP showed that LY30 induces an initial increase and later decrease of cFLIP.

- Non-canonical production of ROS by LY30. Our study demonstrated that LY30-ETC model cannot match measured ROS levels, suggesting that LY30 triggers ROS production through other pathways instead of canonical mitochondria ROS pathway.

- Non-specific oxidation of DCFDA, not by H_2O_2. Indeed, our experiments showed that catalase didn't rescue death, even though LY30 causes massive H_2O_2 and H_2O_2 is normally understood to be a strong inducer of apoptosis.

These non-intuitive facts led us pursue further verification and thus revealed interesting biological phenomenon, including:

1) Significant increase of NO and $ONOO^-$ by LY30; 2) Passive leaking of Ca^{2+} by LY30; 3) NOX5 activation by LY30 through Ca^{2+} increase;4) Additive contribution of Ca^{2+} and $ONOO^-$ to additive cell death; and 5) Additive contribution of $ONOO^-$ and H_2O_2 to DCFDA increase.

Through this approach, we were able to uncover a much more complicated pathway of LY30-induced ROS production and TRAIL sensitization (Figure 7.1a) than our initial hypothesized pathway (Figure 7.1b). We found that the production of H_2O_2 and $ONOO^-$ together contributes to the significant DCFDA signal. Furthermore, we also identified intracellular $ONOO^-$ formation and free Ca^{2+} release as the two key players in LY30-induced cell sensitization to TRAIL. Significant DCFDA signal and cell sensitization are connected through $ONOO^-$ which has been demonstrated to play an essential role in both signals.

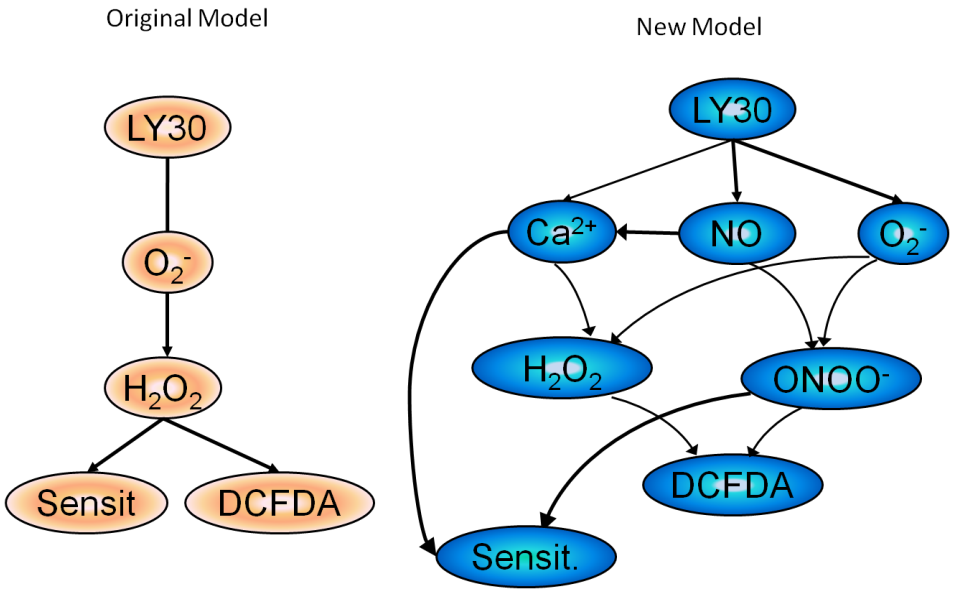

Figure 7.1 Comparison of original LY30 models and proposed new LY30 models. a) In the original model, LY30 induces $O_2^{\bullet-}$, which then converts to H_2O_2. The increased H_2O_2 is responsible for both cell viability and DCFDA signal. b) In the current model, LY30 induces Ca^{2+} release, NO increase, and $O_2^{\bullet-}$ increase. NO and $O_2^{\bullet-}$ interact to form $ONOO^-$. Ca^{2+} release leads to H_2O_2 production (may through NOX5

activation). Both H_2O_2 and $ONOO^-$ increases are responsible for DCFDA signal. Ca^{2+} and $ONOO^-$ are responsible for cell viability in the combination treatment of LY30 and TRAIL.

Our application of a systems biology approach provided a platform for analyzing complex indirect evidence about the function of LY30 in HeLa. The approach could also be extended to other cell lines, or repeated with other compounds. Note that LNCAP, SHEP-1 and Jurkat exhibit LY30-induced sensitization to TRAIL-induced apoptosis, but recent evidence (unpublished work) suggests the mechanisms may be different what we found for HeLa. It might be possible to use some of HeLa causality as a starting model for other cell types and then with collection of data in other cell lines, allow MCMC search to suggest modifications of the network topology, or allow BN parameter estimation process to infer the relative importance (or irrelevance) of the causal links for that cell type.

Another interesting goal for future work would be to measure the levels of NOS and NOS isoforms, particularly in different cell lines, and to test whether the mechanism of death is altered, in parallel with the capacity to produce different forms of reactive species, ROS and RNS. This might help understand the differential regulation of sensitization in these cell lines, and ultimately in different forms of cancer.

Reference

1. Thun, *Cancer statistics, 2009.* CA Cancer J. Clin., 2009(59): p. 25.

2. Organization, W.H., *The global burden of disease: 2004 update* Geneva (2008), 2008.

3. Goodman, M., et al., *Clinical trials of antioxidants as cancer prevention agents: past, present, and future.* Free Radic Biol Med, 2011. **51**(5): p. 1068-84.

4. Cancer, I.A.f.R.o., *World cancer report 2008*, in *IARC*, 2008, Lyon

5. Rizzuto, R., et al., *Calcium and apoptosis: facts and hypotheses.* Oncogene, 2003. **22**(53): p. 8619-27.

6. Green, D.R., ed. *Means to an end : apoptosis and other cell death mechanisms*. 2011., Cold Spring Harbor, N.Y. : Cold Spring Harbor Laboratory Press.

7. Kerr, J.F., A.H. Wyllie, and A.R. Currie, *Apoptosis: a basic biological phenomenon with wide-ranging implications in tissue kinetics.* Br J Cancer, 1972. **26**(4): p. 239-57.

8. Wyllie, A.H., J.F. Kerr, and A.R. Currie, *Cell death: the significance of apoptosis.* Int Rev Cytol, 1980. **68**: p. 251-306.

9. Vaux, D.L., S. Cory, and J.M. Adams, *Bcl-2 gene promotes haemopoietic cell survival and cooperates with c-myc to immortalize pre-B cells.* Nature, 1988. **335**(6189): p. 440-2.

10. Lane, D.P., *Cancer. p53, guardian of the genome.* Nature, 1992. **358**(6381): p. 15-6.

11. Donehower, L.A., et al., *Mice deficient for p53 are developmentally normal but susceptible to spontaneous tumours.* Nature, 1992. **356**(6366): p. 215-21.

12. Ashkenazi, A., *Targeting death and decoy receptors of the tumour-necrosis factor superfamily.* Nat Rev Cancer, 2002. **2**(6): p. 420-30.

13. Boldin, M.P., et al., *A novel protein that interacts with the death domain of Fas/APO1 contains a sequence motif related to the death domain.* J Biol Chem, 1995. **270**(14): p. 7795-8.

14. Kischkel, F.C., et al., *Cytotoxicity-dependent APO-1 (Fas/CD95)-associated proteins form a death-inducing signaling complex (DISC) with the receptor.* EMBO J, 1995. **14**(22): p. 5579-88.

15. Chinnaiyan, A.M., et al., *FADD, a novel death domain-containing protein, interacts with the death domain of Fas and initiates apoptosis.* Cell, 1995. **81**(4): p. 505-12.

16. Ghobrial, I.M., T.E. Witzig, and A.A. Adjei, *Targeting apoptosis pathways in cancer therapy.* CA Cancer J Clin, 2005. **55**(3): p. 178-94.

17. Ashkenazi, A., *Directing cancer cells to self-destruct with pro-apoptotic receptor agonists.* Nat Rev Drug Discov, 2008. **7**(12): p. 1001-12.

18. Henry-Mowatt, J., et al., *Role of mitochondrial membrane permeabilization in apoptosis and cancer.* Oncogene, 2004. **23**(16): p. 2850-60.

19. Srinivasula, S.M., et al., *Molecular determinants of the caspase-promoting activity of Smac/DIABLO and its role in the death receptor pathway.* J Biol Chem, 2000. **275**(46): p. 36152-7.

20. Malhi, H. and G.J. Gores, *TRAIL resistance results in cancer progression: a TRAIL to perdition?* Oncogene, 2006. **25**(56): p. 7333-5.

21. Mellier, G., et al., *TRAILing death in cancer.* Mol Aspects Med, 2010. **31**(1): p. 93-112.

22. Boatright, K.M., et al., *A unified model for apical caspase activation.* Mol Cell, 2003. **11**(2): p. 529-41.

23. Cory, S. and J.M. Adams, *The Bcl2 family: regulators of the cellular life-or-death switch.* Nat Rev Cancer, 2002. **2**(9): p. 647-56.

24. Ndebele, K., et al., *Tumor necrosis factor (TNF)-related apoptosis-inducing ligand (TRAIL) induced mitochondrial pathway to apoptosis and caspase activation is potentiated by phospholipid scramblase-3.* Apoptosis, 2008. **13**(7): p. 845-56.

25. Bouralexis, S., D.M. Findlay, and A. Evdokiou, *Death to the bad guys: targeting cancer via Apo2L/TRAIL.* Apoptosis, 2005. **10**(1): p. 35-51.

26. Abdulghani, J. and W.S. El-Deiry, *TRAIL receptor signaling and therapeutics.* Expert Opin Ther Targets, 2010. **14**(10): p. 1091-108.

27. Amm, H.M., et al., *Combined modality therapy with TRAIL or agonistic death receptor antibodies.* Cancer Biol Ther, 2011. **11**(5): p. 431-49.

28. Krakstad, C. and M. Chekenya, *Survival signalling and apoptosis resistance in glioblastomas: opportunities for targeted therapeutics.* Mol Cancer, 2010. **9**: p. 135.

29. Mashima, T. and T. Tsuruo, *Defects of the apoptotic pathway as therapeutic target against cancer.* Drug Resist Updat, 2005. **8**(6): p. 339-43.

30. *clinicaltrials.gov*.

31. Shankar, S. and R.K. Srivastava, *Enhancement of therapeutic potential of TRAIL by cancer chemotherapy and irradiation: mechanisms and clinical implications.* Drug Resist Updat, 2004. **7**(2): p. 139-56.

32. Zhang, L. and B. Fang, *Mechanisms of resistance to TRAIL-induced apoptosis in cancer.* Cancer Gene Ther, 2005. **12**(3): p. 228-37.

33. Ding, L., et al., *Cisplatin Restores TRAIL Apoptotic Pathway in Glioblastoma-Derived Stem Cells through Up-regulation of DR5 and Down-regulation of c-FLIP.* Cancer Invest, 2011. **29**(8): p. 511-20.

34. Kataoka, T., *The caspase-8 modulator c-FLIP.* Crit Rev Immunol, 2005. **25**(1): p. 31-58.

35. Johnson, T.R., et al., *The proteasome inhibitor PS-341 overcomes TRAIL resistance in Bax and caspase 9-negative or Bcl-xL overexpressing cells.* Oncogene, 2003. **22**(32): p. 4953-63.

36. Zhang, L. and B. Fang, *Mechanisms of resistance to TRAIL-induced apoptosis in cancer.* Cancer gene therapy, 2005. **12**(3): p. 228-37.

37. Lee, J.Y., et al., *The NO TRAIL to YES TRAIL in cancer therapy (review).* International journal of oncology, 2007. **31**(4): p. 685-91.

38. Wang, S., *The promise of cancer therapeutics targeting the TNF-related apoptosis-inducing ligand and TRAIL receptor pathway.* Oncogene, 2008. **27**(48): p. 6207-15.

39. Micheau, O., *Cellular FLICE-inhibitory protein: an attractive therapeutic target?* Expert Opin Ther Targets, 2003. **7**(4): p. 559-73.

40. Shirley, S. and O. Micheau, *Targeting c-FLIP in cancer.* Cancer Lett, 2010.

41. Wilson, T.R., et al., *c-FLIP: a key regulator of colorectal cancer cell death.* Cancer Res, 2007. **67**(12): p. 5754-62.

42. Chang, D.W., et al., *c-FLIP(L) is a dual function regulator for caspase-8 activation and CD95-mediated apoptosis.* EMBO J, 2002. **21**(14): p. 3704-14.

43. Safa, A.R. and K.E. Pollok, *Targeting the Anti-Apoptotic Protein c-FLIP for Cancer Therapy.* Cancers (Basel), 2011. **3**(2): p. 1639-1671.

44. Safa, A.R., T.W. Day, and C.H. Wu, *Cellular FLICE-like inhibitory protein (C-FLIP): a novel target for cancer therapy.* Curr Cancer Drug Targets, 2008. **8**(1): p. 37-46.

45. Kataoka, T., et al., *The caspase-8 inhibitor FLIP promotes activation of NF-kappaB and Erk signaling pathways.* Curr Biol, 2000. **10**(11): p. 640-8.

46. Kim, S., et al., *Overexpression of cFLIPs inhibits oxaliplatin-mediated apoptosis through enhanced XIAP stability and Akt activation in human renal cancer cells.* J Cell Biochem, 2008. **105**(4): p. 971-9.

47. Li, F.Y., et al., *Crystal structure of a viral FLIP: insights into FLIP-mediated inhibition of death receptor signaling.* J Biol Chem, 2006. **281**(5): p. 2960-8.

48. Budd, R.C., W.C. Yeh, and J. Tschopp, *cFLIP regulation of lymphocyte activation and development.* Nat Rev Immunol, 2006. **6**(3): p. 196-204.

49. Leverkus, M., P. Diessenbacher, and P. Geserick, *FLIP ing the coin? Death receptor-mediated signals during skin tumorigenesis.* Exp Dermatol, 2008. **17**(7): p. 614-22.

50. Guicciardi, M.E. and G.J. Gores, *Life and death by death receptors.* FASEB J, 2009. **23**(6): p. 1625-37.

51. Fisher, M.J., et al., *Nucleotide substitution in the ectodomain of trail receptor DR4 is associated with lung cancer and head and neck cancer.* Clin Cancer Res, 2001. **7**(6): p. 1688-97.

52. Lee, S.H., et al., *Alterations of the DR5/TRAIL receptor 2 gene in non-small cell lung cancers.* Cancer Res, 1999. **59**(22): p. 5683-6.

53. Chen, X., et al., *Constitutively active Akt is an important regulator of TRAIL sensitivity in prostate cancer.* Oncogene, 2001. **20**(42): p. 6073-83.

54. Pai, S.I., et al., *Rare loss-of-function mutation of a death receptor gene in head and neck cancer.* Cancer Res, 1998. **58**(16): p. 3513-8.

55. Shin, M.S., et al., *Mutations of tumor necrosis factor-related apoptosis-inducing ligand receptor 1 (TRAIL-R1) and receptor 2 (TRAIL-R2) genes in metastatic breast cancers.* Cancer Res, 2001. **61**(13): p. 4942-6.

56. Horak, P., et al., *Contribution of epigenetic silencing of tumor necrosis factor-related apoptosis inducing ligand receptor 1 (DR4) to TRAIL resistance and ovarian cancer.* Mol Cancer Res, 2005. **3**(6): p. 335-43.

57. Moriwaki, K., S. Shinzaki, and E. Miyoshi, *GDP-mannose-4,6-dehydratase (GMDS) deficiency renders colon cancer cells resistant to tumor necrosis factor-related apoptosis-inducing ligand (TRAIL) receptor- and CD95-mediated apoptosis by inhibiting complex II formation.* J Biol Chem, 2011. **286**(50): p. 43123-33.

58. LaCasse, E.C., et al., *IAP-targeted therapies for cancer.* Oncogene, 2008. **27**(48): p. 6252-75.

59. Chawla-Sarkar, M., et al., *Downregulation of Bcl-2, FLIP or IAPs (XIAP and survivin) by siRNAs sensitizes resistant melanoma cells to Apo2L/TRAIL-induced apoptosis.* Cell Death Differ, 2004. **11**(8): p. 915-23.

60. Ndozangue-Touriguine, O., et al., *A mitochondrial block and expression of XIAP lead to resistance to TRAIL-induced apoptosis during progression to metastasis of a colon carcinoma.* Oncogene, 2008. **27**(46): p. 6012-22.

61. Lee, T.J., et al., *Acquired TRAIL resistance in human breast cancer cells are caused by the sustained cFLIP(L) and XIAP protein levels and ERK activation.* Biochem Biophys Res Commun, 2006. **351**(4): p. 1024-30.

62. Lippa, M.S., et al., *Expression of anti-apoptotic factors modulates Apo2L/TRAIL resistance in colon carcinoma cells.* Apoptosis, 2007. **12**(8): p. 1465-78.

63. Mori, T., et al., *Effect of the XIAP inhibitor Embelin on TRAIL-induced apoptosis of pancreatic cancer cells.* J Surg Res, 2007. **142**(2): p. 281-6.

64. Gill, C., et al., *Effects of cIAP-1, cIAP-2 and XIAP triple knockdown on prostate cancer cell susceptibility to apoptosis, cell survival and proliferation.* Mol Cancer, 2009. **8**: p. 39.

65. Shrader, M., et al., *Gefitinib reverses TRAIL resistance in human bladder cancer cell lines via inhibition of AKT-mediated X-linked inhibitor of apoptosis protein expression.* Cancer Res, 2007. **67**(4): p. 1430-5.

66. Symanowski, J., et al., *A histone deacetylase inhibitor LBH589 downregulates XIAP in mesothelioma cell lines which is likely responsible for increased apoptosis with TRAIL.* J Thorac Oncol, 2009. **4**(2): p. 149-60.

67. Lee, T.J., et al., *Mithramycin A sensitizes cancer cells to TRAIL-mediated apoptosis by down-regulation of XIAP gene promoter through Sp1 sites.* Mol Cancer Ther, 2006. **5**(11): p. 2737-46.

68. Kang, J., et al., *Chemical sensitization and regulation of TRAIL-induced apoptosis in a panel of B-lymphocytic leukaemia cell lines.* Br J Haematol, 2003. **123**(5): p. 921-32.

69. Psahoulia, F.H., et al., *Quercetin enhances TRAIL-mediated apoptosis in colon cancer cells by inducing the accumulation of death receptors in lipid rafts.* Mol Cancer Ther, 2007. **6**(9): p. 2591-9.

70. Siegelin, M.D., et al., *Quercetin promotes degradation of survivin and thereby enhances death-receptor-mediated apoptosis in glioma cells.* Neuro Oncol, 2009. **11**(2): p. 122-31.

71. Ganapathy, S., et al., *Resveratrol enhances antitumor activity of TRAIL in prostate cancer xenografts through activation of FOXO transcription factor.* PLoS One, 2010. **5**(12): p. e15627.

73. Deeb, D., et al., *Curcumin [1,7-bis(4-hydroxy-3-methoxyphenyl)-1-6-heptadine-3,5-dione; C21H20O6] sensitizes human prostate cancer cells to tumor necrosis factor-related apoptosis-inducing ligand/Apo2L-induced apoptosis by suppressing nuclear factor-kappaB via inhibition of the prosurvival Akt signaling pathway.* J Pharmacol Exp Ther, 2007. **321**(2): p. 616-25.

74. Poh, T.W., et al., *LY303511 amplifies TRAIL-induced apoptosis in tumor cells by enhancing DR5 oligomerization, DISC assembly, and mitochondrial permeabilization.* Cell Death Differ, 2007. **14**(10): p. 1813-25.

75. Shenoy, K., Y. Wu, and S. Pervaiz, *LY303511 enhances TRAIL sensitivity of SHEP-1 neuroblastoma cells via hydrogen peroxide-mediated mitogen-activated protein kinase activation and up-regulation of death receptors.* Cancer Res, 2009. **69**(5): p. 1941-50.

76. Thayaparasingham, B., et al., *Sensitization of melanoma cells to TRAIL by UVB-induced and NF-kappaB-mediated downregulation of xIAP.* Oncogene, 2009. **28**(3): p. 345-62.

77. Baritaki, S., et al., *Chemotherapeutic drugs sensitize cancer cells to TRAIL-mediated apoptosis: up-regulation of DR5 and inhibition of Yin Yang 1.* Mol Cancer Ther, 2007. **6**(4): p. 1387-99.

78. Lee, J.Y., et al., *The NO TRAIL to YES TRAIL in cancer therapy (review).* Int J Oncol, 2007. **31**(4): p. 685-91.

79. Kwon, D., et al., *Hydrogen peroxide enhances TRAIL-induced cell death through up-regulation of DR5 in human astrocytic cells.* Biochem Biophys Res Commun, 2008. **372**(4): p. 870-4.

80. Hernandez, A., et al., *Sensitization of human colon cancer cells to TRAIL-mediated apoptosis.* J Gastrointest Surg, 2001. **5**(1): p. 56-65.

81. Kauh, J., et al., *c-FLIP degradation mediates sensitization of pancreatic cancer cells to TRAIL-induced apoptosis by the histone deacetylase inhibitor LBH589.* PLoS One, 2010. **5**(4): p. e10376.

82. Prasad, S., et al., *ROS and CHOP are critical for dibenzylideneacetone to sensitize tumor cells to TRAIL through induction of death receptors and downregulation of cell survival proteins.* Cancer Res, 2011. **71**(2): p. 538-49.

83. Muhlethaler-Mottet, A., et al., *Drug-mediated sensitization to TRAIL-induced apoptosis in caspase-8-complemented neuroblastoma cells proceeds via activation of intrinsic and extrinsic pathways and caspase-dependent cleavage of XIAP, Bcl-xL and RIP.* Oncogene, 2004. **23**(32): p. 5415-25.

84. Davies, S.P., et al., *Specificity and mechanism of action of some commonly used protein kinase inhibitors.* The Biochemical journal, 2000. **351**(Pt 1): p. 95-105.

85. Poh, T.W. and S. Pervaiz, *LY294002 and LY303511 sensitize tumor cells to drug-induced apoptosis via intracellular hydrogen peroxide production independent of the phosphoinositide 3-kinase-Akt pathway.* Cancer Res, 2005. **65**(14): p. 6264-74.

86. Gharbi, S.I., et al., *Exploring the specificity of the PI3K family inhibitor LY294002.* The Biochemical journal, 2007. **404**(1): p. 15-21.

87. Jacobs, M.D., et al., *Pim-1 ligand-bound structures reveal the mechanism of serine/threonine kinase inhibition by LY294002.* The Journal of biological chemistry, 2005. **280**(14): p. 13728-34.

88. Poh, T.W., et al., *LY303511 amplifies TRAIL-induced apoptosis in tumor cells by enhancing DR5 oligomerization, DISC assembly, and mitochondrial permeabilization.* Cell death and differentiation, 2007. **14**(10): p. 1813-25.

89. Poh, T.W. and S. Pervaiz, *LY294002 and LY303511 sensitize tumor cells to drug-induced apoptosis via intracellular hydrogen peroxide production independent of the phosphoinositide 3-kinase-Akt pathway.* Cancer research, 2005. **65**(14): p. 6264-74.

90. Shenoy, K., Y. Wu, and S. Pervaiz, *LY303511 enhances TRAIL sensitivity of SHEP-1 neuroblastoma cells via hydrogen peroxide-mediated mitogen-activated protein kinase activation and up-regulation of death receptors.* Cancer research, 2009. **69**(5): p. 1941-50.

91. Piras, V., et al., *Enhancing apoptosis in TRAIL-resistant cancer cells using fundamental response rules.* Sci Rep, 2011. **1**: p. 144.

92. Orrenius, S., *Reactive oxygen species in mitochondria-mediated cell death.* Drug Metab Rev, 2007. **39**(2-3): p. 443-55.

93. Houot, V., et al., *Hydrogen peroxide induces programmed cell death features in cultured tobacco BY-2 cells, in a dose-dependent manner.* J Exp Bot, 2001. **52**(361): p. 1721-30.

94. Pellinen, R.I., et al., *Hydrogen peroxide activates cell death and defense gene expression in birch.* Plant Physiol, 2002. **130**(2): p. 549-60.

95. Dumont, A., et al., *Hydrogen peroxide-induced apoptosis is CD95-independent, requires the release of mitochondria-derived reactive oxygen species and the activation of NF-kappaB.* Oncogene, 1999. **18**(3): p. 747-57.

96. Chen, L., et al., *Hydrogen peroxide-induced neuronal apoptosis is associated with inhibition of protein phosphatase 2A and 5, leading to activation of MAPK pathway.* Int J Biochem Cell Biol, 2009. **41**(6): p. 1284-95.

97. El-Kholy, W., et al., *The phosphatidylinositol 3-kinase inhibitor LY294002 potently blocks K(V) currents via a direct mechanism.* FASEB J, 2003. **17**(6): p. 720-2.

98. Kristof, A.S., et al., *LY303511 (2-piperazinyl-8-phenyl-4H-1-benzopyran-4-one) acts via phosphatidylinositol 3-kinase-independent pathways to inhibit cell proliferation via mammalian target of rapamycin (mTOR)- and non-mTOR-dependent mechanisms.* J Pharmacol Exp Ther, 2005. **314**(3): p. 1134-43.

99. D'Autreaux, B. and M.B. Toledano, *ROS as signalling molecules: mechanisms that generate specificity in ROS homeostasis.* Nat Rev Mol Cell Biol, 2007. **8**(10): p. 813-24.

100. Apel, K. and H. Hirt, *Reactive oxygen species: metabolism, oxidative stress, and signal transduction.* Annu Rev Plant Biol, 2004. **55**: p. 373-99.

101. Turrens, J.F., *Superoxide production by the mitochondrial respiratory chain.* Biosci Rep, 1997. **17**(1): p. 3-8.

102. Liu, Y., G. Fiskum, and D. Schubert, *Generation of reactive oxygen species by the mitochondrial electron transport chain.* J Neurochem, 2002. **80**(5): p. 780-7.

103. McLennan, H.R. and M. Degli Esposti, *The contribution of mitochondrial respiratory complexes to the production of reactive oxygen species.* J Bioenerg Biomembr, 2000. **32**(2): p. 153-62.

104. Chen, Q., et al., *Production of reactive oxygen species by mitochondria: central role of complex III.* J Biol Chem, 2003. **278**(38): p. 36027-31.

105. Yeldandi, A.V., M.S. Rao, and J.K. Reddy, *Hydrogen peroxide generation in peroxisome proliferator-induced oncogenesis.* Mutat Res, 2000. **448**(2): p. 159-77.

106. Li, Y., et al., *Expression of the hydrogen peroxide-generating enzyme fatty acyl CoA oxidase activates NF-kappaB.* DNA Cell Biol, 2000. **19**(2): p. 113-20.

107. Baudhuin, P., *Liver peroxisomes, cytology and function.* Ann N Y Acad Sci, 1969. **168**(2): p. 214-28.

108. Bedard, K. and K.H. Krause, *The NOX family of ROS-generating NADPH oxidases: physiology and pathophysiology.* Physiol Rev, 2007. **87**(1): p. 245-313.

109. McCord, J.M. and I. Fridovich, *Superoxide dismutase. An enzymic function for erythrocuprein (hemocuprein).* J Biol Chem, 1969. **244**(22): p. 6049-55.

110. Rhee, S.G., *Redox signaling: hydrogen peroxide as intracellular messenger.* Exp Mol Med, 1999. **31**(2): p. 53-9.

111. Levine, A., et al., *H2O2 from the oxidative burst orchestrates the plant hypersensitive disease resistance response.* Cell, 1994. **79**(4): p. 583-93.

112. Alvarez, M.E., et al., *Reactive oxygen intermediates mediate a systemic signal network in the establishment of plant immunity.* Cell, 1998. **92**(6): p. 773-84.

113. Benhar, M., D. Engelberg, and A. Levitzki, *ROS, stress-activated kinases and stress signaling in cancer.* EMBO Rep, 2002. **3**(5): p. 420-5.

114. Kamata, H. and H. Hirata, *Redox regulation of cellular signalling.* Cell Signal, 1999. **11**(1): p. 1-14.

115. Benhar, M., et al., *Enhanced ROS production in oncogenically transformed cells potentiates c-Jun N-terminal kinase and p38 mitogen-activated protein kinase activation and sensitization to genotoxic stress.* Mol Cell Biol, 2001. **21**(20): p. 6913-26.

116. Smirnoff, N. and G.L. Wheeler, *Ascorbic acid in plants: biosynthesis and function.* Crit Rev Biochem Mol Biol, 2000. **35**(4): p. 291-314.

117. Mittler, R., *Oxidative stress, antioxidants and stress tolerance.* Trends Plant Sci, 2002. **7**(9): p. 405-10.

118. Gill, S.S. and N. Tuteja, *Reactive oxygen species and antioxidant machinery in abiotic stress tolerance in crop plants.* Plant Physiol Biochem, 2010. **48**(12): p. 909-30.

119. Dougall, W.C. and H.S. Nick, *Manganese superoxide dismutase: a hepatic acute phase protein regulated by interleukin-6 and glucocorticoids.* Endocrinology, 1991. **129**(5): p. 2376-84.

120. Crapo, J.D., et al., *Copper,zinc superoxide dismutase is primarily a cytosolic protein in human cells.* Proc Natl Acad Sci U S A, 1992. **89**(21): p. 10405-9.

121. Pinto, A.L., H.W. Hellinga, and J.P. Caradonna, *Construction of a catalytically active iron superoxide dismutase by rational protein design.* Proc Natl Acad Sci U S A, 1997. **94**(11): p. 5562-7.

122. Mates, J.M., et al., *Intracellular redox status and oxidative stress: implications for cell proliferation, apoptosis, and carcinogenesis.* Arch Toxicol, 2008. **82**(5): p. 273-99.

123. Fiers, W., et al., *More than one way to die: apoptosis, necrosis and reactive oxygen damage.* Oncogene, 1999. **18**(54): p. 7719-30.

124. Martindale, J.L. and N.J. Holbrook, *Cellular response to oxidative stress: signaling for suicide and survival.* J Cell Physiol, 2002. **192**(1): p. 1-15.

125. Bubici, C., et al., *Mutual cross-talk between reactive oxygen species and nuclear factor-kappa B: molecular basis and biological significance.* Oncogene, 2006. **25**(51): p. 6731-48.

126. Pap, M. and G.M. Cooper, *Role of glycogen synthase kinase-3 in the phosphatidylinositol 3-Kinase/Akt cell survival pathway.* J Biol Chem, 1998. **273**(32): p. 19929-32.

127. Jing, Y., et al., *Arsenic trioxide selectively induces acute promyelocytic leukemia cell apoptosis via a hydrogen peroxide-dependent pathway.* Blood, 1999. **94**(6): p. 2102-11.

128. Denning, M.F., et al., *Activation of the epidermal growth factor receptor signal transduction pathway stimulates tyrosine phosphorylation of protein kinase C delta.* J Biol Chem, 1996. **271**(10): p. 5325-31.

129. Derynck, R. and Y.E. Zhang, *Smad-dependent and Smad-independent pathways in TGF-beta family signalling.* Nature, 2003. **425**(6958): p. 577-84.

130. Larrick, J.W. and S.C. Wright, *Cytotoxic mechanism of tumor necrosis factor-alpha.* FASEB J, 1990. **4**(14): p. 3215-23.

131. Catlett-Falcone, R., et al., *Constitutive activation of Stat3 signaling confers resistance to apoptosis in human U266 myeloma cells.* Immunity, 1999. **10**(1): p. 105-15.

132. Di-Poi, N., et al., *Antiapoptotic role of PPARbeta in keratinocytes via transcriptional control of the Akt1 signaling pathway.* Mol Cell, 2002. **10**(4): p. 721-33.

133. Berridge, M.J., P. Lipp, and M.D. Bootman, *The versatility and universality of calcium signalling.* Nat Rev Mol Cell Biol, 2000. **1**(1): p. 11-21.

134. Yu, F.H. and W.A. Catterall, *Overview of the voltage-gated sodium channel family.* Genome Biol, 2003. **4**(3): p. 207.

135. Kitano, H., *Computational systems biology.* Nature, 2002. **420**(6912): p. 206-10.

136. Liu, B., *Probabilistic Approximation and Analysis Techniques for Bio-Pathway Models*, 2011, National University of Singapore.

137. Papin, J.A. and B.O. Palsson, *Topological analysis of mass-balanced signaling networks: a framework to obtain network properties including crosstalk.* J Theor Biol, 2004. **227**(2): p. 283-97.

138. Vaseghi, S., et al., *Signal transduction dynamics of the protein kinase-A/phosphofructokinase-2 system in Saccharomyces cerevisiae.* Metab Eng, 2001. **3**(2): p. 163-72.

139. Priami, C., *Computational methods in systems biology*2003: Springer.

140. Suderman, M. and M. Hallett, *Tools for visually exploring biological networks.* Bioinformatics, 2007. **23**(20): p. 2651-9.

141. Breitling, R., et al., *A structured approach for the engineering of biochemical network models, illustrated for signalling pathways.* Brief Bioinform, 2008. **9**(5): p. 404-21.

142. Albeck, J.G., et al., *Quantitative analysis of pathways controlling extrinsic apoptosis in single cells.* Mol Cell, 2008. **30**(1): p. 11-25.

143. Albeck, J.G., et al., *Modeling a snap-action, variable-delay switch controlling extrinsic cell death.* PLoS Biol, 2008. **6**(12): p. 2831-52.

144. Zhang, T., et al., *Investigation into the regulation mechanisms of TRAIL apoptosis pathway by mathematical modeling.* Acta Biochim Biophys Sin (Shanghai), 2010. **42**(2): p. 98-108.

145. Kojima, H., et al., *Detection and imaging of nitric oxide with novel fluorescent indicators: diaminofluoresceins.* Anal Chem, 1998. **70**(13): p. 2446-53.

146. Carter, W.O., P.K. Narayanan, and J.P. Robinson, *Intracellular hydrogen peroxide and superoxide anion detection in endothelial cells.* J Leukoc Biol, 1994. **55**(2): p. 253-8.

147. Afanas'ev, I.B., *Lucigenin chemiluminescence assay for superoxide detection.* Circ Res, 2001. **89**(11): p. E46.

148. *http://www.nationaldiagnostics.com/article_info.php/articles_id/133*.

149. Wong, L.C., et al., *Fully-automated image processing software to analyze calcium traces in populations of single cells.* Cell Calcium, 2010. **48**(5): p. 270-4.

150. White, J.E.T.J.F.A.A.R.C.B.T.J., *Recycling Circuit Simulation Techniques for Mass-Action Biochemical Kinetics*, in *Advanced Simulation and Verification of Electronic and Biological Systems*2011. p. 115-136

151. Hoops, S., et al., *COPASI--a COmplex PAthway SImulator.* Bioinformatics, 2006. **22**(24): p. 3067-74.

152. Albeck, J.G., et al., *Quantitative analysis of pathways controlling extrinsic apoptosis in single cells.* Molecular cell, 2008. **30**(1): p. 11-25.

153. *Plot : Main - Home Page browse*.

154. *Plot Introduction*, http://plot.micw.eu/Doc/Plot.

155. McStay, G.P., G.S. Salvesen, and D.R. Green, *Overlapping cleavage motif selectivity of caspases: implications for analysis of apoptotic pathways.* Cell Death Differ, 2008. **15**(2): p. 322-31.

156. Murphy, K.P., *The Bayes Net Toolbox for Matlab.* Computing Science and Statistics: Proceedings of Interface,, 2001.

157. Francois, P.L.O., *BNT Structure Learning Package: Documentation and Experiments*, 2004.

158. D., D.A.L.N.R., *Maximum likelihood from incompete data via the EM algorithm.* Journal of the Royal Statistical Society, 1977. **39**: p. 38.

159. Pearl, J. *Reverend Bayes on inference engines: A distributed hierarchical approach*. in *Proceedings of the Second National Conference on Artificial Intelligence*. 1982.

160. Sachs, K., et al., *Causal protein-signaling networks derived from multiparameter single-cell data.* Science, 2005. **308**(5721): p. 523-9.

161. Ross, T.C.I.S.J., *Toward a systematic determination of complex reaction mechanisms.* J. Phys. Chem, 1993. **97**(26): p. 12.

162. HIRSCH, M.W., SMALE, S., AND DEVANEY, R. L., ed. *Differential Equations, Dynamical Systems and In Introduction to Chaos. 2 edition., 2004.* 2nd ed. Elsevier2004.

163. Lavrik, I.N., *Systems biology of apoptosis signaling networks.* Curr Opin Biotechnol, 2010. **21**(4): p. 551-5.

164. Spencer, S.L. and P.K. Sorger, *Measuring and modeling apoptosis in single cells.* Cell, 2011. **144**(6): p. 926-39.

165. Lavrik, I.N., et al., *Understanding apoptosis by systems biology approaches.* Mol Biosyst, 2009. **5**(10): p. 1105-11.

166. Nakamura, K., et al., *Parameter estimation of in silico biological pathways with particle filtering towards a petascale computing.* Pac Symp Biocomput, 2009: p. 227-38.

167. Moles, C.G., P. Mendes, and J.R. Banga, *Parameter estimation in biochemical pathways: a comparison of global optimization methods.* Genome Res, 2003. **13**(11): p. 2467-74.

168. Koh, G., et al., *A decompositional approach to parameter estimation in pathway modeling: a case study of the Akt and MAPK pathways and their crosstalk.* Bioinformatics, 2006. **22**(14): p. e271-80.

169. Fujarewicz, K., et al., *Adjoint systems for models of cell signaling pathways and their application to parameter fitting.* IEEE/ACM Trans Comput Biol Bioinform, 2007. **4**(3): p. 322-35.

170. Wolkenhauer, K.-H.C.S.-Y.S.W.K.O., *Experimental Design in Systems Biology,Based on Parameter Sensitivity Analysis Using a Monte Carlo Method: A Case Study for the TNFα-Mediated NF-κB Signal Transduction Pathway.* SIMULATION,, 2003. **Vol. 79,** (Issue 11–12).

171. Yang, K., et al., *Finding multiple target optimal intervention in disease-related molecular network.* Mol Syst Biol, 2008. **4**: p. 228.

172. de Pillis, L.G., A.E. Radunskaya, and C.L. Wiseman, *A validated mathematical model of cell-mediated immune response to tumor growth.* Cancer Res, 2005. **65**(17): p. 7950-8.

173. Bentele, M., et al., *Mathematical modeling reveals threshold mechanism in CD95-induced apoptosis.* J Cell Biol, 2004. **166**(6): p. 839-51.

174. von Dassow, G., et al., *The segment polarity network is a robust developmental module.* Nature, 2000. **406**(6792): p. 188-92.

175. Salter, M.K., R. G.; Pogson,, *Metabolic control.* Essays Biochem 1994(28): p. 12.

176. Chan, A.S.S.T.K.P.-S., *A Quantitative Model-Independent Method for Global Sensitivity Analysis of Model Output.* Technometrics, 1999. **41**(1): p. 18.

177. Wolkenhauer, K.-h.C.W.K.O., *Experimental design in systems biology, based on parameter sensitivity analysis using a Monte Carlo method: A case study for the TNFα-mediated NF-κB signal transduction pathway* SIMULATION,, 2003.

178. Stennicke, H.R., et al., *Pro-caspase-3 is a major physiologic target of caspase-8.* J Biol Chem, 1998. **273**(42): p. 27084-90.

179. Tewari, M., et al., *Yama/CPP32 beta, a mammalian homolog of CED-3, is a CrmA-inhibitable protease that cleaves the death substrate poly(ADP-ribose) polymerase.* Cell, 1995. **81**(5): p. 801-9.

180. Cowling, V. and J. Downward, *Caspase-6 is the direct activator of caspase-8 in the cytochrome c-induced apoptosis pathway: absolute requirement for removal of caspase-6 prodomain.* Cell Death Differ, 2002. **9**(10): p. 1046-56.

181. Eissing, T., et al., *Bistability analyses of a caspase activation model for receptor-induced apoptosis.* The Journal of biological chemistry, 2004. **279**(35): p. 36892-7.

182. Bagci, E.Z., et al., *Bistability in apoptosis: roles of bax, bcl-2, and mitochondrial permeability transition pores.* Biophysical journal, 2006. **90**(5): p. 1546-59.

183. Kreuz, S., et al., *NF-kappaB inducers upregulate cFLIP, a cycloheximide-sensitive inhibitor of death receptor signaling.* Molecular and cellular biology, 2001. **21**(12): p. 3964-73.

184. Nitobe, J., et al., *Reactive oxygen species regulate FLICE inhibitory protein (FLIP) and susceptibility to Fas-mediated apoptosis in cardiac myocytes.* Cardiovascular research, 2003. **57**(1): p. 119-28.

185. Pervaiz, S. and M.-V. Clément, *A permissive apoptotic environment: function of a decrease in intracellular superoxide anion and cytosolic acidification.* Biochemical and biophysical research communications, 2002. **290**(4): p. 1145-50.

186. Yamakawa, H., et al., *Activation of caspase-9 and -3 during H2O2-induced apoptosis of PC12 cells independent of ceramide formation.* Neurol Res, 2000. **22**(6): p. 556-64.

187. Pervaiz, S. and M.-V. Clement, *Superoxide anion: oncogenic reactive oxygen species?* The international journal of biochemistry & cell biology, 2007. **39**(7-8): p. 1297-304.

188. Akram, S., et al., *Reactive oxygen species-mediated regulation of the Na+-H+ exchanger 1 gene expression connects intracellular redox status with cells' sensitivity to death triggers.* Cell Death Differ, 2006. **13**(4): p. 628-41.

189. Zuo, Y., et al., *Oxidative modification of caspase-9 facilitates its activation via disulfide-mediated interaction with Apaf-1.* Cell Res, 2009. **19**(4): p. 449-57.

190. Cardoso, S.M., et al., *Apoptotic cell death induced by hydrogen peroxide in NT2 parental and mitochondrial DNA depleted cells.* Neurochem Int, 2004. **45**(5): p. 693-8.

191. Albeck, J.G., et al., *Modeling a snap-action, variable-delay switch controlling extrinsic cell death.* PLoS biology, 2008. **6**(12): p. 2831-52.

192. Peter, M.E., *The flip side of FLIP.* Biochem J, 2004. **382**(Pt 2): p. e1-3.

193. Fukazawa, T., et al., *Accelerated degradation of cellular FLIP protein through the ubiquitin-proteasome pathway in p53-mediated apoptosis of human cancer cells.* Oncogene, 2001. **20**(37): p. 5225-31.

194. Lee, T.J., et al., *Withaferin A sensitizes TRAIL-induced apoptosis through reactive oxygen species-mediated up-regulation of death receptor 5 and down-regulation of c-FLIP.* Free Radic Biol Med, 2009. **46**(12): p. 1639-49.

195. Clément, M.V. and S. Pervaiz, *Intracellular superoxide and hydrogen peroxide concentrations: a critical balance that determines survival or death.* Redox report : communications in free radical research, 2001. **6**(4): p. 211-4.

196. Tang, H., et al., *The scavenging of superoxide radicals promotes apoptosis induced by a novel cell-permeable fusion protein, sTRAIL:FeSOD, in tumor necrosis factor-related apoptosis-inducing ligand-resistant leukemia cells.* BMC Biol, 2011. **9**: p. 18.

197. Lim, S. and M.V. Clement, *Phosphorylation of the survival kinase Akt by superoxide is dependent on an ascorbate-reversible oxidation of PTEN.* Free Radic Biol Med, 2007. **42**(8): p. 1178-92.

198. Zhu, P., et al., *Angiopoietin-like 4 protein elevates the prosurvival intracellular O2(-):H2O2 ratio and confers anoikis resistance to tumors.* Cancer Cell, 2011. **19**(3): p. 401-15.

199. Trachootham, D., et al., *Redox regulation of cell survival.* Antioxid Redox Signal, 2008. **10**(8): p. 1343-74.

200. Gibellini, L.P., M.; Nasi, M.; De Biasi, S.; Roat, E.; Bertoncelli, L.; Cossarizza, A. , *Interfering with ROS Metabolism in Cancer Cells: The Potential Role of Quercetin.* . Cancers, 2010. **2**: p. 24.

201. Iyer, A.K., et al., *Role of S-nitrosylation in apoptosis resistance and carcinogenesis.* Nitric Oxide, 2008. **19**(2): p. 146-51.

202. Ivanov, V.N., et al., *Resveratrol sensitizes melanomas to TRAIL through modulation of antiapoptotic gene expression.* Exp Cell Res, 2008. **314**(5): p. 1163-76.

203. Juan, M.E., et al., *Resveratrol induces apoptosis through ROS-dependent mitochondria pathway in HT-29 human colorectal carcinoma cells.* J Agric Food Chem, 2008. **56**(12): p. 4813-8.

204. Geserick, P., et al., *Suppression of cFLIP is sufficient to sensitize human melanoma cells to TRAIL- and CD95L-mediated apoptosis.* Oncogene, 2008. **27**(22): p. 3211-20.

205. Hietakangas, V., et al., *Erythroid differentiation sensitizes K562 leukemia cells to TRAIL-induced apoptosis by downregulation of c-FLIP.* Mol Cell Biol, 2003. **23**(4): p. 1278-91.

206. Kim, Y.H., et al., *Rosiglitazone promotes tumor necrosis factor-related apoptosis-inducing ligand-induced apoptosis by reactive oxygen species-mediated up-regulation of death receptor 5 and down-regulation of c-FLIP.* Free Radic Biol Med, 2008. **44**(6): p. 1055-68.

207. Krueger, A., et al., *Cellular FLICE-inhibitory protein splice variants inhibit different steps of caspase-8 activation at the CD95 death-inducing signaling complex.* J Biol Chem, 2001. **276**(23): p. 20633-40.

208. Eissing, T., et al., *Bistability analyses of a caspase activation model for receptor-induced apoptosis.* J Biol Chem, 2004. **279**(35): p. 36892-7.

209. Smieja, J., et al., *Model-based analysis of interferon-beta induced signaling pathway.* Bioinformatics, 2008. **24**(20): p. 2363-9.

210. Hua, F., et al., *Effects of Bcl-2 levels on Fas signaling-induced caspase-3 activation: molecular genetic tests of computational model predictions.* J Immunol, 2005. **175**(2): p. 985-95.

211. Zimmerman, M.C. and I.H. Zucker, *Mitochondrial dysfunction and mitochondrial-produced reactive oxygen species: new targets for neurogenic hypertension?* Hypertension, 2009. **53**(2): p. 112-4.

212. Rocha, M., et al., *Mitochondria-targeted antioxidant peptides.* Curr Pharm Des, 2010. **16**(28): p. 3124-31.

213. Migdal, C. and M. Serres, *[Reactive oxygen species and oxidative stress].* Med Sci (Paris), 2011. **27**(4): p. 405-12.

214. Audi, S.H., et al., *Pulmonary arterial endothelial cells affect the redox status of coenzyme Q0.* Free Radic Biol Med, 2003. **34**(7): p. 892-907.

215. Mitochondria, T.E.T.S.o. *http://www.ruf.rice.edu/~bioslabs/studies/mitochondria/mitets.html*.

216. Isabel A. Abreu, A.H., Haiqain An, Harry S. Nick, David N. Silverman, and Diane E. Cabelli, *The Kinetic Mechanism of Manganese-Containing Superoxide Dismutase from Deinococcus radiodurans: A Specialized Enzyme for the Elimination of High Superoxide Concentrations.* Biochemstry, 2008. **47**(8): p. 2350-2356.

217. Flohe, L., et al., *Glutathione peroxidase, V. The kinetic mechanism.* Hoppe Seylers Z Physiol Chem, 1972. **353**(6): p. 987-99.

218. Privalle, C.T. and I. Fridovich, *Anaerobic biosynthesis of the manganese-containing superoxide dismutase in Escherichia coli. Effects of diazenedicarboxylic acid bis(N,N'-dimethylamide) (diamide).* J Biol Chem, 1990. **265**(35): p. 21966-70.

219. Lee, B.G.K.J.H., *Determination of Hydroperoxyl/superoxide Anion Radical (HO2·/O2·−) Concentration in the Decomposition of Ozone Using a Kinetic Method.* Bull. Korean Chem. Soc. , 2006. **27**(11).

220. Flohe, L., *Glutathione peroxidase: fact and fiction.* Ciba Found Symp, 1978(65): p. 95-122.

221. Pinto, A.S.F.A.R.E., *Kinetic Modelling of in Vitro Lipid Peroxidation Experiments - 'Low Level' Validation of a Model of in Vivo Lipid Peroxidation.* Free Radical Research, 1995. **23**(2): p. 151-172.

222. Buettner, G.R., et al., *A new paradigm: manganese superoxide dismutase influences the production of H2O2 in cells and thereby their biological state.* Free Radic Biol Med, 2006. **41**(8): p. 1338-50.

223. 5-(and-6)-Carboxy-2', -.D.D.C.-D., *http://products.invitrogen.com/ivgn/product/C369.*

224. *http://probes.invitrogen.com/media/pis/mp36008.pdf MitoSOX™ Red mitochondrial superoxide indicator* for live-cell.*

225. Wei, C., *Localization and modelling of LY303511 induced ROS generation in LNCaP cells*, in *Department of Physiology*2009, National University of Singapore: Singapore.

226. Yokoyama, H., et al., *Targeting reactive oxygen species, reactive nitrogen species and inflammation in MPTP neurotoxicity and Parkinson's disease.* Neurol Sci, 2008. **29**(5): p. 293-301.

227. Cleeter, M.W., et al., *Reversible inhibition of cytochrome c oxidase, the terminal enzyme of the mitochondrial respiratory chain, by nitric oxide. Implications for neurodegenerative diseases.* FEBS Lett, 1994. **345**(1): p. 50-4.

228. Brookes, P.S., et al., *Calcium, ATP, and ROS: a mitochondrial love-hate triangle.* Am J Physiol Cell Physiol, 2004. **287**(4): p. C817-33.

229. Brown, G.C. and V. Borutaite, *Interactions between nitric oxide, oxygen, reactive oxygen species and reactive nitrogen species.* Biochem Soc Trans, 2006. **34**(Pt 5): p. 953-6.

230. Patel, R.P., et al., *Biological aspects of reactive nitrogen species.* Biochim Biophys Acta, 1999. **1411**(2-3): p. 385-400.

231. Grisham, M.B., D. Jourd'Heuil, and D.A. Wink, *Nitric oxide. I. Physiological chemistry of nitric oxide and its metabolites:implications in inflammation.* Am J Physiol, 1999. **276**(2 Pt 1): p. G315-21.

232. Beckman, J.S. and W.H. Koppenol, *Nitric oxide, superoxide, and peroxynitrite: the good, the bad, and ugly.* Am J Physiol, 1996. **271**(5 Pt 1): p. C1424-37.

233. Poderoso, J.J., et al., *The regulation of mitochondrial oxygen uptake by redox reactions involving nitric oxide and ubiquinol.* J Biol Chem, 1999. **274**(53): p. 37709-16.

234. Alderton, W.K., C.E. Cooper, and R.G. Knowles, *Nitric oxide synthases: structure, function and inhibition.* Biochem J, 2001. **357**(Pt 3): p. 593-615.

235. Brown, G.C., *Regulation of mitochondrial respiration by nitric oxide inhibition of cytochrome c oxidase.* Biochim Biophys Acta, 2001. **1504**(1): p. 46-57.

236. McAndrew, J., et al., *The interplay of nitric oxide and peroxynitrite with signal transduction pathways: implications for disease.* Semin Perinatol, 1997. **21**(5): p. 351-66.

237. Fielden, E.M., et al., *Mechanism of action of superoxide dismutase from pulse radiolysis and electron paramagnetic resonance. Evidence that only half the active sites function in catalysis.* Biochem J, 1974. **139**(1): p. 49-60.

238. Brune, B., *Nitric oxide: NO apoptosis or turning it ON?* Cell Death Differ, 2003. **10**(8): p. 864-9.

239. Crow, J.P. and J.S. Beckman, *Reactions between nitric oxide, superoxide, and peroxynitrite: footprints of peroxynitrite in vivo.* Adv Pharmacol, 1995. **34**: p. 17-43.

240. Huie, R.E. and S. Padmaja, *The reaction of no with superoxide.* Free Radic Res Commun, 1993. **18**(4): p. 195-9.

241. Wiseman, H. and B. Halliwell, *Damage to DNA by reactive oxygen and nitrogen species: role in inflammatory disease and progression to cancer.* Biochem J, 1996. **313 (Pt 1)**: p. 17-29.

242. Szabo, C., H. Ischiropoulos, and R. Radi, *Peroxynitrite: biochemistry, pathophysiology and development of therapeutics.* Nat Rev Drug Discov, 2007. **6**(8): p. 662-80.

243. Hidalgo, C. and P. Donoso, *Crosstalk between calcium and redox signaling: from molecular mechanisms to health implications.* Antioxid Redox Signal, 2008. **10**(7): p. 1275-312.

244. Yan, Y., et al., *Cross-talk between calcium and reactive oxygen species signaling.* Acta Pharmacol Sin, 2006. **27**(7): p. 821-6.

245. Banfi, B., et al., *A Ca(2+)-activated NADPH oxidase in testis, spleen, and lymph nodes.* J Biol Chem, 2001. **276**(40): p. 37594-601.

246. Cadenas, E. and A. Boveris, *Enhancement of hydrogen peroxide formation by protophores and ionophores in antimycin-supplemented mitochondria.* Biochem J, 1980. **188**(1): p. 31-7.

247. Sousa, S.C., et al., *Ca2+-induced oxidative stress in brain mitochondria treated with the respiratory chain inhibitor rotenone.* FEBS Lett, 2003. **543**(1-3): p. 179-83.

248. Zoratti, M. and I. Szabo, *The mitochondrial permeability transition.* Biochim Biophys Acta, 1995. **1241**(2): p. 139-76.

249. Petrosillo, G., et al., *Ca2+-induced reactive oxygen species production promotes cytochrome c release from rat liver mitochondria via mitochondrial permeability transition (MPT)-dependent and MPT-independent mechanisms: role of cardiolipin.* J Biol Chem, 2004. **279**(51): p. 53103-8.

250. Banfi, B., et al., *Mechanism of Ca2+ activation of the NADPH oxidase 5 (NOX5).* J Biol Chem, 2004. **279**(18): p. 18583-91.

251. Pourrut, B., et al., *Potential role of NADPH-oxidase in early steps of lead-induced oxidative burst in Vicia faba roots.* J Plant Physiol, 2008. **165**(6): p. 571-9.

252. Jiang, F., Y. Zhang, and G.J. Dusting, *NADPH oxidase-mediated redox signaling: roles in cellular stress response, stress tolerance, and tissue repair.* Pharmacol Rev, 2011. **63**(1): p. 218-42.

253. LaFerla, F.M., *Calcium dyshomeostasis and intracellular signalling in Alzheimer's disease.* Nat Rev Neurosci, 2002. **3**(11): p. 862-72.

254. Pinton, P., et al., *Calcium and apoptosis: ER-mitochondria Ca2+ transfer in the control of apoptosis.* Oncogene, 2008. **27**(50): p. 6407-18.

255. Giorgi, C., et al., *Ca2+ signaling, mitochondria and cell death.* Curr Mol Med, 2008. **8**(2): p. 119-30.

256. Choi, D.W., *Calcium: still center-stage in hypoxic-ischemic neuronal death.* Trends Neurosci, 1995. **18**(2): p. 58-60.

257. Martikainen, P., et al., *Programmed death of nonproliferating androgen-independent prostatic cancer cells.* Cancer Res, 1991. **51**(17): p. 4693-700.

258. Kruman, I., Q. Guo, and M.P. Mattson, *Calcium and reactive oxygen species mediate staurosporine-induced mitochondrial dysfunction and apoptosis in PC12 cells.* J Neurosci Res, 1998. **51**(3): p. 293-308.

259. Lynch, K., et al., *Basic fibroblast growth factor inhibits apoptosis of spontaneously immortalized granulosa cells by regulating intracellular free calcium levels through a protein kinase Cdelta-dependent pathway.* Endocrinology, 2000. **141**(11): p. 4209-17.

260. Pinton, P. and R. Rizzuto, *Bcl-2 and Ca2+ homeostasis in the endoplasmic reticulum.* Cell Death Differ, 2006. **13**(8): p. 1409-18.

261. Bindokas, V.P., et al., *Superoxide production in rat hippocampal neurons: selective imaging with hydroethidine.* J Neurosci, 1996. **16**(4): p. 1324-36.

262. Li, N., et al., *Mitochondrial complex I inhibitor rotenone induces apoptosis through enhancing mitochondrial reactive oxygen species production.* J Biol Chem, 2003. **278**(10): p. 8516-25.

263. Chance, B., H. Sies, and A. Boveris, *Hydroperoxide metabolism in mammalian organs.* Physiol Rev, 1979. **59**(3): p. 527-605.

264. Kojima, H., et al., *Development of a fluorescent indicator for nitric oxide based on the fluorescein chromophore.* Chem Pharm Bull (Tokyo), 1998. **46**(2): p. 373-5.

265. Itoh, Y., et al., *Determination and bioimaging method for nitric oxide in biological specimens by diaminofluorescein fluorometry.* Anal Biochem, 2000. **287**(2): p. 203-9.

266. Grynkiewicz, G., M. Poenie, and R.Y. Tsien, *A new generation of Ca2+ indicators with greatly improved fluorescence properties.* J Biol Chem, 1985. **260**(6): p. 3440-50.

267. Gee, K.R., et al., *Chemical and physiological characterization of fluo-4 Ca(2+)-indicator dyes.* Cell Calcium, 2000. **27**(2): p. 97-106.

268. Lytton, J., M. Westlin, and M.R. Hanley, *Thapsigargin inhibits the sarcoplasmic or endoplasmic reticulum Ca-ATPase family of calcium pumps.* J Biol Chem, 1991. **266**(26): p. 17067-71.

269. Jensen, T.P., L.E. Buckby, and R.M. Empson, *Expression of plasma membrane Ca2+ ATPase family members and associated synaptic proteins in acute and cultured organotypic hippocampal slices from rat.* Brain Res Dev Brain Res, 2004. **152**(2): p. 129-36.

270. Rang, H.P., *Pharmacology.* , 2003: Edinburgh: Churchill Livingstone. p. 53.

271. Probe, m. *Fluo-4 NW Calcium Assay Kits (F36205, F36206): http://probes.invitrogen.com/media/pis/mp36205.pdf*. 2006.

272. Carreras, M.C., et al., *Kinetics of nitric oxide and hydrogen peroxide production and formation of peroxynitrite during the respiratory burst of human neutrophils.* FEBS Lett, 1994. **341**(1): p. 65-8.

273. Zhou, J., et al., *Modulatory effects of quercetin on hypobaric hypoxic rats.* Eur J Pharmacol, 2012. **674**(2-3): p. 450-4.

274. Loke, W.M., et al., *Pure dietary flavonoids quercetin and (-)-epicatechin augment nitric oxide products and reduce endothelin-1 acutely in healthy men.* Am J Clin Nutr, 2008. **88**(4): p. 1018-25.

275. Martinez-Florez, S., et al., *Quercetin attenuates nuclear factor-kappaB activation and nitric oxide production in interleukin-1beta-activated rat hepatocytes.* J Nutr, 2005. **135**(6): p. 1359-65.

276. Kim, Y.H., et al., *LY294002 inhibits LPS-induced NO production through a inhibition of NF-kappaB activation: independent mechanism of phosphatidylinositol 3-kinase.* Immunol Lett, 2005. **99**(1): p. 45-50.

277. Diaz-Guerra, M.J., et al., *Negative regulation by phosphatidylinositol 3-kinase of inducible nitric oxide synthase expression in macrophages.* J Immunol, 1999. **162**(10): p. 6184-90.

278. Sengpiel, B., et al., *NMDA-induced superoxide production and neurotoxicity in cultured rat hippocampal neurons: role of mitochondria.* Eur J Neurosci, 1998. **10**(5): p. 1903-10.

279. Hongpaisan, J., C.A. Winters, and S.B. Andrews, *Calcium-dependent mitochondrial superoxide modulates nuclear CREB phosphorylation in hippocampal neurons.* Mol Cell Neurosci, 2003. **24**(4): p. 1103-15.

280. Guzik, T.J., et al., *Calcium-dependent NOX5 nicotinamide adenine dinucleotide phosphate oxidase contributes to vascular oxidative stress in human coronary artery disease.* J Am Coll Cardiol, 2008. **52**(22): p. 1803-9.

281. Missiaen, L., et al., *Hypotonically induced calcium release from intracellular calcium stores.* J Biol Chem, 1996. **271**(9): p. 4601-4.

282. Camello, C., et al., *Calcium leak from intracellular stores--the enigma of calcium signalling.* Cell Calcium, 2002. **32**(5-6): p. 355-61.

283. Hess, P., J.B. Lansman, and R.W. Tsien, *Different modes of Ca channel gating behaviour favoured by dihydropyridine Ca agonists and antagonists.* Nature, 1984. **311**(5986): p. 538-44.

284. Keef, K.D., J.R. Hume, and J. Zhong, *Regulation of cardiac and smooth muscle Ca(2+) channels (Ca(V)1.2a,b) by protein kinases.* Am J Physiol Cell Physiol, 2001. **281**(6): p. C1743-56.

285. Slonim, D.K., *From patterns to pathways: gene expression data analysis comes of age.* Nat Genet, 2002. **32 Suppl**: p. 502-8.

286. Friedman, N., et al., *Using Bayesian networks to analyze expression data.* J Comput Biol, 2000. **7**(3-4): p. 601-20.

287. Friedman, N., *Inferring cellular networks using probabilistic graphical models.* Science, 2004. **303**(5659): p. 799-805.

288. Lauffenburger, J.P.W.D.A., *Bayesian network inference of phosphoproteomic signaling networks*, in *Seventh Annual Workshop on Bayes Applications*2009.

289. Sachs, K., et al., *Bayesian network approach to cell signaling pathway modeling.* Sci STKE, 2002. **2002**(148): p. pe38.

290. *http://en.wikipedia.org/wiki/Bayes'_theorem: Bayes' theorem.*

291. Zhang, L.C.R.-S.W.X.-S., *Biomolecular Networks: Methods and Applications in Systems Biology* Wiley Series, 2009

292. Heckerman, D., *Bayesian Networks for Data Mininig.* Data Mining and knowledge Discovery, 1997. **1**: p. 41.

293. Murphy, K.P., *In praise of Bayes* Economist, 2000.

294. *http://www.itl.nist.gov/div898/handbook/eda/section3/eda3652.htm, Maximum Likelihood*.

295. *http://en.wikipedia.org/wiki/A_priori_(statistics): Prior.*

296. *http://en.wikipedia.org/wiki/Posterior_probability_distribution Posterior probability*.

297. *BAYESIAN PARAMETER ESTIMATION*
http://fish.washington.edu/classes/fish497/Bayesian%20Stats.pdf

298. HECKERMAN, D.M.C.D., *Efficient Approximations for the Marginal Likelihood of Bayesian Networks with Hidden Variables.* Machine Learning, 1997.

299. Jaakkola, H.S.T.S., *On the Dirichlet Prior and Bayesian Regulation.*

300. *Expectation–maximization algorithm:*
http://en.wikipedia.org/wiki/Expectation%E2%80%93maximization_algorithm
.

301. Leray, O.F.P., *Generation of Incompliete Test-Data usinng Bayesinan Networks,* in *IJCNN* 2007: . p. 6.

302. Sebe, N., *Machine learning in computer vision*2005 Springer.

303. D, H., *A tutorial on learning with Bayesian networks.* Learning in Graphical Models, 1998: p. 54.

304. Robinson, *Counting unlabeled acyclic digraphs,* in *Combinatorial Mathematics V*1977, springer. p. 16.

305. *Markov Chain Monte Carlo Method.* *http://support.sas.com/documentation/cdl/en/statug/63033/HTML/default/viewer.htm#statug_introbayes_sect007.htm:Markov*

306. Sahu, S. *Tutorial Lectures on MCMC:* *http://www.soton.ac.uk/~sks/utrecht/mcmc.pdf*. 2000.

307. Rao, R.S.N.T.M.M.R.B., *Bayesian Network Learning with Parameter Constraints.* Journal of Machine Learning Research 7, 2006: p. 25.

308. P.Murphy, K., *The Bayes Net toolbox for Matlab*. Comput Sci Stat 2001(33): p. 20.

309. Sachs, K., *Bayesian network models of biological signaling pathways,* in *Biological Engineering*2006, MIT: Boston.

310. Bédard, M., *Optimal acceptance rates for Metropolis algorithms: Moving beyond 0.234.* 2006.

311. *Tuning the Proposal Distribution:* *http://support.sas.com/documentation/cdl/en/statug/63033/HTML/default/viewer.htm#statug_mcmc_sect022.htm*.

312. Erkanli, L.E.A., *Markov Chain Monte Carlo Approaches to Analysis of Genetic and Environmental Components of Human Developmental Change and G X E Interaction.* Behavior Genetics, 2003. **33**(3).

313. P., R.S.N., *Artificial Intelligence: A Modern Approach*. Prentice Hall 2009.

314. Pryor, W.A. and G.L. Squadrito, *The chemistry of peroxynitrite: a product from the reaction of nitric oxide with superoxide.* Am J Physiol, 1995. **268**(5 Pt 1): p. L699-722.

315. Pechenik, J.A., et al., *Nitric oxide inhibits metamorphosis in larvae of Crepidula fornicata, the slippershell snail.* Biol Bull, 2007. **213**(2): p. 160-71.

316. Rolfe, V. and R.J. Levin, *Enterotoxin Escherichia coli STa activates a nitric oxide-dependent myenteric plexus secretory reflex in the rat ileum.* J Physiol, 1994. **475**(3): p. 531-7.

317. Estevez, A.G. and J. Jordan, *Nitric oxide and superoxide, a deadly cocktail.* Ann N Y Acad Sci, 2002. **962**: p. 207-11.

318. Baehner, R.L., et al., *The role of superoxide anion and hydrogen peroxide in phagocytosis-associated oxidative metabolic reactions.* J Clin Invest, 1975. **56**(3): p. 571-6.

319. Burdon, R.H., *Superoxide and hydrogen peroxide in relation to mammalian cell proliferation.* Free Radic Biol Med, 1995. **18**(4): p. 775-94.

320. Craciun, G., Y. Tang, and M. Feinberg, *Understanding bistability in complex enzyme-driven reaction networks.* Proc Natl Acad Sci U S A, 2006. **103**(23): p. 8697-702.

321. Saez-Rodriguez, J., et al., *Multistability of signal transduction motifs.* IET Syst Biol, 2008. **2**(2): p. 80-93.

322. Samaga, R., et al., *The logic of EGFR/ErbB signaling: theoretical properties and analysis of high-throughput data.* PLoS Comput Biol, 2009. **5**(8): p. e1000438.

323. Liu, J., et al., *Study on mapping quantitative trait loci for animal complex binary traits using Bayesian-Markov chain Monte Carlo approach.* Sci China C Life Sci, 2006. **49**(6): p. 552-9.

324. Garbett, V.Q.S.P., *Not all noise is waste.* Nature Methods, 2010. **7**: p. 4.

325. Bu, D., et al., *Topological structure analysis of the protein-protein interaction network in budding yeast.* Nucleic Acids Res, 2003. **31**(9): p. 2443-50.

326. Possel, H., et al., *2,7-Dihydrodichlorofluorescein diacetate as a fluorescent marker for peroxynitrite formation.* FEBS Lett, 1997. **416**(2): p. 175-8.

327. Keston, A.S. and R. Brandt, *The Fluorometric Analysis of Ultramicro Quantities of Hydrogen Peroxide.* Anal Biochem, 1965. **11**: p. 1-5.

328. Zamek-Gliszczynski, M.J., et al., *Pharmacokinetics of 5 (and 6)-carboxy-2',7'-dichlorofluorescein and its diacetate promoiety in the liver.* J Pharmacol Exp Ther, 2003. **304**(2): p. 801-9.

329. Myhre, O., et al., *Evaluation of the probes 2',7'-dichlorofluorescin diacetate, luminol, and lucigenin as indicators of reactive species formation.* Biochem Pharmacol, 2003. **65**(10): p. 1575-82.

330. Huerta, S., S. Chilka, and B. Bonavida, *Nitric oxide donors: novel cancer therapeutics (review).* Int J Oncol, 2008. **33**(5): p. 909-27.

331. Ledenev, A.N., et al., *A simple assay of the superoxide generation rate with Tiron as an EPR-visible radical scavenger.* Biochem Int, 1986. **13**(2): p. 391-6.

332. Weiss, R.H., et al., *Evaluation of activity of putative superoxide dismutase mimics. Direct analysis by stopped-flow kinetics.* J Biol Chem, 1993. **268**(31): p. 23049-54.

333. Khattab, M.M., *TEMPOL, a membrane-permeable radical scavenger, attenuates peroxynitrite- and superoxide anion-enhanced carrageenan-induced paw edema and hyperalgesia: a key role for superoxide anion.* Eur J Pharmacol, 2006. **548**(1-3): p. 167-73.

334. Battinelli, E. and J. Loscalzo, *Nitric oxide induces apoptosis in megakaryocytic cell lines.* Blood, 2000. **95**(11): p. 3451-9.

335. Ghosh, M., H.D. Wang, and J.R. McNeill, *Tiron exerts effects unrelated to its role as a scavenger of superoxide anion: effects on calcium binding and vascular responses.* Can J Physiol Pharmacol, 2002. **80**(8): p. 755-60.

336. Heikkila, R.E., F.S. Cabbat, and G. Cohen, *In vivo inhibition of superoxide dismutase in mice by diethyldithiocarbamate.* J Biol Chem, 1976. **251**(7): p. 2182-5.

337. Mulsch, A., et al., *Diethyldithiocarbamate inhibits induction of macrophage NO synthase.* FEBS Lett, 1993. **321**(2-3): p. 215-8.

338. Li, D.X., et al., *Diethyldithiocarbamate inhibits iNOS expression in human lens epithelial cells stimulated by IFN-gamma and LPS.* Acta Pharmacol Sin, 2005. **26**(3): p. 359-63.

339. Iyer, A.K., et al., *Antioxidant c-FLIP inhibits Fas ligand-induced NF-kappaB activation in a phosphatidylinositol 3-kinase/Akt-dependent manner.* J Immunol, 2011. **187**(6): p. 3256-66.

340. Wang, L., et al., *The Fas death signaling pathway connecting reactive oxygen species generation and FLICE inhibitory protein down-regulation.* J Immunol, 2008. **180**(5): p. 3072-80.

341. Levrand, S., et al., *Peroxynitrite is a potent inhibitor of NF-{kappa}B activation triggered by inflammatory stimuli in cardiac and endothelial cell lines.* J Biol Chem, 2005. **280**(41): p. 34878-87.

342. Micheau, O., et al., *NF-kappaB signals induce the expression of c-FLIP.* Mol Cell Biol, 2001. **21**(16): p. 5299-305.

343. HECKERMAN, D., *Learning Bayesian Networks: The Combination of Knowledge and Statistical Data.* Machine Learning, 1995(20): p. 7.